Towards Tomography-Controlled Multiphase Flows

A Study of the Dynamics and Real-Time Control in Gas-Liquid Axial Cyclone Separators

Martinez Garcia, Matheus

DOI
10.4233/uuid:1838c850-3cd5-4667-8c6a-5c18b24c0b03

Publication date
2025

Document Version
Final published version

Citation (APA)
Martinez Garcia, M. (2025). *Towards Tomography-Controlled Multiphase Flows: A Study of the Dynamics and Real-Time Control in Gas-Liquid Axial Cyclone Separators*. [Dissertation (TU Delft), Delft University of Technology]. https://doi.org/10.4233/uuid:1838c850-3cd5-4667-8c6a-5c18b24c0b03

Towards Tomography-Controlled Multiphase Flows

A Study of the Dynamics and Real-Time Control in Gas-Liquid Axial Cyclone Separators

Matheus M. Garcia

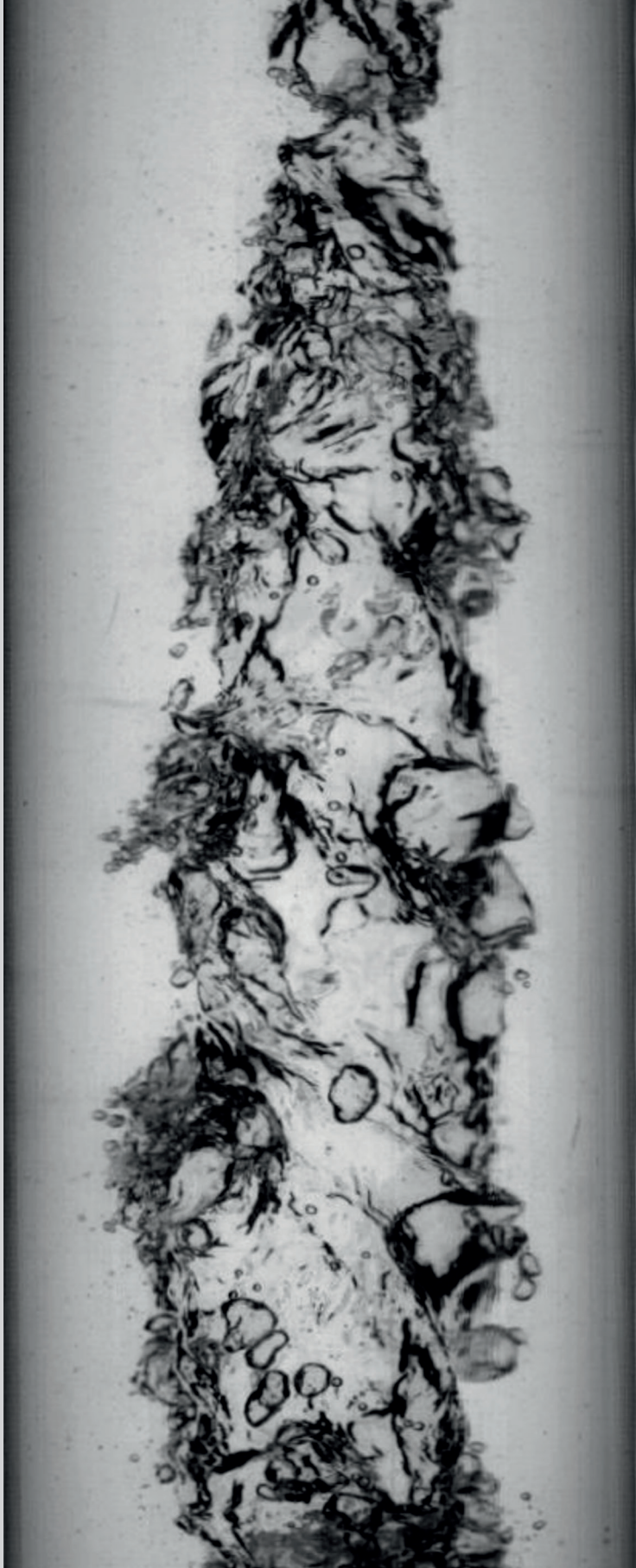

TOWARDS TOMOGRAPHY-CONTROLLED MULTIPHASE FLOWS

A STUDY OF THE DYNAMICS AND REAL-TIME CONTROL IN GAS-LIQUID AXIAL CYCLONE SEPARATORS

TOWARDS TOMOGRAPHY-CONTROLLED MULTIPHASE FLOWS

A STUDY OF THE DYNAMICS AND REAL-TIME CONTROL IN GAS-LIQUID AXIAL CYCLONE SEPARATORS

Dissertation

for the purpose of obtaining the degree of doctor
at Delft University of Technology,
by the authority of the Rector Magnificus prof. dr. ir. T.H.J.J. van der Hagen,
Chair of the Board of Doctorates,
to be defended publicly on
Monday 13 October 2025 at 15:00 o'clock

by

Matheus MARTINEZ GARCIA

Master of Science in Mechanical Engineering,
State University of Campinas, Brazil
born in Jundiaí, Brazil

This dissertation has been approved by the promotors.

Composition of the doctoral committee:

Rector Magnificus,	chairperson
Prof. dr. ir. C.R. Kleijn	Delft University of Technology, promotor
Dr. Eng. L.M. Portela	Delft University of Technology, copromotor

Independent members:

Prof. dr. R.F. Mudde	Delft University of Technology
Prof. dr. ir. R.A.W.M. Henkes	Delft University of Technology
Prof. dr. D. Lohse	University of Twente, Netherlands
Prof. dr. P. Angeli	University College London, United Kingdom
Prof. Dr.-Ing. habil. Dr. h. c. U. Hampel	Helmholtz-Zentrum Dresden-Rossendorf & Dresden University of Technology, Germany

TU Delft

TOMOCON
Smart Tomographic Sensors for Advanced Industrial Process Control

This project has received funding from the European Union's Horizon 2020 research and innovation program under the Marie Skłodowska-Curie grant agreement No 764902.

Keywords: Tomography, Multiphase flow, Dynamics, Real-time control, Gas-liquid, Axial cyclone, Hydrocyclone, Inline fluid separator, Swirl separator, Swirl flow, Electrical resistance tomography, Two-phase flow, Flow patterns, Mechanistic model, Transition criteria, Pressure Drop Ratio

Printed by: Proefschriftspecialist

Front & Back: Picture of a Bursting Column observed in the Axial Cyclone Separator of TU Delft & picture of the experimental setup used in this dissertation, showing the Axial Cyclone Separator, LPO, HPO and Gravity Separators.

ISBN 978-94-93483-05-7

An electronic version of this dissertation is available at
http://repository.tudelft.nl/.

SUMMARY

Tomography can provide non-intrusive measurements of the phase distribution of multiphase flows, typically in the form of images. Tomographic measurements are taken in two steps: data acquisition and image reconstruction. Although the existing hardware can reach relatively fast data acquisitions, the phase distribution reconstruction involves complex calculations that are computationally demanding and, therefore, slow. As consequence, tomographic measurements are traditionally performed acquiring the whole flow data and then processing it offline into phase distribution profiles.

The substantial increase in computation power in the recent years accelerated the image reconstruction of tomography, enabling real-time control applications. The main objective of this thesis is to investigate, for the first time, the possibilities and limitations of tomography-based real-time control of multiphase flows. The investigation is performed in a gas-liquid axial cyclone separator, chosen as representative of quasi-1D multiphase flow processes.

Axial cyclones are composed by (i) a swirl element, where the swirl motion of the mixture is created, (ii) a swirl tube, where the gas-liquid separation takes place due to centripetal forces, and (iii) a pickup tube, designed to capture the lighter phase (gas) around the swirl tube centerline. The separation in axial cyclones is determined by the phase distribution upstream of the pickup tube.

The phase distribution upstream of the pickup tube depends on the swirling gas-liquid flow pattern in the axial cyclone. In chapter 3, the vertical upward swirling gas-liquid pipe-flow patterns were experimentally investigated over a wide range of gas and liquid flow rates and swirl intensities, and mechanistic models for the prediction of the flow pattern transitions were proposed. The analysis performed revealed that the vertical upward swirling gas-liquid pipe-flow patterns can be categorized into four main classes, determined by the swirl impact on the distribution of phases: (i) Non-Columnar flows, (ii) Centered flows, (iii) Columnar flows, and (iv) Swirling Annular flows. Non-Columnar flows are similar to the non-swirling gas-liquid flow patterns (bubbly, slug and churn), occurring in the axial cyclone for weak liquid swirls. As the liquid swirl intensity is increased, the centripetal force imposed in the gas by the liquid causes the agglomeration of the gas regions of bubbly, slug and churn flows around the pipe centerline, characterizing the Centered flow patterns. Columnar flow patterns are obtained with the further increase in the liquid swirl intensity, that results in the coalescence of the gas bubbles into stable gas cores. Swirling Annular flows are formed for high gas velocities, similarly to their non-swirling counterpart. The mechanistic models proposed in chapter 3 to predict the upward vertical swirling gas-liquid pipe-flow pattern transitions showed that the ratio between the centrifugal acceleration of the liquid and gravity, related to the product of the liquid Froude and Swirl numbers, $Fr_l\Omega_l$, is the main quantity describing the transition between Non-Columnar, Centered and Columnar flows; the Swirling Annular flow pattern transition is mainly determined by the gas Froude and Swirl numbers. In the proposed mechanistic models, the flow pattern transitions inside each class are determined by the flow upstream

of the swirl element, being predicted by classical non-swirling mechanistic models.

The tomography-based real-time control of the axial cyclone was investigated in this thesis with an Electrical Resistance Tomography (ERT) sensor that measures the gas-liquid distribution upstream of the pickup tube. Despite the recent increase in computational power, classical ERT algorithms remain too slow compared to the phase distribution dynamics in the axial cyclone. Therefore, a real-time image reconstruction algorithm was proposed in chapter 2 to measure the distribution of phases in Columnar flows. The proposed algorithm reconstructs the flow distribution via simple correlations that relate the electric currents measured by the ERT system to the gas core diameter and centroid position in a cross-section of the axial cyclone. The simplified algorithm, limited to the measurement of the phase distribution of Columnar flows in axial cyclones, is three orders of magnitude faster and up to five times more precise than general non-iterative traditional ERT algorithms based on the inverse problem, reconstructing the gas core diameter and position with an absolute uncertainty of ±8% of the inner diameter of the pipe.

In chapter 4, the ERT system with the novel real-time image reconstruction algorithm was used to study the relation between the time-average gas core diameter upstream of the pickup tube and the efficiency of separation obtained by the axial cyclone. The expectation, prior to the experiments, was that the separation would be maximized for an average gas core diameter equal to the pickup tube diameter, independent of the gas and liquid flow rates in the inlet of the cyclone. However, the results obtained showed that (i) average gas core diameters significantly smaller than the pickup tube diameter are required to maximize the efficiency of separation for flow patterns with strong interface fluctuations, and (ii) the maximum efficiency of separation cannot be described by a single average gas core diameter.

The phase distribution dynamics and real-time control in the axial cyclone were investigated in chapter 5. The results obtained showed that the phase distribution dynamics in the axial cyclone can be split into two components: (i) the intrinsic phase distribution dynamics due to the swirling gas-liquid flow patterns, and (ii) the phase distribution response to external process disturbances, e.g., changes in the flow rates upstream of the swirl element. The intrinsic dynamics are too fast compared to typical flow actuators, such as control valves, and must be filtered out of the calculations of controllers designed to suppress slow external process disturbances in the phase distribution. A tomography-based controller was implemented in the axial cyclone to suppress external process disturbances with time-constants in the order of 10 s in the distribution of phases upstream of the pickup tube. Despite the successful suppression of external disturbances in the local phase distribution, the controller did not significantly improve the efficiency of separation of the axial cyclone due to the large impact of the (uncontrolled) flow pattern fluctuations on the equipment performance.

The results obtained with the axial cyclone suggest that controlling the phase distribution of multiphase flows in relation to external disturbances is insufficient to control the efficiency of the process. Therefore, the way forward towards tomography-controlled multiphase flows relies on the development of fast sensors and actuators to attempt to control the fast flow pattern fluctuations. The full control of the intrinsic flow pattern dynamics is not to be expected due to its chaotic nature. However, fast actuators may be able to act on the largest structures of the flow to improve the efficiency of multiphase flow processes.

SAMENVATTING

Tomografie kan defaseverdeling van meerfasestroming meten zonder de meting te beinvloeden (niet-intrusief), meestal in de vorm van beelden. Tomografische metingen worden in twee stappen uitgevoerd: dataverzameling en beeldreconstructie. Hoewel de bestaande hardware relatief snelle dataverzameling mogelijk maakt, vereist de reconstructie van de faseverdeling complexe berekeningen die veel rekenkracht vereisen en daardoor traag zijn. Als gevolg daarvan worden tomografische metingen traditioneel uitgevoerd door alle stroomgegevens te verzamelen en deze vervolgens offline, na de meting, te verwerken tot faseverdelingsprofielen.

De aanzienlijke toename van de rekenkracht in de afgelopen jaren heeft de beeldreconstructie van tomografie versneld, waardoor realtime besturingstoepassingen mogelijk zijn geworden. Het belangrijkste doel van dit proefschrift is om voor het eerst tomografie gebaseerde realtime besturing van meerfasestromingen te onderzoeken, en de mogelijkheden en beperkingen daarvan. Het onderzoek wordt uitgevoerd in een gas-vloeistof axiale cycloonscheider, gekozen als representatief voor kwasi-1D meerfasestromingsprocessen.

Axiale cyclonen bestaan uit (i) een swirl-element, waar de wervelende beweging van het mengsel wordt gecreëerd, (ii) een swirl-buis, waar de scheiding tussen gas en vloeistof plaatsvindt als gevolg van centripetale krachten, en (iii) een opvangbuis, die is ontworpen om de lichtere fase (gas) rond de centerlijn van de wervelbuis op te vangen. De scheiding in axiale cyclonen wordt bepaald door de faseverdeling na de opvangbuis.

De faseverdeling na de opvangbuis hangt af van het wervelende gas-vloeistofstromingspatroon in de axiale cycloon. In hoofdstuk 3 worden de verticale opwaartse wervelende gas-vloeistofpijpstromingspatronen experimenteel onderzocht over een breed bereik van gas- en vloeistofsnelheden en wervelintensiteiten, en worden mechanistische modellen voor de voorspelling van de stromingspatroonovergangen voorgesteld. De analyse toonde aan dat de verticale opwaartse wervelende gas-vloeistofstroompatronen in vier hoofdklassen kunnen worden ingedeeld, bepaald door de invloed van de werveling op de faseverdeling: (i) niet-kolomvormige stromingen, (ii) gecentreerde stromingen, (iii) kolomvormige stromingen en (iv) wervelende ringvormige stromingen. Niet-kolomvormige stromingen zijn vergelijkbaar met de niet-wervelende gas-vloeistofstromingspatronen (bubbly, slug en churn), die voorkomen in de axiale cycloon bij zwakke vloeistofwervelingen. Naarmate de intensiteit van de vloeistofwerveling toeneemt, veroorzaakt de centripetale kracht die door de vloeistof op het gas wordt uitgeoefend, de agglomeratie van de gasgebieden van bubbly-, slug- en churn-stromingen rond de hartlijn van de buis, wat kenmerkend is voor de gecentreerde stromingspatronen. Kolomvormige stromingspatronen worden verkregen bij een verdere toename van de intensiteit van de vloeistofwerveling, wat resulteert in de coalescentie van de gasbellen tot stabiele gaskernen. Wervelende ringvormige stromingen worden gevormd bij hoge gassnelheden, vergelijkbaar met hun niet-wervelende tegenhangers. De mechanistische modellen die worden voorgesteld in hoofdstuk 3 om de overgangen tussen opwaartse verticale wervelende gas-vloeistof-pijpstromingspatronen

te voorspellen, tonen aan dat de verhouding tussen de centrifugale versnelling van de vloeistof en de zwaartekracht, gerelateerd aan het product van de Froude- en wervelgetallen van de vloeistof, $Fr_l\Omega_l$, de belangrijkste grootheid is die de overgang tussen niet-kolomvormige, gecentreerde en kolomvormige stromingen beschrijft; De overgang naar een wervelende ringvormige stroming wordt voornamelijk bepaald door de gas-Froude- en wervelgetallen. In de voorgestelde mechanistische modellen worden de overgangen in het stromingspatroon binnen elke klasse bepaald door de stroming na het wervelelement, die wordt voorspeld door klassieke mechanistische modellen zonder werveling.

In dit proefschrift word de op tomografie gebaseerde realtime regeling van de axiale cycloon onderzocht met behulp van een Electrical Resistance Tomography (ERT)-sensor die de gas-vloeistofverdeling stroomopwaarts van de opvangbuis meet. Ondanks de recente toename in rekenkracht blijven klassieke ERT-algoritmen te traag in vergelijking met de fasenverdelingsdynamiek in de axiale cycloon. Daarom word in hoofdstuk 2 een algoritme voor realtime beeldreconstructie voorgesteld om de verdeling van fasen in kolomstromingen te meten. Het voorgestelde algoritme reconstrueert de stromingsverdeling via eenvoudige correlaties die de door het ERT-systeem gemeten elektrische stromen relateren aan de gaskerdiameter en de zwaartepuntpositie in een dwarsdoorsnede van de axiale cycloon. Het vereenvoudigde algoritme, dat beperkt is tot het meten van de faseverdeling van kolomstromingen in axiale cyclonen, is drie ordes van grootte sneller en tot vijf keer nauwkeuriger dan algemene niet-iteratieve traditionele ERT-algoritmen op basis van het inverse probleem, en reconstrueert de diameter en positie van de gaskern met een absolute onzekerheid van ±8% van de binnendiameter van de buis.

In hoofdstuk 4 word het ERT-systeem met het nieuwe algoritme voor realtime beeldreconstructie gebruikt om de relatie te bestuderen tussen de tijdgemiddelde gaskerndiameter na de opvangbuis en de efficiëntie van de scheiding die werd verkregen door de axiale cycloon. Voorafgaand aan de experimenten was de verwachting dat de scheiding maximaal zou zijn bij een gemiddelde gaskerndiameter die gelijk was aan de diameter van de opvangbuis, onafhankelijk van de gas- en vloeistofstroomsnelheden in de inlaat van de cycloon. De verkregen resultaten toonden echter aan dat (i) gemiddelde gaskerndiameters die aanzienlijk kleiner zijn dan de diameter van de opvangbuis nodig zijn om de scheidingsefficiëntie te maximaliseren voor stromingspatronen met sterke interfacefluctuaties, en (ii) de maximale scheidingsefficiëntie niet kan worden beschreven door één enkele gemiddelde gaskerndiameter.

In hoofdstuk 5 worden de fasenverdelingsdynamica en realtimeregeling in de axiale cycloon onderzocht. De verkregen resultaten toonden aan dat de fasenverdelingsdynamica in de axiale cycloon kan worden opgesplitst in twee componenten: (i) de intrinsieke fasenverdelingsdynamica als gevolg van de wervelende gas-vloeistofstromingspatronen, en (ii) de fasenverdelingsrespons op externe procesverstoringen, bijvoorbeeld veranderingen in de stroomsnelheden na het wervelelement. De intrinsieke dynamica is te snel in vergelijking met typische stromingsactuatoren, zoals regelkleppen, en moet worden weggefilterd uit de berekeningen van regelaars die zijn ontworpen om langzame externe procesverstoringen in de faseverdeling te onderdrukken. Een op tomografie gebaseerde regelaar werd geïmplementeerd in de axiale cycloon om externe procesverstoringen met tijdconstanten in de orde van 10 s in de verdeling van fasen stroomopwaarts van de opvangbuis te onderdrukken. Ondanks de succesvolle onderdrukking van externe verstoringen in de lokale

faseverdeling, verbeterde de regelaar de efficiëntie van de scheiding van de axiale cycloon niet significant vanwege de grote invloed van de (ongecontroleerde) stromingspatroonfluctuaties op de prestaties van de apparatuur.

De resultaten die met de axiale cycloon zijn verkregen, suggereren dat het beheersen van de faseverdeling van meerfasestromingen in relatie tot externe verstoringen onvoldoende is om de efficiëntie van het proces te beheersen. Daarom is de weg naar tomografiegecontroleerde meerfasestromingen afhankelijk van de ontwikkeling van snelle sensoren en actuatoren om de snelle fluctuaties in het stromingspatroon te beheersen. Volledige controle over de intrinsieke dynamiek van het stromingspatroon is vanwege het chaotische karakter ervan niet te verwachten. Snelle actuators zouden echter kunnen worden gebruikt om de grootste structuren van de stroming om de efficiëntie van meerfasestromingsprocessen te verbeteren.

Contents

NOMENCLATURE

Greek Symbols

α	Gas fraction	[-]
α_{agg}	Gas fraction of the agglomerated bubbly region	[-]
α_{up}	Gas fraction of the upstream flow	[-]
β	Azimuthal velocity profile parameter	[-]
γ	Surface tension	[$\mathrm{N\,m^{-1}}$]
δ	Normalized gas core diameter variation from changes in the LPO valve	[-]
ϵ	Normalized intrinsic gas core diameter dynamics	[-]
ε	Volume fraction	[-]
ζ	Normalized gas core diameter variation from external disturbances	[-]
η	Overall efficiency of separation	[-]
θ	Azimuthal position	[rad]
θ_i	Azimuthal position of the gas core centroid	[rad]
θ_{ert}	Azimuthal position of the gas core measured by ERT	[rad]
ϑ	Angles of the refraction correction algorithm	[rad]
Λ	Distance between the camera and the pipe centerline	[m]
λ	Constant of proportionality of bubble-induced turbulence	[-]
μ	Dynamic viscosity	[Pa s]
ν	Kinematic viscosity	[$\mathrm{m^2\,s^{-1}}$]
ξ_g	Fraction of the total gas mass flow rate captured by the pickup tube	[-]
ξ_l	Fraction of the total liquid flow rate captured by the outer tube	[-]
ρ	Density	[$\mathrm{kg\,m^{-3}}$]
$\sigma(\alpha)$	Standard deviation of the gas fraction	[-]
$\sigma(\imath)$	Standard deviation of the normalized electric current	[-]
$\sigma(\widehat{d}_{ert})$	Standard deviation of the filtered normalized gas core diameter	[-]

$\sigma(d_{ert})$	Standard deviation of the normalized gas core diameter	[-]
$\sigma(d_i)$	Standard deviation of the gas core diameter	[m]
τ	Time constant	[s]
τ_f	Time constant of the low pass filter	[s]
$\tau_{r\theta}$	Azimuthal shear-stress	[Pa]
τ_{rx}	Axial shear-stress	[Pa]
τ_t	Total shear-stress	[Pa]
ϕ_{se}	Final angle of the swirl element vanes	[rad]
χ	Process conditions	[-]
Ω	Swirl number	[-]
ω	Angular frequency	[rad s^{-1}]
ω_p	Pump speed	[rad s^{-1}]
Ω_{se}	Geometrical swirl number	[-]

Roman Symbols

A	Cross-sectional area of the pipe	[m^2]
A_c	Cross-sectional area of the continuous phase	[m^2]
a_m	m-th coefficient of the transfer function denominator	
A_{gs}	Cross-sectional area of the gravity separators	[m]
b_n	n-th coefficient of the transfer function numerator	
C	Controller transfer function	
c	Speed of the interface waves	[m s^{-1}]
C_σ	Gas core standard deviation coefficient	[-]
C_d	Drag coefficient	[-]
C_f	Interface friction factor coefficient	[-]
$\tilde{D}_i$	Disturbed gas core diameter	[m]
$\widehat{d}_{ert}$	Filtered normalized gas core diameter	[-]
D	Inner diameter of the pipe	[m]
d	Normalized gas core diameter in the ERT cross-section	[-]

D_b	Diameter of the swirl element body	[m]
d_b	Bubble diameter	[m]
D_i	Average gas core diameter	[m]
d_i	Gas core diameter	[m]
d_p	Particle diameter	[m]
d_{ert}	Normalized gas core diameter measured by ERT	[-]
d_{ph}	Phantom diameter	[m]
D_{se}	Outer diameter of the swirl element	[m]
$\mathbf{e_r}$	Unit vector in the radial direction	[-]
$\mathbf{e_y}$	Unit vector in the y-direction	[-]
e	Error signal	[-]
Eo	Eötvös number	[-]
$\mathbf{F_b}$	Buoyancy force	[N]
f	Frequency	[Hz]
$f(t)$	Continuous-time function	[-]
$f[k]$	Sequence	[-]
f_i	Interface friction factor	[-]
F_r'	Drag force fluctuations due to turbulent eddies	[N]
f_w	Wall friction factor	[-]
F_{cp}	Centripetal force	[N]
f_{ns}	Friction factor of non-swirling flows	[-]
Fr	Froude number	[-]
Fr_{gls}	Froude number of the gas in the liquid slugs	[-]
$\mathbf{g}$	Gravity vector	[$\mathrm{m\,s^{-2}}$]
G	Conductance	[S]
g	Gravity	[$\mathrm{m\,s^{-2}}$]
h_l	Liquid level	[m]
h_{gs}	Height of the gravity separators	[m]

H	Filter transfer function	
h	Amplitude of the interface waves	[m]
h_{sep}	Distance that the particles must travel for phase separation	[m]
$\imath$	Normalized electric current	[-]
$\langle \imath \rangle$	Average normalized electric current	[-]
I	Electric current	[A]
i	Imaginary unit ($i \triangleq \sqrt{-1}$)	[-]
j	Superficial velocity	[$\mathrm{m\,s^{-1}}$]
K	Controller gain	
k	Sample number	[-]
K_{col}	Coefficient of the Columnar flow pattern transition	[-]
K_{seg}	Coefficient of the Segmented Column flow pattern transition	[-]
$\dot{L}$	Integral flow of angular momentum	[$\mathrm{kg\,m^2\,s^{-2}}$]
ℓ_{se}	Terminal helical pitch of the swirl element vanes	[m]
$\mathscr{L}\{f(t)\}(s)$	Laplace transform of the function $f(t)$	
L_{gs}	Gravity separator length	[m]
l_{slug}	Development length of slug flows	[m]
L_{st}	Swirl tube length	[m]
l_{up}	Pipe length with gas-liquid flow upstream of the swirl element	[m]
m	Integer index	[-]
N	Number of electrodes of the ERT system	[-]
n	Integer index	[-]
n_a	Refractive index of air	[-]
n_p	Refractive index of the pipe wall	[-]
n_w	Refractive index of water	[-]
$\tilde{p}$	Disturbed pressure	[Pa]
P	Plant transfer function	
p	Pressure	[Pa]

p_c	Control pressure	[Pa]
PDR	Pressure Drop Ratio	[-]
q	Volume flow rate	[$m^3\,s^{-1}$]
R	Pipe inner radius	[m]
r	Radial position	[m]
R_b	Radius of the swirl element body	[m]
R_c	Radius of the solid body-uniform azimuthal velocity transition	[m]
R_i	Average gas core radius	[m]
r_i	Radial position of the gas core centroid	[m]
R_{agg}	Radius of the agglomerated bubbly region	[m]
r_{cross}	Cross-correlation coefficient	[-]
$r_{d_{ert}}$	Reference normalized gas core diameter	[-]
r_{ert}	Normalized radial position of the gas core measured by ERT	[-]
R_o	Outer pipe radius	[m]
r_{ph}	Radial position of the phantom centroid	[m]
R_{se}	Outer radius of the swirl element	[m]
$r_{x_{lpo}}$	Reference dimensionless LPO valve diaphragm position	[-]
Re	Reynolds number	[-]
s	Laplace variable	[$rad\,s^{-1}$]
T	Time duration of a measurement	[s]
t	Time	[s]
T_d	Cross-correlation delay	[s]
T_i	Integration time	[s]
T_s	Sample time	[s]
T_{res}	Residence time	[s]
T_{sep}	Time required for phase separation	[s]
T_{wms}	Wire-mesh sensor sample time	[s]
$\mathbf{U}$	Velocity vector	[$m\,s^{-1}$]

$\tilde{U}$	Disturbed velocity	$[\mathrm{m\,s^{-1}}]$
U	Velocity magnitude	$[\mathrm{m\,s^{-1}}]$
u	System input in Appendix D	
u	Velocity profile ($u(r,x)$)	$[\mathrm{m\,s^{-1}}]$
U_t	Total velocity	$[\mathrm{m\,s^{-1}}]$
U_{0B}	Rise velocity of bubbles in stagnant liquids	$[\mathrm{m\,s^{-1}}]$
U_{0TB}	Rise velocity of Taylor bubbles in stagnant liquids	$[\mathrm{m\,s^{-1}}]$
$U_{\theta 1}$	Azimuthal velocity profile parameter	$[\mathrm{m\,s^{-1}}]$
$U_{\theta 2}$	Azimuthal velocity profile parameter	$[\mathrm{m\,s^{-1}}]$
u_{p_c}	Control pressure input	[Pa]
u'_{rl}	Radial velocity fluctuations in a turbulent liquid	$[\mathrm{m\,s^{-1}}]$
U_{wms}	Gas velocity measured by the double-layer wire-mesh sensor	$[\mathrm{m\,s^{-1}}]$
$\mathcal{V}$	Volume	$[\mathrm{m^3}]$
w	Mass flow rate	$[\mathrm{kg\,s^{-1}}]$
x	Axial position	[m]
x_{hpo}	Normalized diaphragm position of the HPO valve	[-]
x_{lpo}	Normalized diaphragm position of the LPO valve	[-]
y	Position in the direction perpendicular to x	[m]
y	System output in Appendix D	
y_D	y-position of the point D inside the liquid	[m]
y_{ert}	Normalized y-position of the gas core measured by ERT	[-]
y_E	Apparent y-position of the point P in the camera images	[m]
y_{ph}	y-position of the phantom	[m]
y_P	y-position of the point P inside the liquid	[m]
$\mathcal{Z}\{f[k]\}(z)$	Z-transform of the sequence $f[k]$	
z	Z-transform variable	[-]
z_{ert}	Normalized z-position of the gas core measured by ERT	[-]
z_{ph}	z-position of the phantom	[m]

z_P	z-position of the point P inside the liquid	[m]

Superscripts

$'$	Variation

Subscripts

θ	Azimuthal
c	Continuous phase
cam	Camera
g	Gas
hgs	Heavy phase outlet gravity separator
hpo	Heavy phase outlet
i	Interface
in	Inlet
l	Liquid
lgs	Light phase outlet gravity separator
lpo	Light phase outlet
nc	Non-conductive phase
p	Particle
r	Radial component
se	Swirl element
wms	Wire-mesh sensor
x	Axial
y	y-component

Mathematics

$\angle$	Phase
$\ddot{\square}$	Second order time derivative
$\dot{\square}$	First order time derivative
$\overline{\square}$	Time-average
$\square^{(m)}$	Time derivative of order m

$\triangleq$	Equal to by definition
$\lvert\ \rvert$	Magnitude

Abbreviations

ABS	Acrylonitrile Butadiene Styrene
CAD	Computer-Aided Design
EPR	Electro-Pneumatic Regulator
ERT	Electrical Resistance Tomography
GN	Gauss-Newton
HPO	Heavy Phase Outlet
LBP	Linear Back Projection
LPO	Light Phase Outlet
MFC	Mass Flow Controller
ODE	Ordinary Differential Equation
PDE	Partial Differential Equation
PDR	Pressure Drop Ratio
PI	Proportional-Integral
SE	Swirl Element
UDP	User Datagram Protocol
WMS	Wire-Mesh Sensor
ZOH	Zero-Order Holding

CHAPTER 1

INTRODUCTION

Multiphase flows are commonly found in the process and energy industries, for instance, in heat exchangers [1, 2], bubble column reactors [3], nuclear reactors, oil extraction, etc.

The distribution of phases plays a major role in the performance of multiphase flow equipment and, therefore, different techniques have been developed over the last decades to measure the distribution of phases of multiphase flows. Among those is industrial tomography, that stands out for its non-intrusive phase distribution measurements.

Tomographic measurements are performed in two steps: data acquisition and image reconstruction. Many tomographic systems can reach acquisition frequencies compatible with the time-constants of multiphase flows. However, the complex calculations involved in the image reconstruction step considerably reduces the measuring rate of the phase distribution. Therefore, tomographic measurements of multiphase flows have been traditionally performed offline, i.e., with the whole raw data of the flow first acquired and then slowly processed into phase distribution profiles.

Industrial multiphase flow processes are always subjected to process disturbances, such as flow rate or concentration fluctuations in the inlet(s) of the system. These fluctuations propagate downstream via convection, impacting the distribution of phases inside the equipment and, as consequence, its performance. Real-time process controllers are used to minimize the impact of process disturbances on the performance of flow equipment, e.g., by manipulating control valves based on a measured quantity strongly related to the efficiency of the process (controlled variable). Due to the strong connection between the distribution of phases and the efficiency of multiphase flow processes, the distribution of phases is the ideal candidate for controlled variable. However, until recently, the data processing of tomography was too slow for real-time phase distribution measurements, and variables indirectly related to the equipment performance, such as pressure, have been used in the real-time control of multiphase flows.

The computational power has substantially increased in the recent years, reducing the time required for the image reconstruction step of tomography. This opened the door to real-time tomography and real-time tomography-based control applications, potentially allowing a direct control of the phase distribution in multiphase flow processes. It is expected that the introduction of tomography to the real-time control of multiphase flows leads to a better suppression of process disturbances, and maintenance of an optimal equipment performance, than traditional control loops based on indirect flow variables.

The concept of tomography-based real-time control is recent and not yet investigated in literature. In this context, the European Union's Horizon 2020 project "Smart Tomographic Sensors for Advanced Industrial Process Control", TOMOCON, was proposed to investigate the tomography-based real-time control of industrial processes. This PhD the-

sis is part of TOMOCON, and has as its main objective the proof of concept demonstration of tomography-based real-time control of multiphase flows, investigating its possibilities and limitations. A gas-liquid axial cyclone was chosen for the demonstration due to (i) the industrial relevance of cyclones, (ii) the quasi-1D flow behavior inside the equipment, simplifying the study of the flow dynamics and the design and implementation of tomography-based controllers, (iii) the sensitivity of cyclones to process disturbances, and (iv) the small time-constants of the distribution of phases inside the equipment.

The research performed has a multidisciplinary nature, combining the physics behind fluid separation processes, industrial tomography, system dynamics and real-time control. Density-based fluid separation in gravity separators and cyclones are described in section 1.1. An overview of tomography in the measurement of multiphase flows, with focus on Electrical Resistance Tomography, is provided in section 1.2. The fields of fluid separation and tomography are combined into an original electrical resistance tomography-controlled axial cyclone in section 1.3, and the research objectives and thesis outline are presented in section 1.4.

1.1. DENSITY-BASED FLUID SEPARATION PROCESSES

Industrial separation processes commonly rely on the density difference between the mixture components, e.g, in gravity separators and cyclones. Cyclones are a compact alternative to gravity separators, where centripetal accelerations orders of magnitude above gravity are used to separate the mixture. An introduction to gravity separators is fundamental for the complete understanding of the axial cyclone capabilities, being provided in subsection 1.1.1.

1.1.1. GRAVITY SEPARATORS

Gravity separators are the simplest equipment available for the separation of mixtures of phases with different densities. In the oil and gas industry, gravity separators are large vessels (typically reaching diameters up to 3-4 m and lengths up to 20-25 m [4, 5]) where the phases are separated by gravitational effects. An example of a gravity separator for three-phase mixtures is illustrated in Figure 1.1.

The phases in the separator are categorized as dispersed (solid particles, gas bubbles or liquid droplets) or continuous (surrounding fluid). The vertical balance of linear momentum in the gravity separator at low dispersed phase concentrations (dilute flow [6]) results in a hydrostatic pressure distribution inside the continuous phase,

$$\frac{\partial p}{\partial y} = -\rho_c g, \tag{1.1}$$

responsible for the well-known Buoyancy force $\mathbf{F_b}$ on the dispersed phase particles (bubbles, droplets or solids) present in the fluid:

$$\mathbf{F_b} = \rho_c g \mathcal{V}_p \mathbf{e_y} \tag{1.2}$$

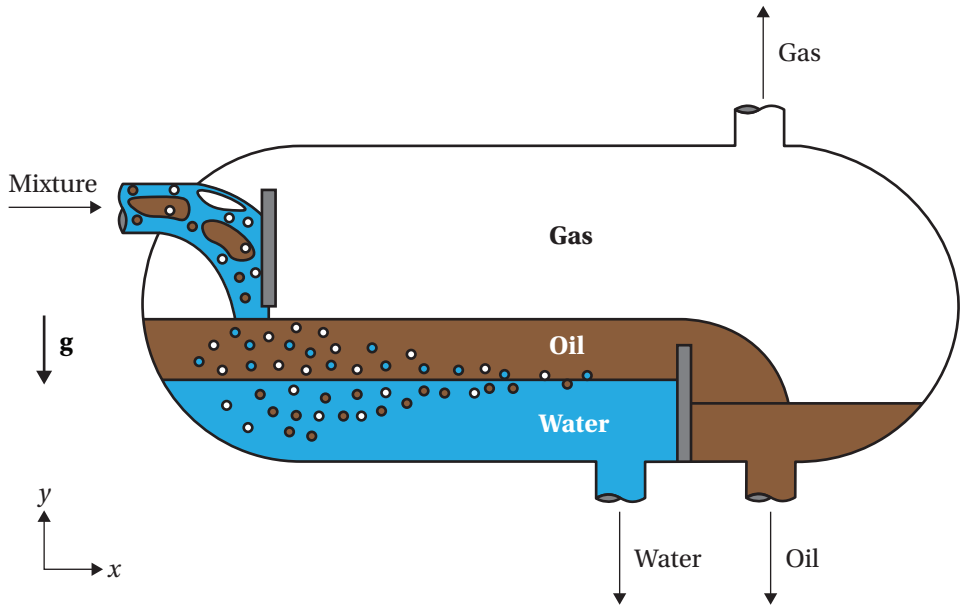

Figure 1.1: Illustration of a gravity separator for water-oil-gas mixtures.

The rise/settling velocity of particles is determined by the balance between buoyancy, weight and drag acting on it[1]. For a single spherical particle, this balance of forces leads to the slip velocity between the particle and the continuous phase:

$$|\mathbf{U_p} - \mathbf{U_c}| \left(U_{yp} - U_{yc}\right) = \frac{4}{3} \frac{\left(\rho_c - \rho_p\right)}{\rho_c} \frac{d_p g}{C_d} \tag{1.3}$$

The slip velocity $|\mathbf{U_p} - \mathbf{U_c}|$ is only significant in the vertical direction, due to the absence of external driving forces in the remaining directions. Additionally, the vertical velocity of the continuous phase, U_{yc}, is negligible in gravity separators, simplifying Equation 1.3 to:

$$|U_{yp}| U_{yp} = \frac{4}{3} \frac{\left(\rho_c - \rho_p\right)}{\rho_c} \frac{d_p g}{C_d} \tag{1.4}$$

Equation 1.4 shows that the dispersed phase rises if its density ρ_p is lower than the density of the continuous phase ρ_c, e.g., for bubbles in liquids, or settles if its density is larger than the density of the continuous fluid, e.g., for solid particles in gases. The particles do not slip if the dispersed and continuous phases have the same density.

The drag coefficient C_d of the particle is a function of the particle Reynolds number,

$$Re_p \triangleq \frac{|\mathbf{U_p} - \mathbf{U_c}| d_p}{\nu_c}, \tag{1.5}$$

[1]The particle acceleration, virtual mass force and Basset force are negligible in gravity separators and cyclones [7–9]

being well approximated by

$$C_d = \frac{24}{Re_p}\left(1 + 0.15 Re_p^{0.687}\right) + \frac{0.42}{1 + 4.25 \cdot 10^4 Re_p^{-1.16}} \tag{1.6}$$

for $Re_p < 3 \cdot 10^5$ [7]. The drag coefficient is presented as function of Re_p in Figure 1.2.

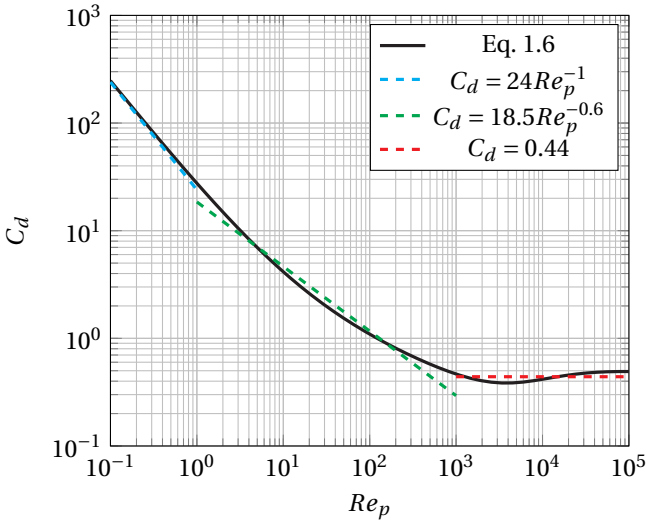

Figure 1.2: Drag Coefficient of a sphere as function of the Reynolds number. Continuous line: Equation 1.6 [7]. Dashed lines: simple drag coefficient approximations [10].

Three drag coefficient approximations from Flemmer and Banks [10] are used to better illustrate the impact of the density difference and gravity on the separation of the phases:

i. The drag coefficient tends to the Stokes' law for very low Reynolds numbers,

$$C_d = \frac{24}{Re_p}, \tag{1.7}$$

providing a reasonable approximation of the drag coefficient for $Re_p < 1$. Combining Equations 1.4 and 1.7 leads to

$$U_{yp} = \frac{1}{18}\frac{(\rho_c - \rho_p)}{\rho_c}\frac{d_p^2 g}{\nu_c}, \tag{1.8}$$

showing that small particles rise/settle with a velocity proportional to gravity times the particle size squared.

ii. The drag coefficient can be approximated to

$$C_d \approx \frac{18.5}{Re_p^{0.6}} \tag{1.9}$$

in the range $1 \leq Re_p < 1000$, leading to the particle rising/settling velocity:

$$U_{yp} \approx 0.15 \frac{\rho_c - \rho_p}{|\rho_c - \rho_p|} \left(\frac{|\rho_c - \rho_p|}{\rho_c} \right)^{5/7} \frac{d_p^{8/7} g^{5/7}}{\nu_c^{3/7}} \tag{1.10}$$

Equation 1.10 shows that the departure from the Stokes regime leads to a reduction in the slip velocity dependency on gravity from a power of one to a power of (around) 5/7, and on the particle diameter from a power of 2 to a power of (around) 8/7.

iii. The drag coefficient is approximately 0.44 in the range $10^3 \leq Re_p < 2 \cdot 10^5$, resulting in the dispersed phase slip velocity:

$$U_{yp} \approx 1.74 \frac{\rho_c - \rho_p}{|\rho_c - \rho_p|} \left(\frac{|\rho_c - \rho_p|}{\rho_c} \right)^{1/2} d_p^{1/2} g^{1/2} \tag{1.11}$$

Equation 1.11 shows that the slip velocity of large particles, with approximately constant C_d, scales with the square root of gravity times the particle diameter.

The dispersed phase slip velocity obtained from Equations 1.4 and 1.6, and its approximation by Equations 1.8, 1.10 and 1.11, are presented as function of the particle diameter in Figure 1.3 for multiple dispersed-continuous phase combinations.

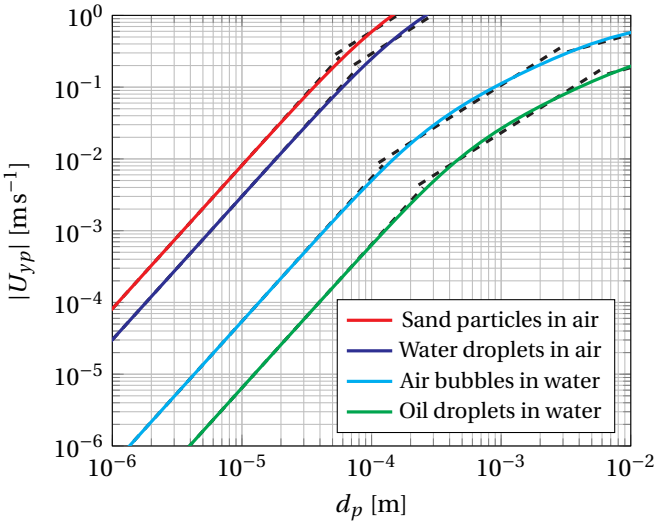

Figure 1.3: Rising/settling velocity of different mixtures in gravity separators. Continuous lines: slip velocity computed with C_d from Equation 1.6. Dashed lines: slip velocity approximation by Equations 1.8, 1.10 and 1.11. Plots based on an air density of 1.2 kg m^{-3} and kinematic viscosity of $15 \cdot 10^{-6}$ m^2 s^{-1}, water density of 998 kg m^{-3} and kinematic viscosity of $1 \cdot 10^{-6}$ m^2 s^{-1}, oil density of 880 kg m^{-3} [11] and dust density of 2700 kg m^{-3} [8].

As shown in Figure 1.3, the slip velocity in dispersed liquid-liquid flows is about one order of magnitude lower than the slip velocity of gases in liquids, and about three orders

of magnitude lower than the slip velocity of solid particles and liquid droplets in gases for the same particle size, due to the low density and dynamic viscosity of gases compared to liquids and solids. It is worth mentioning that the slip velocity of deformable particles (large bubbles and droplets) deviates from the spherical drag coefficient correlation due to the changes in the geometry of the dispersed phase, that can become ellipsoidal, spherical-cap, etc [7].

The time required for the separation in gravity separators depends on the distance h_{sep} that the dispersed phase must travel vertically to reach the interface between the phases, divided by the vertical velocity of the particles:

$$T_{sep} = \frac{h_{sep}}{U_{yp}} \tag{1.12}$$

Equation 1.12 shows that the time required for the separation scales with the inverse of the slip velocity, showing that large particles are separated substantially faster than small particles based on Figure 1.3 (or Equations 1.8, 1.10 and 1.11).

Since the particles move in the horizontal direction with the continuous phase velocity U_{xc}, the residence time of the dispersed phase in the separator is described by:

$$T_{res} = \frac{L_{gs}}{U_{xc}} = \frac{A_c L_{gs}}{q_c}, \tag{1.13}$$

where A_c is the cross-sectional area of the continuous phase, L_{gs} is the length of the gravity separator and q_c is the flow rate of the continuous phase. Equation 1.13 shows that long and wide vessels are necessary to obtain a high purity in the outlet streams of gravity separators, since the gravity separator dimensions and flow rate determine T_{res}, the separation requires $T_{res} \geq T_{sep}$, and T_{sep} increases when decreasing the particle size.

In summary, this subsection showed that:

- The slip velocity in gravity separators is directly related to the density difference between the phases, and phases with similar density cannot be separated by gravity.
- Small particles are harder to separate in gravity separators than large particles, particularly in the Stokes regime, due to the scaling of the slip velocity with the particle diameter squared. The dependency of the slip velocity on the particle size decreases as the particle size increases, stabilizing in a square root relation for large particles.
- Similarly to the particle size, the dependency of the process on gravity decreases as the particle size increases, departing from a linear relation in the Stokes regime to a square root relation for large particles.
- The separation velocity scales with the inverse of the continuous phase viscosity in the Stokes regime. The dependency of the slip velocity on the viscosity decreases as the particle size increases, ultimately leading to a viscosity-independent velocity for sufficiently large particles.
- The time required for the separation in gravity separators quickly increases with the decrease in the dispersed phase particle diameter, in practice leading to (i) large vessels to maximize the residence time of the dispersed phase in the separator, and (ii) a minimum particle size that can be separated in continuous processes.

1.1.2. CYCLONES

Cyclones have been used for many decades in the separation of immiscible phases of different densities. The equipment was initially introduced for the removal of solid particles from gases, and later adapted to fluid (liquid-liquid and gas-liquid) separation [8]. Figure 1.4 illustrates three different cyclone geometries commonly found in industry. Figure 1.4a corresponds to a tangential cyclone of conical geometry, Figure 1.4b to a tangential cyclone of cylindrical geometry, and Figure 1.4c to an axial cyclone of cylindrical geometry.

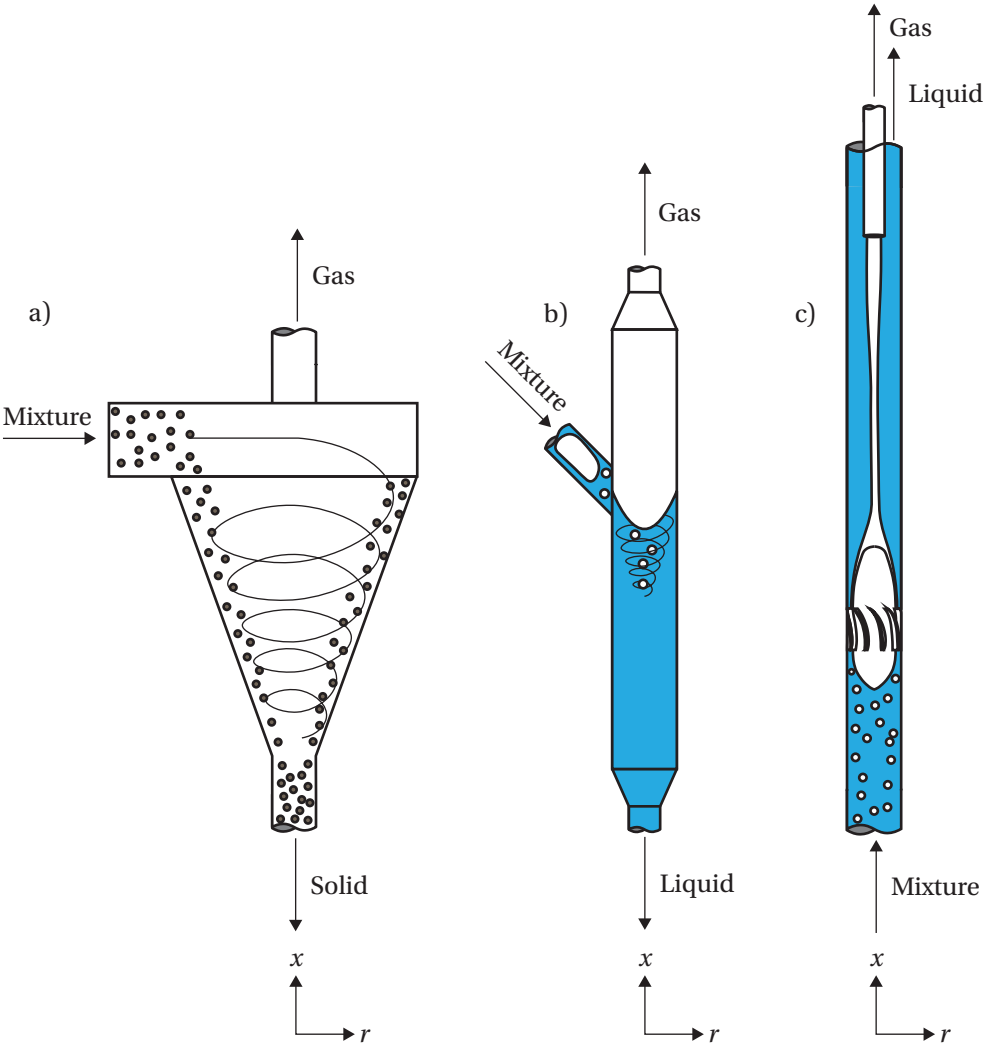

Figure 1.4: Cyclone geometries commonly found in industry. a) Conic gas-solid tangential cyclone, b) Cylindrical gas-liquid tangential cyclone, c) Cylindrical gas-liquid axial cyclone.

In the Oil and Gas industry, de-oiling (liquid-liquid) cyclones are typically installed downstream of gravity separators to clean produced water [12, 13] to environmental regulation levels before disposing it in the ocean [14–17] or used as downhole separators [18–21]. Downhole cyclones are separators installed in the bottom of the well to reinject part of the produced water back to the reservoir instead of pumping it to the offshore oil platform, maintaining a high reservoir pressure, reducing the space required by gravity separators in the oil platform and saving pumping costs [22, 23]. Similarly, gas-liquid cyclones have been developed as compact alternatives to offshore gravity separators [24–28] and as downhole separators [29, 30]. In the generation of Nuclear Energy, swirl-vane separators (axial cyclones) have been used to remove water from steam upstream of dryers and turbines in Boiling Water Reactors and Pressure Water Reactors [31–36], and to remove fission gases from molten salt (liquid) in Molten Salt Reactors [37–40]. Other applications of gas-liquid cyclones involve multiphase flow metrology, where the mixture is divided into single-phase streams that have their flow rates individually measured [41–43], the separation of supercritical carbon dioxide from brine in geothermal energy generation [44], and the separation of supercritical carbon dioxide from solvents (e.g., toluene) in the production of aerogels [45].

The mixture rotation in tangential cyclones is created by their injection tangentially to the circular cross-section of the separator, while the rotation of the mixture in axial cyclones is created by an insert of helical geometry in the pipe, the Swirl Element. Irrespective of the method of generation of swirl, the azimuthal velocity of confined vortices outside the wall layer is well-approximated by the superposition between a solid body rotation and a Gaussian vortex [46–48],

$$u_\theta(r) = \frac{U_{\theta 1} R}{2\pi r}\left[1 - \exp\left(-\beta \frac{r^2}{R^2}\right)\right] + U_{\theta 2}\frac{r}{R}, \tag{1.14}$$

where $U_{\theta 1}$, β and $U_{\theta 2}$ are functions of the swirl intensity and R is the inner radius of the separator. An example of azimuthal velocity profile of confined swirl flows, and its resulting centripetal acceleration profile (u_θ^2/r), are presented in Figure 1.5.

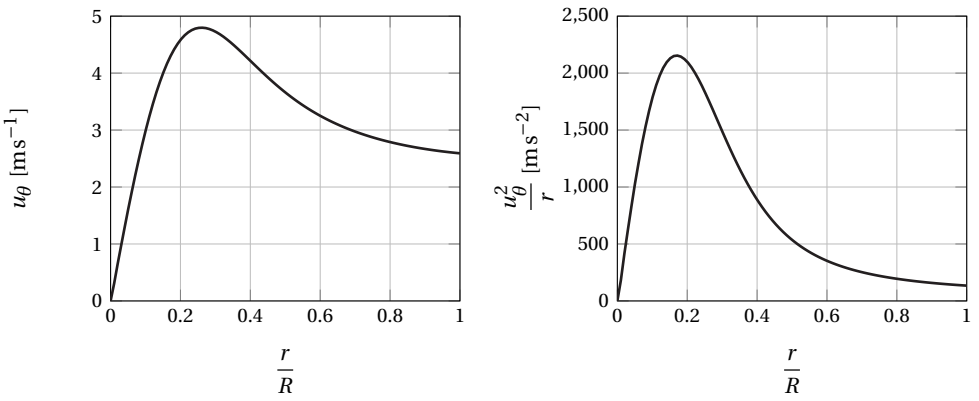

Figure 1.5: Example of azimuthal velocity (left) and centripetal acceleration (right) of confined single-phase swirl flows. Curves obtained with $U_{\theta 1} = 10\ \mathrm{m\,s^{-1}}$, $\beta = 20$, $U_{\theta 2} = 1\ \mathrm{m\,s^{-1}}$ and $R = 0.05$ m.

The analysis of order of magnitude of the Navier-Stokes equations reveals that the radial pressure distribution in a cyclone balances the centrifugal acceleration of the continuous phase,

$$\frac{\partial p}{\partial r} \approx \rho_c \frac{u_\theta^2}{r}, \tag{1.15}$$

leading to a buoyancy-like force on small particles that points to the equipment centerline:

$$\mathbf{F_b} = -\rho_c \frac{u_\theta^2}{r} \mathcal{V}_p \mathbf{e_r} \tag{1.16}$$

The particle motion in the radial direction is determined by the balance between the centrifugal force of the particle, the centripetal buoyancy force from Equation 1.16 and the drag force. Since the radial velocity of confined swirling flows is typically negligible [47, 49], this balance of forces results in the radial dispersed phase slip velocity:

$$\frac{4}{3}\left(\rho_c - \rho_p\right) d_p \rho_c \frac{u_\theta^2}{r} = C_d \rho_c |U_{rp}| U_{rp} \tag{1.17}$$

Equation 1.17 shows that the centripetal force pushes the less dense component of the mixture to the center of the cyclone, while the denser phase is driven towards the wall by the centrifugal force. The separation is achieved capturing the phases in different outlets. Tangential cyclones (Figures 1.4a and 1.4b) have opposing outlets for the capture of the light and heavy phases, while axial cyclones (Figure 1.4c) have two concentric outlets: the pickup tube (inner tube), which captures the lighter phase in the center of the separator, and the outer tube, of annular geometry, that captures the heavier phase near the cyclone walls. Independent of the cyclone geometry, the control of the separation is usually made via control valves installed downstream of the separator outlets.

Cyclones are designed to create centripetal accelerations orders of magnitude above g, as illustrated by the approximately $200g$ peak centripetal acceleration of Figure 1.5-right, with centripetal accelerations as high as $3000g$ mentioned in literature [17, 50]. Due to a much higher driving force behind the separation:

- The slip velocity of the dispersed phase in cyclones is much larger than in gravity separators for the same inlet conditions (phases, particle size distribution, flow rates, etc). The faster separation results in lower residence times, in the order of seconds in cyclones versus minutes in gravity separators [50], and more compact devices, which is a large advantage for offshore and downhole applications[25, 30, 51].

- Cyclones can target much smaller particles than gravity separators. For instance, de-oiling cyclones can separate oil droplets as small as 10-15 μm from water, while gravity separators are limited to oil droplets above 150 μm [52]. For solid particles, settling chambers are limited to solid particles above around 10 μm, while cyclones can separate particles larger than 2 μm [8].

However, cyclones also have some disadvantages in relation to gravity separators:

- The higher velocities achieved in cyclones substantially increase the shear in small deformable particles (bubbles and droplets), which may break them into smaller components that are harder to separate [11, 53–55].

- Cyclones are sensitive to process disturbances. This occurs since changes in the inlet conditions of the cyclone are not damped by a large volume of fluid, as in gravity separators, quickly propagating to the outlets of the equipment and impacting its performance. As consequence, real-time controllers are crucial for the optimal operation of cyclones [15, 50, 56].

The real-time control of cyclones is traditionally performed based on pressure measurements in the cyclone outlets [14, 57–63]. The pressure field is indirectly related to the distribution of phases in the separator and, therefore, the pressure measurements used in traditional cyclone control are indirectly related to the capture of each phase by its respective outlet. Since tomography provides a direct measurement of the distribution of phases in the separator, the tomography-based real-time control of cyclones proposed in this research can potentially improve the cyclone performance in the presence of process disturbances. A tomography-controlled axial cyclone is presented in section 1.3.

1.2. TOMOGRAPHY IN MULTIPHASE FLOWS

Tomography is a non-intrusive technique to obtain internal information of an object or process, typically in the form of images. Due to its non-intrusiveness, tomography is widely applied in the medical field to "see" inside the human body, for instance via Ultrasound, X-Ray and Magnetic Resonance Imaging (MRI).

Applications of tomography in multiphase flows include: (i) measurements of the distribution of phases [28, 64–66], flow pattern identification [67–70] and dispersed/non-conductive phase velocity (via the cross-correlation of the conductivity distribution between two measurement planes) [71, 72] with Electrical Capacitance and Electrical Resistance Tomography; (ii) measurements of phase distribution, velocity distribution and flow pattern identification with Ultrasound [73–75]; (iii) measurements of gas distribution, gas velocity and bubble size distribution with X-Ray tomography [76–78]; (iv) measurements of gas distribution, bubble/gas velocity and bubble size distribution with MRI [79–81].

Despite the rich information provided by tomography, with little to no intrusiveness, and the wide success of the technique in offline measurements, tomography has not yet been applied in the real-time control of industrial processes due to the high computational demand of the data processing/image reconstruction step [82]. However, the substantial increase in computational power in the recent years has enabled faster image reconstructions, opening the door to real-time tomography [83, 84] and, as consequence, to the tomography-based real-time control of multiphase flows.

1.2.1. ELECTRICAL RESISTANCE TOMOGRAPHY

Electrical Resistance Tomography (ERT) is used in this research for the proof of concept of tomography-based real-time control due to its low implementation cost and high

measurement speed compared to other tomographic techniques [85], something crucial to capture the small time-constants of multiphase flows.

The ERT measurements are made with several electrodes installed on the boundary of the domain. An ERT system with sixteen equidistant electrodes measuring the gas-liquid separation in an axial cyclone is illustrated in Figure 1.6.

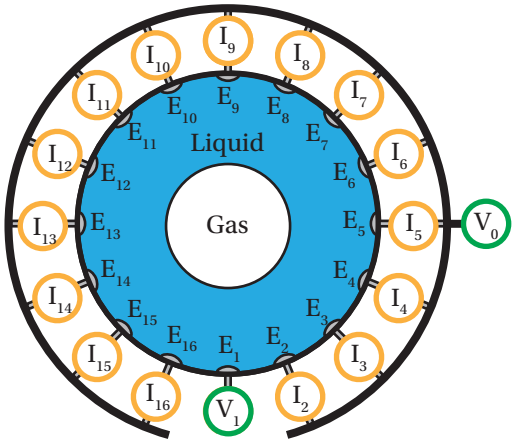

Figure 1.6: Electrical Resistance Tomography electrodes, in the Voltage-Current scheme, measuring a cross-section of the flow in the axial cyclone. In the image, Electrode 1 (E_1) is acting as a voltage source with potential V_1, while the remaining electrodes (E_2-E_{16}) are grounded at V_0 and have their currents measured (I_2-I_{16}).

The electric field measurements in the Voltage-Current scheme, depicted in Figure 1.6, are made imposing an electric potential in one electrode (voltage source) while grounding the remaining electrodes and measuring their electric currents (current sinks). The process is repeated for each electrode as voltage source, leading to a total of $N(N-1)$ measurements per frame, where N is the number of electrodes of the ERT system. Two hundred forty electric current measurements are performed by a 16-electrode ERT for each frame, from which only one hundred twenty are independent ($N(N-1)/2$).

The currents measured in the grounded electrodes depend on their distance to the source electrode and on the distribution of electrical conductivity in the domain. Traditionally, the conductivity profile is reconstructed from the voltage-current electrode measurements in the boundaries of the domain via an inverse problem based on the electrostatic Maxwell's equations [85–87]. During the conductivity/image reconstruction step, the domain is discretized via the Finite Element Method into significantly more mesh elements (and, therefore, variables) than boundary measurements, resulting in an underdetermined system of equations and an ill-posed problem. The inverse problem can be solved with non-iterative schemes of low spatial accuracy, such as Linear Back Projection (LBP) [85], or iterative schemes of higher spatial accuracy, e.g., Gauss-Newton (GN) [87].

Once the distribution of electrical conductivity is obtained solving the inverse problem, the distribution of phases can be recovered based on the properties of the fluids. For instance, if the conductivity of the gas is negligibly small compared to the liquid (e.g., for tap water and air), the local liquid fraction can be assumed directly proportional to

the ratio between the reconstructed conductivity distribution and the liquid conductivity. Figure 1.7 shows an example of volume fraction distribution of the non-conductive phase measured by ERT with the Linear Back Projection and Gauss-Newton algorithms.

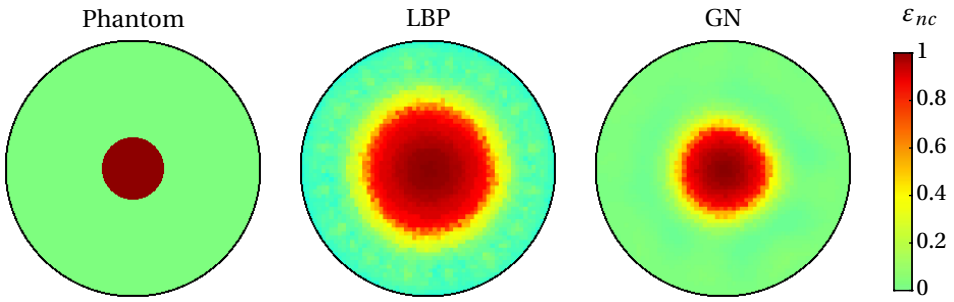

Figure 1.7: Volume fraction of the non-conductive phase (ε_{nc}) reconstructed by ERT for a cylindrical phantom of diameter 20mm in tap water, mimicking the gas core in the cyclone. Left: Ideal image reconstruction based on the phantom dimensions (reference). Middle: Image reconstructed from the ERT measurements with Linear Back Projection (LBP). Right: Result obtained with a single Gauss-Newton (GN) iteraction. Images adapted from Sattar *et al.* [88].

Despite the recent increase in computational power, ERT measurements with sufficient spatial accuracy for real-time control via traditional general image reconstruction algorithms, such as LBP and GN, remain computationally demanding and too slow to capture the relevant multiphase flow dynamics. One important contribution of this work is the development of a fast application-specific ERT image reconstruction algorithm for the distribution of phases in axial cyclones, minimizing the computational time of the image reconstruction step and pushing the real-time ERT measurement speed to the limits of the data acquisition hardware. The algorithm was developed in cooperation with M. A. Sattar from Lodz University of Technology and is detailed in chapter 2.

1.3. A TOMOGRAPHY-CONTROLLED AXIAL CYCLONE

As mentioned in the beginning of this chapter, a gas-liquid axial cylindrical cyclone is used in this research to demonstrate, for the first time, the tomography-based real-time control of multiphase flows. The choice of axial cyclones for the demonstration was made taking into account its industrial relevance, its sensitivity to process disturbances, the fast dynamics of the distribution of phases inside the equipment and, for the gas-liquid (air-water) flow, the absence of emulsions which impact the performance of the separator, something present, e.g., in oil-water systems.

Currently, the feedback control of the separation in cyclones is performed with control valves in the outlets of the separator, using pressure-related quantities as controller set-point [14, 57–63]. Although robust, pressure measurements provide limited information on the separation and the capture of the phases by their respective outlets, thus providing an indirect measurement of the equipment performance. A potentially better variable for the real-time control of the cyclone is the distribution of phases measured by tomography,

directly related to the phases captured by the cyclone outlets and, as consequence, to the separator performance.

The tomography-controlled gas-liquid axial cyclone proposed in this research is presented in Figure 1.8.

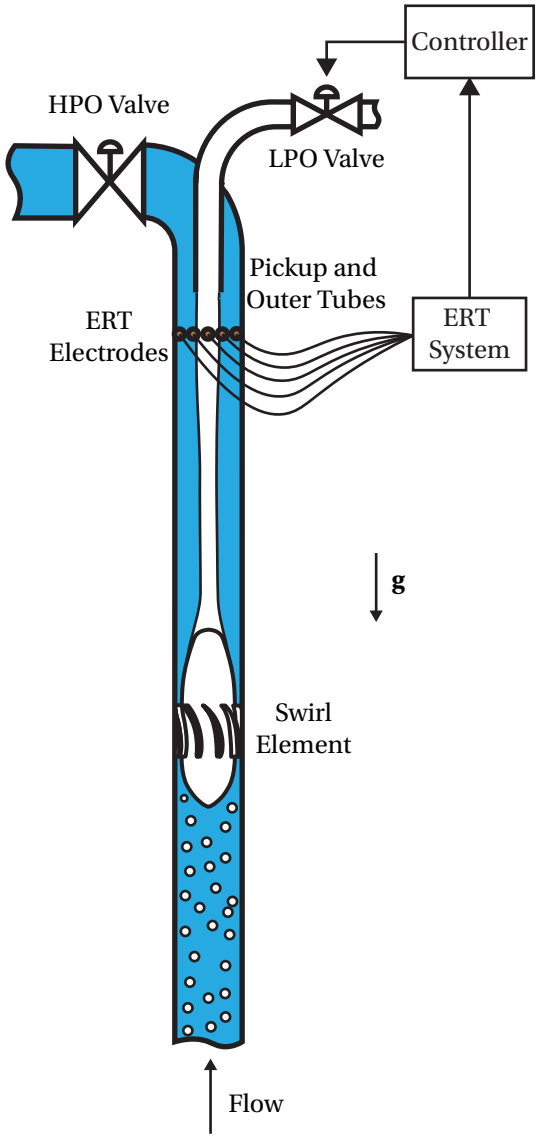

Figure 1.8: Gas-liquid axial cyclone with tomography-based real-time control. The controller uses the gas core diameter measured by Electrical Resistance Tomography (ERT) to act on the Light Phase Outlet (LPO) valve.

Departing from the bottom of Figure 1.8, swirl is imposed to the gas-liquid flow as the mixture crosses the Swirl Element, resulting in the centripetal force that quickly pushes the

air to the center of the separator and the centrifugal force that moves the liquid towards the wall. The separation is achieved further downstream by the capture of gas by the Pickup Tube and the capture of water by the surrounding annular outlet (Outer Tube). The flow split between the pickup and outer tubes and, as consequence, the gas liquid distribution upstream of the pickup tube, are manipulated via the Light Phase Outlet (LPO) and Heavy Phase Outlet (HPO) control valves.

Electrical Resistance Tomography electrodes are installed upstream of the pickup tube to monitor the local gas-liquid distribution and, therefore, the gas capture by the outlet. Since the gas core is centered in the axial cyclone, the most relevant variable of the gas-liquid distribution measured by the ERT system is the gas core diameter. The separation is controlled in real-time using the gas core diameter measured by the ERT to compute actions in the Light Phase Outlet (LPO) control valve. A natural controller setpoint for the gas core diameter that maximizes the separation is the inner diameter of the pickup tube, in principle resulting in the capture of all the gas by its outlet without any liquid.

1.4. OBJECTIVES AND OUTLINE

The main objective of this thesis is to investigate the possibilities and limitations of tomography-based real-time control of multiphase flows. The study is conducted with a gas-liquid axial cyclone, where Electric Resistance Tomography is used to monitor the distribution of phases in the separator in real-time and the gas core diameter upstream of the pickup tube is used to control the separation via the LPO valve. The following steps are performed in the tomography-based real-time control investigation:

- Build an axial cyclone experimental facility and develop a real-time Electrical Resistance Tomography for control applications. The axial cyclone facility was designed as part of the PhD project described in this thesis, and the real-time ERT was developed in cooperation with M. A. Sattar, a TOMOCON PhD candidate of Lodz University of Technology, being the focus his PhD thesis [89]. The experimental facility and real-time ERT (hardware and novel real-time image reconstruction algorithm for swirling gas-liquid flows) are described in chapter 2.

- Experimentally investigate the flow behavior in the axial cyclone separator, to identify the swirling gas-liquid flow patterns that can be present in the system and propose mechanistic models for their prediction. The flow patterns in the cyclone have a substantial role in the dynamics of the distribution of phases inside the separator, impacting the control system design and providing a physics understanding of the results obtained in the remaining chapters of this thesis. The swirling gas-liquid flow physics is the focus of chapter 3.

- Study the relation between the gas core diameter upstream of the pickup tube measured by Electrical Resistance Tomography and the axial cyclone performance. Additionally, compare the gas core diameter with pressure-based variables traditionally used in the real-time control of cyclones as performance indicator, to investigate the advantages of tomography-based controllers over the current pressure-based controllers. The results obtained are presented in chapter 4.

- Investigate the phase distribution dynamics and tomography-based real-time control possibilities in the axial cyclone. Design and implement a tomography-based real-time controller in the axial cyclone to verify its ability to suppress process disturbances in the distribution of phases (gas core diameter) upstream of the pickup tube. The results obtained are presented in chapter 5.

Finally, a reflection on the results obtained with the gas-liquid axial cyclone and their generalization to the tomography-based control of multiphase flows is made in chapter 6, concluding the thesis. The research data presented in this dissertation was uploaded in the 4TU repository and can be accessed at doi.org/10.4121/22140299

CHAPTER 2

EXPERIMENTAL METHODOLOGY

2.1. INTRODUCTION

The main objective of this thesis is to investigate the tomography-based real-time control of multiphase flows. The investigation is performed with a gas-liquid axial cyclone separator, where the gas core upstream of the pickup tube, measured by Electrical Resistance Tomography (ERT), is used by a tomography-based controller to compute actions in the Light Phase Outlet (LPO) valve, as shown in Figure 2.1.

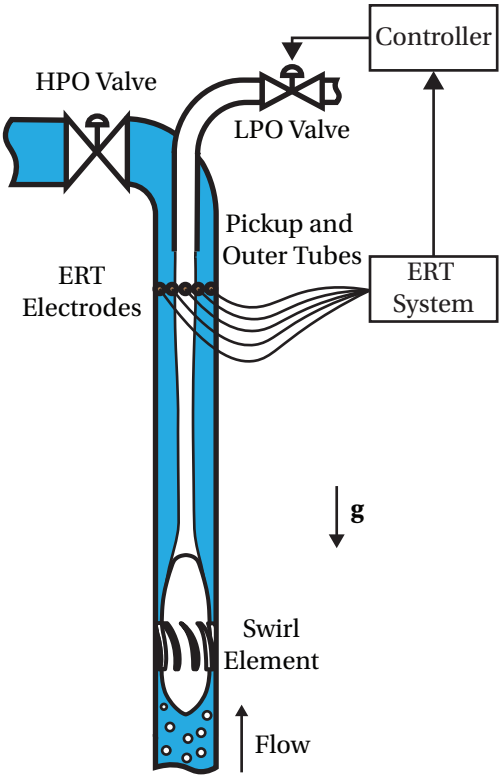

Figure 2.1: Tomography-controlled gas-liquid axial cyclone separator.

Parts of this chapter were published in Sattar *et al.* [90].

An experimental facility and real-time Electrical Resistance Tomography sensor (hardware and image processing) were developed in this research. The experimental facility was designed for both traditional multiphase flow studies with statistically-steady boundary conditions (e.g., time-average flow rates), such as in the study of the vertical upward swirling gas-liquid pipe-flow patterns of chapter 3, and for the investigation of the possibilities and limitations of tomography-based real-time control of the phase distribution, as in chapter 5, where the LPO valve dynamics (tomography-based controller actuator) become relevant. The axial cyclone experimental facility of Delft University of Technology is described in part I of the current chapter.

Electrical Resistance Tomography measures the phase distribution in two steps: data acquisition and image reconstruction. Although the data acquisition of commercial ERT systems can reach relatively high measurement speeds, in the order of 10 frames per second, traditional ERT image reconstruction algorithms are computationally demanding and, therefore, slow compared to the phase distribution dynamics in axial cyclones. A fast application-specific image reconstruction algorithm was developed in cooperation with Lodz University of Technology to reconstruct the gas core upstream of the pickup tube. The algorithm proposed is based on the expected distribution of phases in the axial cyclone (consisting of a roughly circular gas core surrounded by a liquid annulus, as shown in Figure 2.1) and it is three orders of magnitude faster than traditional ERT algorithms, making it suitable for real-time control. The real-time ERT hardware and application-specific algorithm, previously published in [90], are presented in part II of this chapter.

PART I: THE AXIAL CYCLONE FACILITY OF DELFT UNIVERSITY OF TECHNOLOGY

This part describes the experimental facility built in the Faculty of Applied Sciences of Delft University of Technology to investigate the gas-liquid swirl flow in the axial cyclone separator and its tomography-based real-time control. It is divided into five sections: the flow loop and its components are detailed in section 2.2; the four swirl elements used in this research, and the geometrical swirl number used to characterize the swirl intensity produced by them, are introduced in section 2.3; the working principle and specifications of a double-layer wire-mesh sensor, used to measure the gas-liquid distribution upstream of the swirl element in chapter 5, are described in section 2.4; the working principle of the pneumatic LPO and HPO valves and the LPO valve dynamics, actuator of the tomography-based controller shown in Figure 2.1, are presented in section 2.5; variations in the liquid flow rate of the experimental facility due to changes in the LPO valve, impacting the phase distribution dynamics in the axial cyclone, are investigated in section 2.6.

2.2. FLOW LOOP

The flow diagram of the gas-liquid axial cyclone facility of Delft University of Technology is presented in Figure 2.2. The relevant flow loop dimensions are shown in Figure 2.3.

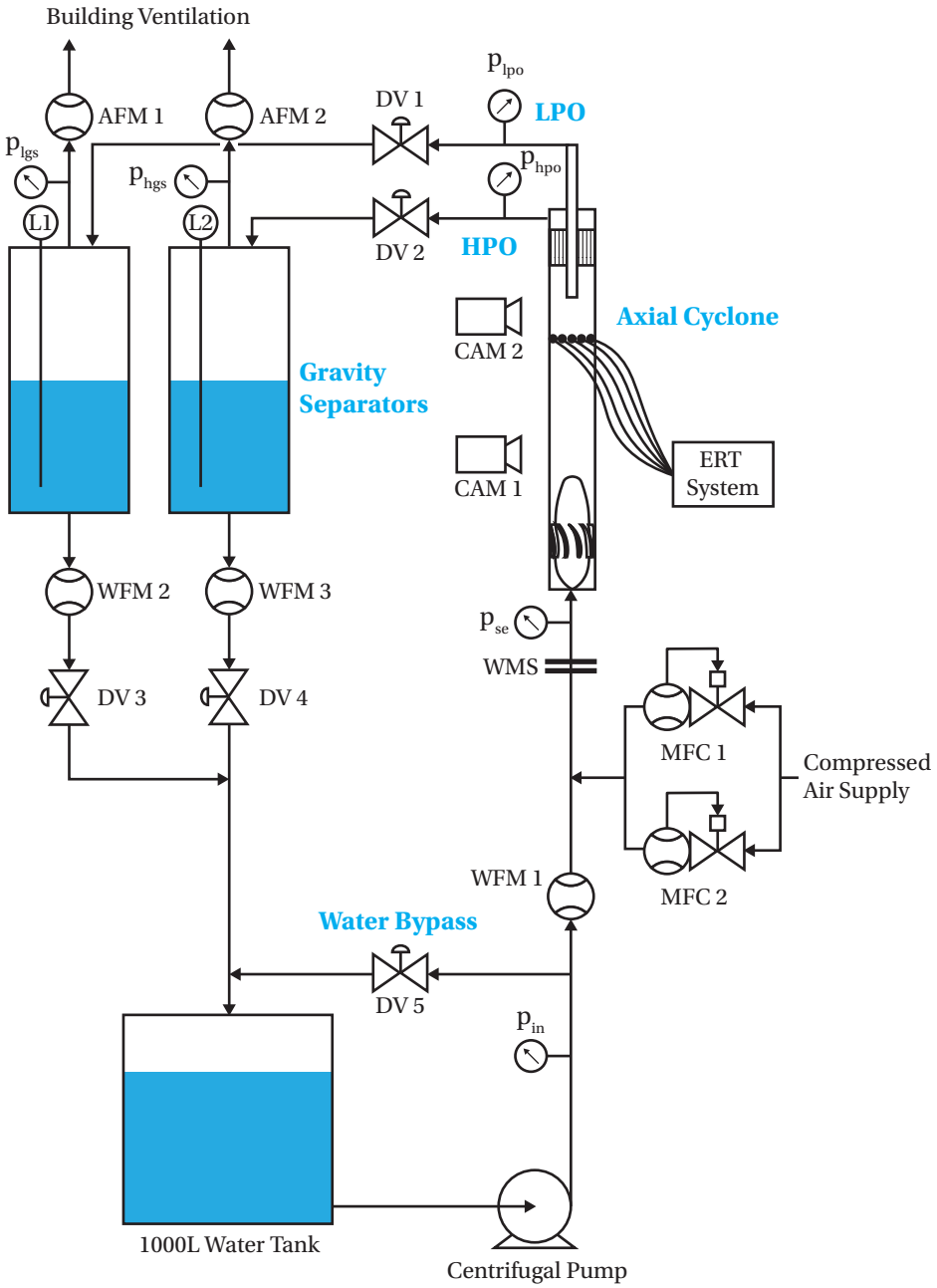

Figure 2.2: Schematic of the Axial Cyclone facility of Delft University of Technology.

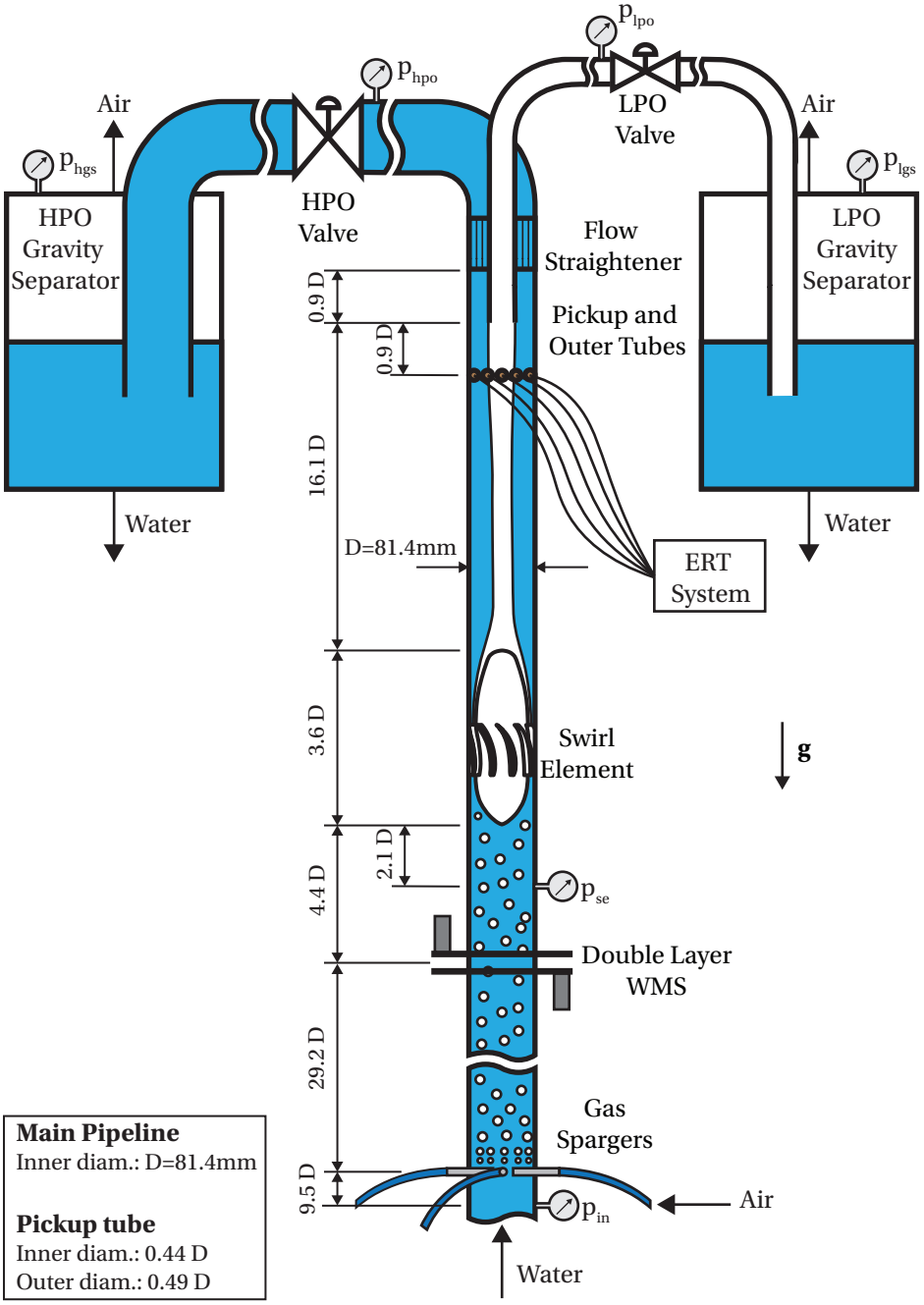

Figure 2.3: Simplified drawing with dimensions of the main section of the flow loop. Image not to scale.

Departing from the 1000 L Water Tank in Figure 2.2, water with electrical conductivity around 200 $\mu S\,cm^{-1}$ is pumped to a vertical pipe of inner diameter D = 81.4 mm by a Iwaki MX-402 Magnetic Drive (Centrifugal) Pump. The pressure p_{in} and water volume flow rate are measured downstream of the pump by a General Electric (GE) UNIK 5000 pressure sensor and a KROHNE OPTIFLUX 2100 C electromagnetic flow meter (WFM 1), respectively.

Air is injected in the system downstream of the water flow meter WFM 1 by two Mass Flow Controllers (MFC 1 and MFC 2), connected between the compressed air supply of the Applied Sciences building and gas spargers. MFC 1 is a Bronkhorst EL-FLOW Select F-203AV air mass flow controller of nominal range 20-1000 Ln/min[1] (1.55-77.58 $kg\,h^{-1}$), used in the experiments of chapters 3, 4 and 5, and MFC 2 is a Bronkhorst EL-FLOW F-202AC CO_2 mass flow controller of full scale 20 Ln/min, used to extend the lower gas mass flow rate range of the experimental facility in the flow pattern identification experiments of chapter 3. A conversion factor of 1.35 is applied to the MFC 2 readout to convert it from CO_2 to air [2], leading to the air-equivalent MFC 2 full scale of 27Ln/min (2.095 $kg\,h^{-1}$).

Once formed, the gas-liquid mixture flows vertically for $33.6D$ before reaching the Swirl Element (Figure 2.3), resulting in developed vertical upward gas-liquid flow patterns upstream of the cyclone. The gas-liquid distribution is measured $4.4D$ upstream of the swirl element by a double-layer Wire-Mesh Sensor (WMS), and the pressure in the inlet of the cyclone, p_{se}, is measured $2.1D$ upstream of the Swirl Element by a second GE UNIK 5000 pressure sensor. The swirl elements used in the experiments are detailed in section 2.3, and the double-layer wire-mesh sensor is described in section 2.4.

The gas-liquid separation takes place downstream of the swirl element in a pipe of inner diameter D = 81.4 mm and length $16.1D$, after which the central region of the flow, corresponding to a gas core for perfect phase separation, is captured by the pickup tube of inner diameter $0.44D$ and outer diameter $0.49D$, and the surrounding flow, corresponding to a liquid annulus for perfect phase separation, is captured by the outer tube.

Basler acA1920-150uc cameras (CAM 1 and CAM 2) are used to record the gas-liquid distribution in the axial cyclone in the experiments of chapters 3 and 5, and the gas core is monitored $0.9D$ upstream of the pickup tube with Electrical Resistance Tomography (ERT) in the experiments of chapters 4 and 5. Different regions of the cyclone were recorded by the cameras during the experiments, being detailed locally in each chapter. The routine developed to process the camera recordings is presented in Appendix A, and the ERT system and image reconstruction algorithm are described in part II.

The pickup tube and outer tubes are connected to the Light Phase Outlet (LPO) and Heavy Phase Outlet (HPO) of the separator, respectively. Each outlet contains a GE UNIK 5000 pressure sensor (p_{lpo} and p_{hpo}), followed by a Normally Open ASV Stübbe MV 310 pneumatic diaphragm valve (DV 1 and DV 2). The LPO and HPO valves are used to manipulate the flow split between the two outlets of the cyclone and, as consequence, the gas core diameter upstream of the pickup tube and the amount of gas and liquid captured by the pickup and outer tubes. The LPO valve (DV1) has a nominal diameter of 25 mm and the HPO valve (DV2) has a nominal diameter of 50 mm. SMC ITV2050 Electro-Pneumatic

[1] Ln stands for Normal Liters, computed dividing the gas mass flow rate measured by the sensor by the gas density at 0 °C and 1 atm. The gas mass flow rates are always converted back to $kg\,h^{-1}$ in this thesis.

[2] The conversion factor was obtained from the Bronkhorst FLUIDAT website, www.fluidat.com

Regulators are used to set the control pressure of the diaphragm valves, adjusting their opening as described in section 2.5.

The LPO and HPO are individually connected to Gravity Separators, splitting the two-phase flows of the LPO and HPO (for imperfect phase separation) into single-phase gas and liquid flows that can be measured with conventional flow meters. The air mass flow rate departing from the top of the LPO gravity separator is measured by a Bronkhorst MASS-STREAM D-6370 (AFM 1), and the liquid mass flow rate leaving the bottom of the separator is measured by an Endress+Hauser Promag 10 electromagnetic flow meter (WFM 2). Similarly, the air flow departing from the top of the HPO gravity separator is measured by a Bronkhorst MASS-STREAM D-6360 (AFM 2), and the water flow is measured by a KROHNE OPTIFLUX 2100 C (WFM 3). The pressures p_{lgs} and p_{hgs} in the LPO and HPO gravity separators, respectively, are also measured by GE UNIK 5000 pressure sensors. The cyclone performance is evaluated based on the LPO and HPO gas and liquid flow rates (chapter 4), estimated from the gas and liquid flow rates measured in the outlets of the gravity separators as described in Appendix B.

The air departing from the LPO and HPO gravity separators is injected in the ventilation system of the Applied Sciences building, being released to the atmosphere. The water departing from the gravity separators returns to the 1000 L Water Tank, closing the water loop (Figure 2.2). Normally Open ASV Stübbe MV 310 pneumatic diaphragm valves with SMC ITV2050 Electro-Pneumatic Regulators are installed in the liquid outlets of the LPO and HPO gravity separators to control their water level, measured by the ROSEMOUNT 3302 Guided Wave Radar Level and Interface Transmitters L1 and L2, via a PI feedback control loop with water level setpoint of 0.7 m (half of the gravity separator height). The LPO Gravity Separator valve DV 3 has a nominal diameter of 25 mm, being similar to the LPO valve DV 1, and the HPO Gravity Separator valve DV 4 has a nominal diameter of 50 mm, being similar to the HPO valve DV 2.

The flow equipment (MFCs, valves, flow meters, pressure sensors, etc) are controlled and logged in LabVIEW at a frequency of 10 Hz. The measurement range and uncertainty of the devices, obtained from calibration certificates provided by the suppliers, are summarized in Table 2.1. The pressure sensors were re-calibrated before the experiments.

Table 2.1: Full scale, sample rate and uncertainty of the experimental facility sensors.

Equipment	Full Scale	Sample Rate	Uncertainty
WFM 1	21 $m^3 h^{-1}$	2 Hz	$\pm$(0.3% reading + 0.007 $m^3 h^{-1}$)
WFM 2	12 $m^3 h^{-1}$	2 Hz	$\pm$(0.5% reading + 0.004 $m^3 h^{-1}$)
WFM 3	21 $m^3 h^{-1}$	2 Hz	$\pm$(0.3% reading + 0.007 $m^3 h^{-1}$)
MFC 1	77.58 $kg h^{-1}$	2 Hz	$\pm$(0.5% reading + 0.08 $kg h^{-1}$)
MFC 2	2.095 $kg h^{-1}$	2 Hz	$\pm$(0.5% reading + 0.002 $kg h^{-1}$)
AFM 1	77.6 $kg h^{-1}$	2 Hz	$\pm$(1% reading + 0.4 $kg h^{-1}$)
AFM 2	15.52 $kg h^{-1}$	2 Hz	$\pm$(1% reading + 0.08 $kg h^{-1}$)
Pressure sensors	4 barg	3.5 kHz	$\pm$0.01 bar
L1 and L2	1.4 m	2 Hz	$\pm$5 mm

2.3. SWIRL ELEMENTS

Four Swirl Elements, previously designed by van Campen [11] and Star [91], are used in the experiments of this research. The CAD drawings of the Swirl Elements are presented in Figure 2.4. The Swirl Elements designed by Star [91] and van Campen [11] have a body diameter (inner diameter of the swirl element vanes) D_b = 80 mm and an outer diameter D_{se} = 100 mm, which is larger than the inner diameter D = 81.4 mm of the experimental facility pipeline. Therefore, the swirl elements are installed between concentric reducers, as shown in Figure 2.5 together with the relevant swirl element dimensions.

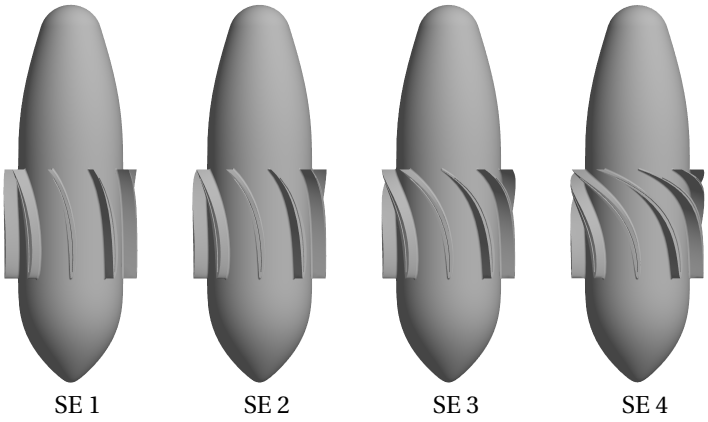

Figure 2.4: CAD drawings of the Swirl Elements (SE) used in the experiments of this thesis. The swirl elements are numbered from 1 (weakest) to 4 (strongest) in ascending order of swirl intensity created by their vanes.

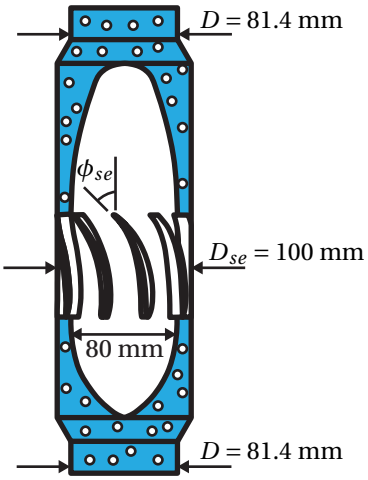

Figure 2.5: Main dimensions of the Swirl Elements and concentric reducers.

The Swirl Element geometry is directly related to the swirl intensity in the axial cyclone. The flow pattern experiments of chapter 3 were performed with all four Swirl Elements available to investigate the impact of swirl intensity on the swirling gas-liquid flow patterns. However, only Swirl Element 3 was used in the experiments of chapters 4 and 5, since it provides a good balance between (i) the formation of centered gas columns upstream of the pickup tube, required by the real-time Electrical Resistance Tomography algorithm described in part II and not always observed for weaker swirl elements, and (ii) a good sensitivity of the gas core to disturbances in the gas mass flow rate of the cyclone and actions in the LPO valve, required for the tomography-based real-time control experiments of chapter 5.

Figures 2.4 and 2.5 show that the swirl element vanes start parallel to the upstream flow, bending to a helix in the axial direction. The intensity of the swirl created by the swirl element is directly related to the terminal helical pitch of its vanes ℓ_{se}, defined as the distance in the axial direction required for one complete rotation of an helix tangent to the tip of the swirl element vanes. The final angle of the swirl element vanes ϕ_{se}, illustrated in Figure 2.5, is a function of the radial position and related to the terminal pitch of the helical vanes via:

$$\tan\phi_{se}(r) = \frac{2\pi r}{\ell_{se}} \tag{2.1}$$

2.3.1. GEOMETRICAL SWIRL NUMBER

The swirl elements are characterized in this research, particularly in chapter 3, by the geometrical swirl number Ω_{se}. The geometrical swirl number corresponds to an estimate of the swirl number of single phase flows departing from the swirl element based on the swirl element geometry.

Considering a single-phase flow across a swirl element of body radius R_b and outer radius R_{se}, the conservation of mass across the swirl element leads to the relation between the axial velocity in the cross-section of the vanes $U_{x,se}$, assumed uniform, and the average axial velocity U_x in the pipe (upstream and downstream of the swirl element):

$$\frac{U_{x,se}}{U_x} = \frac{R^2}{R_{se}^2 - R_b^2} \tag{2.2}$$

Since the flow in the swirl element is parallel to its vanes, the azimuthal and axial velocities at the exit of the swirl element vanes are related to the terminal helical pitch of the vanes ℓ_{se} via:

$$\frac{u_{\theta,se}}{U_{x,se}} = \frac{2\pi r}{\ell_{se}} \tag{2.3}$$

Therefore, the flow of angular momentum $\dot{L}_{se}$ departing from the swirl element vanes is:

$$\dot{L}_{se} = 2\pi \int_{R_b}^{R_{se}} \rho u_{x,se} u_{\theta,se} r^2 dr = \rho U_x^2 \frac{\pi^2 R^4}{\ell_{se}} \frac{(R_{se}^4 - R_b^4)}{(R_{se}^2 - R_b^2)^2} \tag{2.4}$$

The geometrical swirl number is defined as the dimensionless single-phase flow of angular momentum right downstream the swirl element, assuming that $\dot{L}_{se}$ is conserved between the tip of the swirl element vanes and the pipe. By definition, the flow of angular momentum is normalized the product wU_xR, where w is the mass flow rate of the system:

$$\Omega_{se} \triangleq \frac{\dot{L}_{se}}{wU_xR} = \frac{\pi R}{\ell_{se}} \frac{R_{se}^2 + R_b^2}{R_{se}^2 - R_b^2} \tag{2.5}$$

As shown by Equation 2.5, the geometrical swirl number is only a function of the swirl element and pipe geometries. The relevant dimensions and geometrical swirl number of the swirl elements used in the research of this thesis are summarized in Table 2.2.

Table 2.2: Main dimensions and geometrical swirl number of the Swirl Elements used in this research. The Swirl Elements have body radius R_b, outer radius R_{se} and terminal helical vane pitch ℓ_{se}. The final vane angles of the table are presented based on the outer radius of the swirl element, $\phi_{se}(R_{se})$.

Swirl Element	1	2	3	4
R_b [m]	0.040	0.040	0.040	0.040
R_{se} [m]	0.050	0.050	0.050	0.050
ℓ_{se} [m]	0.370	0.255	0.166	0.101
$\phi_{se}(R_{se})$	40°	51°	62°	72°
Ω_{se}	1.57	2.28	3.51	5.77

2.4. DOUBLE-LAYER WIRE-MESH SENSOR

In chapter 5, a double-layer wire-mesh sensor is used together with a high speed camera to investigate the propagation of phase distribution fluctuations upstream of the swirl element to the gas core inside the cyclone. Once downstream of the swirl element, the phase distribution fluctuations travel towards the cyclone outlets, impacting the separation when arriving at the pickup tube. In principle, if the phase distribution upstream of the swirl element and inside the cyclone are strongly correlated, future gas core fluctuations in the tip of the pickup tube can be predicted from upstream phase distribution measurements, and acted upon by model-based controllers before reaching the outlet.

Wire-mesh sensors are a well-established technique to measure the cross-sectional distribution of phases in gas-liquid [77, 92], liquid-liquid [93, 94] and three-phase [95, 96] flows at high acquisition frequencies (5 kHz in this research). The wire-mesh sensor consists of two planes of parallel wires, transmitter and receiver, installed separated by a small distance (3.8 mm in the current hardware) and rotated 90° in relation to each other, forming a virtual grid of points between the wires. A picture of one wire-mesh layer with 16x16 wires, used in this thesis, is presented in the left image of Figure 2.6.

The cross-sectional conductance profile of the flow is measured by the wire-mesh sensor (i) imposing an electric potential between one transmitter wire and all the receiver wires, that have their resulting currents measured, and (ii) repeating the procedure for each wire of the transmitter plane as voltage source. The approach leads to one electric

current measurement per virtual crossing of the wire-mesh sensor per frame, related to the conductance of each virtual point by the voltage used during the measurements. The distribution of phases is recovered from the conductance profile measured by the wire-mesh sensor assuming a proportional relation between conductance and liquid volume fraction (ε_l) [97],

$$\varepsilon_l[m,n] = \frac{G[m,n]}{G_l[m,n]}, \tag{2.6}$$

where $G[m,n]$ is the conductance measured by the wire-mesh sensor for two-phase flows in the virtual crossing $[m,n]$ and $G_l[m,n]$ is the conductance measured in each crossing with the domain filled with water prior to the experiments (calibration step). An example of the distribution of phases (gas volume fraction profile) obtained by a wire-mesh sensor is shown in Figure 2.6-right.

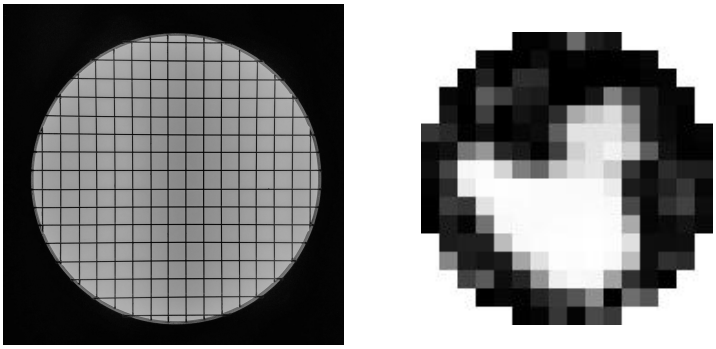

Figure 2.6: Wire-mesh sensor picture (left) and gas-liquid distribution measured by the wire-mesh sensor (right). The gas volume fraction of each pixel in the right image is proportional to its grayscale value (black corresponds to 100% liquid and white to 100% gas).

The cross-sectional average gas fraction in the wire-mesh sensor location is computed from the 2D liquid fraction distribution measured by the sensor via

$$\alpha_{wms}(t) = 1 - \frac{1}{\pi R^2}\int_0^{2\pi}\int_0^{R} \varepsilon_l(r,\theta,t)\, r\, dr\, d\theta, \tag{2.7}$$

where r and θ are related to the coordinates of the virtual wire-mesh points $[m,n]$ and the time instant t is related to the k-th sample of the wire-mesh sensor (frame) and wire-mesh sensor sample time T_{wms} via $t = kT_{wms}$ ($T_{wms} = 0.2$ ms for the acquisition frequency of 5 kHz used in this research).

The double-layer wire-mesh sensor consists of two individual WMS installed separated by a few centimeters in the axial direction (25.7 mm for the current double-layer wire-mesh based on the middle of each layer). The gas velocity is estimated cross-correlating in time the liquid fraction profiles or cross-sectional average gas fractions measured by each wire-mesh sensor layer, and dividing the distance between the two layers by the time shift which maximizes the cross-correlation.

2.5. LIGHT PHASE OUTLET AND HEAVY PHASE OUTLET VALVES

As shown in Figure 2.1, in the beginning of the current chapter, the Light Phase Outlet (LPO) valve of the axial cyclone is used for the tomography-based real-time control of the gas core upstream of the pickup tube, while the Heavy Phase Outlet (HPO) valve is kept at fixed positions related to the operating point of the separator. The LPO valve was chosen for real-time control since it is considerably smaller than the HPO valve, reacting faster to changes in the control pressure created by the SMC ITV2050 Electro-Pneumatic Regulator.

The gas core upstream of the pickup tube is impacted by changes in the LPO and HPO pressures, created by user-inputs or control actions in the LPO valve. The geometry and block diagram of the LPO and HPO control valves are presented in subsection 2.5.1, the strategy used to accelerate the LPO valve response for real-time control is described in subsection 2.5.1, and the LPO valve dynamics is investigated in subsection 2.5.3.

2.5.1. INTERNAL VALVE GEOMETRY

A simplified drawing of the LPO and HPO ASV Stübbe MV 310 pneumatic diaphragm valve internals is presented in Figure 2.7.

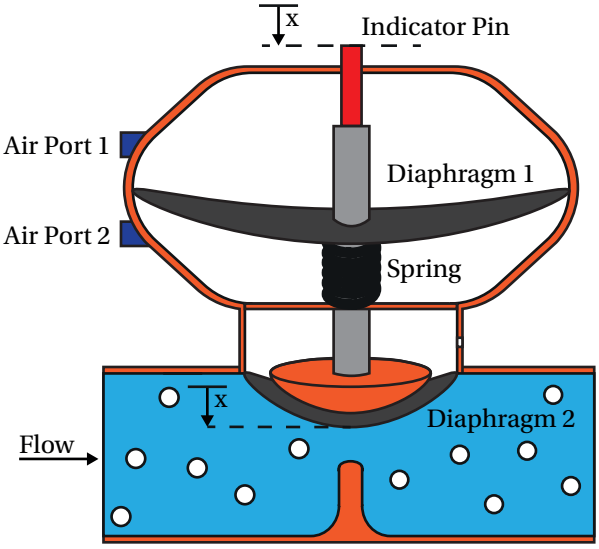

Figure 2.7: Simplified drawing of the internal ASV Stübbe MV 310 valve components.

The SMC ITV2050 Electro-Pneumatic Regulator used to control the opening of the LPO and HPO valves is connected to Air Port 1 of Figure 2.7, imposing the control pressure above Diaphragm 1. The control pressure acts against an internal spring of the valve, the pressure below Diaphragm 1 and the flow force on Diaphragm 2; the resulting balance of forces determines the position of the internal rod of the valve and Diaphragm 2, related to the valve opening. An indicator pin on top of the valve, connected to the rod, is used

to track the position of the control valve diaphragms. In this thesis, the diaphragm position (based on the indicator pin) x is reported normalized by its total range, where $x = 0$ corresponds to the valve fully open and $x = 1$ to the valve fully closed.

The block diagram of the LPO and HPO control valves is presented in Figure 2.8. The control pressure input u_{p_c} is sent to the SMC ITV2050 Electro-Pneumatic Regulator by LabVIEW based on user inputs or tomography-based controller output. Changes in the control pressure input u_{p_c} results in changes in the control pressure p_c in the cavity of the valve above Diaphragm 1, following the Electro-Pneumatic Regulator dynamics, and changes in the control pressure p_c in the cavity of the valve results in changes in the diaphragm position x, following the pneumatic valve dynamics. The valve position determines the flow resistances in the LPO and HPO, related to the flow split between the pickup and outer tubes and, as consequence, to the phase distribution upstream of the pickup tube.

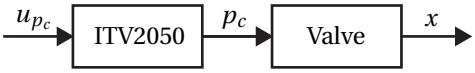

Figure 2.8: Block diagram of the combination between the SMC ITV2050 Electro-Pneumatic Regulator and the ASV Stübbe MV 310 pneumatic diaphragm valve.

2.5.2. CONTROL PRESSURE DYNAMICS

The actuator of the tomography-based controller investigated in this thesis is represented by the block diagram of Figure 2.8, that shows that both the SMC ITV2050 Electro-Pneumatic Regulator dynamics and the pneumatic valve dynamics impact the actuator response. Therefore, a slow response of the Electro-Pneumatic Regulator can limit the actuator response and, as consequence, the response of the tomography-based controller.

The Electro-Pneumatic Regulators of the axial cyclone facility are connected to (i) a compressed air line at around 8 barg, (ii) the pneumatic valves and (iii) the lab air atmosphere at 0 barg. A solenoid valve inside the SMC ITV2050 connects the compressed air line to the internal cavity of the pneumatic valve when the control pressure setpoint of the Electro-Pneumatic Regulator is increased, resulting in an air flow that fills the volume above Diaphragm 1 and closes the valve. A second solenoid valve inside the SMC ITV2050 connects the cavity above Diaphragm 1 to the lab atmosphere when the control pressure setpoint of the SMC ITV2050 is decreased, creating an air flow from the cavity of the valve to the lab that opens the equipment.

The rate of change of the control pressure in the pneumatic diaphragm valves depends on the pressure difference between the inner volume above Diaphragm 1 and the SMC ITV2050 connection. Since the pneumatic valves of the experimental facility fully close for relatively low control pressures (less than 1 barg for the LPO valve and less than 2 barg for the HPO valve), a large pressure difference is obtained between the compressed air line at 8 barg and the cavity of the valve when increasing the SMC ITV2050 control pressure setpoint, resulting in a large flow rate to the cavity that quickly rises the pressure above Diaphragm 1 and closes the valve (it takes around 0.1 s between the change in the SMC

ITV2050 pressure setpoint and the desired value being reached in the cavity of the LPO valve). However, a low pressure difference between the valve cavity and the lab takes place when reducing the SMC ITV2050 pressure setpoint, resulting in a low air flow rate from the valve to the lab and, as consequence, a slow decay of the pressure above Diaphragm 1 and valve opening (it takes around 1 s between lowering the SMC ITV2050 setpoint and obtaining the desired pressure in the cavity of the LPO valve).

The difference between the closing and opening speeds of the LPO valve due to the asymmetric control pressure behavior is undesired for the tomography-based control of the gas-liquid distribution in the cyclone. To speed up the control pressure decrease in the cavity of the LPO valve and, as consequence, its opening motion, a second SMC ITV2050 with constant control pressure setpoint of 4 barg was connected to the Air Port 2 of the LPO valve, shifting the range of operation of the valve and SMC ITV2050 Electro-Penumatic Regulator connected to Air Port 1 from 0-1 barg to 4-5 barg. This significant increase in the pressure difference between the valve cavity and the lab atmosphere lowered the time interval between reducing the control pressure setpoint of the SMC ITV2050 and obtaining the desired pressure in the top cavity of the LPO valve to around 0.1 s, matching the control pressure increase time-constant and resulting in similar opening and closing speeds of the valve. A picture of the LPO valve with two Electro-Pneumatic Regulators is presented in Figure 2.9.

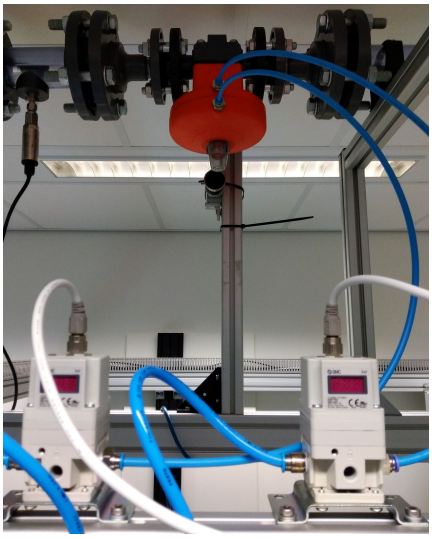

Figure 2.9: LPO valve (ASV Stübbe MV 310 of nominal diameter 25 mm) connected to two SMC ITV2050 Electro-Pneumatic Regulators. Besides the LPO valve and two Electro-Pneumatic Regulators, the image shows the p_{lpo} pressure sensor upstream of the LPO valve and the camera used record the indicator pin of the LPO valve during the experiments.

The HPO valve is not used for real-time control, being maintained at fixed positions during the experiments. Since similar opening and closing times of the HPO valve are not required, the Air Port 2 of the HPO valve is kept open to the lab (i.e., at 0 barg), maintaining

the original 0-2 barg range of operation of the equipment.

2.5.3. LPO VALVE DYNAMICS

Figure 2.10 presents the measured position of the LPO and HPO valve diaphragms for quasi-steady state control pressure changes in Air Port 1. The plots of Figure 2.10 show that the diaphragm position of the LPO and HPO valves takes different paths when increasing the control pressure, closing the valve, or decreasing the control pressure, opening the equipment. The behavior characterizes a hysteresis in the control pressure-diaphragm position relation, due to Coulomb friction between the internal valve components [98, 99].

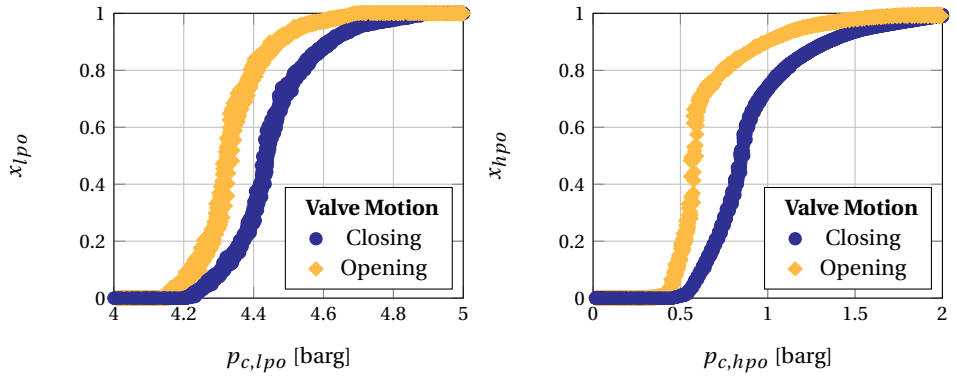

Figure 2.10: LPO and HPO valve hysteresis for quasi-steady state control pressure changes. Left: LPO valve hysteresis obtained with 10 periods of a triangle wave with frequency 0.005 Hz in the control pressure $p_{c,lpo}$, covering the range 4-5 barg (the Air Port 2 of the valve was maintained at 4 barg during the experiments). Right: HPO valve hysteresis obtained for 10 periods of a sinusoidal control pressure $p_{c,hpo}$ with frequency 0.001 Hz, covering the range 0-2 barg.

The Light Phase Outlet valve dynamics is investigated based on the diaphragm position variations, $x'_{lpo}(t) = x_{lpo}(t) - \overline{x}_{lpo}$, measured for different sinusoidal control pressure input variations, $u'_{p_c}(t) = u_{p_c}(t) - \overline{u}_{p_c}$, where $\overline{x}_{lpo}$ is the time-average LPO valve diaphragm position and $\overline{u}_{p_c}$ is the time-average control pressure input (sine wave offset). A wide range of frequencies was covered in the inputs, made in discrete-time with sample time $T_s = 0.1$ s and summarized in Table 2.3. The magnitude and phase of the LPO valve dynamics measured in the frequencies excited by the inputs are presented in Figure 2.11.

Table 2.3: Offset and amplitude of the sine inputs used to obtained the LPO valve response of Figure 2.11. Note that the amplitude of Inputs 1 and 2 increase with the frequency of excitation f. Inputs 1 and 2 were also used in the system identification experiments of chapter 5 (section 5.5). $T_s = 0.1$ s.

Number	Input Offset	Sine Amplitude	Frequencies
0	$\overline{u}_{p_c} = 4.47$ barg	$\lvert u'_{p_c}\rvert = 0.125$	0.01 Hz to 1 Hz
1	$\overline{u}_{p_c} = 4.39$ barg	$\lvert u'_{p_c}\rvert = 0.1\sqrt{21.96 - 21.6\cos(2\pi f T_s)}$	0.01 Hz to 2 Hz
2	$\overline{u}_{p_c} = 4.39$ barg	$\lvert u'_{p_c}\rvert = 0.2\sqrt{21.96 - 21.6\cos(2\pi f T_s)}$	0.01 Hz to 1 Hz

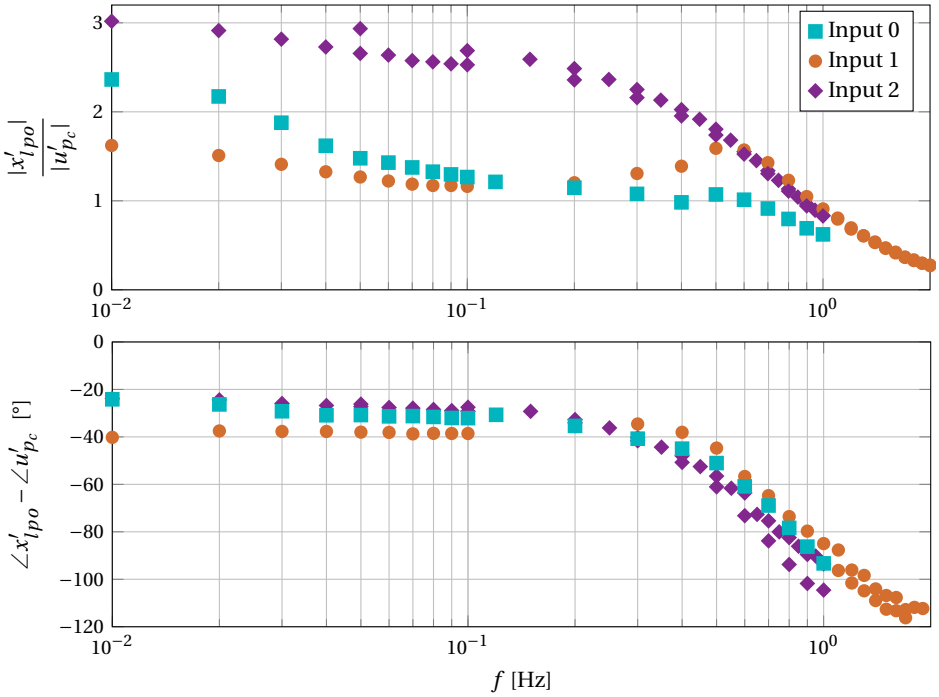

Figure 2.11: Relation between variations in the LPO valve diaphragm position, x'_{lpo}, and variations in the control pressure input, u'_{p_c}, measured in the frequency of excitation for individual sine inputs. Top: ratio between the magnitudes of x'_{lpo} and u'_{p_c}. Bottom: phase between x'_{lpo} and u'_{p_c}. The inputs performed are described in Table 2.3.

Figure 2.11 shows that the LPO valve hysteresis results in a strong nonlinear valve response to control pressure inputs, characterized by: (i) different magnitudes in the ratio $|x'_{lpo}|/|u'_{p_c}|$ for different control pressure inputs, in contrast to a $|x'_{lpo}|/|u'_{p_c}|$ independent of the amplitude of the input for linear systems (the magnitude of a transfer function is only a function of the frequency); (ii) a phase of around 30 ° between x'_{lpo} and u'_{p_c} for quasi-steady state inputs (at very low frequencies), in contrast to a phase that tends to zero for $f \to 0$ in linear systems.

The nonlinear effects observed in the magnitude and phase of the LPO valve response occur since the diaphragm of the valve gets stuck whenever the direction of the input is reversed due to Coulomb friction, resulting in no motion of the valve until an absolute difference of around 0.06 barg is obtained between the current control pressure input and the last control pressure input before the reversal. Hysteresis impacts the LPO valve response over the entire range of frequencies, although it is more significant for small control pressure variations due to a larger fraction of u'_{p_c} being consumed by Coulomb friction.

Figure 2.11 also shows a strong damping behavior of the LPO valve, that reduces the magnitude and increases the phase of the LPO valve response as the frequency of excitation is increased. This damping behavior results in a LPO valve step response in the order

of 1 s, limiting the frequency of phase distribution fluctuations that can be controlled with the equipment. For instance, some swirling gas-liquid flow patterns have strong phase distribution fluctuations with time-constants in the order of 0.1 s (chapter 5), making them too fast to be suppressed with the LPO valve.

2.6. LIQUID FLOW RATE VARIATIONS

Since the flow pattern fluctuations cannot be controlled, the tomography-based real-time controller proposed in Figure 2.1 is evaluated based on the suppression of external disturbances in the phase distribution (gas core) upstream of the pickup tube, created manipulating the gas mass flow rate of the installation via Mass Flow Controller 1 (chapter 5).

Changes in the gas mass flow rate of the installation during the generation of process disturbances, and in the LPO valve diaphragm by the controller for their suppression, impact the pressure distribution in the entire experimental facility. Since a centrifugal pump is used to create the liquid flow in the setup, changes in the pressure downstream of the pump impact the liquid flow rate created by the equipment. For instance, in the study of the gas core response upstream of the pickup tube to actions in the LPO valve in chapter 5, the liquid flow rate oscillated between 6.6 $m^3 h^{-1}$ and 8.6 $m^3 h^{-1}$ for the LPO valve control pressure Input 2 with frequency 0.01 Hz, and between 6.6 $m^3 h^{-1}$ and 9.4 $m^3 h^{-1}$ for the LPO valve control pressure Input 4 with frequency 0.01 Hz, significantly contributing to the gas core response to the LPO valve observed during the experiments[3].

The liquid flow rate-pressure jump relation created by centrifugal pumps is a function of the pump shaft speed ω_p [100, 101]. In the experimental facility, the shaft speed of the Iwaki MX-402 pump is controlled by a CONTROL TECHNIQUES Commander SK with shaft speed setpoint set via user inputs in LabVIEW. Figure 2.12 presents the relation between the average water flow rate q_l created by the pump and the average pressure p_{in} upstream of the gas inlet, measured in the experimental facility for $\omega_p = 2430$ rpm and $\omega_p = 2700$ rpm.

The quasi-steady state relation between the liquid flow rate q_l (in $m^3 h^{-1}$) and p_{in} (in barg) of Figure 2.12 is well approximated by

$$q_l = \begin{cases} -8.4 p_{in} + 16.0, & \text{for } \omega_p = 2430 \text{ rpm} \\ -8.4 p_{in} + 18.7, & \text{for } \omega_p = 2700 \text{ rpm} \end{cases}, \tag{2.8}$$

indicating that the liquid flow rate pumped to the axial cyclone decreases as the pressure of the setup increases, for instance, when (partially) closing the LPO or HPO valves or reducing the gas mass flow rate of the installation (via the hydrostatic pressure). Note that Equation 2.8 is valid for quasi-steady state changes in the flow loop pressure, and the dynamics of the flow, pump and frequency regulator can cause a significant deviation of the liquid flow rate-pressure coupling from Equation 2.8 with the increase in the frequency

[3] The valve inputs 2 and 4 are described in section 5.5. For $f = 0.01$ Hz, Input 2 results in the LPO valve control pressure input $u_{p_c} \approx 4.39 + 0.12 \sin(0.02\pi(t + 0.5))$ for a pump shaft speed $\omega_p = 2430$ rpm, gas mass flow rate $w_g = 8.53$ kg h^{-1} and normalized HPO diaphragm position $x_{hpo} = 0.74$; Input 4 results in the LPO valve control pressure $u_{p_c} \approx 4.39 + 0.12 \sin(0.02\pi(t + 0.5))$ for $\omega_p = 2700$ rpm, $w_g = 8.53$ kg h^{-1} and $x_{hpo} = 0.80$.

of excitation of the system (for instance, when performing fast changes in the LPO valve opening).

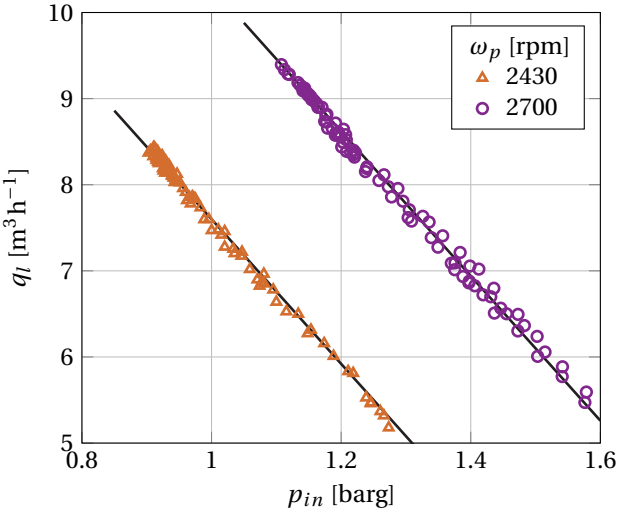

Figure 2.12: Time-average liquid flow rate q_l as function of the time-average pressure downstream of the pump p_{in}, measured for the Iwaki MX-402 pump with shaft speed setpoints ω_p = 2430 rpm and ω_p = 2700 rpm. The plotted data was obtained for multiple gas flow rates and LPO and HPO valve positions, matching the experiments of chapter 4. The continuous black lines of the figure are described by Equation 2.8.

The pressure-liquid flow rate coupling of the pump has a significant impact on the relation between the average gas core diameter and LPO valve position obtained in chapter 4, and on the model of the gas core dynamics obtained in chapter 5. This occurs since the experiments of these chapters are performed with fixed pump shaft speeds, resulting in changes in the liquid flow rate upstream of the axial cyclone separator when the LPO valve opening is changed which impact the gas core diameter inside the equipment via conservation of mass. The pump relations are unimportant for the swirling gas-liquid flow pattern identification experiments of chapter 3, that are performed adjusting the pump shaft speed and water bypass valve based on the desired liquid flow rate before each experimental point is measured.

This thesis does not focus on any particular application of the axial cyclone, and the liquid flow rate dynamics in the experimental facility does not limit the tomography-based real-time control evaluation performed in the current research. However, in general, it is important that simplified experimental facilities used to design tomography-based controllers for industrial multiphase flow processes mimic the flow rate dynamics of the real application, resulting in a phase distribution dynamics in the simplified setup representative of the real process. For instance, if the flow rates of the real process are not affected by pressure changes related to control actions, then positive displacement pumps are preferred over centrifugal pumps in the simplified experimental facility.

PART II: REAL-TIME ELECTRICAL RESISTANCE TOMOGRAPHY

Multiphase flow measurements with Electrical Resistance Tomography are traditionally performed acquiring all the flow data at relatively high frequencies (in the order of 10 Hz) and then slowly processing it offline into cross-sectional phase distribution profiles. The offline image processing step is required due to the high computational demand of traditional image reconstruction algorithms based on inverse problems, where iterative schemes are often used to increase the spatial accuracy of the resulting tomograms.

Despite the substantial computation power increase in the recent years, traditional general image reconstruction algorithms remain too slow compared to the multiphase flow time scales, with phase distribution fluctuations at frequencies above 1 Hz due to the multiphase flow patterns [102, 103]. Moreover, traditional image reconstruction algorithms provide a limited spatial accuracy in the reconstructed images, due to the underdetermined and ill-posed inverse problem. For instance, tests performed measuring and processing the gas-liquid distribution in the axial cyclone in real-time with the current ERT hardware and fastest traditional ERT image reconstruction algorithms available (Linear Back Projection and Gauss-Newton with a single iteraction) resulted in a maximum measurement frequency of around 3 Hz, with reconstructed gas cores up to five times wider than the real gas core inside the cyclone [88].

The slow and inaccurate image reconstruction of fast traditional ERT algorithms imposes a major limitation to the tomography-based real-time control of the axial cyclone. Therefore, a new application-specific image reconstruction algorithm was developed in cooperation with dr. Sattar, during his PhD in the Lodz University of Technology [89], to monitor the gas core upstream of the pickup tube.

Different from traditional ERT image reconstruction techniques, the algorithm proposed uses the existing knowledge of the swirling gas-liquid flow physics to track a single roughly-circular gas core in the axial cyclone cross-section. The gas core is reconstructed based on three variables (the gas core diameter, radial centroid position and azimuthal centroid position) instead of hundreds or thousands variables as in the general ill-posed inverse problem (the discrete conductivity distribution in the ERT cross-section). The vast reduction in the number of variables in the image reconstruction step resulted in phase distribution measurements in the axial cyclone substantially more accurate and three orders of magnitude faster than traditional ERT schemes.

This part is divided in two sections: the ERT hardware used in the experiments of this dissertation is described in section 2.7, and the proposed real-time ERT image reconstruction algorithm for gas cores in axial cyclone separators, previously published in [90], is presented in section 2.8.

2.7. DATA ACQUISITION SYSTEM

The tomographic measurements of this thesis are performed by a Rocsole Flow Watch data acquisition system (ERT hardware) with 16 electrodes, installed in the pipe cross-section $0.9D$ upstream of the tip of the pickup tube. The distance of $0.9D$ between the

electrodes and the tip of the pickup tube was chosen to minimize the influence of the electrically insulating pickup tube in the electric field measured by the ERT system. Additionally, a metal shield is used around the ERT electrodes to reduce external electromagnetic disturbances in the measurements. A picture of the ERT electrodes, signal conditioning units (connected to the electrodes) and electromagnetic shield is presented in Figure 2.13.

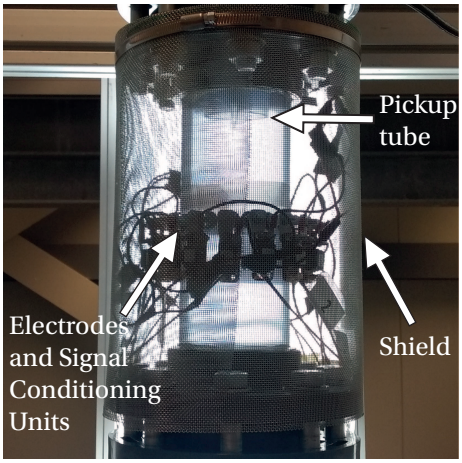

Figure 2.13: ERT electrodes installed $0.9D$ upstream of the pickup tube.

The Flow Watch system operates in the Voltage-Current scheme, where voltage is applied to the source electrode and electric current is measured in the remaining electrodes, acting as sinks. Every one of the 16 electrodes is used as source for each frame measured by the ERT system, resulting in two hundred forty electric current measurements per frame. The Flow Watch system can reach a maximum stable acquisition frequency of 12 frames per second, being configured to measure the gas core in the axial cyclone and communicate with the flow loop computer at a frequency of 10 Hz.

A Windows 10 Central Processing Unit with Intel Core i7 1.80 GHz and 16 GB RAM is used to process the data acquired by the Flow Watch System in real-time, converting the electrical currents measured by the ERT system into the gas-liquid distribution in the ERT cross-section via the image reconstruction algorithm of section 2.8. The gas core diameter is then forwarded to the computer of the experimental facility with LabVIEW via the User Datagram Protocol (UDP), where it is saved with the remaining flow loop variables and used in the tomography-based feedback control calculations.

2.8. IMAGE RECONSTRUCTION ALGORITHM

The application-specific ERT algorithm developed in this research for the tomography-based real-time control of axial cyclones assumes that a single gas core with roughly circular cross-section is formed inside the separator, based on the swirling gas-liquid flow physics observed in the axial cyclone for sufficiently high liquid flow rates in chapter 3. A drawing of the ERT electrodes measuring the gas core is presented in Figure 2.14.

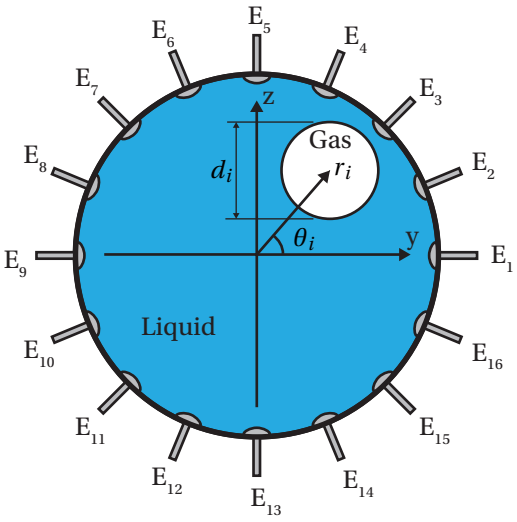

Figure 2.14: Gas core in the axial cyclone cross-section with ERT electrodes. The gas core has diameter d_i, radial centroid position r_i and azimuthal centroid position θ_i.

As shown in Figure 2.14, the gas core is described by three parameters in the proposed real-time ERT image reconstruction algorithm: the gas core diameter d_i, the gas core centroid radial position r_i, and the gas core centroid azimuthal position θ_i. The gas core diameter and radial position are measured by the image reconstruction algorithm normalized by the inner diameter of the pipe, i.e., as $d_{ert} \triangleq d_i/D$ and $r_{ert} \triangleq r_i/D$, respectively. The azimuthal position measured by the algorithm is represented by θ_{ert}.

2.8.1. IMAGE RECONSTRUCTION CORRELATIONS

The whole image reconstruction is based on twelve electrical current measurements $I[m]$, from which eight are between opposite electrodes (electrode pairs 1-9, 2-10, 3-11, 4-12, 5-13, 6-14, 7-15, 8-16, corresponding to $m = 1$ to $m = 8$, respectively) and four are in 90 ° angles (electrode pairs 1-5, 5-9, 9-13, 13-1, corresponding to $m = 9$ to $m = 12$, respectively). Prior to the gas core measurements, the electrical current $I_l[m]$ between the electrode pairs is measured with the system filled with water (calibration step).

Due to the electrically-insulating characteristic of air, the electric current between electrodes drops from $I[m] = I_l[m]$ when the pipe is filled with water to $I[m] = 0$ when the pipe is filled with air. The image reconstruction algorithm calculations are made independent of the liquid conductivity using the normalized electric current ι, defined as:

$$\iota[m] \triangleq \frac{I_l[m] - I[m]}{I_[m]} \tag{2.9}$$

By definition, $\iota[m] = 0$ for the pipe filled with water and $\iota[m] = 1$ for the pipe filled with air.

The relation between normalized electric current, gas core diameter and gas core centroid position was obtained from experiments performed with 3D-printed Acrylonitrile Butadiene Styrene (ABS) phantoms of known diameter and position, mimicking the electrically insulating gas core in the axial cyclone. The picture of a phantom being measured by the ERT system during the experiments is presented in Figure 2.15.

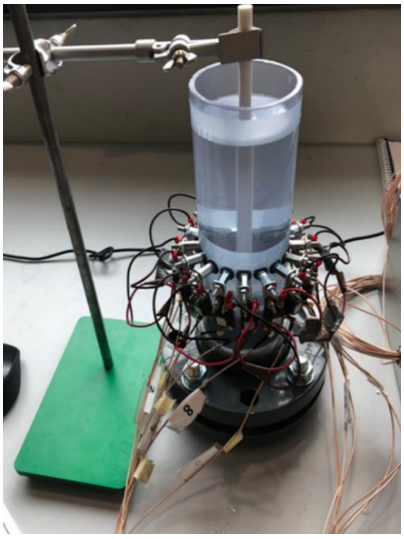

Figure 2.15: ERT system measuring an ABS phantom.

GAS CORE DIAMETER

The ABS phantoms and gas core are electrically insulating, increasing the equivalent resistance between the source and sink ERT electrodes when present in the pipe and, as consequence, decreasing the electric currents in the sink electrodes and increasing $\iota[m]$. Figure 2.16 presents illustrations of the electric field lines between the source electrode (E_1) and the sink electrode (E_9) for a pure conductive liquid (left) and for a conductive liquid with an insulating gas core/phantom in the center of the domain (right).

Figure 2.16-left shows that the electric field lines between opposite source and sink electrodes take the shortest path possible in the absence of an insulating gas core, resulting in the highest currents in the sink electrodes that can be created by the ERT system. As shown in Figure 2.16-right, the electric field lines get distorted when a phantom/gas core is present in the domain, increasing the energy dissipation in the water and, as consequence, lowering the electric currents observed in the sink electrode compared to the undisturbed (water) scenario for the same electric potential. The electric field lines get more distorted with the increase in the phantom/gas core diameter, further decreasing the electric current measured in the sink electrode.

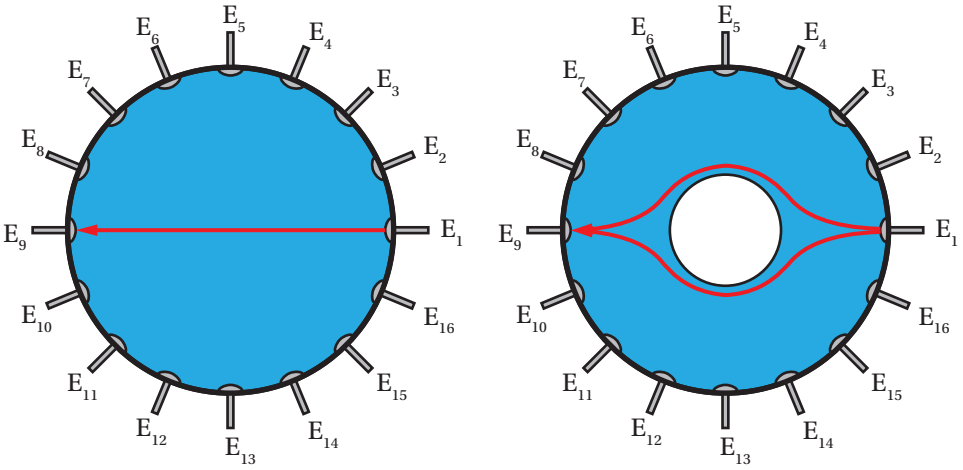

Figure 2.16: Illustration of some electric field lines (in red) between opposite ERT electrodes in the absence (left) and presence (right) of an electrically insulating gas core.

The conductivity distribution in the ERT cross-section is symmetric for centered gas cores, as illustrated by the electric field lines between E_1 (source) and E_9 (sink), and between E_5 (source) and E_{13} (sink), in Figure 2.17-left. Symmetry is lost when the insulating region is moved out of center, resulting in different electric field lines between opposite electrodes, as shown in Figure 2.17-right. Note that the electrode field lines of Figure 2.17 are not simultaneously present in the system, since the ERT system uses a single electrode as source per current measurement (one frame is obtained for multiple current measurements, covering each electrode of the ERT system as source).

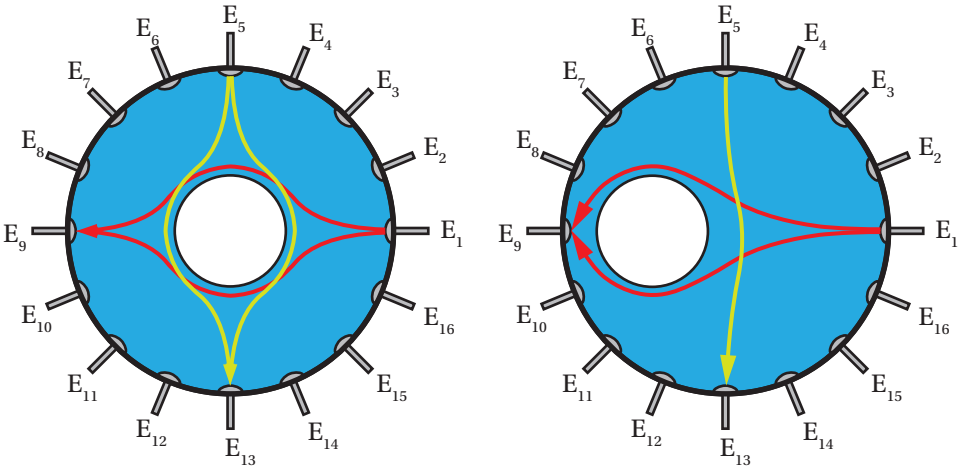

Figure 2.17: Electric field lines between opposite ERT electrodes for two distinct current measurements (red and yellow) of an electrically insulating gas core centered in the pipe (left) and away from the pipe centerline (right).

When the system is symmetric, the same electric current is measured by all eight opposite electrode pairs in each frame. However, different electric currents are measured per opposite electrode pair when the gas core is not centered in the pipe. Figure 2.17 shows that the electric field lines between E_1 and E_9 are more distorted for the phantom out of center than for the centered phantom, reducing the electric current measured in E_9 in relation to the centered phantom/gas core condition. On the other hand, the electric field lines between E_5 and E_{13} are less distorted for the out of center phantom than for the centered one, increasing the electric current measured in the sink electrode E_{13} in relation to the symmetric condition.

Part of the electric currents between opposite electrode pairs increases, and part decreases, when the phantom is moved out of center. Therefore, the average normalized current between opposite electrode pairs,

$$\langle \imath \rangle \triangleq \frac{1}{8} \sum_{m=1}^{8} \imath[m], \tag{2.10}$$

is used to compute the gas core/phantom diameter based on the electric currents measured by the ERT system, independent of the radial position of the insulating region.

Figure 2.18 presents the average normalized current measured for phantoms in the center of the pipe, covering a wide range of phantom diameters and water conductivities.

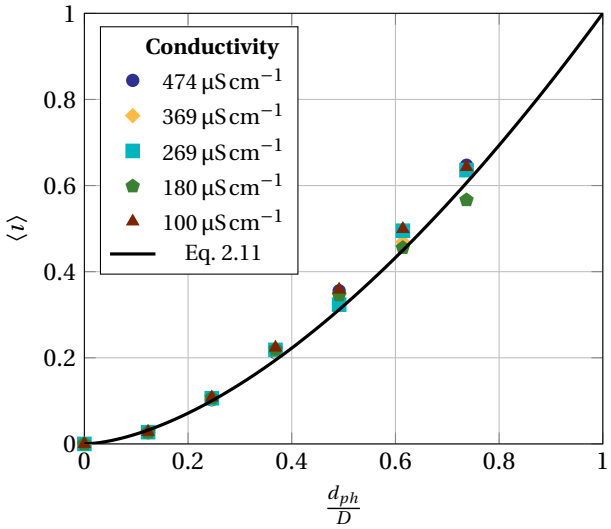

Figure 2.18: Average normalized current $\langle \imath \rangle$ as function of the phantom diameter d_{ph} for multiple water conductivities. Measurements performed with the phantoms centered in the pipe.

Figure 2.18 shows that the average normalized current $\langle \imath \rangle$ increases with the phantom diameter d_{ph} and can be approximated by the power law

$$\langle \imath \rangle \approx \left(\frac{d_{ph}}{D} \right)^{1.64}, \tag{2.11}$$

independent of the liquid conductivity. The power law fit of the data ensures that $\langle \iota \rangle = 0$ for $d_{ph} = 0$ (pure water in the domain) and $\langle \iota \rangle = 1$ for $d_{ph} = D$ (pure air in the domain).

The equation used to compute the gas core diameter normalized by the inner diameter of the pipe, departing from the normalized electric currents measured by the ERT system, is obtained inverting Equation 2.11:

$$d_{ert} = \langle \iota \rangle^{0.61} \tag{2.12}$$

As shown in Figure 2.18, the ERT currents have a low sensitivity to phantom/gas core diameters below 10% of the pipe diameter, significantly reducing the accuracy of the technique for thin gas cores.

RADIAL GAS CORE POSITION

Since different currents are measured between opposite electrode pairs when the gas core is out of center, the radial position of the insulating region is related to the standard deviation of the normalized electric current $\iota[m]$ for $m \leq 8$,

$$\sigma(\iota) \triangleq \sqrt{\frac{1}{7} \sum_{m=1}^{8} (\iota[m] - \langle \iota \rangle)^2} \tag{2.13}$$

Apart from the radial position of the electrically insulating region in the pipe, the standard deviation of $\iota[m]$ is also impacted by the gas core/phantom diameter. For instance, the electric current between opposite electrodes is always more or less the same for a small insulating region, even if it is closer to one of the electrodes, due to the small disturbance in the electric field created by it. On the other hand, large insulating regions strongly distort the electric field, resulting in larger differences in the electric currents measured between opposite electrodes when out of center. Since the diameter of the insulating region can be related to the average normalized current $\langle \iota \rangle$, the gas core diameter effect on the current differences can be captured including $\langle \iota \rangle$ in the computation of the radial position of the insulating region centroid. As the difference between the electric currents increases with the phantom/gas core diameter, the radial position is obtained in the proposed algorithm based on the ratio $\sigma(\iota)/\langle \iota \rangle$.

The relation between $\sigma(\iota)/\langle \iota \rangle$ and the radial position of the phantom centroid, measured for a water conductivity of 194 $\mu S\,cm^{-1}$, is presented in Figure 2.19. The radial positions of the phantom centroid reported in the figure are computed based on the distance of the phantom to electrodes 1, 5, 9 and 13, measured with a ruler during the experiments.

Figure 2.19 shows that the ratio $\sigma(\iota)/\langle \iota \rangle$ is insensitive to the radial position of the phantom centroid for $r_{ph} < 0.1D$, due to the electric field being close to symmetric and the currents between opposite electrodes being close to each other. The experimental data of Figure 2.19 can be approximated by the power law:

$$\frac{\sigma(\iota)}{\langle \iota \rangle} \approx 69.2 \left(\frac{r_{ph}}{D} \right)^{2.61} \tag{2.14}$$

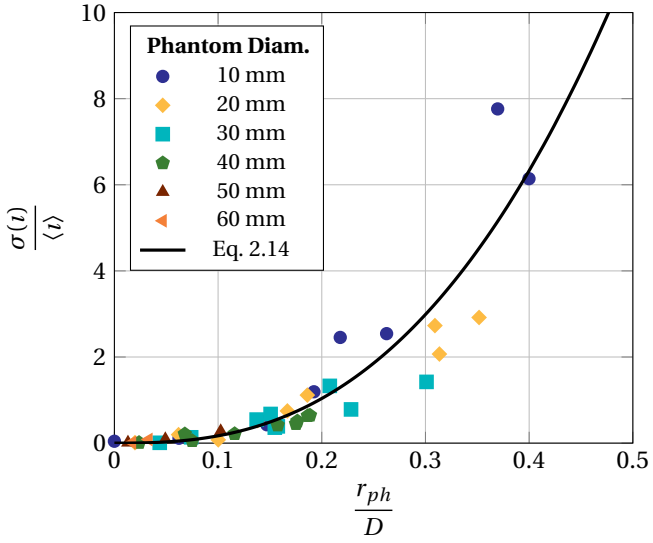

Figure 2.19: Standard deviation of the normalized electric current divided by the average normalized current, $\sigma(\iota)/\langle\iota\rangle$, as function of the radial position of the phantom r_{ph} measured with a ruler.

In the proposed image reconstruction algorithm, the radial centroid position of the gas core is computed from the electric currents measured by the ERT system inverting Equation 2.14:

$$r_{ert} = 0.197\left(\frac{\sigma(\iota)}{\langle\iota\rangle}\right)^{0.38} \tag{2.15}$$

AZIMUTHAL GAS CORE POSITION

The ERT domain is divided into four quadrants in the reconstruction of the azimuthal position of the gas core centroid. By definition, Electrode 1 determines $\theta_{ert} = 0\,°$ and, since sixteen electrodes are used in the system, E2 determines $\theta_{ert} = 22.5\,°$, E3 determines $\theta_{ert} = 45\,°$ and so on. The quadrants are determined by the azimuthal positions of electrodes 1 ($\theta_{ert} = 0\,°$), 5 ($\theta_{ert} = 90\,°$), 9 ($\theta_{ert} = 180\,°$) and 13 ($\theta_{ert} = 270\,°$).

The gas core centroid azimuthal position is obtained in two steps. First, the four 90 ° normalized electric currents measured between electrode pairs 1-5, 5-9, 9-13 and 13-1 ($9 \leq m \leq 12$) are used to find the quadrant where the gas core is located. Then, the normalized electric current between opposite electrodes ($m \leq 8$) is used to find the electrode of the quadrant containing the gas core closest to the electrically insulating region.

The electric field lines for 90 ° electric current measurements of a centered and out of center gas core in the ERT cross-section are illustrated in Figure 2.20.

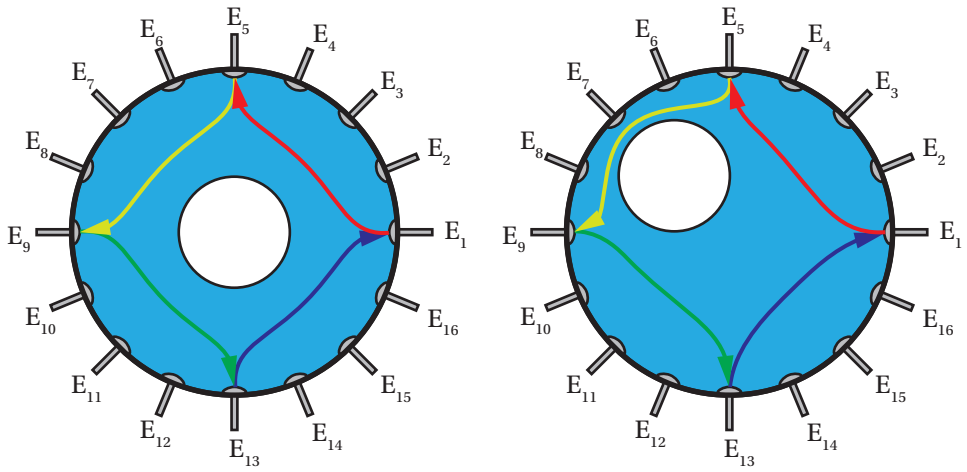

Figure 2.20: Illustration of some electric field lines for 90 ° current measurements of an electrically insulating gas core in the center of the pipe (left) and away from the pipe centerline (right).

Figure 2.20 shows that the electric field between E_5 and E_9 is significantly impacted by the electrically insulating region as the gas core is moved from the center of the pipe to nearby an electrode in the quadrant $E_5 - E_9$. Therefore, the image reconstruction algorithm assumes that the insulating region is closest to the pair of electrodes with the largest 90 ° current deviation in relation to the liquid calibration, i.e., with largest $\imath[m]$ for $9 \leq m \leq 12$. In Figure 2.20-right, the most affected 90 ° electric current is measured between E5 and E9, indicating that the gas core is in that quadrant.

In addition to the quadrant information, the gas core is assumed to be in the line between opposite electrodes which were most affected by the insulating region, i.e., with the largest $\imath[m]$ for $1 \leq m \leq 8$. In Figure 2.20-right, this corresponds to the line between electrodes 7 and 15.

Since the same electric currents are measured between electrodes 7 and 15 when E7 is acting as source and E15 as sink, and when E15 is acting as source and E7 as sink, the quadrant information is essential to determine which of the two electrodes of the pair is the closest to the gas core. In Figure 2.20-right, only electrode 7 is in the (most affected) quadrant E5-E9, indicating that E7 and not E15 is the closest electrode to the gas core. Since Electrode 7 determines $\theta_{ert} = 135$ °, this is considered the azimuthal centroid position of the gas core in Figure 2.20-right. On the other hand, if the most affected opposite pair remained E7-E15, but the most affected 90 ° electric current was measured between E13 and E1, the closest electrode to the gas core would be E15, resulting in $\theta_{ert} = 315$ °. Note that θ_{ert} is described in steps of 22.5 ° in the proposed algorithm since a hardware with 16 electrodes was used in the experiments.

In some rare occasions, the most affected opposite electrode pair is not compatible with the most affected quadrant, for instance when the gas core is around the center of the pipe and the electrical currents are too close to each other. In this scenario, the algorithm proposed computes θ_{ert} based on the highest opposite electric current measurement compatible with the most affected quadrant.

PHASE DISTRIBUTION RECONSTRUCTION

Once the phantom/gas core diameter, radial centroid position and azimuthal centroid position are known, the liquid distribution in the pipe cross-section can be reconstructed setting the liquid fraction to $\varepsilon_l = 0$ inside the reconstructed phantom/gas core and to $\varepsilon_l = 1$ outside it. Figure 2.21 shows a comparison between some phantoms reconstructed by the application-specific ERT algorithm and the true phantoms inside the pipe.

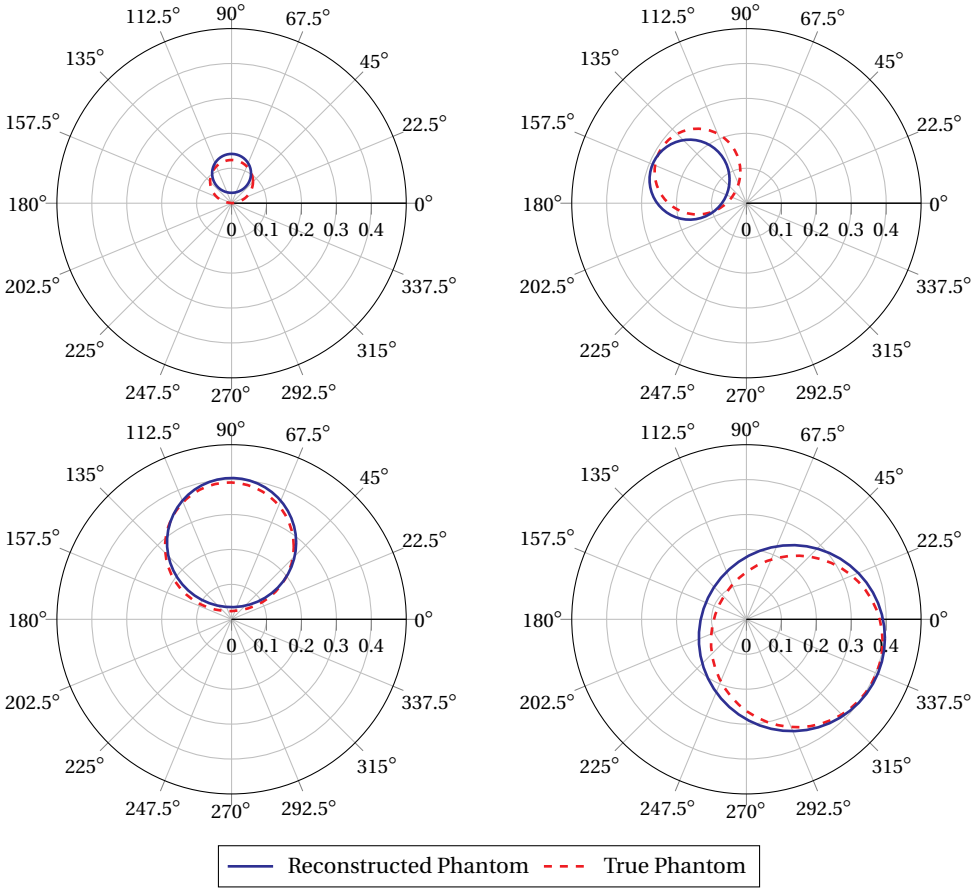

Figure 2.21: Comparison between the phantoms reconstructed by the application-specific ERT algorithm (blue circles) and the true phantoms inside the pipe (red dashed circles). Plots for phantoms of diameter 10 mm, 20 mm, 30 mm and 40 mm at different positions in the pipe cross-section. The radial position of the plots is normalized by the pipe inner diameter.

Figure 2.21 shows a good qualitative match between the proposed algorithm reconstructions and the true conditions inside the pipe, independent of the phantom diameter and position. Tests performed with the non-iterative Gauss-Newton method and the proposed application-specific algorithm showed that the proposed algorithm can reconstruct the phase distribution three orders of magnitude faster than the traditional algorithm [90].

2.8.2. MEASUREMENT ACCURACY

The phantom diameter reconstructed by the real-time ERT algorithm d_{ert} is presented as function of the true phantom diameter d_{ph} for the entire dataset obtained with the phantoms in Figure 2.22.

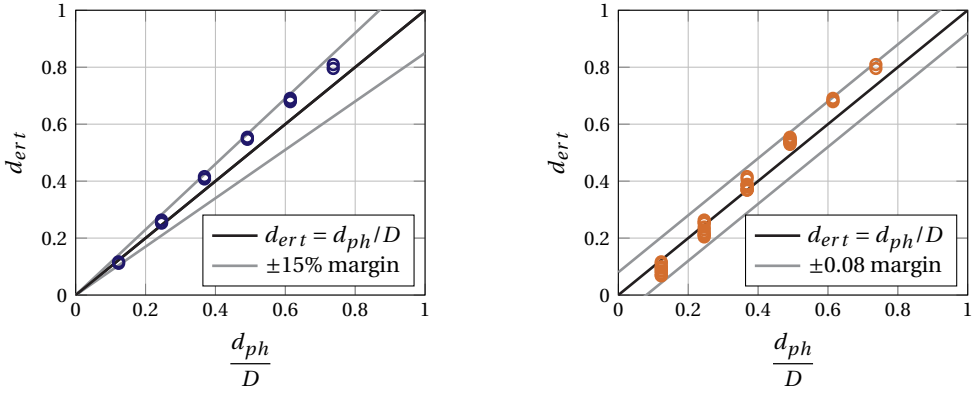

Figure 2.22: Comparison between the phantom diameter predicted by the ERT image reconstruction algorithm (d_{ert}) and the phantom diameter divided by the pipe diameter (d_{ph}/D). Left: measurements for $r_{ph}/D \leq 0.1$ (phantoms around the pipe centerline). Right: measurements for $r_{ph}/D \leq 0.4$ (entire dataset).

Figure 2.22-left shows that the application-specific ERT has a relative measurement uncertainty in the gas core diameter normalized by the pipe diameter of around ±15% for centered phantoms/gas cores wider than 10% of the pipe diameter. The accuracy of the reconstructed normalized gas core diameter decreases for out of center phantoms, as shown in Figure 2.22-right, where an absolute measurement uncertainty of ±0.08 is obtained. Despite being relatively high, the general absolute measurement uncertainty of ±0.08 in the normalized gas core diameter obtained by the algorithm is considerably smaller than traditional ERT algorithms, where absolute measurement errors as high as 0.5, i.e., half of the pipe diameter, were observed for the same phantoms used in the current chapter [88].

The azimuthal gas core position is undefined in the center of the pipe. Therefore, the proposed ERT algorithm resolution in relation to the reconstructed gas core position is evaluated based on the normalized centroid y and z positions, obtained based on the coordinate system of Figure 2.14 via

$$y_{ert} = r_{ert} \cos\theta_{ert} \tag{2.16}$$

and

$$z_{ert} = r_{ert} \sin\theta_{ert}, \tag{2.17}$$

respectively.

Figure 2.23 presents the comparison between the y and z phantom positions reconstructed by the ERT algorithm and measured with the ruler, showing that the application-

specific ERT algorithm has an absolute measurement uncertainty of around ±0.08 in y_{ert} and z_{ert}.

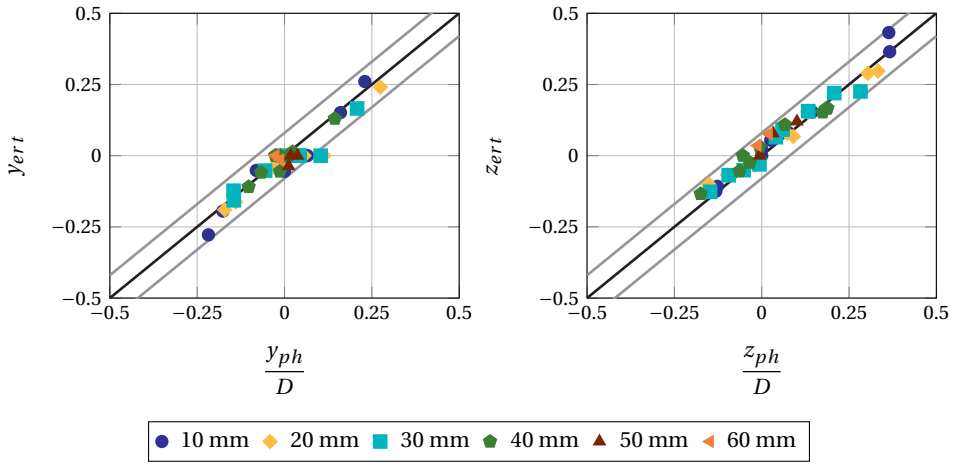

Figure 2.23: Phantom position reconstructed by the application-specific Electrical Resistance Tomography algorithm (y_{ert} and z_{ert}) versus true phantom position divided by the pipe diameter (y_{ph}/D and z_{ph}/D). Left: y-coordinate. Right: z-coordinate. Legend for both plots: phantom diameter.

The tomography-based real-time control investigation of this thesis is performed for gas cores around the axial cyclone centerline and, therefore, only the gas core diameter measured by the ERT system is used in the real-time control of the separator. For such gas cores, the normalized gas core diameter d_{ert} measured by the ERT system has an uncertainty of ±15% of the measured value (Figure 2.22-left). Since the gas core is centered in the pipe, the error margin in the gas core position is irrelevant to the analysis performed in the remaining of this thesis; the radial and azimuthal gas core positions may be relevant for the real-time control of axial cyclones with eccentric pickup tubes. It is important to emphasize that the ±15% error margin is only valid for gas cores wider than 10% of the pipe diameter, since the ERT currents are insensitive to the gas core diameter below that (Figure 2.18). Moreover, the quality of the gas core diameter measured by ERT is impacted by changes in the water conductivity during the experiments, e.g., due to the increase in the flow temperature. To ensure an optimal ERT performance, it is crucial to remeasure $I_l[m]$ and update it in the image reconstruction calculations as frequently as possible during the experiments.

2.8.3. MEASUREMENT RATE

The time required by the proposed application-specific image reconstruction algorithm to reconstruct the distribution of phases in the axial cyclone is negligible compared to the frame rate of Electrical Resistance Tomography hardware. Therefore, the frequency of the real-time gas-liquid distribution measurements is determined by the maximum frequency that the data acquisition system can reach, corresponding to 12 Hz for the ERT hardware of this research. The ERT is used to measure the phase distribution at 10 Hz in

the experiments of this thesis, slightly below the maximum measurement rate that can be reached by the ERT hardware.

The maximum acquisition frequency of the Flow Watch system remains relatively close to the frequency of the gas core fluctuations in the axial cyclone due to swirling gas-liquid flow patterns, and faster acquisition systems are desired for the optimal tomography-based control of axial cyclones. Since the gas-liquid distribution in the cyclone can be reconstructed departing from twelve electric current measurements in the proposed algorithm, in contrast to the fixed 240 electric currents per frame measured by the Flow Watch system, hardware with simpler and faster electronics than traditional ERT systems (as Flow Watch) can be developed in future research for phase distribution measurements orders of magnitude faster than in the current dissertation.

2.9. CONCLUSION

This chapter described the axial cyclone experimental facility and the real-time Electrical Resistance Tomography image reconstruction algorithm developed in this research to investigate the the tomography-based real-time control of multiphase flows.

The experimental facility was described in part I of the chapter. It was designed for both classical multiphase flow experiments with statistically-steady boundary conditions, such as the swirling gas-liquid flow patterns investigation of chapter 3, and for real-time control, where the dynamics of control valves and liquid flow rate become relevant. The swirl intensity in the axial cyclone is strongly related to the Swirl Element geometry, and four different Swirl Element geometries are available to vary the swirl intensity of the flow in the experiments of the next chapters, as described in section 2.3.

The Electrical Resistance Tomography hardware and real-time image reconstruction algorithm developed to measure gas cores in axial cyclones were described in part II of the current chapter. The proposed algorithm is based on the expectation of a single roughly-circular gas core in the pipe cross-section measured by ERT system, that is reconstructed based on twelve electric current measurements performed by the ERT hardware. The developed image reconstruction algorithm is more precise and three orders of magnitude faster than traditional non-iterative ERT image reconstruction algorithms based on the inverse problem.

The real-time ERT sensor is used to measure the gas core upstream of the pickup tube at 10 Hz in the tomography-based real-time control investigation of chapter 5, due to limitations in the acquisition frequency that can be reached by the hardware used in the experiments (Flow Watch system). Hardware developed based on the image reconstruction algorithm proposed in this research can potentially increase the measurement frequency of the gas core in axial cyclones to frequencies above 1 kHz, allowing non-intrusive phase distribution measurements at frequencies close to (intrusive) wire-mesh sensors. However, different from wire-mesh sensors, electric resistance tomography is insensitive to small changes in the phase distribution in the center of the pipe, limiting the tomographic measurement of the distribution of phases in the axial cyclone to conditions where a gas core wider than about 10% of the pipe diameter is formed upstream of the pickup tube (section 2.8). This limitation impacts the range of process conditions and swirling gas-liquid flow patterns that can be controlled in the axial cyclone using electrical resistance

tomography, as discussed in chapters 4 and 5.

In the general context of tomography-based real-time control of multiphase flows:

- Section 2.5 showed that pneumatic control valves, common actuators of flow processes, can have asymmetric time-responses to control actions depending on their control pressure ranges and the response of their (electro-)pneumatic regulators. Moreover, even if the control pressure range of the valve is optimized, for instance by using two electro-pneumatic regulators as in this research, pneumatic control valves have a relatively slow response with hysteresis that limits the frequency of disturbances in the phase distribution (gas core diameter) that can be suppressed by tomography-based controllers based on the equipment. The hysteresis due to Coulomb friction and relatively slow response presented in this chapter for the pneumatic diaphragm LPO valve is also observed for other types of control valves [99].

- Section 2.6 showed that the liquid flow rate of the Axial Cyclone experimental facility is impacted by disturbances in the gas mass flow rate and/or actions made on the LPO valve during the tomography-based real-time control of the gas core upstream of the pickup tube. Since the phase distribution in the axial cyclone depends on its inlet liquid and gas flow rates, the liquid flow rate dynamics in the experimental facility contributes to the phase distribution response to actions on the LPO valve observed in chapter 5. In general, it is important that simplified experimental facilities developed to study the phase distribution dynamics and/or design tomography-based controllers of industrial processes have the same flow rate dynamics of the real application.

- Simple application-specific tomographic image reconstruction algorithms are essential to reach the temporal and spatial resolution required for the real-time measurement and control of the distribution of phases in multiphase flows.

CHAPTER 3

VERTICAL UPWARD SWIRLING GAS-LIQUID PIPE-FLOW PATTERNS AND MECHANISTIC TRANSITION CRITERIA

3.1. INTRODUCTION

The prediction of the swirling gas-liquid flow patterns in axial cyclone separators is fundamental to an optimal equipment design and process controller implementation.

The separation in gas-liquid axial cyclones relies on the accumulation of gas around the swirl tube centerline, promoted by the centripetal force acting on the gas, where it is captured by the pickup tube. To maximize phase separation, the swirl element vanes must be designed to create centered continuous gas cores upstream of the pickup tube for the inlet gas and liquid flow rates relevant to the process, accounting for the swirl decay in the swirl tube due to the azimuthal wall shear-stress at the pipe wall.

In relation to the real-time control of the axial cyclone, process conditions which result in gas cores with minor interface oscillations can be controlled by slow control actions, compensating, for instance, slow drifts in the flow rates of the system (e.g., with time-constants in the order of 10 s). On the other hand, process conditions with strong and frequent gas core oscillations would require real-time controllers with time-constants below 0.1 s for the complete control the separation, something that is not always achievable with typical flow equipment, such as control valves.

Non-swirling upward gas-liquid flows in vertical pipes were extensively studied in the past. The main flow regimes of vertical (non-swirling) gas-liquid flows are well-established as bubbly, slug, churn and annular [104], and multiple transition criteria between these flow patterns have been proposed in literature [105–108]. In general, the flow patterns of non-swirling upward vertical gas-liquid flows in smooth pipes can be written as function of the dimensionless numbers [109]

$$\frac{\rho_g}{\rho_l}, Fr_g, Fr_l, Re_g, Re_l, Eo, \frac{x}{D}, \tag{3.1}$$

where $Fr_g \triangleq j_g/\sqrt{gD}$ is the Froude number of the gas based on the superficial gas velocity j_g, $Fr_l \triangleq j_l/\sqrt{gD}$ is the Froude number of the liquid based on the superficial liquid velocity j_l, $Re_g \triangleq \rho_g j_g D/\mu_g$ is the Reynolds number of the gas, $Re_l \triangleq \rho_l j_l D/\mu_l$ is the Reynolds number of the liquid, $Eo \triangleq \left(\rho_l - \rho_g\right) gD^2/\gamma$ is the Eötvös number of the mixture (γ is the

This chapter is in preparation of two papers to be submitted to the International Journal of Multiphase Flow.

surface tension), and x/D is the position where the flow patterns are being investigated in relation to the inlet. The axial position of the flow pattern map is relevant for the transition models which consider churn as an entrance flow pattern of slug, e.g., in Taitel *et al.* [106]. From the dimensionless numbers presented, Fr_g and Fr_l are the most relevant for the prediction of the non-swirling upward gas-liquid flow patterns of weakly-viscous fluids in pipe diameters in the order of centimeters [109].

The literature of upward vertical swirling gas-liquid flows is much more scarce and recent than its non-swirling counterpart. The upward swirling gas-liquid flow patterns have been described and experimentally mapped, e.g., by Shakutsui *et al.* [110, 111] for swirls created via the injection of the fluids tangentially to the pipe, and by Wang *et al.* [29], Liu et al. [112, 113] and Yang *et al.* [114] for swirls created by the passage of the gas-liquid flow through a swirl element of fixed helical blades. Independent of the method of generation of swirl, swirl-exclusive upward gas-liquid flow patterns were always observed by the authors in addition to the well known non-swirling flow regimes.

The swirl-exclusive upward gas-liquid flow patterns arise due to the centripetal force created by the rotation of the fluids. The addition of swirl to the mixture results in two additional velocity scales to the set of variables describing the flow patterns, related to the azimuthal velocities of the two phases, and represented by the swirl numbers of the gas Ω_g and liquid Ω_l. The swirl number corresponds to the dimensionless flow of angular momentum, and is equal to $2U_\theta/(3U_x)$ for single phase flows with uniform axial and azimuthal velocity profiles (subsection 3.5.2). Then, upward swirling gas-liquid flows in vertical pipes can be described by the dimensionless numbers

$$\frac{\rho_g}{\rho_l}, Fr_g, Fr_l, \Omega_g, \Omega_l, Re_g, Re_l, Eo, \frac{x}{D}, \tag{3.2}$$

where the swirl number of the liquid Ω_l plays a fundamental role together with Fr_g and Fr_l on the flow pattern transitions.

The vertical upward swirling gas-liquid pipe-flow patterns are not as well established as their non-swirling counterpart, and the available literature is limited in relation to the impact of swirl intensity on the upward swirling gas-liquid flow pattern transitions. For instance, the experimental flow pattern maps obtained by Wang *et al.* [29], Liu and Bai [112], Yang *et al.* [114] are dimensional and limited to the swirl element geometry, pipe diameter, fluids and visualization window used by the authors (due to swirl decay). Additionally, the existing literature lacks of simple mechanistic models to predict the swirling gas-liquid flow pattern transitions for a generic pair of fluids, swirl number, pipe diameter and position in the pipe, accounting for swirl decay effects in the flow patterns. From the upward swirling gas-liquid flow patterns currently reported in literature, only the Churn-Swirling Annular flow pattern transition has been studied and mechanistic modeled [115–118]; models for the remaining swirling gas-liquid flow pattern transitions remain an open topic in literature, being proposed in the current chapter.

The objectives of this chapter, divided in two parts, are:

- To investigate the flow behavior and map the vertical upward swirling gas-liquid pipe-flow patterns at different locations in the swirl tube for a wide range of swirl numbers and flow rates (part I). The swirl intensity is systematically varied using four swirl elements, and the gas-liquid flow patterns are mapped (i) upstream of

the swirl element, to investigate the relation between the upstream and swirl flows, (ii) at $x = 2D$ downstream of the swirl elements, to investigate the impact of swirl intensity on the flow pattern transitions, and (iii) at $x = 14D$ downstream of the swirl element, to study the swirl decay effects on the flow patterns.

- To propose mechanistic transition criteria for upward swirling gas-liquid pipe-flows (part II). The mechanistic models proposed in the current chapter are physically-based and include swirl decay effects in the flow, allowing to predict the upward swirling gas-liquid flow patterns for a wide range of swirl elements, pipe diameters and axial positions in the swirl tube. The models are designed for systems where swirl is added to a previously existing gas-liquid flow, e.g., by a swirl element, gases with density much smaller than the liquid density, weakly-viscous fluids, pipe diameters in the order of centimeters and swirl numbers in the order of 1.

The summary and conclusion of the chapter are provided in section 3.8.

PART I: FLOW PATTERNS

In this part, the vertical upward swirling gas-liquid pipe-flow patterns are studied over a wide range of gas and liquid flow rates for four swirl elements, to investigate the impact of swirl intensity on the flow pattern transitions. Moreover, the flow patterns are mapped upstream of the swirl element, to investigate the impact of the upstream flow patterns on the swirling gas-liquid flow patterns inside the axial cyclone, and at two different axial positions downstream of the swirl element, to investigate the swirl decay effects on the flow regimes. The experiments performed are described in section 3.2.

Since the swirling gas-liquid flow patterns in pipes are not as well-established as the non-swirling gas-liquid pipe-flow patterns, and different flow pattern classifications were adopted in recent experimental flow pattern maps of Wang *et al.* [29], Liu and Bai [112] and Yang *et al.* [114], the swirling gas-liquid flow patterns observed during the experiments of the current chapter are described in section 3.3. The experimental flow pattern maps obtained in this research with the different swirl intensities and axial positions in the swirl tube are presented in section 3.4, concluding the first part of the current chapter.

3.2. EXPERIMENTAL METHODS

The experiments of this chapter were performed in the Axial Cyclone facility of Delft University of Technology, detailed in chapter 2. As shown in Figure 3.1, the axial cyclone separator used in the experiments has the inner pipe diameter $D = 81.4$ mm, and the upward gas-liquid flow patterns were visually mapped in three visualization windows of length $2D$: (i) right upstream of the swirl element, (ii) centered at $x = 2D$ downstream of the swirl element, and (iii) centered at $x = 14D$ downstream of the swirl element.

The two visualization windows downstream of the swirl element were recorded for 20 seconds at 20 frames per second to refine the visual flow pattern identification. The flow images were recorded in 8-bit grayscale by two BASLER acA1920-150uc cameras with

8 mm lenses by Computar. The obtained images have a resolution of around 3.2 pixels per mm at $x = 2D$ and 4.3 pixels per mm at $x = 14D$. The valves in the outlets of the axial cyclone separator were kept fully open during the experiments, to minimize the impact of the outlet conditions on the flow regimes upstream of the pickup tube.

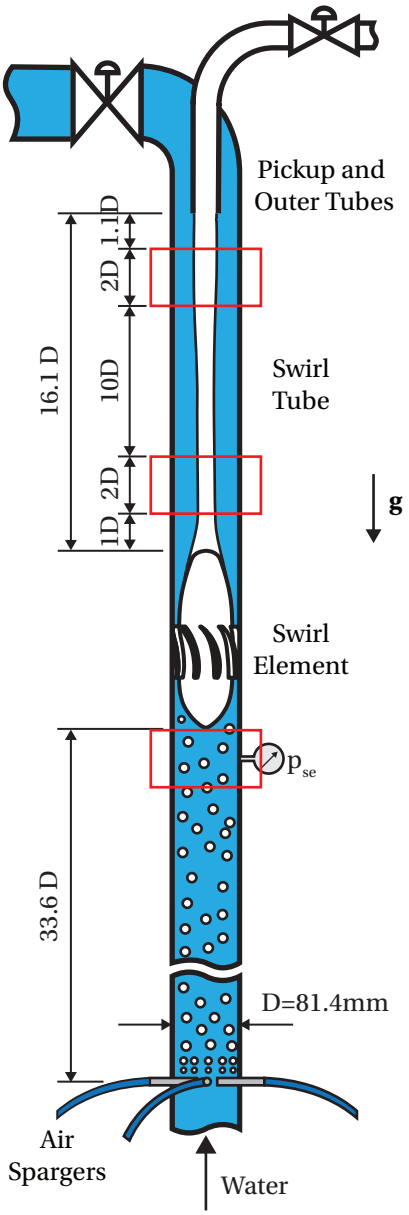

Figure 3.1: Schematics of the axial cyclone facility showing the main setup dimensions and the three visualization windows where the flow patterns were mapped (red rectangles).

The swirl elements are characterized in this research by the geometrical swirl number Ω_{se}, corresponding to an estimate of the swirl number of single-phase flows departing from the swirl element based on the swirl element geometry. The four swirl elements used in the current chapter, and the computation of their geometrical swirl numbers, are described in section 2.3 of chapter 2; the resulting Ω_{se} are summarized in Table 3.1.

Table 3.1: Geometrical swirl number (Ω_{se}) of the four swirl elements used in the current chapter. The swirl elements and the geometrical swirl number calculation are described in section 2.3 of chapter 2.

Swirl Element	1	2	3	4
Ω_{se}	1.57	2.28	3.51	5.77

A total of 299 liquid-gas flow rate pairs were covered per swirl element during the experiments, consisting of the combination between thirteen water flow rates in the range 0.9-14.4 $m^3 h^{-1}$ and twenty-three air flow rates in the range 0.078-23.3 $kg h^{-1}$, chosen to form a uniform grid of points in the usual logarithm scale of flow pattern maps.

The flow pattern maps obtained in this research are presented as plots of superficial liquid velocity versus superficial gas velocity for each swirl element and axial position investigated. The superficial liquid velocity upstream of the swirl element is computed from the water volume flow rate q_l, measured upstream of the injection of air in the system, via

$$j_l = \frac{q_l}{A}, \tag{3.3}$$

where $A = 0.0052$ m^2 is cross-sectional area of the pipe.

The superficial gas velocity j_g upstream of the swirl element is computed based on the gas mass flow rate w_g, measured by Mass Flow Controllers upstream of the air spargers, and local air density $\rho_{g,se}$ via:

$$j_g = \frac{w_g}{\rho_{g,se} A} \tag{3.4}$$

The air density upstream of the swirl element, $\rho_{g,se}$, is computed based on the controlled lab temperature of 20 °C and pressure p_{se} measured upstream of the swirl element.

3.3. UPWARD SWIRLING GAS-LIQUID PIPE-FLOW PATTERNS

The vertical upward swirling gas-liquid pipe-flow patterns identified during the experiments of this chapter are grouped into four classes, determined by the swirl impact on the phase distribution: Non-Columnar flows, Centered flows, Columnar flows and Swirling Annular flows.

The dimensionless numbers Fr_l, Fr_g and Ω_l play the major role in vertical upward swirling gas-liquid flows outside the Swirling Annular regime. Since centripetal acceleration is behind the swirl-exclusive flow patterns, and the azimuthal liquid velocity scales with $j_l \Omega_l$, the superficial gas and liquid velocities corresponding to each flow pattern are strongly dependent on (i) the swirl element geometry, as Ω_l is close to Ω_{se} at the exit of the swirl element, and (ii) the axial position of the flow pattern map, due to swirl decay.

For conciseness, the current section describes the flow behavior and swirling gas-liquid flow patterns observed for Swirl Element 2, with comments about the conditions where these flow patterns are observed for the remaining swirl elements. Additionally, the experimental flow pattern maps obtained at $x = 2D$ and $x = 14D$ for Swirl Elements 2 and 4 are presented in section 3.4, clearly showing the impact of swirl intensity and swirl decay on the flow pattern transitions; the data obtained for Swirl Elements 1 and 3 are presented together with the mechanistic model predictions in the results of part II (section 3.7).

3.3.1. NON-COLUMNAR FLOWS

Homogeneous bubbly flow was observed both upstream and downstream of the swirl element for the lowest superficial gas and liquid velocities covered in the experiments. Despite a noticeable rotation of the bubbles around the pipe centerline, no significant impact of the swirl on the distribution of phases was observed for low superficial liquid velocities. The increase in the superficial gas velocity in the condition results in the increase in the number of bubbles and gas fraction of the flow, as shown in Figure 3.2.

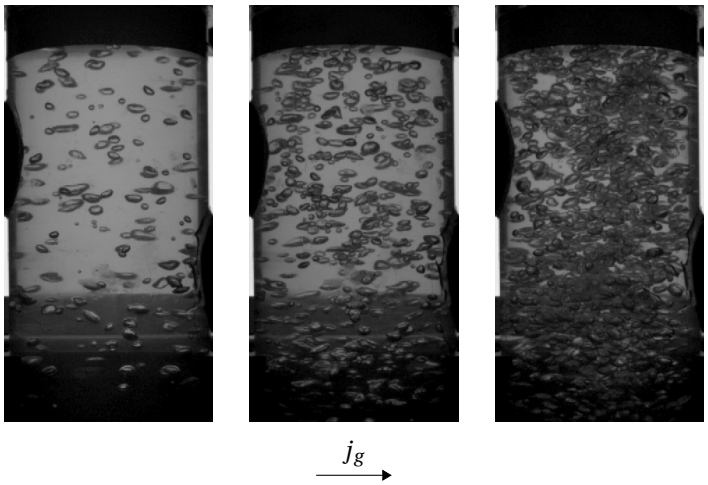

Figure 3.2: Bubbly flows at $x = 2D$ downstream of Swirl Element 2. Left: $j_g = 0.0029\,\mathrm{m\,s^{-1}}$ and $j_l = 0.046\,\mathrm{m\,s^{-1}}$. Center: $j_g = 0.0088\,\mathrm{m\,s^{-1}}$ and $j_l = 0.049\,\mathrm{m\,s^{-1}}$. Right: $j_g = 0.024\,\mathrm{m\,s^{-1}}$ and $j_l = 0.050\,\mathrm{m\,s^{-1}}$.

Bubble coalescence is promoted at high bubble concentrations, with larger bubbles eventually formed in the upstream flow for sufficiently high superficial gas velocities (and gas fractions). These larger bubbles travel across the swirl element into the swirling region of flow. When the size of the larger bubbles is clearly above the mean bubble diameter, but considerably below the pipe diameter, the flow is categorized as Heterogeneous Bubbly. The picture of a Heterogeneous Bubbly flow is presented in Figure 3.3-left.

The further increase in the gas flow rate and average gas fraction results in the growth of the larger bubbles, and the transition of the upstream and swirling flows to Slug. Slug flows are characterized by the alternation between (i) gas pockets of width close to the pipe diameter and length typically greater than the pipe diameter, surrounded by a thin

liquid film, known as Taylor bubbles, and (ii) liquid-dominant regions containing discrete bubbles, known as liquid slugs. A Slug flow picture is presented in Figure 3.3-center.

The Taylor bubbles upstream and downstream of the swirl element become longer, and the liquid slugs shorter, with the increase in the average gas fraction of the flow via the gas flow rate. The flow transitions to Churn when a strong interaction between consecutive Taylor bubbles take place due to insufficiently-long liquid slugs, resulting in an oscillatory motion of the liquid [106]. A Churn flow picture is presented in Figure 3.3-right.

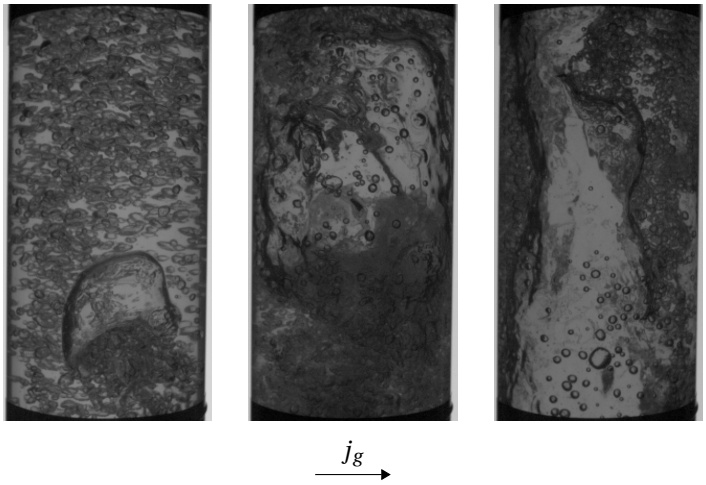

Figure 3.3: Non-Columnar flows at $x = 14D$ downstream of Swirl Element 2. Left: Heterogeneous Bubbly flow obtained for $j_g = 0.038\ \mathrm{m\,s^{-1}}$ and $j_l = 0.19\ \mathrm{m\,s^{-1}}$. Center: Slug flow obtained for $j_g = 0.23\ \mathrm{m\,s^{-1}}$ and $j_l = 0.19\ \mathrm{m\,s^{-1}}$. Right: Churn flow obtained for $j_g = 0.87\ \mathrm{m\,s^{-1}}$ and $j_l = 0.19\ \mathrm{m\,s^{-1}}$.

Similarly to homogeneous bubbly flows, no significant change in the distribution of phases of Heterogeneous Bubbly, Slug and Churn flows was observed between the upstream flow and the swirling flow for low liquid flow rates.

3.3.2. CENTERED FLOWS

Returning to the conditions of upstream homogeneous bubbly flow (low liquid and low gas flow rates), the increase in the centripetal force via the superficial liquid velocity leads to the agglomeration of the majority of the bubbles downstream of the swirl element in a small region around the pipe centerline, characterizing the Centered Homogeneous Bubbly flow pattern. Centered Homogeneous Bubbly flows were also reported, for instance, by Liu *et al.* [119] and Yang *et al.* [114].

The width of the bubble agglomeration region increases with the number of bubbles of the flow, as shown in Figure 3.4. The bubble agglomeration region deviates from the pipe centerline and eventually breaks into homogeneous bubbly flows with the increase in the superficial gas velocity for a fixed superficial liquid velocity, indicating an impact of the number of bubbles on the balance of forces behind this pattern. The centrality and stability of the agglomerated flow at large bubble concentrations is restored when the

centripetal force on the bubbles is increased via the superficial liquid velocity.

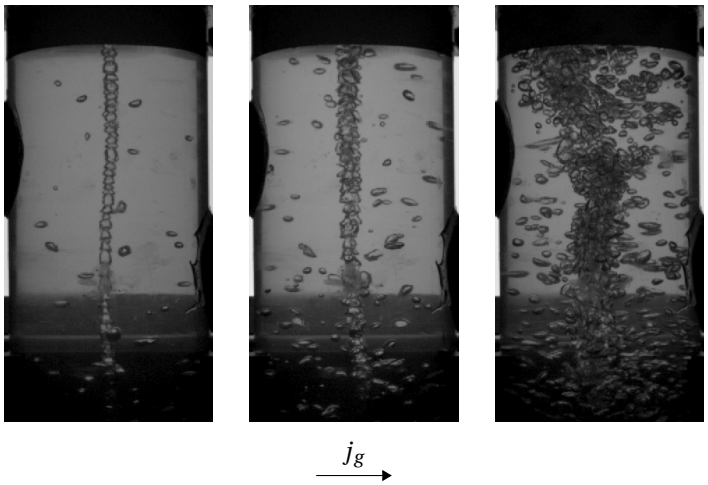

Figure 3.4: Centered Homogeneous Bubbly flows at $x = 2D$ downstream of Swirl Element 2. Left: $j_g = 0.0029\ \mathrm{m\,s^{-1}}$ and $j_l = 0.13\ \mathrm{m\,s^{-1}}$. Center: $j_g = 0.0087\ \mathrm{m\,s^{-1}}$ and $j_l = 0.12\ \mathrm{m\,s^{-1}}$. Right: $j_g = 0.024\ \mathrm{m\,s^{-1}}$ and $j_l = 0.12\ \mathrm{m\,s^{-1}}$.

The upstream flow transitions from Homogeneous Bubbly to Heterogeneous Bubbly with the increase in the superficial gas velocity, resulting in larger bubbles in bubble agglomeration region downstream of the swirl element. The presence of relatively large bubbles in the agglomerated bubbly flow characterizes the Centered Heterogeneous Bubbly flow pattern, that is presented in Figure 3.5.

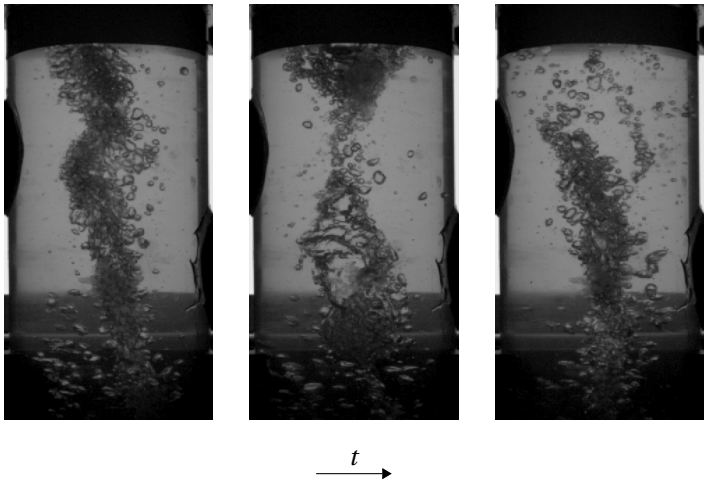

Figure 3.5: Large bubble (in the center image) crossing the agglomerated region of a Centered Heterogeneous Bubbly flow. Images obtained at $x = 2D$ downstream of Swirl Element 2 for $j_g = 0.038\ \mathrm{m\,s^{-1}}$ and $j_l = 0.19\ \mathrm{m\,s^{-1}}$. The consecutive frames of this figure are spaced by 0.1 s.

The upstream flow transitions to Slug with further increase in the superficial gas velocity. When crossing the swirl element, the Taylor bubbles distance from the wall and the discrete bubbles of the liquid slugs agglomerate in the central region of the pipe due to the centrifugal force, as shown in Figure 3.6. The combination between Taylor bubbles detached from the wall and bubble agglomeration in the liquid slugs characterizes the Centered Slug flow pattern.

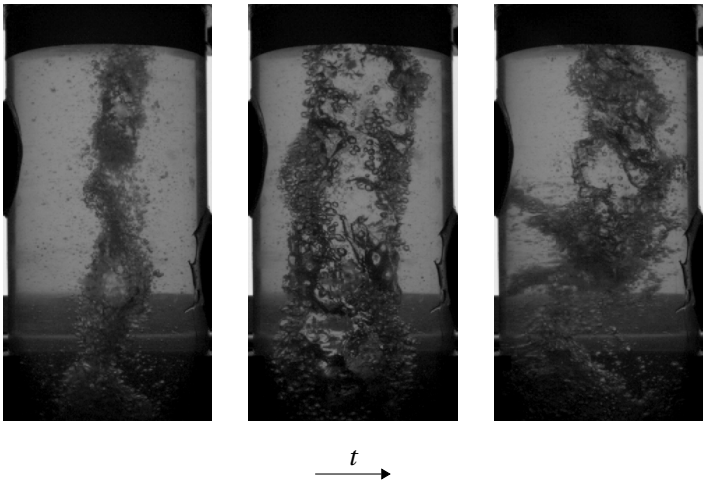

Figure 3.6: Pictures of bubble agglomeration in the liquid slugs (left) and Taylor bubble detached from the wall (center) in a Centered Slug flow at $x = 2D$ downstream of Swirl Element 2 for $j_g = 0.23\,\mathrm{m\,s^{-1}}$ and $j_l = 0.19\,\mathrm{m\,s^{-1}}$. Images spaced by 0.1 s.

The upstream flow transitions from Slug to Churn with the increase in the superficial gas velocity, resulting in the transition from Centered Slug to Centered Churn downstream of the swirl element. The gas pockets occupy the the majority of Centered Churn flow patterns. Similarly to the Taylor bubbles in Centered Slug flows, the gas pockets of Centered Churn flows are also detached from the wall, as shown in Figure 3.7. The rare regions of the flow dominated by the liquid show a clear agglomeration of the discrete bubbles around the pipe centerline, matching the observations of Liu *et al.* [113].

The superficial liquid velocity required for the formation of centered flows downstream of the swirl element is substantially lower for stronger swirl elements. The data obtained in the visualization window downstream of the swirl element ($x = 2D$) for all four swirl elements suggests that Centered Bubbly flows are obtained for $Fr_l\Omega_{se} \gtrsim 0.2$ and Centered Slug/Churn flows are obtained for $Fr_l\Omega_{se} \gtrsim 0.4$ at the location. Due to the strong swirl decay in the axial direction, centered flows typically transition back to Bubbly, Slug or Churn before arriving at the visualization window centered at $x = 14D$. Please note that the values mentioned in this paragraph are a first approximation used to illustrate the role of swirl intensity in the transition to Centered flows. The transition to Centered flows is modeled based on the flow physics and liquid swirl number, accounting for swirl decay, in subsection 3.6.2 of part II.

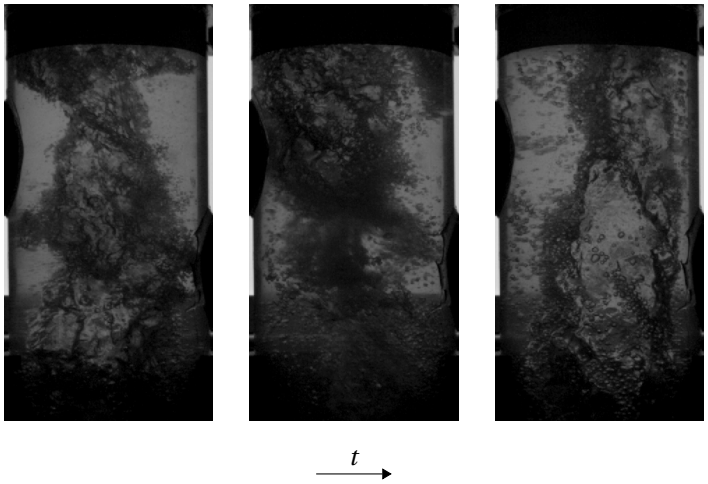

Figure 3.7: Pictures of the gas pockets detached from the wall (left, right) and the dispersed bubble agglomeration (center) of a Centered Churn flow at $x = 2D$ downstream of Swirl Element 2 with $j_g = 0.87\ \mathrm{m\,s^{-1}}$ and $j_l = 0.19\ \mathrm{m\,s^{-1}}$. Images spaced by 0.1 s.

3.3.3. COLUMNAR FLOWS

Back to the conditions of Homogeneous Bubbly flow upstream of the swirl element and Centered Homogeneous Bubbly flow downstream of the swirl element (low gas flow rate and intermediary liquid flow rate), the increase in the centripetal force via the superficial liquid velocity results in the coalescence of the agglomerated bubbles into a continuous gas column around the pipe centerline. The obtained gas column has interface waves of relatively low amplitude, characterizing the Weakly Oscillating Column flow pattern. As shown in Figure 3.8, the width of the weakly oscillating column increases with the superficial gas velocity and upstream gas fraction.

The continuous increase of the superficial gas velocity eventually leads to the transition of the upstream flow from Homogeneous to Heterogeneous Bubbly. As shown in Figure 3.9, the larger bubbles of the upstream flow are transformed into sporadic pulses in the gas core downstream of the swirl element, characterizing the Pulsating Column flow pattern. The impact of larger bubbles upstream of the swirl element on the gas core downstream of the swirl element, prior to the upstream Slug flow transition, was also observed by Liu *et al.* [113].

The frequency and intensity of the pulses increase with the growth of the upstream large bubbles near the upstream Slug flow transition. When Slug and Churn flows are formed upstream of the swirl element, strong fluctuations in the gas core are caused by the alternating high-gas and high-liquid regions crossing the swirl element. Such fluctuations often release small bubbles that are quickly driven back to the gas core. A centered gas column with frequent and strong interface oscillations that releases small bubbles characterizes the Bursting Column flow pattern, presented in Figure 3.10.

The strong dynamic behavior of Bursting Columns promoted by upstream Slug and

Churn flows was also observed by Liu *et al.* [113]. The direct relation between the phase distribution fluctuations in the upstream Slug flow and in the downstream Bursting Column is confirmed via cross-correlations in chapter 5 of the current thesis.

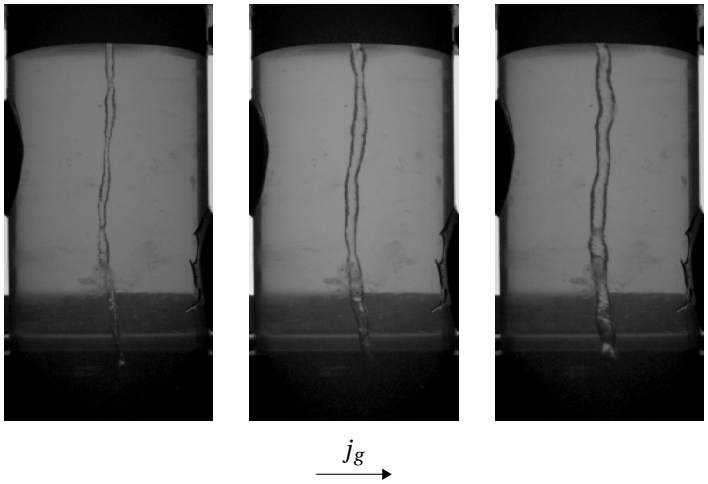

Figure 3.8: Weakly Oscillating Columns at $x = 2D$ downstream of Swirl Element 2 for upstream Homogeneous Bubbly flows. Left: $j_g = 0.0079\ \mathrm{m\,s^{-1}}$ and $j_l = 0.78\ \mathrm{m\,s^{-1}}$. Center: $j_g = 0.021\ \mathrm{m\,s^{-1}}$ and $j_l = 0.78\ \mathrm{m\,s^{-1}}$. Right: $j_g = 0.062\ \mathrm{m\,s^{-1}}$ and $j_l = 0.78\ \mathrm{m\,s^{-1}}$.

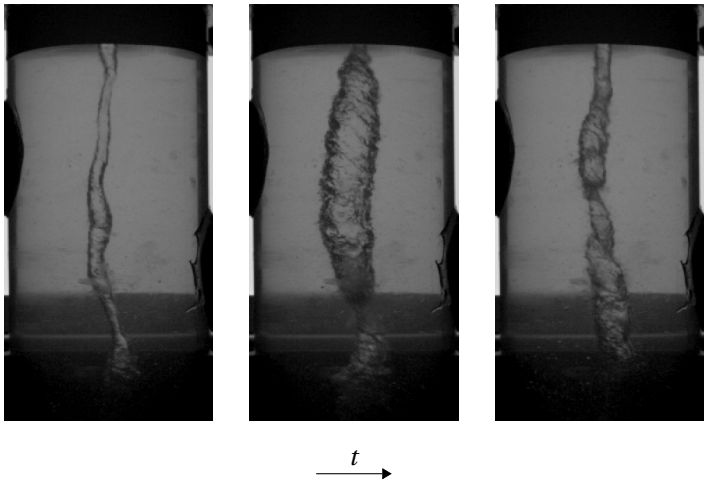

Figure 3.9: Pulse (in the center image) traveling in the gas core of a Pulsating Column at $x = 2D$ downstream of Swirl Element 2 for $j_g = 0.13\ \mathrm{m\,s^{-1}}$ and $j_l = 0.77\ \mathrm{m\,s^{-1}}$. Images spaced by 0.1 s.

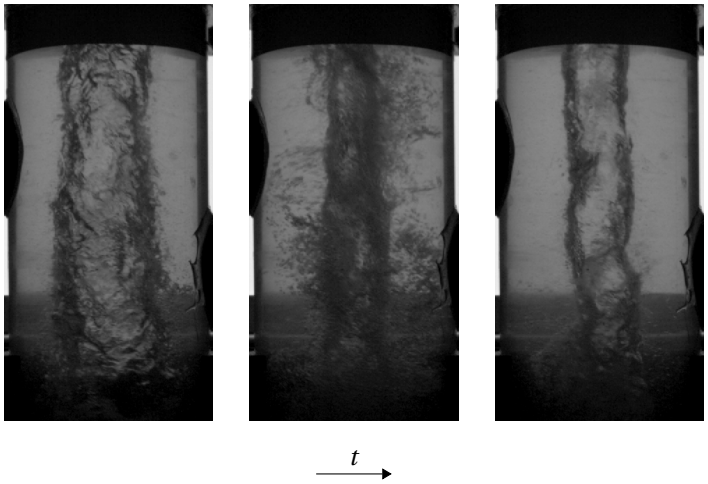

Figure 3.10: Pictures of a Bursting Column at $x = 2D$ downstream of Swirl Element 2 for $j_g = 0.69\ \mathrm{m\,s^{-1}}$ and $j_l = 0.78\ \mathrm{m\,s^{-1}}$. Images spaced by 0.1 s.

The experimental data obtained for all four swirl elements in the visualization window downstream of the swirl element ($x = 2D$) reveals that Weakly Oscillating Columns are obtained at the location for $Fr_l\Omega_{se} \gtrsim 0.4$, while Bursting Columns are obtained at the same location for $Fr_l\Omega_{se} \gtrsim 0.9$. The curves are shifted to $Fr_l\Omega_{se} \gtrsim 0.6$ (Weakly Oscillating Column) and $Fr_l\Omega_{se} \gtrsim 1.4$ (Bursting Columns) in the visualization window centered at $x = 14D$, due to liquid swirl decay between the two locations. The values above are a first approximation of the Columnar flow transition, that is modeled based on the flow physics and liquid swirl number, explicitly accounting for swirl decay, in subsection 3.6.3 of part II.

SEGMENTED COLUMN

As previously shown in Figure 3.8, the width of Weakly Oscillating Columns strongly depends on the superficial gas velocity. Very thin Weakly Oscillating Columns are formed downstream of the swirl element for the lowest superficial gas velocities covered in the experiments, quickly breaking into multiple segments which travel around the pipe centerline. The presence of a discontinuous gas column in the swirl flow characterizes the Segmented Column flow pattern, presented in Figure 3.11.

The length of the column segments increases with both the liquid and gas superficial velocities, and small segments resembling Centered Bubbly flows are observed in the swirl flow region for the lowest superficial gas and liquid velocities investigated. Segmented Columns were also reported by Liu *et al.* [119].

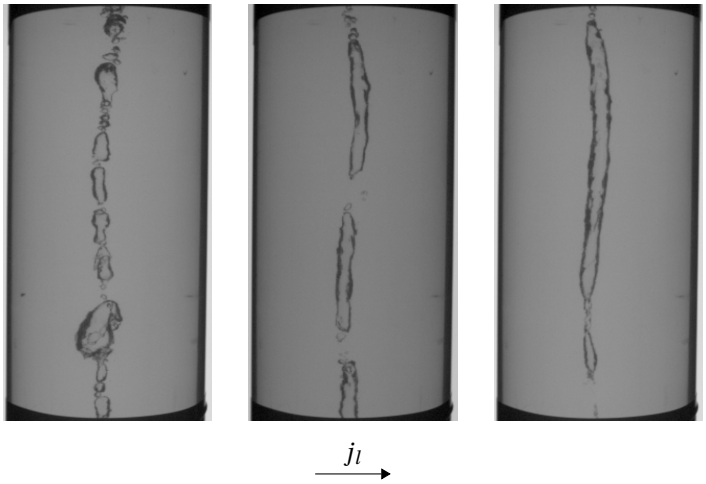

Figure 3.11: Segmented Columns with different segment lengths at $x = 14D$ downstream of Swirl Element 2. Left: $j_g = 0.0028\,\mathrm{m\,s^{-1}}$ and $j_l = 0.30\,\mathrm{m\,s^{-1}}$. Center: $j_g = 0.0028\,\mathrm{m\,s^{-1}}$ and $j_l = 0.49\,\mathrm{m\,s^{-1}}$. Right: $j_g = 0.0026\,\mathrm{m\,s^{-1}}$ and $j_l = 0.78\,\mathrm{m\,s^{-1}}$.

3.3.4. SWIRLING ANNULAR FLOWS

Although the range of superficial gas velocity covered in the experiments is not sufficient for the observation of Swirling Annular flows in the experimental facility, the flow pattern has been reported in multiple studies [112–114, 116, 119]. Swirling Annular flows are similar to their non-swirling counterpart, occurring for considerably high superficial gas velocities and being characterized by a wide gas core, of diameter close to the pipe diameter, surrounded by a thin liquid film. For completeness, Swirling Annular flows are also included in the mechanistic flow pattern transition models proposed in part II.

3.4. EXPERIMENTAL FLOW PATTERN MAPS

Based on the observations of section 3.3, the following classes and upward vertical swirling gas-liquid pipe-flow patterns are considered in this dissertation:

- **Non-Columnar flows**
  - Swirling Homogeneous Bubbly
  - Swirling Heterogeneous Bubbly
  - Swirling Slug
  - Swirling Churn
- **Centered flows**
  - Centered Homogeneous Bubbly

  - Centered Heterogeneous Bubbly
  - Centered Slug
  - Centered Churn
- **Columnar flows**
  - Weakly Oscillating Column
  - Pulsating Column
  - Bursting Column
  - Segmented Column
- **Swirling Annular**

The vertical upward swirling gas-liquid pipe-flow patterns mentioned above are illustrated in Figure 3.12. In relation to the existing literature, Centered Homogeneous Bubbly flows were referred to as "Chain Flow" in [110, 111, 119], Weakly-Oscillating Columns were referred to as "Swirling Gas Column" in [112, 113, 119], and no distinction between Centered Slug, Centered Churn, Pulsating Column and Bursting Column was made in [112, 113, 119], that classified these patterns as "Swirling Intermittent".

The transition between the different swirling gas-liquid flow classes is mainly determined by the product $Fr_l\Omega_{se}$, related to centripetal acceleration of the flow by the azimuthal liquid velocity. Swirling Annular flows are an exception, with the balance of forces being dictated by the gas instead of the liquid. The flow patterns inside each class are determined by the (non-swirling) gas-liquid flow patterns upstream of the swirl element (except for Segmented Columns) and, therefore, strongly dependent on Fr_g. The approximate $Fr_l\Omega_{se}$ range where the different flow patterns were observed at $x = 2D$ and $x = 14D$ for all four swirl elements investigated are summarized in Table 3.2. Since swirl decays in the axial direction, the product $Fr_l\Omega_{se}$ required for the transition to Columnar flows increase with the distance from the swirl element.

Table 3.2: Approximate $Fr_l\Omega_{se}$ required for the observation of Centered and Columnar flows in the visualization windows centered at $x = 2D$ and $x = 14D$ downstream of the swirl element. Values based on experimental data.

Flow Pattern	$x = 2D$	$x = 14D$
Centered Bubbly	$Fr_l\Omega_{se} \gtrsim 0.2$	Typically not observed
Centered Slug or Centered Churn	$Fr_l\Omega_{se} \gtrsim 0.4$	Typically not observed
Weakly Oscillating or Segmented Column	$Fr_l\Omega_{se} \gtrsim 0.4$	$Fr_l\Omega_{se} \gtrsim 0.6$
Bursting Column	$Fr_l\Omega_{se} \gtrsim 0.9$	$Fr_l\Omega_{se} \gtrsim 1.4$

For a fixed pair of fluids, axial position, pipe diameter and swirl element, the swirling gas-liquid flow regimes are only a function of the superficial gas and liquid velocities. The flow pattern maps obtained for Swirl Elements 2 and 4 in the visualization windows centered at $x = 2D$ and $x = 14D$ are presented in Figures 3.13 and 3.14, respectively. The remaining flow pattern maps are presented in part II (section 3.7), together with the flow pattern transitions predicted by the mechanistic models proposed in section 3.6.

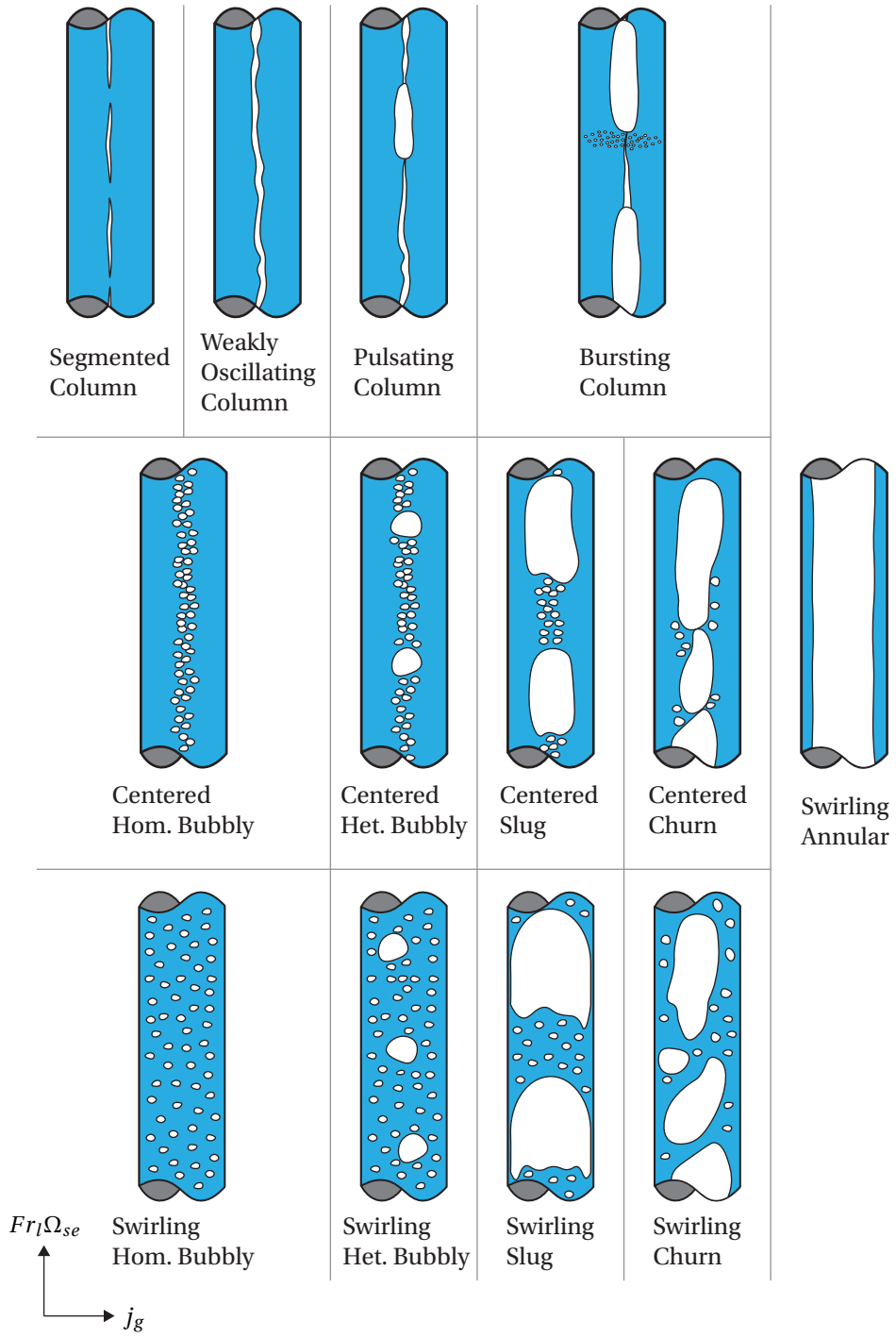

Figure 3.12: Vertical upward swirling gas-liquid pipe-flow patterns.

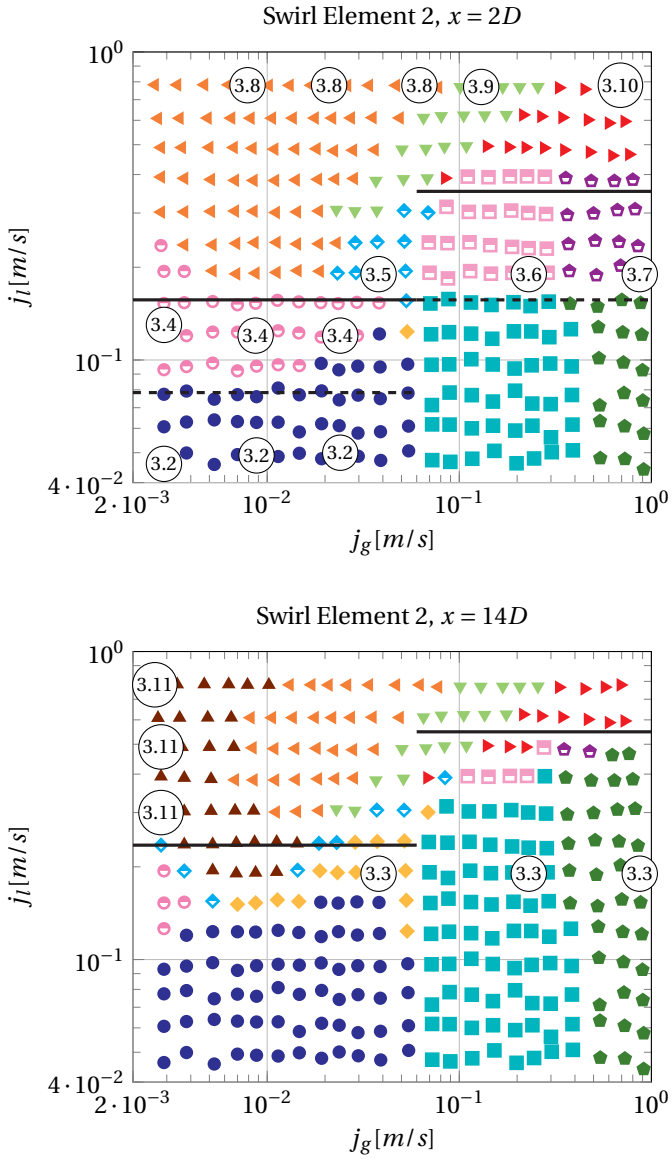

Figure 3.13: Flow pattern maps obtained for Swirl Element 2 ($\Omega_{se} = 2.28$) at $x = 2D$ (top) and $x = 14D$ (bottom). The numbers inside the circles corresponds to the Figure numbers of the pictures presented in section 3.3. The dashed and continuous lines of the plots correspond to the Centered and Columnar flow pattern transition approximations of Table 3.2, respectively.

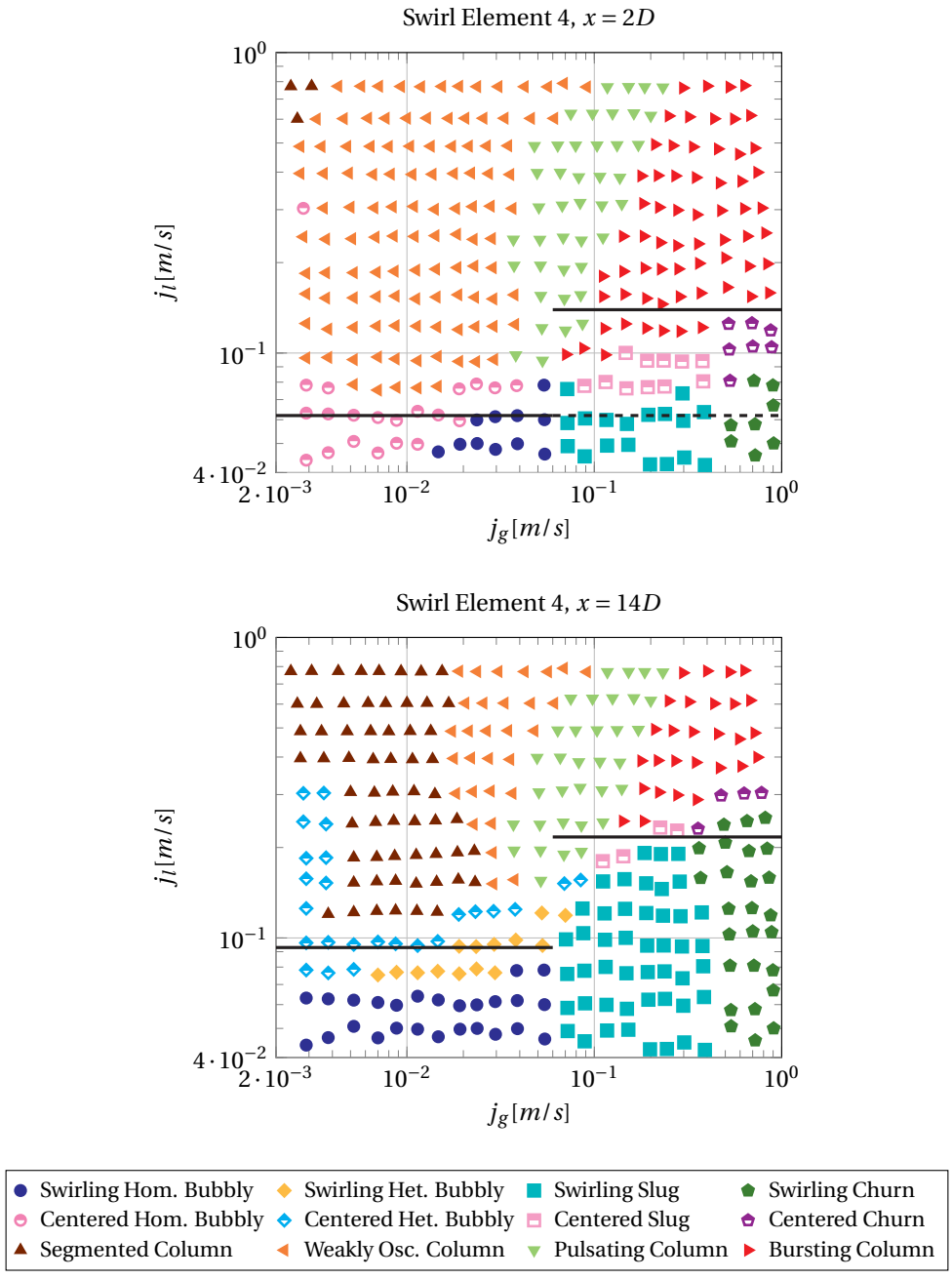

Figure 3.14: Flow pattern maps obtained for Swirl Element 4 ($\Omega_{se} = 5.77$) at $x = 2D$ (top) and $x = 14D$ (bottom). The dashed and continuous lines of the plots correspond to the Centered and Columnar flow pattern transition approximations of Table 3.2, respectively.

PART II: MECHANISTIC TRANSITION CRITERIA

Inspired by the classical works of Taitel *et al.* [106] and Mishima and Ishii [107] for upward (non-swirling) gas-liquid flows, mechanistic models for the upward swirling gas-liquid flow pattern transitions are developed in this part of chapter. The mechanistic models proposed are based on the physics behind the vertical upward swirling gas-liquid pipe-flows, resulting in dimensionless equations that can be used to predict the upward swirling gas-liquid flow patterns for arbitrary fluids, swirl elements, pipe diameters and axial positions (due to swirl decay). The models proposed in the current chapter are expected to work for gases with small density compared to the liquid, weakly-viscous fluids, swirl numbers in the range 1-10 and pipe diameters in the order of centimeters.

The aspects common to multiple flow pattern transitions, such as the liquid azimuthal velocity profile and swirl number, are presented in section 3.5. The swirling gas-liquid flow physics and mechanistic flow pattern transition criteria are described in section 3.6, that is divided per flow pattern class (Non-Columnar flows, Centered flows, Columnar flows and Swirling Annular flows). The mechanistic models proposed are validated against experimental data in section 3.7. The validation is performed based on the flow pattern maps obtained in part I, covering multiple swirl intensities (via four swirl elements) and swirl decay effects (via measurements at $x = 2D$ and $x = 14D$). Since the experiments of part I were performed with a single pipe inner diameter ($D = 81.4$ mm) and do not cover Swirling Annular flows, the validation of the proposed models for different pipe diameters and Swirling Annular flow pattern is made based on the experimental swirling gas-liquid flow pattern map measured by Liu and Bai [112] for $D = 30$ mm.

3.5. MODEL BACKGROUND

This section describes the aspects common to modeling of multiple flow patterns. The simplifying hypothesis used to obtain the flow pattern transition criteria are presented in subsection 3.5.1. The liquid and gas azimuthal velocities (and swirl numbers) as function of the axial position, used in the flow pattern transition models proposed in section 3.6, are estimated based on single-phase flow approximations. The single-phase swirl flow aspects relevant to this research are presented in subsection 3.5.2, and extended to swirling gas-liquid flows in subsection 3.5.3. The Columnar Flow pattern transitions are based on quantities derived from gas core diameter time-average and standard deviation. The measurement of these quantities is described in subsection 3.5.4.

3.5.1. SIMPLIFYING HYPOTHESIS

The upward swirling gas-liquid flows are modeled in the current chapter based on the following simplifying hypothesis:

- Incompressible flow.
- Gas density much smaller than the liquid density, i.e., $\rho_g/\rho_l \ll 1$.

- Turbulent flow and weakly-viscous fluids, with flow behavior well approximated as independent of μ_l and μ_g and, as consequence, independent of Re_l and Re_g.
- Negligible surface tension effects in Columnar flows.
- Uniform axial gas and liquid velocities (the wall region is assumed negligibly small compared to the inner diameter of the pipe).

The gas and liquid azimuthal velocity profiles are flow pattern-dependent and described in subsection 3.5.3.

3.5.2. SINGLE-PHASE AZIMUTHAL VELOCITY PROFILE AND SWIRL NUMBER

For stability reasons, confined single-phase swirl flows always have a solid body rotation around the centerline [47, 120]. In general, the azimuthal velocity distribution can be approximated as the superposition between a forced vortex (solid body rotation) and a Rankine or Gaussian vortex [46, 47]. A simplified vortex distribution of single-phase flows, sufficient for the mechanistic models proposed in this chapter, is

$$u_\theta(r) = \begin{cases} U_\theta \dfrac{r}{R_c}, & \text{for } r < R_c \\ U_\theta, & \text{for } r \geq R_c \end{cases}, \tag{3.5}$$

corresponding to a solid body rotation that transitions to a vortex of uniform azimuthal velocity U_θ at $r = R_c$. The radial position where the transition takes place can be approximated as $R_c \approx 0.25R$ [11].

The Swirl number corresponds to the dimensionless flow of angular momentum, and can be defined for single-phase pipe flows as:

$$\Omega \triangleq \frac{\int r\, u_\theta\, dw}{wRU_x} \tag{3.6}$$

In Equation 3.6, w is the mass flow rate in the pipe, U_x is the (cross-sectional) average axial velocity and R is the pipe radius.

The swirl number of single phase flows is independent of the axial velocity profile and equal to $u_\theta(R)/U_x$ for a free vortex ($r\,u_\theta$ = constant). It remains close to $u_\theta(R)/U_x$ for other vortices, with exact value depending on both the axial and azimuthal velocity profiles. In this research, the swirl number is estimated for a uniform axial velocity U_x and the azimuthal velocity profile u_θ of Equation 3.5. The solid body rotation of Equation 3.5 has a negligible contribution to the flow of angular momentum integral of Equation 3.6, resulting in the swirl number approximation:

$$\Omega \approx \frac{2}{3}\frac{U_\theta}{U_x} \tag{3.7}$$

SWIRL DECAY

The balance of angular momentum for a single-phase swirl flow in a pipe of radius R is given by

$$\frac{d}{dx}\left(2\pi\int_0^R \rho u_x u_\theta r^2 dr\right) = 2\pi R^2 \tau_{r\theta}(R), \tag{3.8}$$

where $\tau_{r\theta}(R)$ is the azimuthal wall shear-stress.

Kitoh [47] showed that (i) the total velocity of single-phase swirl flows follow a log-law close to the wall, and (ii) the wall shear-stress is aligned with the velocity field in the limit $r \to R$. Then, based on the assumption of uniform axial and azimuthal velocities (outside the solid body and wall regions), the total wall shear-stress is estimated based on the total velocity $U_t = \sqrt{U_x^2 + U_\theta^2}$ at the edge of the wall region via

$$\tau_t(R) = -f_w \rho \frac{|U_t| U_t}{2}, \tag{3.9}$$

where $\tau_t(R)$ is the total wall shear-stress and f_w is the Fanning wall friction factor.

As the total wall shear-stress is aligned with the total velocity next to the wall, the axial and azimuthal wall shear-stresses can be obtained from the total wall shear-stress via

$$\tau_{rx}(R) = \frac{U_x}{U_t}\tau_t(R) = -f_w \rho \frac{|U_t| U_x}{2} \tag{3.10}$$

and

$$\tau_{r\theta}(R) = \frac{U_\theta}{U_t}\tau_t(R) = -f_w \rho \frac{|U_t| U_\theta}{2}, \tag{3.11}$$

respectively.

Since $U_\theta \approx 1.5\Omega U_x$ from Equation 3.7, the swirl decay of single-phase flows can be written based on Equations 3.8 and 3.11 as:

$$\frac{d\Omega}{dx} = -\frac{3 f_w}{D}\sqrt{1 + 2.25\Omega^2}\,\Omega \tag{3.12}$$

The initial swirl number of single-phase flows is determined by the swirl element geometry, and given by $\Omega(x = 0) = \Omega_{se}$ (section 2.3). The exact solution of Equation 3.12 describes the swirl number as function of the axial position in the swirl tube according to:

$$\Omega(x) = \frac{\Omega_{se} \exp\left(-3 f_w \frac{x}{D}\right)}{1 + 0.5\left(\sqrt{2.25\Omega_{se}^2 + 1} - 1\right)\left[1 - \exp\left(-6 f_w \frac{x}{D}\right)\right]} \tag{3.13}$$

In literature, the swirl decay is commonly approximated as exponential. An exponential swirl decay is obtained from Equation 3.13 for low swirl numbers:

$$\Omega \approx \Omega_{se} \exp\left(-3 f_w \frac{x}{D}\right), \qquad \text{for } \Omega \ll 1 \tag{3.14}$$

Steenbergen and Voskamp [121] obtained an exponential swirl decay coefficient of approximately $6 f_{ns}$ for $\Omega < 0.18$, where f_{ns} is the Fanning friction factor of non-swirling fully-developed flows. Therefore, based on the swirl decay coefficient $3 f_w$ of Equation 3.14, the friction of swirling flows is approximated as $f_w = 2 f_{ns}$. Taking the Reynolds-independent friction factor approximation $f_{ns} = 0.005$ of non-swirling flows, the wall friction factor of swirling flows is estimated as $f_w = 0.01$ in this research, independent of the swirl number.

3.5.3. GAS-LIQUID AZIMUTHAL VELOCITY PROFILE AND SWIRL NUMBER

Different approximations for the gas-liquid azimuthal velocity profiles and swirl numbers are used depending on the flow pattern class.

CENTERED AND COLUMNAR FLOWS

The balance of angular momentum in Centered and Columnar flows is determined by the liquid, particularly when the gas is confined to a relatively small region around the pipe centerline and surrounded by a thick liquid layer, e.g., in Centered Bubbly flows or Weakly Oscillating Columns. Therefore, it is assumed that these flow patterns behave close to a single-phase flow of liquid, having their azimuthal liquid velocity described by:

$$u_{\theta l}(r) = \begin{cases} U_{\theta l}\dfrac{r}{R_c}, & \text{for } r < R_c \\ U_{\theta l}, & \text{for } r \geq R_c \end{cases} \tag{3.15}$$

The transition radius $R_c \approx 0.05R$ was obtained for upward swirling gas-liquid flows comparing the Columnar flow pattern transition models of subsection 3.6.3 with the experimental flow pattern maps of part I.

The swirl number calculation via Equation 3.6 is insensitive to the conditions in the center of the pipe, resulting in a negligible contribution of the gas and liquid solid body rotation to the liquid swirl number in the Centered and Columnar regimes. As consequence, the liquid swirl number of Centered and Columnar flows is approximated by the single-phase flow relation (Equation 3.7):

$$\Omega_l \approx \frac{2}{3}\frac{U_{\theta l}}{U_{xl}} \tag{3.16}$$

The gas swirl number is unimportant in Centered and Columnar flows.

The distribution of phases in the swirl element is expected to play a role in the swirl number of the liquid at the exit of the swirl element. However, to avoid overcomplicating the analysis, the initial liquid swirl number of the Centered and Columnar flows is approximated based on the swirl element geometry as $\Omega_l(x=0) = \Omega_{se}$. Since the gas occupies a small fraction of the pipe cross-section in these flow patterns, and the liquid is contact with the wall, the liquid swirl number as function of the axial position in the swirl tube is approximated by the single-phase flow relation of Equation 3.13 and computed via

$$\Omega_l(x) = \frac{\Omega_{se}\exp\left(-3f_w\dfrac{x}{D}\right)}{1+0.5\left(\sqrt{2.25\Omega_{se}^2+1}-1\right)\left[1-\exp\left(-6f_w\dfrac{x}{D}\right)\right]}, \tag{3.17}$$

where $f_w \approx 0.01$.

SWIRLING ANNULAR FLOWS

The balance of angular momentum is imposed by the gas in Swirling Annular flows. The flow in the wide gas core is similar to a single-phase flow in a rough pipe, with the gas-

liquid interface acting as wall. Therefore, the gas swirl number of Swirling Annular flows is approximated by the single-phase flow relation of Equation 3.7:

$$\Omega_g \approx \frac{2}{3}\frac{U_{\theta g}}{U_{xg}} \tag{3.18}$$

The swirl number of the liquid is assumed $\Omega_l \approx \Omega_g$ in Swirling Annular flows, as described in subsection 3.6.4.

The initial gas swirl number of Swirling Annular flows is also approximated independent of the phase distribution in the swirl element, and given by $\Omega_g(x=0) = \Omega_{se}$. Since the gas-liquid interface behaves like a rough wall from the perspective of the gas, the swirl number of the gas as function of the axial position in the swirl tube is approximated replacing (i) the wall friction factor of single-phase flows by the interface friction factor f_i, and (ii) the inner diameter of the pipe by the average gas core diameter D_i, in Equation 3.13:

$$\Omega_g(x) = \frac{\Omega_{se}\exp\left(-3f_i\dfrac{x}{D_i}\right)}{1+0.5\left(\sqrt{2.25\Omega_{se}^2+1}-1\right)\left[1-\exp\left(-6f_i\dfrac{x}{D_i}\right)\right]} \tag{3.19}$$

The interface friction factor of swirling annular flows is substantially different from the wall friction factor. The interface friction factor proposed by Wallis [122],

$$f_i = 0.005\left[1+150\left(1-\frac{D_i}{D}\right)\right], \tag{3.20}$$

is often used to model non-swirling annular flows. Following the ratio of two between the friction factor of swirling and non-swirling flows, described in subsection 3.5.2, the friction factor of Swirling Annular flows is extrapolated from Equation 3.20 as:

$$f_i = 0.01\left[1+150\left(1-\frac{D_i}{D}\right)\right] \tag{3.21}$$

3.5.4. MEASUREMENT OF THE GAS CORE STATISTICS

The gas core diameter time-average and standard deviation are used to obtain the interface friction factor and amplitude of the interface waves in the Columnar flow pattern transition criteria proposed in subsection 3.6.3. The gas core statistics are extracted from the flow pattern recordings downstream of the swirl element made in part I via the image processing routine of Appendix A.

It is worth mentioning that the flow pattern transitions are gradual and flow regime maps are traditionally presented in the log-scale, making the proposed flow pattern transition criteria robust to measurement errors. The research performed does not aim at obtaining precise interface friction factor measurements in gas-liquid swirl flows, and an approximation of the values is sufficient for the research of the current chapter; the obtained correlations must be used with care outside the context of flow pattern prediction.

3.6. FLOW PATTERN TRANSITION CRITERIA

This section describes the mechanistic models developed to predict the vertical upward swirling gas-liquid pipe-flow patterns described in part I. The section is divided in subsections based on the flow pattern classes, related to the swirl intensity of the flow.

3.6.1. NON-COLUMNAR FLOWS

As described in section 3.3, the addition of small azimuthal velocities to upward gas-liquid flows results in a simple rotation of the fluids without a significant impact of the centripetal force on the distribution of phases. As consequence, the swirling gas-liquid flow patterns for low superficial liquid velocities in the Non-Columnar regime are determined by the upstream flow, and can be predicted by classical upward non-swirling gas-liquid flow pattern transition models. The transition criteria proposed by Taitel *et al.* [106] are used to model the upstream flow pattern transitions in this research and, as consequence, the Non-Columnar swirling flow pattern transitions downstream of the swirl element. The only exception is the transition between Swirling Homogeneous and Swirling Heterogenous Bubbly flows, that is proposed in the current chapter.

The flow pattern transition models developed in this section depart from Homogeneous Bubbly Flows upstream and downstream of the swirl element, obtained for $j_g \to 0$ and $j_l \to 0$.

TRANSITION TO SWIRLING HETEROGENEOUS BUBBLY FLOW

Although not typically present in non-swirling vertical gas-liquid flow pattern maps, the transition to Heterogeneous Bubbly flows is particularly important for the swirling gas-liquid flow models proposed in this work. This occurs since larger bubbles in the upstream flow are transformed into pulses in the gas core, characterizing Pulsating Columns.

In Taitel *et al.* [106], the gas velocity of bubbly flows is modeled as:

$$U_{xg} = U_{xl} + U_{0B}, \tag{3.22}$$

where U_{0B} is the rise velocity of ellipsoidal bubbles in stagnant liquids, given by:

$$U_{0B} = 1.53 \left[\frac{(\rho_l - \rho_g) g \gamma}{\rho_l^2} \right]^{0.25} \tag{3.23}$$

Since $U_{xg} = j_g/\alpha$ and $U_{xl} = j_l/(1-\alpha)$, where α is the gas volume fraction, Equation 3.22 can be rewritten as:

$$j_g = \frac{\alpha}{1-\alpha} j_l + \alpha U_{0B} \tag{3.24}$$

Different correlations exist in literature for the transition between the Homogeneous and Heterogeneous flows in bubble columns. A simple empirical correlation for this transition is $\alpha = 0.12$ [123]. Replacing $\alpha = 0.12$ in Equation 3.24 results in the Swirling Homogeneous Bubbly-Swirling Heterogeneous Bubbly flow pattern transition criterion:

$$j_g \geq 0.14\, j_l + 0.12 U_{0B} \tag{3.25}$$

Rewriting Equation 3.25 dimensionless ($\rho_g/\rho_l \ll 1$):

$$Fr_g \geq 0.14 Fr_l + 0.18 Eo^{-0.25} \tag{3.26}$$

TRANSITION TO SWIRLING SLUG FLOW

Bubble coalescence in the bubbly regime increases with the number of bubbles and gas fraction of the flow, ultimately leading to the transition to slug when α is in the range 0.25-0.3 [106, 107]. Combining the mechanistic criterion of Taitel *et al.* [106], which assumes that bubbly flows exist for gas fractions up to $\alpha = 0.25$, with Equation 3.24 results in the transition criterion between Swirling Heterogeneous Bubbly and Swirling Slug flow:

$$j_g \geq \frac{j_l}{3} + \frac{U_{0B}}{4} \tag{3.27}$$

In dimensionless form, Equation 3.27 can be written as ($\rho_g/\rho_l \ll 1$):

$$Fr_g \geq 0.33 Fr_l + 0.38 Eo^{-0.25} \tag{3.28}$$

TRANSITION BETWEEN SWIRLING SLUG AND SWIRLING CHURN

In Taitel *et al.* [106], Churn flow is considered as an entry pattern of Slug flow. According to the authors, short Taylor bubbles and liquid slugs are formed at the inlet of the system. These short liquid slugs are unstable, falling back and merging with the consecutive liquid slugs as the flow moves upward, which results in the coalescence of the Taylor bubbles and the visual shaking effect of Churn flows. The liquid slugs and Taylor bubbles approximately double in length in each merging of the liquid slugs. The process repeats itself until sufficiently long stable liquid slugs are formed between the Taylor bubbles, characterizing the transition from Churn to Slug flow.

Based on a model for the relative velocity between two consecutive Taylor bubbles as function of their distance (liquid slug length), Taitel *et al.* [106] obtained that the pipe length required for the formation of non-swirling Slug flows is:

$$\frac{l_{slug}}{D} = 40.6(Fr_l + Fr_g + 0.22) \tag{3.29}$$

Despite a significant distance between the visualization windows at $x = 2D$ and $x = 14D$ downstream of the swirl element, and the expectation that Churn flows would continue to develop towards Slug in the swirling region, no clear visual distinction between upstream Churn flows and Swirling Churn flows at $x = 2D$ and $x = 14D$ was observed during the experiments of part I. Therefore, it is assumed that the Swirling Slug-Swirling Churn flow pattern transition in the whole region downstream of the swirl element is determined by the upstream flow according to $l_{slug} > l_{up}$, where l_{up} is the pipe length with (non-swirling) gas-liquid flow upstream of the swirl element. Replacing $l_{slug} > l_{up}$ in Equation 3.29 leads to the Swirling Slug-Swirling Churn flow pattern transition criterion:

$$Fr_g > -Fr_l + 0.22\left(0.112\frac{l_{up}}{D} - 1\right) \tag{3.30}$$

It is worth mentioning that the inclusion of the distance between the swirl element and the highest visualization window of the experimental setup in Equation 3.30 results in an increase of only 15% in the $Fr_l + Fr_g$ required for the Slug-Churn flow pattern transition. The relatively small shift of the Froude numbers predicted by the model, combined with gradual gas-liquid flow pattern transitions, can be the reason behind the mapping of the same flow patterns in the three locations during the experiments of part I. Another possible reason is that the Churn-Slug flow pattern transition is distance-independent, e.g., in the non-swirling Slug-Churn flow pattern transition criterion of Mishima and Ishii [107].

Since Swirling Slug flows do not exist for $l_{slug} > l_{up}$, the flow transitions directly from Swirling Heterogeneous Bubbly to Swirling Churn flow via Equation 3.30 for superficial liquid velocities above the match between Equations 3.28 and 3.30.

3.6.2. CENTERED FLOWS

Back to homogeneous bubbly flows, eddies in the turbulent liquid carry the rising bubbles to random directions perpendicular to the rising motion. Departing from the drag force, the instantaneous force in the radial direction that a liquid eddy with radial velocity u'_{rl} applies to a single rising bubble can be written as

$$F'_r = C_d \frac{\pi d_b^2}{8} \rho_l |U_{xg} - U_{xl}| u'_{rl}, \tag{3.31}$$

where $U_{xg} - U_{xl}$ is the slip velocity of the bubble in the axial direction, C_d is the drag coefficient and d_b is the bubble diameter.

Assuming that the drag coefficient is the same in the radial and vertical directions, Equation 3.31 can be rewritten based on the vertical balance between drag ($-C_d \pi d_b^2 \rho_l |U_{xg} - U_{xl}|(U_{xg} - U_{xl})/8$) and buoyancy ($(\rho_l - \rho_g) g \pi d_b^3/6$) as:

$$F'_r = (\rho_l - \rho_g) g \frac{\pi d_b^3}{6} \frac{u'_{rl}}{U_{xg} - U_{xl}} \tag{3.32}$$

In non-swirling flows, the turbulent fluctuations of the liquid spread the bubbles uniformly in the flow cross-section, with a peak in the bubble concentration next to the wall [124, 125]. In swirling flows, the spreading of the bubbles by the liquid fluctuations is countered by the centripetal force, that tends to agglomerate all the bubbles of the flow in a small region around the pipe centerline.

Departing from a situation where all the bubbles are agglomerated around the pipe centerline, and assuming that (i) the agglomerated region is a cylinder of radius R_{agg} concentric to the pipe, and (ii) the bubbles in the edge of the agglomerated region have the liquid azimuthal velocity, the centripetal force acting on a bubble in the edge of the agglomerated region can be written as:

$$F_{cp} = (\rho_l - \rho_g) \frac{\pi d_b^3}{6} \frac{u_{\theta l}^2(R_{agg})}{R_{agg}} \tag{3.33}$$

Bubble agglomeration will only be maintained in the flow if the centripetal force acting on the bubbles is larger than the radial force imposed by the liquid eddies. Combining Equations 3.32 and 3.33 leads to the bubble agglomeration criterion:

$$\frac{u_{\theta l}^2(R_{agg})}{gD} \geq \frac{1}{2}\frac{R_{agg}}{R}\frac{u'_{rl}}{U_{xg}-U_{xl}} \tag{3.34}$$

The radius of the agglomerated region is estimated assuming that the bubbles rise with the same axial velocity upstream and downstream of the swirl element. From conservation of mass, the hypothesis requires that the same cross-sectional area is occupied by the gas in both regions, which allows to write the gas area A_g in the swirling region based on the upstream gas fraction α_{up} as $A_g = \alpha_{up} A$.

Approximating the bubbles as spheres, the gas fraction in the agglomerated region, $\alpha_{agg} \triangleq A_g/(\pi R_{agg}^2)$, is estimated based on the maximum volume fraction of a random packing of spheres in a cylindrical pipe, $\alpha_{agg} \approx 0.6$ [126]. Then, the radius of the agglomerated region is estimated based on the upstream gas fraction via

$$R_{agg} = \sqrt{\frac{\alpha_{up}}{\alpha_{agg}}}R \tag{3.35}$$

The solid body region of the liquid is relatively small and does not impact the transition to centered flows, that is determined by the region of uniform azimuthal liquid velocity. Replacing Equation 3.35 and $u_\theta(R_{agg}) = U_{\theta l} = 1.5\Omega_l U_{xl}$ in Equation 3.34 leads to:

$$Fr_l\Omega_l \geq \frac{1}{\sqrt{4.5}}\left(\frac{u'_{rl}}{U_{xg}-U_{xl}}\right)^{0.5}\left(\frac{\alpha_{up}}{\alpha_{agg}}\right)^{0.25}(1-\alpha_{up}) \tag{3.36}$$

The liquid fluctuations and upstream gas fraction are flow pattern-dependent, being individually investigated for Centered (Homogeneous and Heterogeneous) Bubbly, Centered Slug and Centered Churn flows.

CENTERED BUBBLY FLOWS

The turbulent eddies in the liquid are influenced by the liquid momentum and by bubble-induced turbulence. The liquid velocity contribution to its turbulent fluctuations scale with the friction velocity, i.e., $u'_{rl} \sim \mathcal{O}(\sqrt{0.5 f_w}U_t)$.

In bubbly flows, the energy dissipated by the drag force is converted to turbulent kinetic energy in the wake of the bubble [127], increasing the turbulent fluctuations. In stagnant liquids with gas fractions up to $\alpha = 0.14$, Riboux *et al.* [128] showed that the liquid velocity fluctuations perpendicular to the bubbles rising motion scale with $u'_{rl} = \lambda U_{0B}\alpha^{0.4}$, where λ is a constant of order 1 that depends on the bubble size (Riboux *et al.* [128] obtained λ in the range 0.57 to 0.82 for equivalent bubble diameters between 1.6 and 2.5mm).

During the experiments of part I, bubble agglomeration was observed downstream of the swirl element for considerably low superficial liquid velocities, suggesting that the bubbles are the major contributors to the turbulent fluctuations in the liquid. Neglecting the liquid momentum contribution to u'_{rl}, and assuming that model of Riboux *et al.* [128]

for bubble-induced turbulence remains valid in the agglomerated bubbly region (where $\alpha_{agg} \approx 0.6$), u'_{rl} is estimated as:

$$u'_{rl} \approx \lambda U_{0B} \alpha_{agg}^{0.4} \tag{3.37}$$

Note that the approximation of negligible liquid contribution to the turbulent fluctuations, made in the derivation of Equation 3.37, is not valid for liquid swirl numbers much smaller than one. This occurs since the centripetal force acting on the bubbles, required to counter the turbulent dispersion force, is determined the azimuthal liquid velocity. The azimuthal liquid velocity scales with $U_{xl}\Omega_l$, and large axial velocities are required in the system to obtain significant centripetal accelerations for $\Omega_l \ll 1$, resulting in a significant contribution of the liquid momentum to the turbulent fluctuations.

Combining Equations 3.36 and 3.37 with the slip velocity of bubbly flows from Equation 3.22 and $\alpha_{agg} \approx 0.6$ leads to:

$$Fr_l \Omega_l \geq 0.48 \sqrt{\lambda} \alpha_{up}^{0.25} (1 - \alpha_{up}) \tag{3.38}$$

Instead of directly using the values of λ reported by Riboux *et al.* [128] for stagnant liquids, the constant is replaced by the experimental value 1.3 to accommodate the several approximations made along this subsection. Replacing $\lambda = 1.3$ in Equation 3.38 leads to Centered Homogeneous Bubbly flows downstream of the swirl element for

$$Fr_l \Omega_l \geq 0.55 \alpha_{up}^{0.25} (1 - \alpha_{up}), \tag{3.39}$$

where α_{up} is computed from the liquid and gas superficial velocities via Equation 3.24.

Centered Homogeneous Bubbly flows are limited to $\alpha_{up} < 0.12$. Above this limit, large bubbles are eventually formed in the upstream flow, propagating across the swirl element to the swirling region and characterizing the transition from Centered Homogeneous to Centered Heterogeneous Bubbly flow. The Centered Homogeneous Bubbly-Centered Heterogeneous Bubbly flow pattern transition is modeled based on the upstream Homogeneous Bubbly-Heterogeneous Bubbly flow pattern transition, described by Equation 3.26.

It is assumed that eventual large bubbles in Centered Heterogeneous Bubbly flows do not substantially increase the turbulent fluctuations in the bubble agglomeration region in relation to Centered Homogeneous Bubbly flows. Therefore, Equation 3.39 is also used to model the flow pattern transition from Swirling Heterogeneous Bubbly to Centered Heterogeneous Bubbly flow.

CENTERED SLUG AND CENTERED CHURN FLOWS

The hypothesis of a negligible contribution of the large bubbles to the turbulent intensity of the liquid becomes invalid with the upstream transition to Slug flow. Since the Taylor bubbles are much larger than the dispersed bubbles in the liquid slugs, it is is assumed that they are the major contributors to the liquid fluctuations.

The Taylor bubbles occupy the majority of the pipe diameter and have rising velocity $U_{0TB} = 0.35\sqrt{gD}$ in stagnant liquids [106]. Then, a first approximation for the liquid fluctuations in Slug flows, obtained extrapolating Equation 3.37 for the Taylor bubble velocity in stagnant liquids and $\alpha \approx 1$, is:

$$u'_{rl} \approx \lambda U_{0TB} \tag{3.40}$$

Assuming that the bubbles in the liquid slugs rise with the bubbly flow velocity $U_{xg} - U_{xl} = U_{0B}$ (Equation 3.22), the ratio between the liquid velocity fluctuations induced by the Taylor bubbles and the slip velocity in the liquid slugs can be written as ($\rho_g/\rho_l \ll 1$):

$$\frac{u'_{rl}}{U_{xg} - U_{xl}} \approx \lambda \frac{U_{0TB}}{U_{0B}} \approx 0.23\lambda Eo^{0.25} \tag{3.41}$$

As in Taitel *et al.* [106], the gas fraction in the liquid slugs is approximated as 0.25 independent of j_g and j_l. Replacing Equation 3.41, $\alpha_{agg} = 0.6$ and $\alpha_{up} = 0.25$ in Equation 3.36 results in the bubble agglomeration criterion in the liquid slugs:

$$Fr_l \Omega_l \geq 0.14\sqrt{\lambda} Eo^{0.125} \tag{3.42}$$

As in the Centered Bubbly flow model, λ is replaced by the experimental constant 1.3, resulting in Centered Slug flows downstream of the swirl element for:

$$Fr_l \Omega_l \geq 0.15 Eo^{0.125} \tag{3.43}$$

Equation 3.43 is extended to Centered Churn flows based on the experimental evidence of a constant superficial liquid velocity for the transition between Swirling Intermittent flows (Swirling Slug and Swirling Churn) and Centered Intermittent flows (Centered Slug and Centered Churn), both in the current research and in Liu and Bai [112].

The flow pattern transitions between (i) Centered Heterogeneous Bubbly and Centered Slug, and (ii) Centered Slug and Centered Churn, are determined by the upstream flow. The Slug and Churn upstream flow pattern transitions are modeled in the current research by the mechanistic models proposed by Taitel *et al.* [106], previously described in subsection 3.6.1 and determined by Equations 3.28 and 3.30, respectively.

3.6.3. COLUMNAR FLOWS

The transition from Centered to Columnar flow depends on the coalescence of the agglomerated bubble region into stable gas columns around the pipe centerline. In the current subsection, the transition to Columnar flow is first modeled for Weakly Oscillating Columns, and then extended to Pulsating, Bursting and Segmented Columns.

The gas column stability is evaluated based on a linear stability analysis performed around the average flow solution, obtained from a separated phases model of the flow. The separated phases and linear stability models are derived in Appendix C and, for conciseness, only the resulting equations are presented in the current chapter.

TRANSITION TO WEAKLY OSCILLATING COLUMN

Weakly Oscillating Columns are formed for relatively low superficial gas velocities, associated to Homogeneous Bubbly flows upstream of the swirl element. Weakly oscillating columns are modeled as a centered gas core of average diameter D_i with interface waves of amplitude h, as shown in Figure 3.15.

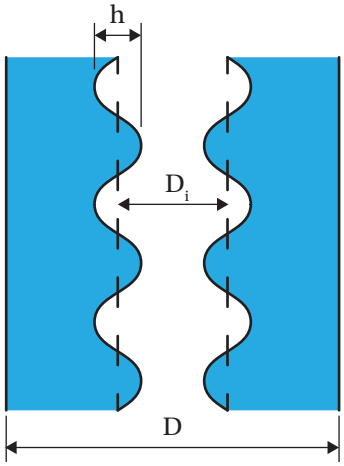

Figure 3.15: Schematics of a Weakly Oscillating Column with average gas core diameter D_i and interface waves of amplitude h.

The balances of mass, linear momentum and angular momentum of vertical separated flows can be written as (section C.1 of Appendix C):

$$U_{xg} = \frac{D^2}{D_i^2} j_g \tag{3.44}$$

$$U_{xl} = \frac{D^2}{D^2 - D_i^2} j_l \tag{3.45}$$

$$2\frac{f_i}{D_i}\sqrt{1+2.25\Omega_g^2}\rho_g U_{xg}^2 - 2\frac{f_w}{D}\sqrt{1+2.25\Omega_l^2}\rho_l U_{xl}^2 = \frac{D^2 - D_i^2}{D^2}\left(\rho_l - \rho_g\right) g \tag{3.46}$$

$$\frac{dU_{\theta g}}{dx} = -3\frac{f_i}{D_i}\sqrt{1+2.25\Omega_g^2}\left(U_{\theta g} - U_{\theta l}\right) \tag{3.47}$$

$$\frac{dU_{\theta l}}{dx} = 3\left[\frac{D^2 - D_i^2}{D^3 - D_i^3}\frac{\rho_g j_g}{\rho_l j_l} f_i \sqrt{1+2.25\Omega_g^2}\left(U_{\theta g} - U_{\theta l}\right) - \frac{D^2}{D^3 - D_i^3} f_w \sqrt{1+2.25\Omega_l^2} U_{\theta l}\right] \tag{3.48}$$

Equation 3.46 shows that an axial gas velocity orders of magnitude above the axial liquid velocity is required to counter the gravity effects in the flow, due to scaling of the interface shear-stress with the gas density and $\rho_g/\rho_l \ll 1$. Since the axial gas velocity and j_g are coupled via conservation of mass (Equation 3.44), the requirement of $U_{xg} \gg U_{xl}$ implies in the formation of thin gas cores ($D_i/D \ll 1$) in Weakly Oscillating Columns for low superficial gas velocities, as previously observed in Figure 3.8.

While gravity promotes a large slip between the gas and the liquid in the axial direction, no driving force is present in the azimuthal direction to maintain a large slip between $U_{\theta g}$

and $U_{\theta l}$. Moreover, Equation 3.47 shows that the difference between the gas and liquid azimuthal velocities decay with the inverse of the gas core diameter. Since $D_i/D \ll 1$ in Weakly Oscillating Columns, the azimuthal gas velocity quickly tends to $U_{\theta g} \approx U_{\theta l}$.

The analysis of order of magnitude of Equation 3.46 reveals that the wall shear-stress has a much smaller contribution than gravity to the vertical balance of momentum of Columnar flows. Additionally, since $U_{\theta g} \approx U_{\theta l}$, the swirl number of the gas scales with $\Omega_g \sim U_{\theta g}/U_{xg} \sim U_{\theta l}/U_{xg} \sim (U_{xl}/U_{xg})\Omega_l$. Since $U_{xl}/U_{xg} \ll 1$, $\Omega_g \ll \Omega_l$ and, for liquid swirl numbers in the order of 1, $\Omega_g \ll 1$. Therefore, Equation 3.46 is simplified to

$$2\frac{f_i}{D_i}\rho_g U_{xg}^2 \approx \left(\rho_l - \rho_g\right) g, \tag{3.49}$$

and Equation 3.48 is simplified to ($D_i/D \ll 1$, $U_{\theta l} \approx 1.5\Omega_l U_{xl}$):

$$\frac{d\Omega_l}{dx} \approx -3\frac{f_w}{D}\sqrt{1+2.25\Omega_l^2}\,\Omega_l \tag{3.50}$$

Equation 3.50 confirms that Equation 3.17, introduced in section 3.5, can be used to predict the liquid swirl number of Columnar flows.

The interface friction factor of Weakly Oscillating Columns, required to solve Equation 3.49, is obtained from experimental data rewriting Equation 3.49 as

$$f_i \approx \frac{1}{2}\frac{\left(\rho_l - \rho_g\right)}{\rho_g}\frac{1}{Fr_g^2}\frac{D_i^5}{D^5}, \tag{3.51}$$

where Fr_g is computed based on the superficial gas velocity and pipe diameter used in the experiments, and D_i/D is obtained processing the flow recordings (subsection 3.5.4).

The interface acts like a corrugated pipe wall from the perspective of the gas in Weakly Oscillating Columns, with roughness related to the amplitude of the interface waves. The interface waves are clearly visible by naked eye and in the order of 10% the gas core diameter downstream of the swirl element, becoming larger in the visualization window at $x = 14D$. Based on the high relative roughness of the interface and the high axial gas velocity in the gas column, the gas flow is approximated as complete turbulent and the interface friction factor assumed independent of the gas viscosity.

The interface friction factor of Weakly Oscillating Columns as function of the average gas core diameter, measured in the visualization windows centered at $x = 2D$ and $x = 14D$, is presented in Figure 3.16. Figure 3.16 shows that the interface friction factor substantially increases between the two visualization windows, and is well approximated by[1]:

$$f_i = C_f\left(\Omega_l, \frac{x}{D}\right)\frac{D}{D_i}, \tag{3.52}$$

where C_f is described by the power laws:

$$C_f\left(\Omega_l, \frac{x}{D}\right) \approx \begin{cases} 0.010 + 6.0\cdot 10^{-4}\Omega_l^{1.4}, & \text{for } x = 2D \\ 0.010 + 9.0\cdot 10^{-2}\Omega_l^{3.4}, & \text{for } x = 14D \end{cases} \tag{3.53}$$

[1] The experimental data suggests that the interface friction factor of Bursting Columns significantly deviates from Equations 3.52 and 3.53, due to the large gas core oscillations characteristic of the flow regime.

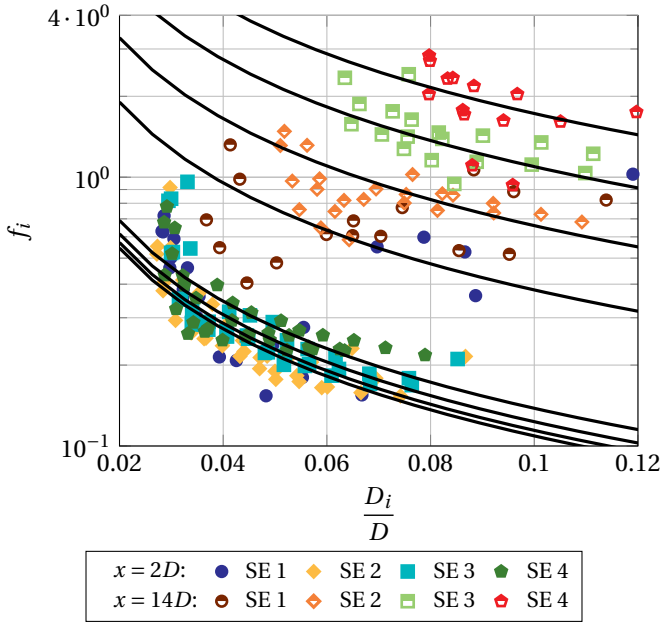

Figure 3.16: Comparison between the interface friction factor of Weakly Oscillating Columns computed from the gas core measurements (marks) and Equation 3.52 (continuous lines), for multiple superficial liquid velocities and Swirl Elements (SE).

A potential reason for the substantial increase in the interface friction factor between $x = 2D$ and $x = 14D$ observed in Figure 3.16 is the impact of swirl decay on the axial liquid velocity.

In single-phase swirl flows, swirl decay results in a positive axial pressure gradient in the center of pipe that can cause the reversal of the flow around the centerline. Swirl decay is stronger for stronger swirls, resulting in an increase in the flow reversal area and magnitude with the swirl number [47, 129]. In gas-liquid flows, swirl decay effects on the axial liquid velocity nearby thin weakly oscillating columns are also expected, at least to some extent.

The axial liquid velocity reversal near the gas core acts as a destabilizing effect on the gas-liquid interface, increasing the amplitude of the interface waves and interface friction factor. The distance between the outlet of the swirl element and the visualization window centered at $x = 2D$ is not sufficient for the development of backflow in the liquid, explaining the weak dependency of f_i on Ω_l at the location. On the other hand, the visualization window at $x = 14D$ is sufficiently far from the generation of swirl for the reversal of the axial liquid velocity next to the gas-liquid interface, explaining the strong dependency of Equations 3.52 and 3.53 on Ω_l.

The distance x/D required for a strong dependency of the interface friction factor of Weakly Oscillating Columns on Ω_l was not investigated in this research. Both C_f expressions of Equation 3.53 are used to validate the mechanistic models proposed in this chapter based on the flow pattern maps of part I, due to the availability of experimental data.

In general, the expression obtained at $x = 14D$ is recommended for the prediction of the flow pattern transitions based on the swirl decay explanation above, since it captures the whole swirl flow physics.

Equations 3.51 and 3.52 are combined into the average gas core diameter expression:

$$\frac{D_i}{D} \approx \left[2C_f \frac{\rho_g}{(\rho_l - \rho_g)}\right]^{1/6} Fr_g^{1/3} \tag{3.54}$$

Equation 3.54 is compared to the experimental data obtained in the axial cyclone in Figure 3.17. Figure 3.17 shows that the average gas core diameter significantly increases between $x = 2D$ and $x = 14D$, due to the increase in the interface friction factor between the two locations.

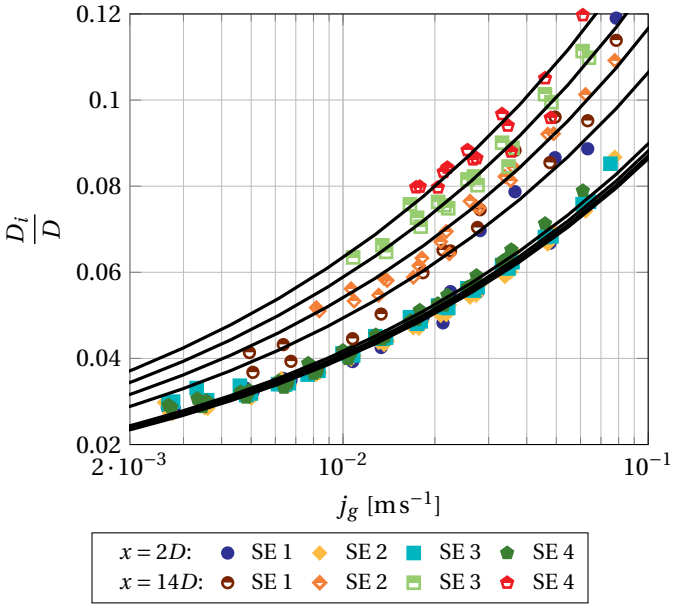

Figure 3.17: Comparison between the experimental average gas core diameter in Weakly Oscillating Columns (marks) and Equation 3.54 (continuous lines) for multiple superficial liquid velocities and Swirl Elements (SE).

The maintenance of Weakly Oscillating Columns in the flow is determined by the gas core stability. In this research, the gas core stability is analyzed around the average flow solution of Equation 3.54, based on the flow response to a solitary wave traveling on the gas-liquid interface. The linear stability analysis, detailed in section C.2 of Appendix C, results in stable gas cores if:

$$\rho_l \frac{u_{\theta l}^2(R_i)}{D_i} - \rho_g \frac{u_{\theta g}^2(R_i)}{D_i} \geq \frac{2}{D_i}\rho_g U_{xg}^2 + \frac{2D_i}{(D^2 - D_i^2)}\rho_l U_{xl}^2 \tag{3.55}$$

Since $D_i/D \ll 1$, $U_{xg} \gg U_{xl}$ and $u_{\theta g}(R_i) \approx u_{\theta l}(R_i)$ in Weakly Oscillating Columns, the axial liquid velocity contribution to Equation 3.55 is neglected and the gas core stability

condition is approximated as:

$$u_{\theta l}(R_i) \geq \sqrt{2\frac{\rho_g}{\rho_l - \rho_g}} U_{xg} \tag{3.56}$$

Equations 3.44 and 3.54 can be used to rewrite Equation 3.56 as:

$$\frac{u_{\theta l}(R_i)}{\sqrt{gD}} \geq \left[\frac{2}{C_f^2}\frac{\rho_g}{(\rho_l - \rho_g)}\right]^{1/6} Fr_g^{1/3} \tag{3.57}$$

As described in section 3.5, the azimuthal liquid velocity is approximated as a region of uniform angular velocity surrounded by a region of uniform azimuthal liquid velocity (Equation 3.15).

For gas-liquid interfaces in the solid body region ($R_i < R_c$), where $u_{\theta l}(R_i) = U_{\theta l} R_i / R_c$, Equation 3.57 can be written as:

$$\frac{U_{\theta l}}{\sqrt{gD}} \geq \frac{1}{\sqrt{C_f}}\frac{R_c}{R} \tag{3.58}$$

For gas cores with interface in the region of uniform azimuthal liquid velocity ($R_i \geq R_c$), where $u_{\theta l}(R_i) = U_{\theta l}$, Equation 3.57 is equivalent to:

$$\frac{U_{\theta l}}{\sqrt{gD}} \geq \left[\frac{2}{C_f^2}\frac{\rho_g}{(\rho_l - \rho_g)}\right]^{1/6} Fr_g^{1/3} \tag{3.59}$$

As $U_{\theta l} \approx 1.5\, j_l \Omega_l$, the conditions required for the existence of stable Weakly Oscillating Columns in upward swirling gas-liquid flows are

$$Fr_l \Omega_l \geq \begin{cases} \dfrac{2}{3}\dfrac{R_c}{R}\dfrac{K_{col}}{\sqrt{C_f}}, & \text{for } R_i < R_c \\ \dfrac{2}{3} K_{col}\left[\dfrac{2}{C_f^2}\dfrac{\rho_g}{(\rho_l - \rho_g)}\right]^{1/6} Fr_g^{1/3}, & \text{for } R_i \geq R_c \end{cases}, \tag{3.60}$$

where K_{col} is a factor of order 1 added to the equation to accommodate the approximations made along this section (e.g., uniform axial gas and liquid velocities, simplified azimuthal liquid velocity profile, linear stability analysis of a solitary wave, etc). A good match between Equation 3.60 and the experimental flow pattern maps of part I is obtained for $K_{col} = 1.2$ and $R_c/R = 0.05$.

TRANSITION TO PULSATING COLUMN

As mentioned in subsection 3.3.3, large bubbles of upstream Heterogeneous Bubbly flows are transformed into high-speed pulses in the gas core for sufficiently-high azimuthal liquid velocities. Therefore, the transition from Weakly Oscillating Column to Pulsating Column is assumed to take place when the upstream flow transitions from Homogeneous to Heterogeneous Bubbly flow, which is described by Equation 3.26.

Since the gas core pulses are not very strong nor very frequent, Equation 3.60 is also used to model the formation of stable Pulsating Columns in the flow.

TRANSITION TO BURSTING COLUMN

As described in part I, the transition between Pulsating and Bursting columns occurs when the flow upstream of the swirl element transitions from Heterogeneous Bubbly to Slug or Churn, with the alternating wide and thin gas core sections observed in Bursting Columns arising from the alternating high and low gas fraction regions of the upstream flow (Taylor bubbles and liquid slugs). The Bubbly-Slug flow pattern transition upstream of the swirl element is modeled via Equation 3.28 and, since the upstream flow patterns determine the columnar flow patterns, the same equation is used to model the Pulsating-Bursting transition.

Bursting columns can be seen as a flow pattern where Weakly Oscillating Columns (thin gas core sections) alternate with distorted Taylor bubbles (wide gas core sections), where the weakly oscillating portion of the flow is created by the coalescence of the discrete bubbles contained in the liquid slugs upstream of the swirl element. The Taylor bubbles are already surrounded by a liquid film and stable in the non-swirling flow upstream of the swirl element. Therefore, since the centripetal force has a stabilizing effect on the flow, the distorted Taylor bubbles regions downstream of the swirl element are also stable.

The Bursting column stability is then determined by the weakly oscillating portion of the flow, related to the upstream liquid slugs. As in the Swirling Slug and Centered Slug models of subsections 3.6.1 and 3.6.2, it is assumed that the maximum gas fraction in the upstream liquid slugs is 0.25. The relation between the superficial gas and liquid velocities of Bubbly flows is described by Equation 3.24. Equation 3.24 results in the gas flow rate transported by the liquid slugs determined by $Fr_{gls} = 0.33Fr_l + 0.38Eo^{-0.25}$ for $\alpha = 0.25$, where Fr_{gls} is Froude number of the gas in the liquid slugs; the remaining gas injected in the system is transported by the Taylor Bubbles, that grow with the increase in Fr_g.

The Bursting Column stability criterion is obtained evaluating the Weakly Oscillating Column criterion of Equation 3.60 for Fr_{gls}. Since the gas flow rate in the upstream liquid slugs is independent of the total gas flow rate of the system, the resulting Bursting Column flow pattern transition criterion is independent of Fr_g:

$$Fr_l\Omega_l \geq \frac{2}{3}K_{col}\left[\frac{2}{C_f^2}\frac{\rho_g}{(\rho_l-\rho_g)}\right]^{1/6}\left[0.33Fr_l + \frac{0.38}{Eo^{0.25}}\right]^{1/3} \tag{3.61}$$

The Centered flow pattern transition criteria (Equation 3.39 for Centered Homogeneous and Centered Heterogeneous Bubbly flows, and Equation 3.43 for Centered Slug and Centered Churn flows) usually require Fr_l below the gas column stability criteria (Equation 3.60 for Weakly Oscillating and Pulsating Columns, and Equation 3.61 for Bursting Columns), resulting in the transition between Centered and Columnar flows by the coalescence of the bubble agglomeration regions into stable continuous gas cores.

However, Centered flows sometimes require Fr_l above the gas core stability criteria to exist in the pipe. If this occurs close to the swirl element, it is considered that the flow remains in the Non-Columnar regimes until Centered flows can be created in the system, since Columnar flows cannot be formed unless the gas bubbles of the upstream flow are brought together by the centripetal force. If the behavior occurs after continuous columns were already formed downstream of the swirl element, the Columnar flow is maintained in the system until Ω_l becomes too small to fulfill the stability criteria. After the gas core

stability is lost, the flow transitions directly from Columnar to Non-Columnar, skipping the Centered regimes, if the centrifugal force is not strong enough to maintain the gas column fragments together.

COLUMN SEGMENTATION

It is assumed that Weakly Oscillating Columns transition to Segmented Columns when the crest of the interface waves touch, splitting the gas core into multiple segments.

The Segmented Column transition is modeled based on the standard deviation of the gas core diameter, $\sigma(d_i)$, since the amplitude of the interface waves scales with $\sigma(d_i)$. For instance, an idealized sinusoidal interface described by $d_i(x,t) = D_i + h\sin(\omega(t - x/c))$, where c is the speed of the interface waves, has the amplitude of the interface waves related to the standard deviation of the gas core diameter measured at a fixed axial position via $h = \sqrt{2}\cdot\sigma(d_i)$.

The standard deviation of the gas core diameter measured in the visualization windows centered at $x = 2D$ and $x = 14D$ are presented in Figure 3.18.

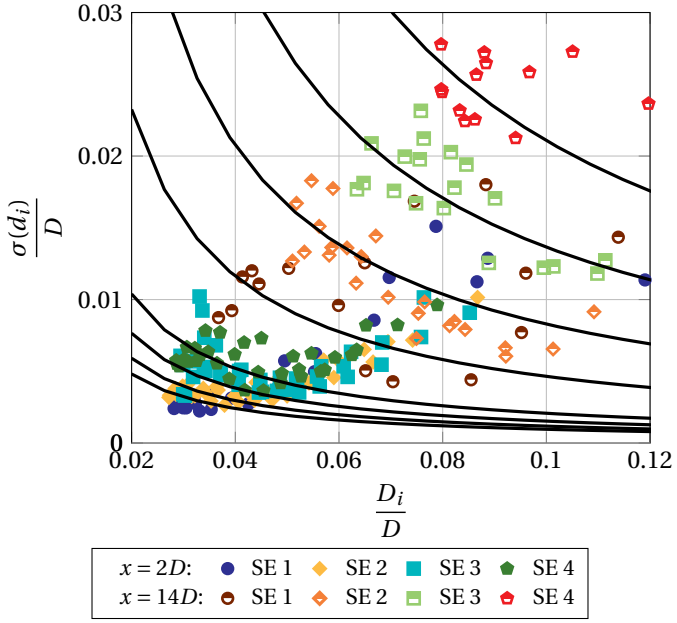

Figure 3.18: Standard deviation of the gas core diameter in Weakly Oscillating Columns. The marks represent the experimental data obtained for multiple superficial liquid velocities and Swirl Elements (SE), and the continuous lines represent the empirical fits of Equation 3.62.

As shown in Figure 3.18, the standard deviation of the gas core scales approximately with the inverse of the average gas core diameter, presenting a strong dependency on the swirl number of the liquid and axial position. The standard deviation of the gas core diameter is approximated by

$$\frac{\sigma(d_i)}{D} \approx C_\sigma\left(\Omega_l, \frac{x}{D}\right)\frac{D}{D_i}, \tag{3.62}$$

where:

$$C_\sigma\left(\Omega_l, \frac{x}{D}\right) = \begin{cases} 5.0\cdot10^{-5} + 3.2\cdot10^{-5}\Omega_l^{1.2}, & \text{for } x = 2D \\ 5.0\cdot10^{-5} + 1.2\cdot10^{-3}\Omega_l^{3.1}, & \text{for } x = 14D \end{cases} \tag{3.63}$$

The increase in the amplitude of the interface fluctuations (scaling with $\sigma(d_i)$) between $x = 2D$ and $x = 14D$, observed in Figure 3.18, is also explained by the development of a flow reversal in the liquid, next to the gas-liquid interface, between the two locations. The flow reversal increases with the swirl number of the liquid, due to a stronger swirl decay, resulting in the strong dependency of $\sigma(d_i)$ on Ω_l observed at $x = 14D$. The liquid flow reversal has a destabilizing effect in the gas-liquid interface, that reduces as the gas core widens and the gas-liquid interface departs from the center of the pipe, explaining the decrease in the amplitude of the gas core fluctuations with the increase in the average gas core diameter.

The segmentation of the idealized sinusoidal interface occurs when $d_i(x,t) = 0$, obtained for $h = D_i$ or $\sigma(d_i) = D_i/\sqrt{2}$. The interface of Weakly Oscillating Columns is not sinusoidal, containing waves of multiple amplitudes and frequencies. The gas column segmentation is assumed to occur when the largest interface waves touch, occurring for average gas core diameters

$$\frac{D_i}{D} \leq K_{seg}\sqrt{2}\frac{\sigma(d_i)}{D}, \tag{3.64}$$

where $K_{seg} \geq 1$ is an empirical constant related to the ratio between the amplitude of the largest interface waves of Weakly Oscillating Columns and h of the idealized sinusoidal interface.

Combining Equation 3.64 with the gas core diameter average and standard deviation of Weakly Oscillating Columns, obtained from Equations 3.54 and 3.62, results in the gas core segmentation criterion:

$$Fr_g \leq 2^{1/4}K_{seg}^{3/2}\left[\frac{C_\sigma^3}{C_f}\frac{(\rho_l - \rho_g)}{\rho_g}\right]^{1/2} \tag{3.65}$$

A good match between Equation 3.65 and the experimental flow pattern maps of part I is obtained for $K_{seg} = 2$. Segmented columns were rarely observed in the visualization window at $x = 2D$ during the experiments, due to the relatively low amplitude of the interface waves at the location (Figure 3.18).

3.6.4. SWIRLING ANNULAR FLOW

Three mechanisms are commonly found in classical models for the vertical annular flow transition in non-swirling flows: (i) the upward flow of the liquid film [107, 122], (ii) the bridging of the gas core [108, 122], and (iii) the droplet entrainment in the gas core [107, 122].

An annular flow can only be maintained in a vertical pipe with the upward flow of the liquid film, as the backflow of the film would necessarily result in the formation of liquid slugs to maintain the upward net liquid flow rate imposed in the pipe inlet [122]. The transition to vertical non-swirling Annular flow based on 1D separated phases models can be predicted with the approximation $U_{xl} = 0$, corresponding to the limiting condition for upward flow of the liquid film [107] and resulting in a good approximation of the vertical non-swirling annular flow transition for low superficial liquid velocities ($Fr_l \ll 1$).

Liquid departing from the film can form bridges in the gas core for high liquid flow rates, transitioning the Annular flow back to Slug/Churn. While the criterion of upward liquid film flow is well-approximated as independent of the liquid flow rate, bridging introduces a strong dependency of the superficial gas velocity required for Annular flows on the superficial liquid velocity. Bridging models can be empirical [122] or based on the gas fraction of the flow [108].

Another important criterion for the transition to non-swirling Annular flow in vertical pipes of large diameter is the entrainment of portion of the liquid as droplets in the gas core, resulting in (non-swirling) annular-mist flows [107]. The amount of liquid entrained in the gas core depends on a balance between droplet removal and deposition with the liquid film, increasing with the superficial gas velocity. Due to the high liquid density compared to the gas, entrained droplets can have a significant impact on the balance of momentum of the gas [130, 131].

From the three aforementioned criteria, the upward flow of the liquid film and bridging are fundamental to the Swirling Annular flow transition. The entrainment criterion is most likely absent in strong swirl flows, since eventual liquid droplets initially present in the gas core are quickly driven to the liquid film by the centrifugal force. However, droplet entrainment can play a role in the Swirling Annular flow pattern transition for weak swirls, with the effect increasing with the swirl decay in the streamwise direction [132]. The interplay between droplet entrainment and swirl intensity, and the characterization of strong or weak swirls in the context of droplet entrainment, are not investigated in this thesis.

Swirling Annular flows are separated flows and, therefore, also described by Equations 3.44-3.48 used to model Weakly Oscillating Columns in subsection 3.6.3. However, a major difference between Swirling Annular flows and Columnar flows is that Swirling Annular flows are obtained for $Fr_g \gg Fr_l$, resulting in thick gas cores ($D_i/D \sim \mathcal{O}(1)$), $U_{\theta g} \gg U_{\theta l}$ and non-negligible Ω_g.

Equation 3.46, obtained combining the balances of linear momentum of the gas core and liquid film, can be written in dimensionless form as:

$$\sqrt{\frac{\rho_g}{\rho_l - \rho_g}} Fr_g = \left(\frac{D_i}{D}\right)^{2.5} \left[\frac{D^2 - D_i^2}{D^2} \frac{1}{2 f_i \sqrt{1 + 2.25\Omega_g^2}} + \left(\frac{D^2}{D^2 - D_i^2}\right)^2 \frac{f_w}{f_i} \sqrt{\frac{1 + 2.25\Omega_l^2}{1 + 2.25\Omega_g^2}} \left(\sqrt{\frac{\rho_l}{\rho_l - \rho_g}} Fr_l \right)^2 \right]^{0.5} \tag{3.66}$$

The liquid and gas balances of angular momentum, described by Equations 3.47 and 3.48, can be used to obtain a set of equations describing the coupled swirl decay of the

liquid and gas. However, the approach brings an unnecessary level of complexity to the flow pattern transitions proposed.

From a physics perspective, the azimuthal velocity of the liquid depends on the balance between the accelerating torque imposed at the interface by the gas, and the decelerating torque imposed in the liquid by the wall, resulting in $0 < U_{\theta l} < U_{\theta g}$. Instead of solving the coupled decay of the liquid and gas swirl numbers, the Swirling Annular flow pattern transition is modeled in the current chapter based on the approximation $\Omega_l \approx \Omega_g$. Since $U_{xg} \gg U_{xl}$ in swirling annular flows, it follows from the liquid and gas swirl number definitions that $U_{\theta gl} \gg U_{\theta l}$, allowing to approximate Equation 3.47 as:

$$\frac{dU_{\theta g}}{dx} \approx -3\frac{f_i}{D_i}\sqrt{1+2.25\Omega_g^2}U_{\theta g} \tag{3.67}$$

The solution of Equation 3.67 leads to the gas swirl number as function of the axial position described by Equation 3.19.

Liu *et al.* [113] suggested that the Swirling Annular flow pattern transition takes place for gas fractions between 0.71 and 0.74 ($D_i/D = 0.84 - 0.86$). Hence, $D_i/D \geq 0.85$ is taken as the condition required for the existence of Swirling Annular flows in vertical pipes. The choice of $D_i/D \geq 0.85$ ($\alpha \geq 0.72$) for the Swirling Annular flow pattern transition covers both (i) the upward liquid-film flow criterion, since conservation of mass results in $U_{xl} \geq 3.60\, j_l$ (always greater than zero), and (ii) the bridging criterion, as $\alpha \geq 0.72$ is slightly below the bridging criterion $\alpha \geq 0.76$ of non-swirling flows; $\alpha \geq 0.76$ was used as bridging criterion in the Swirling Annular flow pattern transition model of Liu and Bai [116].

Replacing f_i from Equation 3.21, $f_w = 0.01$, $\Omega_l \approx \Omega_g$ and $D_i \geq 0.85D$ on Equation 3.66 results in the Swirling Annular flow criterion:

$$Fr_g \geq \left[\frac{0.26}{\sqrt{1+2.25\Omega_g^2}}\frac{\rho_l-\rho_g}{\rho_g} + 0.25\frac{\rho_l}{\rho_g}Fr_l^2\right]^{0.5} \tag{3.68}$$

Equation 3.68 shows that the increase in swirl intensity shifts the Annular flow pattern transition to lower Fr_g, as predicted by the Swirling Annular flow model of Liu and Bai [116]. The reduction in the gas flow rate required for the Annular flow pattern transition is explained by the increase in the interface shear-stress caused by the swirl flow, which was also observed by Funahashi *et al.* [133] and Koto *et al.* [132].

Equation 3.68 is compared to the Swirling Annular flow pattern transition measured by Liu and Bai [112] in subsection 3.7.2, resulting in a good match of the model with the experimental transition for $\Omega_g \approx 0.81$ (predicted based on the swirl element geometry and axial position of the flow pattern map via Equation 3.19). Since Swirling Annular flows were not investigated during the experiments of part I, the validity of Equation 3.68 for stronger swirls must be verified in future works.

3.7. MODEL VALIDATION

The mechanistic flow pattern transition models proposed in section 3.6 showed that the upward swirling gas-liquid flow pattern transitions in vertical pipes are strongly im-

pacted by Fr_g, Fr_l, Ω_l and x/D. These dimensionless numbers can be varied via the superficial gas and liquid velocities, swirl element, pipe diameter and axial position where the flow pattern map is made.

Multiple flow rates, swirl numbers and pipe positions were covered in the experiments of part I, and the obtained flow pattern maps are compared with the mechanistic model predictions in subsection 3.7.1. The experiments of the current chapter were performed with a pipe inner diameter D = 81.4 mm and did not include Swirling Annular flows. Therefore, the experimental flow pattern map of Liu and Bai [112], obtained for a pipe inner diameter D = 30 mm and covering the Swirling Annular flow pattern transition, is used to evaluate the accuracy of the proposed flow pattern criteria in smaller pipe diameters in subsection 3.7.2.

In the flow pattern maps of this section:

- The flow pattern transitions between (i) Swirling Homogeneous Bubbly and Swirling Heterogeneous Bubbly, (ii) Centered Homogeneous Bubbly and Centered Heterogeneous Bubbly, and (iii) Weakly Oscillating Column and Pulsating Column, are modeled by Equation 3.26 and represented by curve A.

- The transitions between (i) Swirling Heterogeneous Bubbly and Swirling Slug, (ii) Centered Heterogeneous Bubbly and Centered Slug, and (iii) Pulsating Column and Bursting Column, are modeled by Equation 3.28 and represented by curve B.

- The transitions between (i) Swirling Slug and Swirling Churn, and (ii) Centered Slug and Centered Churn, are modeled by Equation 3.30 and represented by curve C.

- The transition from Non-Columnar (Swirling Homogeneous/Heterogeneous Bubbly, Swirling Slug and Swirling Churn) to Centered flow (Centered Homogeneous/Heterogeneous Bubbly, Centered Slug and Centered Churn) is given by the combination between Equations 3.39 and 3.43, and represented by curve D. Curve D is plotted as a dashed line in the flow pattern maps when the Centered flow pattern transition is above the Columnar flow pattern transition, not playing a role in the upward swirling gas-liquid flow patterns far from the swirl element.

- The transition from Centered to Columnar flow (Segmented, Weakly Oscillating Column, Pulsating Column and Bursting Column) is modeled by the combination between Equations 3.60 and 3.61, and represented by curve E.

- The transition between Segmented Column and Weakly Oscillating Column is described by Equation 3.65, and represented by curve F.

- The transition to Swirling Annular is predicted by Equation 3.68, and represented by curve G.

The flow pattern transitions are summarized in Figure 3.19. Please note that the equations behind curves B and C were proposed by Taitel *et al.* [106] for non-swirling flows, and are not original to this research. However, their application in the Centered and Columnar flow pattern transitions is a contribution of this thesis.

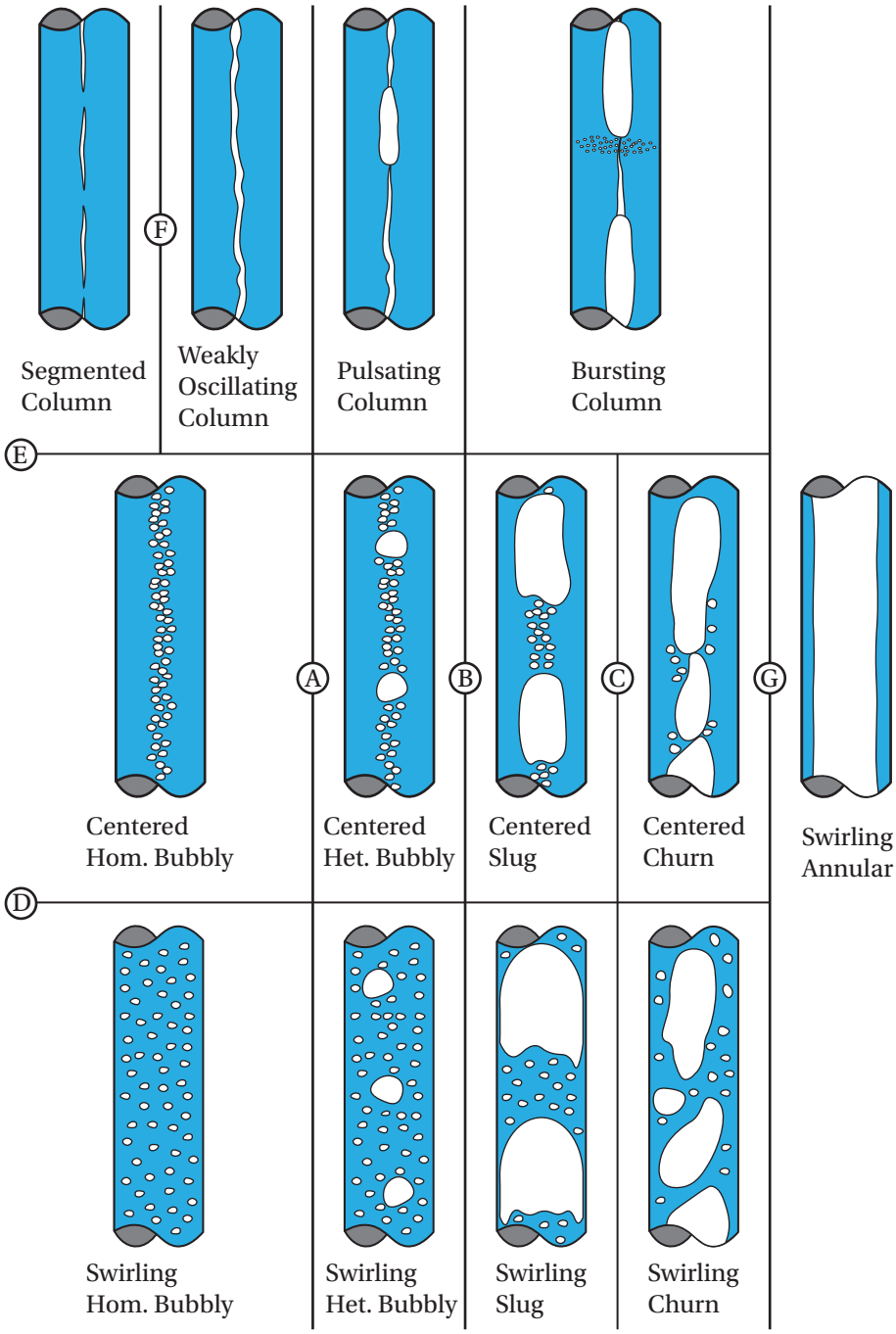

Figure 3.19: Summary of the vertical upward swirling gas-liquid pipe-flow pattern transitions and their labels in the flow pattern maps of section 3.7.

3.7.1. EXPERIMENTAL DATA OF PART I

In this subsection, the mechanistic flow pattern transitions proposed in part II are compared to the experimental flow patterns obtained in part I (i) upstream of the swirl element (non-swirling flow), (ii) at $x = 2D$ downstream of the swirl element, and (iii) at $x = 14D$ downstream of the swirl element.

The region upstream of the swirl element is included in the analysis since the upstream flow patterns determines multiple flow pattern transitions inside the Non-Columnar, Centered and Columnar regimes downstream of the swirl element. For instance, Swirling Bubbly flows, Centered Bubbly flows and Weakly Oscillating Columns are formed downstream of the swirl element for upstream Bubbly flows. Therefore, the accuracy of the swirling gas-liquid flow pattern maps obtained by the mechanistic models proposed in the current chapter is determined to a great extent by the quality of the upstream flow pattern prediction by curves A, B and C.

The liquid swirl number at $x = 2D$ and at $x = 14D$ downstream of all four swirl elements used in the experiments of part I is estimated via Equation 3.17, and summarized in Table 3.3. Table 3.3 shows a substantial decay of the liquid swirl number for relatively short distances downstream of the swirl element ($x = 2D$).

Table 3.3: Liquid swirl number at $x = 2D$ and $x = 14D$ for the four swirl elements used in this research.

Swirl Element	1	2	3	4
$\Omega_l(x=0) = \Omega_{se}$	1.57	2.28	3.51	5.77
$\Omega_l(x=2D)$	1.36	1.88	2.65	3.78
$\Omega_l(x=14D)$	0.71	0.87	1.03	1.19

UPSTREAM FLOW

As expected, the same experimental (non-swirling) gas-liquid flow pattern map was obtained upstream of all four swirl elements.

The upstream flow pattern map obtained in the current research is presented in Figure 3.20. Figure 3.20 shows that Heterogeneous Bubbly flows were observed in the experimental facility to the left of curve A, indicating that large bubbles appear in the upstream flow for gas fractions below 0.12. Similarly, Slug flows were observed in the experiments for superficial gas velocities to the left side of curve B, and gas fractions below 0.25. The transition to Churn flow, either from Slug (curve C) or from Heterogeneous Bubbly (curve B), is well-predicted by the model.

It is worth mentioning that, although the upstream flow can be seen as a swirling gas-liquid flow with $\Omega_l = \Omega_g = 0$, resulting in the shift of the Centered and Columnar flow pattern transitions to $Fr_l \rightarrow \infty$, the flow patterns observed in the swirling region at $x \rightarrow \infty$ ($\Omega_l \rightarrow 0$) do not match the upstream flow, due to the coalescence promoted by the addition of swirl to the flow. For instance, Weakly Oscillating Columns are formed downstream of the swirl element for upstream Homogeneous Bubbly flows, but break into large bubbles/Heterogeneous Bubbly flows when the swirl intensity becomes to weak to maintain a

stable gas column in the system, as observed in the experiments of part I and [119, 134]. In this context, the addition of swirl to the flow can be seen as an irreversible process, where the flow departs from Homogeneous Bubbly upstream of the swirl element for $\Omega_l = 0$, it is transformed into Weakly Oscillating Column downstream of the swirl element for $\Omega_l > 0$, and it is transformed into Heterogeneous Bubbly or Slug flows in the limit $\Omega_l \to 0$. The flow will only return to Homogeneous Bubbly, making the addition of swirl to the flow a reversible process, if the liquid turbulence is sufficient to break the larger bubbles of the flow into smaller components, creating a homogeneous bubble size distribution. However, this only occurs for sufficiently high liquid velocities [106, 135].

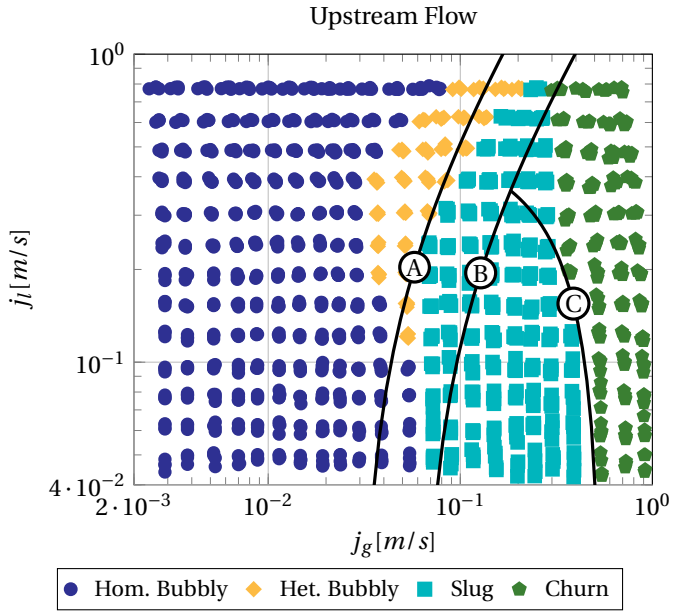

Figure 3.20: Comparison between the upward (non-swirling) gas-liquid flow patterns upstream of the swirl element visually-identified in the part I of the current chapter, and the vertical upward swirling gas-liquid pipe-flow pattern transition criteria for $\Omega_l = 0$. The curves B and C used in this research were adapted from the non-swirling gas-liquid flow pattern models of Taitel *et al.* [106].

TWO DIAMETERS DOWNSTREAM OF THE SWIRL ELEMENT

The flow pattern transition models proposed in the current chapter are compared to the experimental flow pattern maps obtained at $x = 2D$ downstream of the swirl element in Figure 3.21.

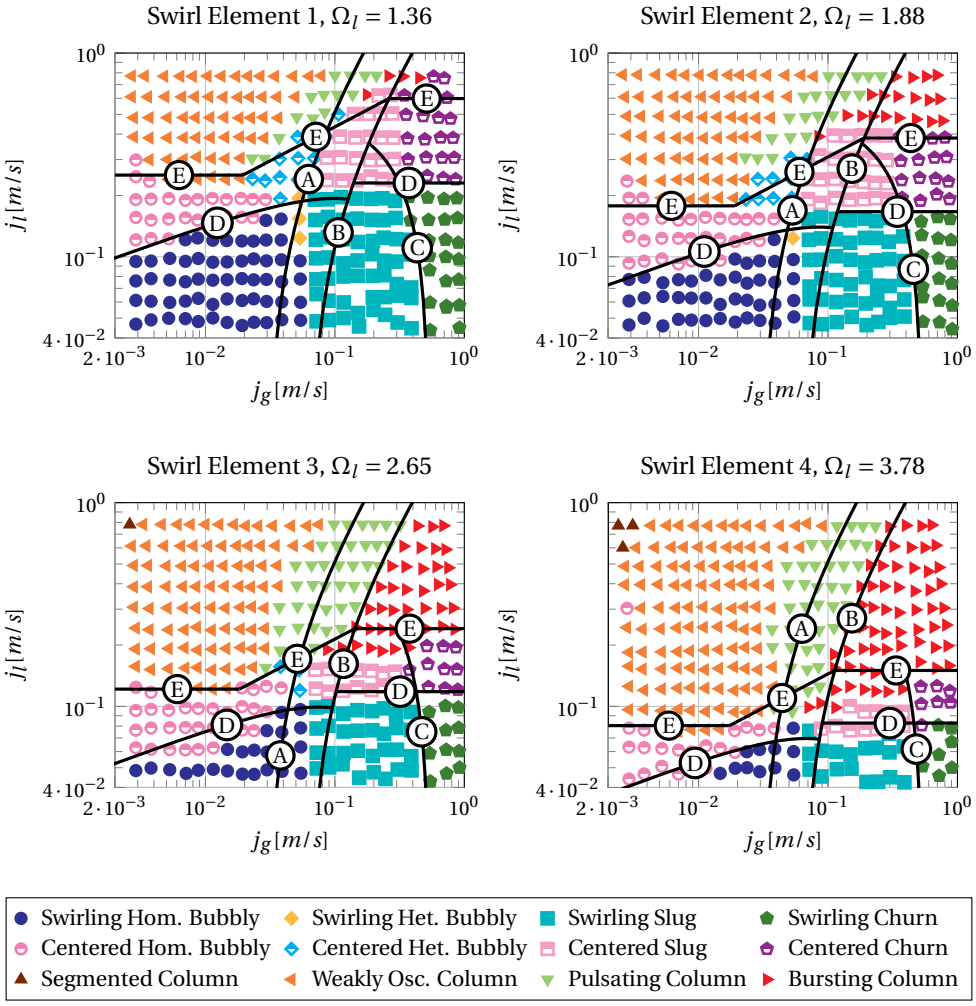

Figure 3.21: Comparison between the upward swirling gas-liquid flow patterns observed at $x = 2D$ downstream of the swirl element (marks) and the mechanistic flow pattern transitions proposed in the current chapter (continuous lines).

Figure 3.21 shows that Swirling Heterogeneous Bubbly flows were not observed during the experiments for $j_l < 0.1\ \mathrm{m\,s^{-1}}$, not appearing in the experimental flow pattern maps obtained for Swirl Elements 3 and 4. For Swirl Elements 1 and 2 and relatively low superficial liquid velocities, the Homogeneous Bubbly-Heterogeneous Bubbly flow transition is well captured by curve A. However, the good capture of the few Heterogeneous Bubbly flow points by the model is a coincidence, since upstream Heterogeneous Bubbly flows were also captured by curve A for these superficial liquid velocities in Figure 3.20.

The absence of Heterogeneous Bubbly flows in the majority of the Non-Columnar flow region (small j_l) results in the direct transition from Swirling Homogeneous Bubbly flow to Swirling Slug flow, observed to the left side of curve B in Figure 3.21 and matching the upstream flow transition (Figure 3.20). A great match between curve C and the experimental Swirling Slug-Swirling Churn flow transition was obtained for all Swirl Elements investigated.

Figure 3.21 shows that the formation of Centered flows at $x = 2D$ with the increase in the superficial liquid velocities is well predicted by curve D. Inside Centered flows, Centered Heterogeneous Bubbly flows were observed for superficial gas velocities significantly lower than predicted by curve A, and Centered Slug flows were observed in the visualization window for superficial gas velocities significantly lower than predicted by curve B, which is directly related to the relatively poor match between curves A and B and the Heterogeneous Bubbly and Slug flow pattern transitions upstream of the swirl element, respectively. The transition to Centered Churn flow, described by curve C for low superficial liquid velocities and by curve B for high superficial liquid velocities, is well predicted by the model, which is directly related to the good prediction of the upstream Churn flow pattern transition.

The transition to Columnar flows is well predicted by curve E for all four swirl elements. Inside Columnar flows, Pulsating Columns are observed for superficial gas velocities to the left side of curve A, which is also associated with the poor prediction of the upstream flow pattern transition to Heterogeneous Bubbly flow by curve A in Figure 3.20. Bursting columns are relatively well predicted by Curve B, despite its mismatch with the upstream Slug flow transition, indicating that the swirl is able to transform Slug flows with small Taylor bubbles into Pulsating Columns. The Taylor bubbles grow with the increase in j_g, eventually leading to the Bursting flow pattern transition.

Segmented Columns are only observed in Figure 3.21 for a few points measured for Swirl Elements 3 and 4, being predicted by the model for superficial gas velocities below $2{\cdot}10^{-3}\ \mathrm{m\,s^{-1}}$ due to the relatively small amplitude of the interface waves at $x = 2D$. Swirling Annular flows are predicted by the model for superficial gas velocities above $1\ \mathrm{m\,s^{-1}}$, thus also not appearing in Figure 3.21.

FOURTEEN DIAMETERS DOWNSTREAM OF THE SWIRL ELEMENT

The flow pattern transition models are compared to the experimental flow pattern maps obtained at $x = 14D$ downstream of the swirl element in Figure 3.22.

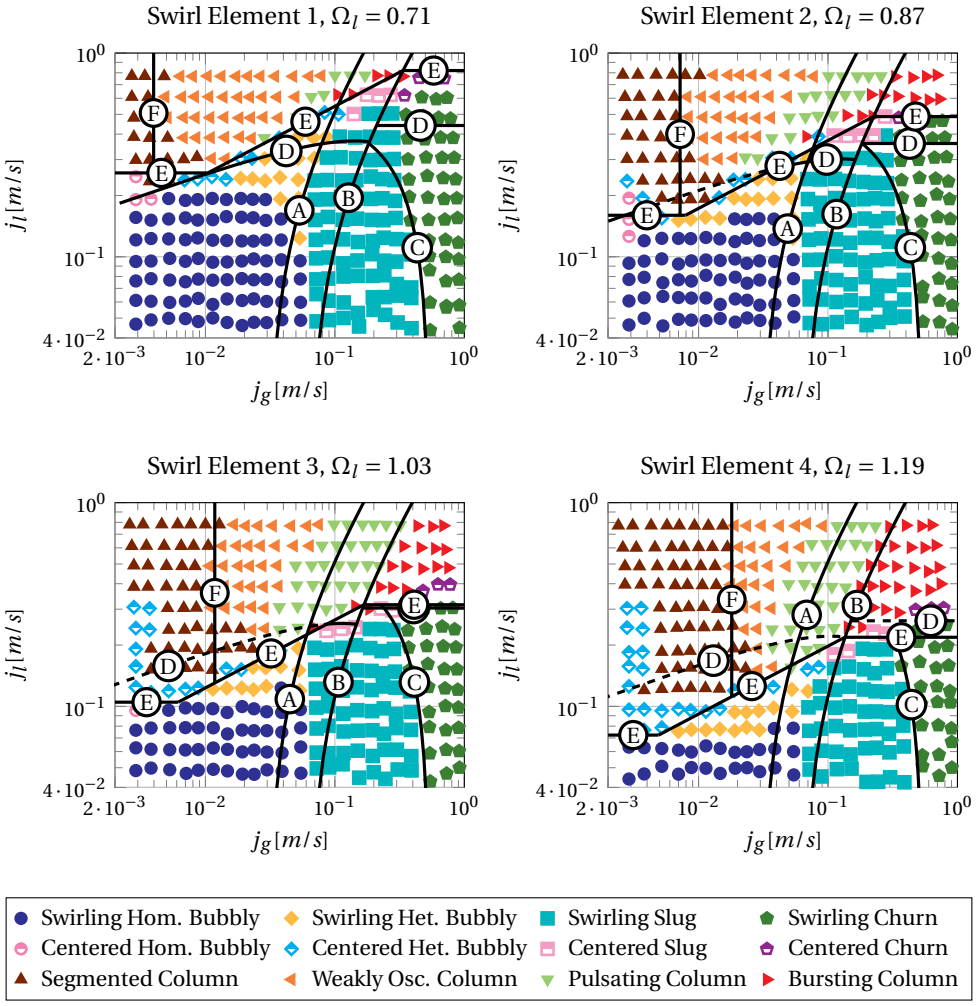

Figure 3.22: Comparison between the upward swirling gas-liquid flow patterns observed at $x = 14D$ downstream of the swirl element (marks) and the mechanistic flow pattern transitions proposed in this chapter (continuous lines).

When compared to the flow pattern maps obtained at $x = 2D$, Figure 3.22 shows that the decay of the liquid swirl shifts the curves D and E towards higher superficial liquid velocities for a fixed swirl element.

For low superficial liquid velocities, the liquid swirl decay also leads to an increase in the region of Heterogeneous Bubbly flow in relation to the Upstream and $x = 2D$ maps. This occurs since Weakly Oscillating Columns formed right downstream of the swirl element become unstable and break into non-uniform fragments as Ω_l decays in the axial direction. The column fragments are redistributed in the pipe cross-section if the centripetal force is not sufficient for their maintenance in the central region of the pipe, i.e., for superficial liquid velocities below Curve D, ultimately leading to Swirling Heterogeneous Bubbly flows at $x = 14D$. Since Swirling Heterogeneous Bubbly flows are formed in this context for Upstream Homogeneous Bubbly flows, Swirling Heterogeneous Bubbly flows are observed in Figure 3.22 for superficial gas velocities substantially lower than predicted by curve A.

Centered flows were not commonly observed at $x = 14D$, occurring mainly due to the decay of Columnar flows near the visualization window and acting as a thin transition region between Columnar and Non-Columnar regimes. In addition, Centered Heterogeneous Bubbly flows were observed above curve E for very low superficial gas velocities and Swirl Elements 3 and 4, due to the segmentation of the gas column into small pieces that resemble Centered Heterogeneous Bubbly flows.

The impact of swirl decay on the Weakly Oscillating Column interface friction factor causes a reduction in the area between curves D and E from $x = 2D$ to $x = 14D$, ultimately resulting in the inversion of the curves for Swirl Elements 3 and 4. As described in subsection 3.6.3, the centripetal acceleration is sufficient maintain stable columns in the flow in this scenario, but insufficient to maintain bubble agglomeration, resulting in direct transition between Columnar and Non-Columnar flows.

The transition to Columnar flow (Segmented, Weakly Oscillating, Pulsating and Bursting Columns) is well predicted at $x = 14D$ by curve E for all four swirl elements investigated. In the Columnar regimes, the transition from Weakly Oscillating Column to Segmented Column is well predicted by Curve F for all flow pattern maps of Figure 3.22. The segmentation of the gas column is particularly relevant far from the swirl element, due to the increase in the amplitude of the interface waves. The transition from Weakly Oscillating Column to Pulsating Column at $x = 14D$ is similar to $x = 2D$, occurring to the left of Curve A and following the upstream flow pattern transition to Heterogeneous Bubbly. As in the flow pattern maps obtained at $x = 2D$, (i) the transition between Pulsating and Bursting Column at $x = 14D$ is well predicted by curve B, and (ii) Swirling Annular flows are absent due to relatively low superficial gas velocities.

3.7.2. LITERATURE DATA

The data of Liu and Bai [112] for air-water swirl flow in a pipe diameter $D = 30$ mm and $l_{up} = 5$ m between the formation of the gas-liquid mixture and the swirl element is used to evaluate the accuracy of the mechanistic flow pattern transitions proposed in the current chapter for smaller pipe diameters. The swirl element of Liu and Bai [112] has an external radius $R_{se} = 15$ mm, a body radius of $R_b = 5$ mm and four helical vanes of pitch

$\ell_{se} = 60$ mm, resulting in the Geometrical Swirl Number $\Omega_{se} \approx 0.98$ based on Equation 2.5 of chapter 2.

The flow patterns observed by the authors in a visualization window of length 200 mm, starting at the outlet of the swirl element, are presented together with the transition curves proposed in the current chapter in Figure 3.23. Taking the center of the visualization window $x = 100$ mm as the axial position of the flow pattern map, Equation 3.17 leads to the liquid swirl number $\Omega_l = 0.83$ for the prediction of the Centered and Columnar flow pattern transitions, and Equation 3.19 leads to the gas swirl number $\Omega_g = 0.81$ for the prediction of the Swirling Annular flow pattern transition.

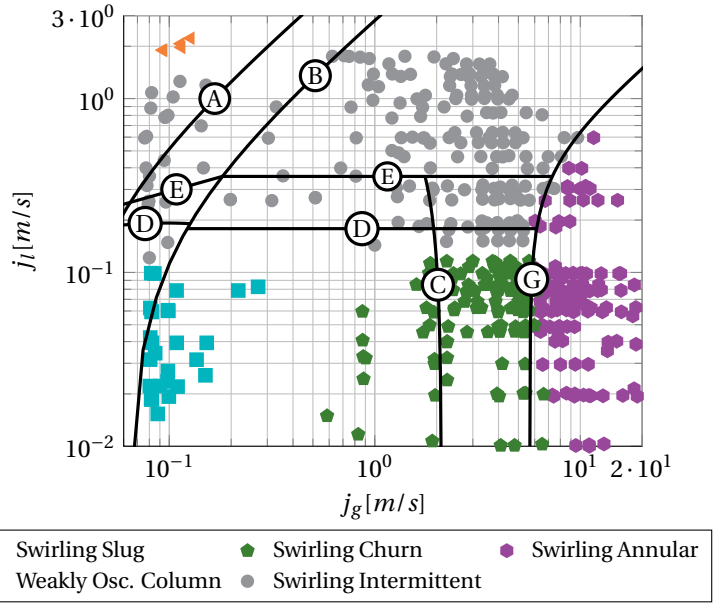

Figure 3.23: Comparison between the proposed models and the experimental flow pattern map of Liu and Bai [112]. Weakly Oscillating Columns were named "Swirling Gas Column" in their paper, and no distinction was made between the Centered Slug, Centered Churn, Pulsating Column and Bursting Column regimes, which were all categorized as "Swirling Intermittent". Curves obtained for $\Omega_l = 0.83$, $\Omega_g = 0.81$ and $C_f = 0.010 + 0.090\Omega_l^{3.4}$ (Equation 3.53 for $x = 14D$).

Swirling Bubbly flows were not covered in the experiments of Liu and Bai [112]. It is hard to evaluate the quality of curves A, B and C in the prediction of the Non-Columnar flow patterns in Figure 3.23, since (i) Bubbly flows were not reported by the authors, making it impossible to evaluate A and B in the region, and (ii) there is a low density of points around curve C.

Centered Slug/Churn flows and Pulsating/Bursting Columns were not distinguished by Liu and Bai [112], that classified these patterns together as "Swirling Intermittent". Based on the description and images provided by the authors, the transition to "Swirling Intermittent" flow is equivalent to the transition to Centered flows of this text, being well captured by Curve D. Since Centered flows were not distinguished by Liu and Bai [112], the flow pattern transitions inside Centered flows cannot be evaluated.

The quality of curve E, representing the transition to Columnar flow, also cannot be directly assessed from Figure 3.23. From the images and description provided by the authors, Bursting Columns are expected for superficial liquid velocities between 0.32 $\mathrm{m\,s^{-1}}$ and 1.08 $\mathrm{m\,s^{-1}}$, matching the mechanistic model prediction using the interface friction factor correlations obtained either at $x = 2D$ or $x = 14D$ in the current research (Equation 3.53). More information about the transition to Columnar flow is obtained from Liu *et al.* [113], that used the same setup of Liu and Bai [112]. The flow images and description provided by Liu *et al.* [113] points to Bursting Columns formed for $j_l > 0.40\ \mathrm{m\,s^{-1}}$, matching Curve E obtained with the friction factor correlation measured at $x = 14D$, as shown in Figure 3.23. As mentioned in section 3.6, the friction factor obtained at $x = 14D$ is recommended in a general context of flow pattern prediction since it accounts for the complete swirl flow physics.

In relation to the Columnar flow patterns, the transition between Weakly Oscillating Column and "Swirling Intermittent" occurs to the left side of Curve A, similarly to the Weakly Oscillating-Pulsating Column transition observed in the flow pattern maps of this research (Figures 3.21 and 3.22). The ability of Curve A to predict this flow pattern transition depends on how well it predicts the formation of large bubbles in the upstream flow, and can be improved in future works. The performance of Curve B in the prediction of the Pulsating-Bursting flow pattern transition cannot be evaluated in Figure 3.23, since these flow patterns were not distinguished by Liu and Bai [112]. Segmented Columns were not observed by the authors.

Curve G shows a good prediction of Swirling Annular flows by the mechanistic model proposed in the current chapter. Overall, a good match between the flow pattern transitions and the experimental data of Liu and Bai [112] was obtained.

3.8. SUMMARY AND CONCLUSION

The objectives of this chapter were to (i) investigate the flow behavior and map the vertical upward swirling gas-liquid pipe-flow patterns for multiple swirl intensities, and (ii) propose mechanistic transition criteria for the flow patterns observed in the experiments and reported in literature.

The Upward Swirling Gas-Liquid Pipe-Flow patterns observed in the experiments of part I can be divided into four classes, containing multiple flow patterns each:

- Non-Columnar flows:
  - Swirling Homogeneous Bubbly
  - Swirling Heterogeneous Bubbly
  - Swirling Slug
  - Swirling Churn
- Centered flows:
  - Centered Homogeneous Bubbly
  - Centered Heterogeneous Bubbly

  - Centered Slug
  - Centered Churn
- Columnar flows
  - Weakly Oscillating Column
  - Pulsating Column
  - Bursting Column
  - Segmented Column
- Swirling Annular

With the exception of Swirling Annular flows, the upward swirling gas-liquid flow patterns are mainly determined by the dimensionless numbers Fr_l, Fr_g, Ω_l and x/D. Among those, the mechanistic models proposed in part II showed that the ratio between the centripetal acceleration of the liquid and gravity, related to the product $Fr_l\Omega_l$ squared, is the main dimensionless number responsible for the transition between Non-Columnar, Centered and Columnar flows. Inside each class, the flow pattern transitions are strongly dependent on the Froude number of the gas, Fr_g.

Centered flows are formed when the centripetal force is able to counter the turbulent dispersion force created by bubbles rising in a small region around the pipe centerline. The dependency of Centered flows on the ratio between the centripetal acceleration and gravity arises from the role of gravity in the rising velocity of the bubbles and, therefore, in the bubble-induced turbulence and radial dispersion force. Centered flows are not typically observed far from the swirl element due to the decay of the swirl.

The transition to Columnar flows occur when Centered flows coalesce into stable gas columns. The stability of the gas column depends on the ratio between the axial gas velocity and the azimuthal liquid velocity, where the axial gas velocity is determined by the balance between the axial interface shear force and the weight of the fluids, leading to the ratio between centripetal acceleration and gravity contained in $Fr_l\Omega_l$.

The transitions inside Non-Columnar, Centered and Columnar flows are determined by the flow pattern transitions upstream of the generation of swirl, being modeled by the (non-swirling) transition criteria of Taitel *et al.* [106], with an additional criterion proposed in the current chapter for the transition between Homogeneous and Heterogeneous Bubbly flows. The transition to Swirling Annular flow is determined by the gas, similarly to its non-swirling counterpart.

The research performed also showed a clear dependency of the swirling flow pattern transitions on the axial position, even when accounting for swirl decay on Ω_l. The effect was associated with the development of a backflow in the liquid as the flow distances from the swirl element, that must be confirmed in future works. The potential liquid backflow next to the gas-liquid interface increases the amplitude of the interface waves and friction factor of Weakly Oscillating Columns, impacting the Segmented and Columnar flow pattern transitions.

The proposed transition models were validated against the experimental data acquired in part I and published by Liu and Bai [112]. The results of section 3.7 show a good match

between the experimental flow pattern maps and the model predictions for both datasets, specially when considering that the flow pattern transitions are gradual. The largest deviation between the proposed models and the experimental data available occurred in the prediction of the non-swirling gas-liquid flows upstream of the swirl element, impacting the flow pattern transitions inside Centered and Columnar flows.

The mechanistic swirling gas-liquid flow pattern transitions proposed in the current chapter are expected to work for weakly-viscous fluids (e.g., water), $\rho_g/\rho_l \ll 1$, pipe diameters in the order of centimeters and swirl numbers in the order of 1. Additional effects and dimensionless numbers neglected in the proposed models can affect the swirling gas-liquid flow patterns outside this range of conditions. For instance, the liquid viscosity/Re_l can be a relevant parameter if working with highly-viscous fluids or small pipe diameters. Moreover, surface tension/Eo is a relevant parameter for pipe diameters in the order of millimeters, due to the dominance of capillary forces over gravitational forces [104].

The observed flow patterns and proposed transition criteria are valid for systems in which swirl is added to a previously existing gas-liquid flow by an insert in the pipe (e.g., the swirl element of axial cyclones). In these systems, the flow patterns upstream of the generation of swirl have a direct impact on the swirling flow patterns (e.g., in the pulsating or burst regimes), and the upward swirling gas-liquid flow patterns are determined by the swirl impact on the upstream flow. Different flow regimes and transition mechanisms may occur for other strategies of generation of swirl, for instance if the swirling gas-liquid mixture is created via tangential gas and liquid inlets, as in Shakutsui *et al.* [110, 111], or if gas is injected in a swirling liquid, e.g., by shifting the gas inlet to downstream of the swirl element. The detailed investigation of the flow regimes and transition criteria in these systems remains an open topic for further research.

CHAPTER 4

GAS CORE DIAMETER, PRESSURE DROP RATIO AND AXIAL CYCLONE PERFORMANCE

4.1. INTRODUCTION

Figure 4.1 illustrates a gas-liquid axial cyclone separator where the phase distribution upstream of the pickup tube is measured by Electrical Resistance Tomography (ERT).

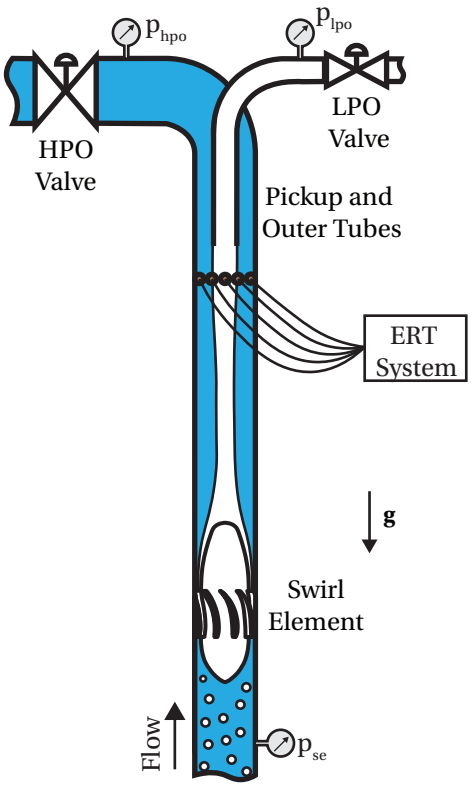

Figure 4.1: Gas-liquid axial cyclone with phase distribution upstream of the pickup tube measured by an Electric Resistance Tomography (ERT) sensor.

Axial cyclone separators work by imposing a rotation to the mixture as it crosses the swirl element. Inside the axial cyclone, the centripetal force pushes the lighter phase (gas) to the center of the equipment, where it coalesces into a continuous (gas) core. The separation is obtained capturing the central region of the flow with the pickup tube and the surrounding region with the outer tube. A perfect separation of the mixture is obtained if the lighter phase (gas core) is completely captured by the pickup tube, and the heavier phase (liquid annulus) is completely captured by the outer tube. As illustrated in Figure 4.1, a perfect phase separation is obtained in gas-liquid axial cyclones for gas cores perfectly centered in the pipe and with the same diameter as the pickup tube.

The efficiency of cyclone separators is typically evaluated based on the concentration [17, 50, 59] and/or flow rates in the outlets of the separator [11, 14]. The cyclone performance indicators investigated in this chapter are:

i. The fraction of the total gas mass flow rate which is captured by the pickup tube,

$$\xi_g \triangleq \frac{w_{g,lpo}}{w_g} \tag{4.1}$$

In Equation 4.1, $w_{g,lpo}$ is the gas mass flow rate in the Light Phase Outlet of the cyclone (LPO), connected to the pickup tube, and w_g is the gas mass flow rate in the cyclone inlet. By definition, $\xi_g = 1$ if all the gas entering in the cyclone is captured by the pickup tube, and $\xi_g = 0$ if the entire gas flow is captured by the outer tube.

ii. The fraction of the total liquid flow which is captured by the outer tube,

$$\xi_l \triangleq \frac{w_{l,hpo}}{w_l} \tag{4.2}$$

In Equation 4.2, $w_{l,hpo}$ is the liquid mass flow rate in the Heavy Phase Outlet of the cyclone (HPO), connected to the outer tube, and w_l is the liquid mass flow rate in the inlet of the cyclone. Since liquids are incompressible, ξ_l can be written based on the liquid volume flow rates as $\xi_l = q_{l,hpo}/q_l$, where $q_{l,hpo}$ and q_l are the HPO and inlet liquid volume flow rates, respectively. By definition, $\xi_l = 1$ if all the liquid entering the axial cyclone is captured by the outer tube, and $\xi_l = 0$ if the entire liquid flow is captured by the pickup tube.

iii. The overall efficiency of separation, introduced in the current thesis to summarize both the capture of gas by the pickup tube and liquid by the outer tube into a single variable. The overall efficiency of separation is defined as

$$\eta \triangleq \sqrt{\xi_g \cdot \xi_l}, \tag{4.3}$$

ensuring that (i) $\eta = 1$ if, and only if, all the gas is captured by the pickup tube and all the liquid is captured by the outer tube, and (ii) $\eta = 0$ if the whole mixture is captured by the pickup tube ($\xi_l = 0$) or by the outer tube ($\xi_g = 0$), indicating that no separation is being promoted by the axial cyclone. Note that $\eta = 0.5$, and not zero, if the gas and liquid flow rates are equally split between the pickup and outer tubes

($\xi_g = 0.5$ and $\xi_l = 0.5$). However, the condition is unlikely to occur due to the light phase accumulation around the separator centerline, promoting the capture of gas by the pickup tube and liquid by the outer tube.

The choice between ξ_g, ξ_l, η or other concentration-based quantities as performance indicator is strongly process-dependent. For instance, gas-liquid axial cyclones are used to separate liquid from steam in nuclear energy reactors [31–36]. In these processes, obtaining low liquid concentrations in the steam is more important than obtaining low gas concentrations in the liquid and, therefore, maximizing ξ_l has priority over maximizing ξ_g or η. The opposite situation occurs in the oil industry, where de-oiling cyclones are used to clean produced water (water extracted together with oil from the reservoir) to oil concentrations in water below 30 ppm, required for its disposal in the ocean [14, 15, 136, 137]. In this context, ensuring that the vast majority of the oil flow in the inlet of the cyclone is captured by the pickup tube, resulting in a clean water flow in the outer tube, is far more important than minimizing the amount of water that is captured together with the oil by the pickup tube. As consequence, the performance of de-oiling processes is mainly determined by "ξ_g" (based on the inlet and LPO oil flow rates instead of gas flow rates). If both phases are equally important to the process, e.g., in metrology loops [41–43] or bulk separation, quantities such as the overall efficiency of separation η can be used as performance indicator.

It is not easy to obtain reliable two-phase flow rate or concentration measurements in the inlet and/or outlets of the cyclone for the instantaneous evaluation of the cyclone performance [14, 17, 138]. Therefore, the real-time control of industrial cyclone separators is traditionally performed with variables that can be measured in real-time, but which are indirectly related to the efficiency of the process, such as pressure [27, 60, 61].

Among the pressure-based quantities is the Pressure Drop Ratio (PDR), commonly used in the real-time control of de-oiling tangential cyclones [14, 15, 50, 57–59] but not yet investigated for axial cyclones. The Pressure Drop Ratio is related to the flow split between the light and heavy phase outlets, being defined as the pressure difference between the cyclone inlet and the LPO, divided by the pressure difference between the inlet and the HPO. It can be written for axial cyclones as

$$\mathrm{PDR} \triangleq \frac{p_{se} - p_{lpo}}{p_{se} - p_{hpo}}, \tag{4.4}$$

where p_{se}, p_{lpo} and p_{hpo} are the pressures upstream of the swirl element, upstream of the LPO valve and upstream of the HPO valve, respectively.

Pressure-based quantities, such as the PDR, are impacted by the gas and liquid flow rates in the cyclone inlet and outlets. Therefore, it is expected that the conditions of maximum cyclone performance cannot be represented by a single PDR for multiple gas and liquid flow rates, resulting in the impact of process disturbances in the inlet conditions of the cyclone on the separator performance, despite the real-time control of the PDR. On the other hand, in principle, gas core diameters equal to the pickup tube diameter result in a perfect phase separation independent of the remaining flow variables in the axial cyclone, making it a direct representative of the cyclone performance and an ideal candidate for real-time control. The gas core diameter upstream of the pickup tube can be measured

with Electrical Resistance Tomography (chapter 2), and the tomography-based real-time control of axial cyclone separators is investigated, for the first time, in chapter 5.

A complication to the pressure-based or tomography-based real-time control of axial cyclone separators is the strong pressure and phase distribution fluctuations of some swirling gas-liquid flow patterns, such as Bursting Columns (chapter 3), significantly impacting the capture of gas by the pickup tube and liquid by the outer tube. The flow pattern fluctuations are much faster than typical control valves (chapter 5), limiting the real-time control of the separation with valves in the LPO and/or HPO to the suppression of slow process disturbances in the gas and liquid flow rates in the inlet of the equipment.

In the limit of quasi-steady process disturbances, the axial cyclone performance with slow real-time controllers (i.e., controllers which do not target the flow pattern fluctuations in the pressure or phase distribution) tends to the separator response at constant time-average PDRs (for pressure-based control) or constant time-average gas core diameters (for phase distribution-based control). The objective of this chapter is to investigate the relation between cyclone performance and time-average gas core diameter upstream of the pickup tube, in order to evaluate if the gas core diameter, measured by tomography and filtered to remove the flow pattern fluctuations, can be used to control the efficiency of axial cyclone separators. Since PDR-based control was not yet investigated for axial cyclones, the relation between cyclone performance and time-average PDR is also investigated in the current chapter. The experiments performed are described in section 4.2, the results obtained are discussed in section 4.3, and the study conclusions are presented in section 4.4.

4.2. METHODS

A vertical gas-liquid axial cyclone similar to Figure 4.1 is used in the experiments. The cyclone has inner diameter $D = 81.4$ mm and its pickup tube has inner diameter $0.44D$ and outer diameter $0.49D$. The pressure p_{se} is measured $2.1D$ upstream of the swirl element and the Light Phase Outlet and Heavy Phase Outlet pressures, p_{lpo} and p_{hpo}, are measured directly upstream of the LPO and HPO control valves, respectively. The experimental facility and its components are detailed in chapter 2. The experiments of this chapter were performed with Swirl Element 3 (section 2.3).

A preliminary investigation of the gas-liquid flow in the axial cyclone was performed to select the conditions covered in the experiments. The investigation aimed for:

i. Gas cores that can be measured by Electrical Resistance Tomography. As detailed in chapter 2, ERT is insensitive to gas cores smaller than about 10% of the pipe inner diameter. Gas cores sufficiently wide for ERT are only obtained upstream of the pickup tube for Bursting Columns, characterized by strong flow pattern fluctuations with small time-constants that cannot be suppressed with control valves.

ii. A significant impact of the LPO valve on the average gas core diameter upstream of the pickup tube, which is related to the liquid flow rate across the axial cyclone and HPO valve opening. A high sensitivity of the gas core diameter to the LPO valve opening is crucial for the analysis performed in the current chapter, and to the use

of the LPO valve as actuator in the tomography-based real-time control of the separation in chapter 5.

The inlet liquid flow rate of the axial cyclone is imposed by a centrifugal pump and the inlet gas mass flow rate is imposed by a mass flow controller. The pump is maintained at constant pump shaft speeds during the experiments, resulting in changes in the liquid flow rate upstream of the cyclone when the LPO valve opening or inlet gas mass flow rate are modified, due to changes in the flow loop pressure (section 2.6). The liquid flow rate is not compensated during the experiments of the current chapter to mimic the tomography-based real-time control conditions of chapter 5, where the liquid flow rate is not controlled. The reader is referred to Cox [139] for experiments made in the same axial cyclone of this dissertation adjusting the liquid flow rate.

Two sets of conditions were selected for the experiments based on the preliminary investigation:

- A pump shaft speed $\omega_p = 2430$ rpm, a normalized HPO valve diaphragm position[1] $x_{hpo} \approx 0.74$, and the gas mass flow rates $w_g = 7.37\ \mathrm{kgh^{-1}}$, $w_g = 8.53\ \mathrm{kgh^{-1}}$ and $9.70\ \mathrm{kgh^{-1}}$.
- A pump shaft speed $\omega_p = 2700$ rpm, a normalized HPO valve diaphragm position $x_{hpo} \approx 0.80$, and the gas mass flow rates $w_g = 6.21\ \mathrm{kgh^{-1}}$, $w_g = 8.53\ \mathrm{kgh^{-1}}$ and $w_g = 10.86\ \mathrm{kgh^{-1}}$.

The experiments are performed varying the normalized diaphragm position of the LPO valve x_{lpo} in steps of around 0.05 for each set of conditions, and recording the resulting flow variables for 100 s. The gas core diameter in the cross-section $0.9D$ upstream of the pickup tube is measured normalized by the inner diameter of the pipe at a frequency of 10 Hz by Electrical Resistance Tomography, using the image reconstruction algorithm proposed in chapter 2. The pressures in the inlet and outlets of the cyclone are also recorded at 10 Hz, being averaged over a 100 s interval for the computation of the time-average Pressure Drop Ratio. The time-average LPO and HPO gas and liquid flow rates, used in the computation of ξ_g, ξ_l and η via Equations 4.1-4.3, are obtained from the gas and liquid flow rates individually measured in the outlets of gravity separators connected to the LPO and HPO using the equations described in Appendix B.

4.3. RESULTS AND DISCUSSION

The experimental results are presented in three subsections. First, the variations in the measured flow variables (e.g., time-average normalized gas core diameter, time-average PDR, ξ_g, ξ_l and η) obtained when changing the LPO valve opening during the experiments are described in subsection 4.3.1. Then, the relation between axial cyclone performance and time-average gas core diameter upstream of the pickup tube is investigated in subsection 4.3.2, and the relation between performance and time-average PDR is analyzed in subsection 4.3.3.

[1] The diaphragm position of the LPO and HPO valves are presented normalized by their maximum ranges in this dissertation, where $x_{lpo} = 0$ and $x_{hpo} = 0$ are obtained for the valves fully open, and $x_{lpo} = 1$ and $x_{hpo} = 1$ are obtained for the valves fully closed.

4.3.1. AVERAGE FLOW RESPONSE TO THE LPO VALVE

The flow resistance in the Light Phase Outlet increases when closing the LPO valve (increasing x_{lpo}), increasing the time-average pressure upstream of the LPO valve $\overline{p}_{lpo}$, as shown in Figure 4.2.

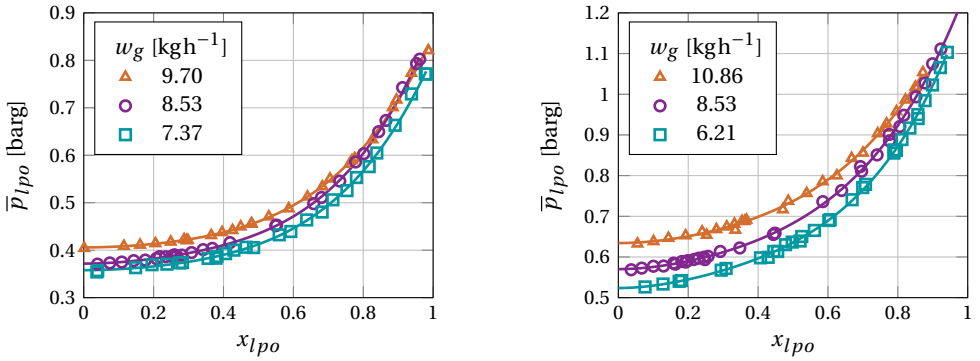

Figure 4.2: Time-average pressure between the pickup tube and the LPO valve ($\overline{p}_{lpo}$) as function of the normalized LPO valve diaphragm position (x_{lpo}) and gas mass flow rate (w_g). Left image: experimental data for a pump shaft speed $\omega_p = 2430$ rpm and normalized HPO valve diaphragm position $x_{hpo} \approx 0.74$. Right image: $\omega_p = 2700$ rpm and $x_{hpo} \approx 0.80$.

The increase in the time-average LPO pressure with the increase in the LPO valve diaphragm position propagates to the tip of the pickup tube, forcing a larger fraction of the flow towards the outer tube. Due to the annular structure of the gas-liquid flow in the axial cyclone, the deviation of the flow towards the outer tube results in a substantial increase in the fraction of the total liquid flow captured by the outer tube, ξ_l, as shown in Figure 4.3.

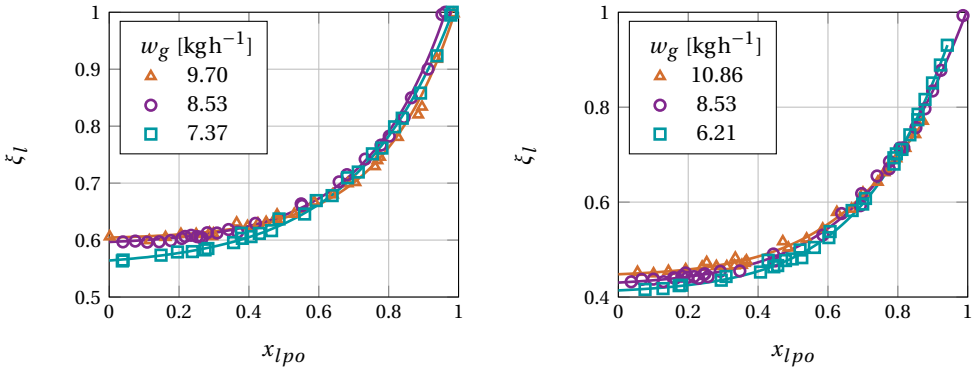

Figure 4.3: Fraction of the total liquid flow captured by the outer tube (ξ_l) as function of the normalized LPO valve diaphragm position (x_{lpo}) and gas mass flow rate (w_g). Left image: experimental data for a pump shaft speed $\omega_p = 2430$ rpm and normalized HPO valve diaphragm position $x_{hpo} \approx 0.74$. Right image: $\omega_p = 2700$ rpm and $x_{hpo} \approx 0.80$.

The HPO valve diaphragm is maintained at a fixed position while closing the LPO valve, resulting in a constant HPO flow resistance. However, despite the fixed resistance, the increase in the liquid flow across the Heavy Phase Outlet obtained when reducing the LPO valve opening results in the increase of the HPO pressure together with the LPO pressure, as shown in Figure 4.4.

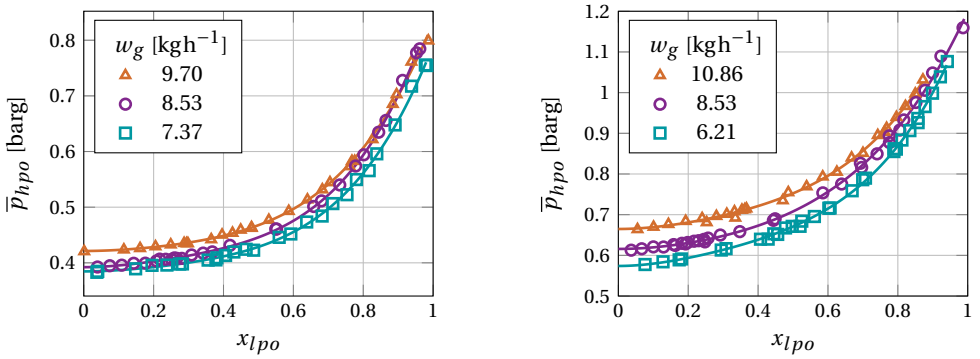

Figure 4.4: Time-average pressure between the outer tube and the HPO valve ($\overline{p}_{hpo}$) as function of the normalized diaphragm position of the LPO valve (x_{lpo}) and gas mass flow rate (w_g). Left image: experimental data for a pump shaft speed $\omega_p = 2430$ rpm and normalized position of the HPO valve diaphragm $x_{hpo} \approx 0.74$. Right image: $\omega_p = 2700$ rpm and $x_{hpo} \approx 0.80$.

The increase of both the LPO and HPO pressures with x_{lpo} results in the increase of the pressure in the whole flow loop with the increase in the LPO valve diaphragm position, including upstream of the swirl element. The different sensitivities of the upstream, LPO and HPO pressures to x_{lpo} determine the relation between the Pressure Drop Ratio and the normalized LPO valve diaphragm position, presented in Figure 4.5.

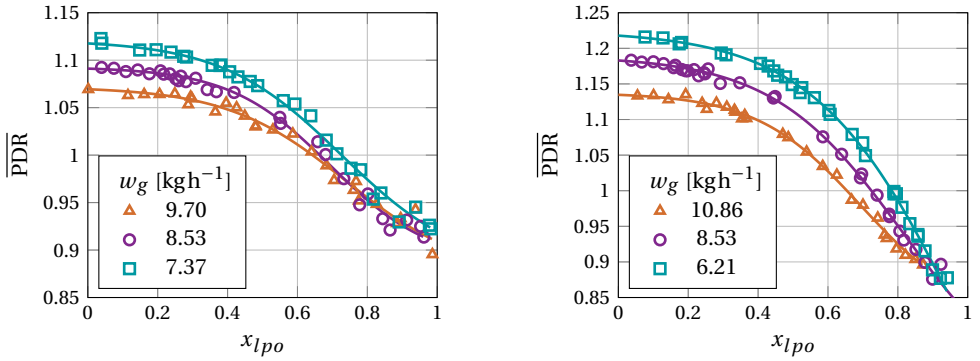

Figure 4.5: Time-average Pressure Drop Ratio ($\overline{\text{PDR}}$) as function of the normalized diaphragm position of the LPO valve (x_{lpo}) and gas mass flow rate (w_g). Left image: pump shaft speed $\omega_p = 2430$ rpm and normalized position of the HPO valve diaphragm $x_{hpo} \approx 0.74$. Right image: $\omega_p = 2700$ rpm and $x_{hpo} \approx 0.80$.

Figure 4.5 shows that the time-average Pressure Drop Ratio decreases when closing the LPO valve. A reduction in the PDR indicates that the pressure difference between the cy-

clone inlet and the Light Phase Outlet reduces relative to the pressure difference between the inlet and the Heavy Phase Outlet. Since the flow tends towards the largest pressure difference, the decrease in the PDR with the increase in x_{lpo} results in a larger fraction of the total flow towards the outer tube, which is directly related to the increase of the total liquid fraction captured by the outlet ξ_l with the increase in x_{lpo} observed in Figure 4.3.

Apart from increasing the fraction of the total liquid flow which is captured by the outer tube, the flow deviation towards the outer tube obtained with the reduction in the time-average Pressure Drop Ratio results in the increase in the time-average gas core diameter upstream of the pickup tube, as shown in Figure 4.6.

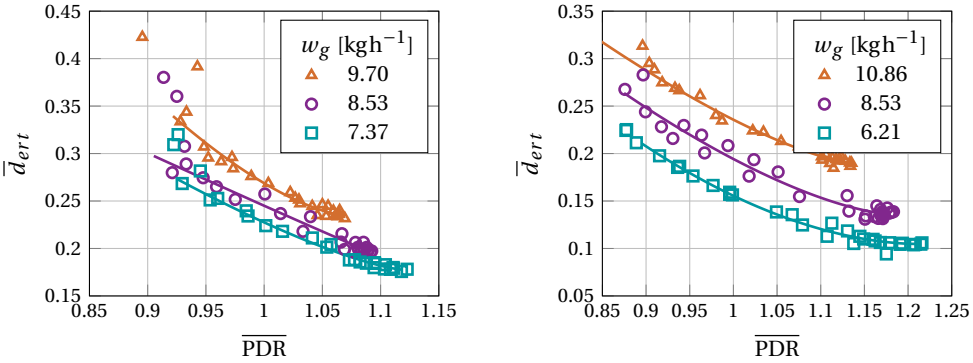

Figure 4.6: Time-average gas core diameter ($\overline{d}_{ert}$) as function of the time-average Pressure Drop Ratio ($\overline{\text{PDR}}$) and gas mass flow rate (w_g). Left image: pump shaft speed $\omega_p = 2430$ rpm and normalized position of the HPO valve diaphragm $x_{hpo} \approx 0.74$. Right image: $\omega_p = 2700$ rpm and $x_{hpo} \approx 0.80$.

Since the time-average gas core diameter increases as the time-average PDR decreases, and $\overline{\text{PDR}}$ decreases when closing the LPO valve, the time-average gas core diameter increases with the increase in x_{lpo}, as shown in Figure 4.7.

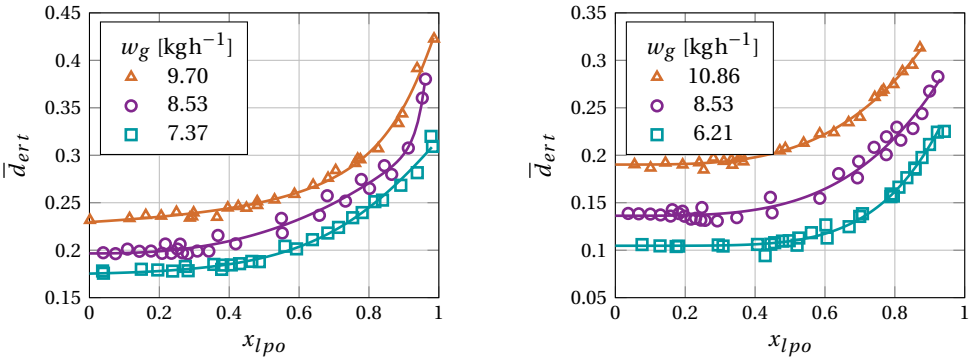

Figure 4.7: Time-average gas core diameter ($\overline{d}_{ert}$) as function of the normalized diaphragm position of the LPO valve (x_{lpo}) and gas mass flow rate (w_g). Left image: pump shaft speed $\omega_p = 2430$ rpm and normalized position of the HPO valve diaphragm $x_{hpo} \approx 0.74$. Right image: $\omega_p = 2700$ rpm and $x_{hpo} \approx 0.80$.

Figure 4.7 shows a weak dependency of the gas core diameter on x_{lpo} when the LPO valve is mostly open, due to a small impact of changes in the LPO valve opening on the LPO flow resistance and time-average PDR (Figure 4.5). The gains of $\overline{d}_{ert}$ and $\overline{\text{PDR}}$ with the opening of the LPO valve increase as the diaphragm position of the LPO valve increases, particularly above $x_{lpo} \approx 0.5$. If large amplitudes in the LPO valve motion are required during the real-time control of the gas core diameter or PDR, a better controller performance is expected if the non-linear impact of the LPO valve on these quantities is taken into account when computing the control actions, e.g., via Hammerstein-Wiener models.

Besides the time-average gas core diameter, the gas core fluctuations in the Bursting Column regime are also impacted by changes in the diaphragm position of the LPO valve, as illustrated by the plots of gas core diameter standard deviation versus x_{lpo} of Figure 4.8.

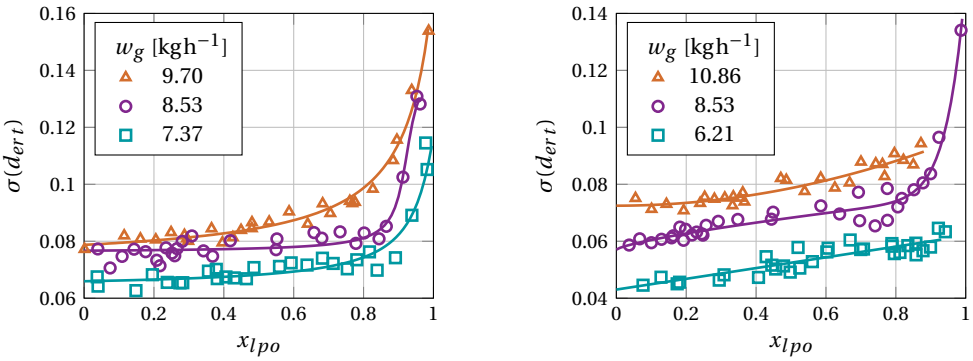

Figure 4.8: Standard deviation of the gas core diameter ($\sigma(d_{ert})$) as function of the normalized diaphragm position of the LPO valve (x_{lpo}) and gas mass flow rate (w_g). Left image: pump shaft speed $\omega_p = 2430$ rpm and normalized position of the HPO valve diaphragm $x_{hpo} \approx 0.74$. Right image: $\omega_p = 2700$ rpm and $x_{hpo} \approx 0.80$.

Figure 4.8 shows that large-amplitude gas core diameter fluctuations occur upstream of the pickup tube in the Bursting Column regime, with gas core diameter standard deviations of 30%-60% the average gas core diameter based on Figure 4.7 for the same conditions. The amplitude of the flow pattern fluctuations depends on the liquid and gas flow rates in the axial cyclone, with larger fluctuations observed upstream of the pickup tube for higher gas mass flow rates. The experimental data presented in Figures 4.7 and 4.8 suggests that the gas core fluctuations upstream of the pickup tube cannot be written as a one-variable function of the local time-average gas core diameter, despite the growth of both quantities with the increase in x_{lpo}. For instance, the time-average gas core diameter for $\omega_p = 2430$ rpm, $w_g = 8.53$ kgh^{-1} and $x_{hpo} \approx 0.74$ (purple curve in the left plots of the current section) increases from $\overline{d}_{ert} \approx 0.21$ for $x_{lpo} = 0.4$ to $\overline{d}_{ert} \approx 0.27$ for $x_{lpo} = 0.8$ (Figure 4.7), while the standard deviation of the gas core diameter remains $\sigma(d_{ert}) \approx 0.08$ in the interval $0.4 \leq x_{lpo} \leq 0.8$ (Figure 4.8).

The time-average gas core diameters presented in Figure 4.7 for the fully open LPO valve ($x_{lpo} = 0$) are significantly smaller than the inner diameter of pickup tube ($0.44D$), resulting in the capture of the vast majority of the gas present in the upstream flow by the pickup tube ($\xi_g \approx 1$) despite the large-amplitude gas core diameter fluctuations of the Bursting Column regime. As shown in Figure 4.9, the fraction of gas captured by the

pickup tube decreases with the increase in x_{lpo}, ultimately leading to no gas captured by the pickup tube ($\xi_g = 0$) when the LPO valve is fully closed ($x_{lpo} = 1$). The decrease in ξ_g with the increase in x_{lpo} is a consequence of the increase in the time-average gas core diameter upstream of the pickup tube with the reduction in the LPO valve opening (increase in x_{lpo}), resulting in the capture of gas by the outer tube during the flow pattern fluctuations for time-average gas core diameters significantly smaller than the inner diameter of the pickup tube.

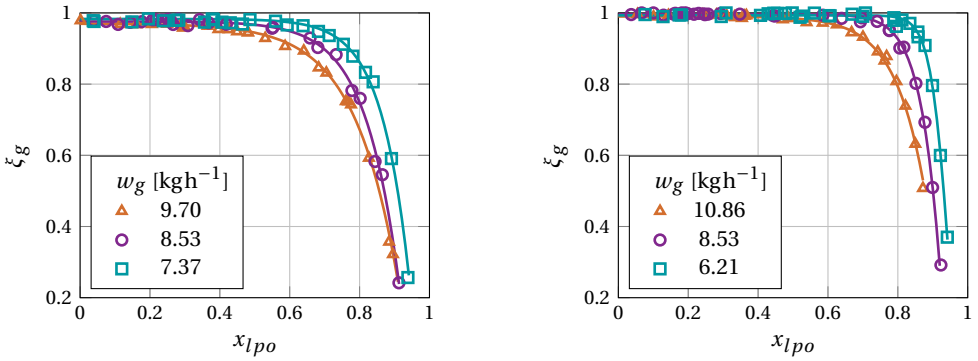

Figure 4.9: Fraction of the total gas mass flow rate captured by the pickup tube (ξ_g) as function of the normalized diaphragm position of the LPO valve (x_{lpo}) and gas mass flow rate (w_g). Left image: experimental data for a pump shaft speed $\omega_p = 2430$ rpm and normalized position of the HPO valve diaphragm $x_{hpo} \approx 0.74$. Right image: $\omega_p = 2700$ rpm and $x_{hpo} \approx 0.80$.

The relation between the overall efficiency of separation η and the LPO valve diaphragm position is presented in Figure 4.10.

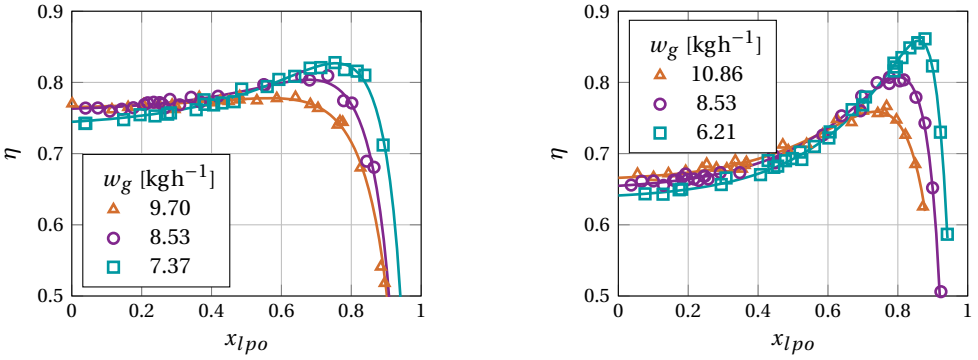

Figure 4.10: Overall efficiency of separation (η) as function of the normalized diaphragm position of the LPO valve (x_{lpo}) and gas mass flow rate (w_g). Left image: pump shaft speed $\omega_p = 2430$ rpm and normalized position of the HPO valve diaphragm $x_{hpo} \approx 0.74$. Right image: $\omega_p = 2700$ rpm and $x_{hpo} \approx 0.80$.

Figure 4.10 shows that the overall efficiency of separation η peaks for the LPO valve significantly but not fully closed for the conditions investigated in the current chapter. The peak in η for such high LPO valve diaphragm positions occurs due to the combined behaviors of ξ_l and ξ_g in relation to the LPO valve opening. Departing from $x_{lpo} = 0$, Figure 4.3 shows that closing the LPO valve always increases the fraction of the total liquid flow that is captured by the outer tube, ξ_l. Meanwhile, Figure 4.9 shows that the fraction of the total gas flow captured by the pickup tube, ξ_g, is not significantly affected by x_{lpo} for $x_{lpo} < 0.5$. As consequence, closing the LPO valve departing from $x_{lpo} = 0$ initially results in an increase in η due to an increase in ξ_l without a significant reduction in ξ_g. However, as the LPO valve becomes almost fully closed, the capture of gas by the pickup tube quickly decreases with the increase in the diaphragm position of the LPO valve, ultimately leading to $\eta = 0$ due to $\xi_g = 0$ for $x_{lpo} = 1$. The peak in η occurs when the increase in ξ_l, obtained closing the LPO valve, no longer compensates the decrease in ξ_g.

4.3.2. GAS CORE DIAMETER AS PERFORMANCE INDICATOR

The axial cyclone performance is determined by the phase distribution upstream of the pickup tube, and a perfect phase separation is expected if an idealized real-time controller is able to maintain a static centered gas core with diameter equal to the pickup tube inner diameter right upstream of the outlet, suppressing flow pattern fluctuations and process disturbances in the local phase distribution. In reality, however, the phase distribution fluctuations due to the flow patterns are too fast compared to the time-response of common flow actuators, such as control valves, making it impossible for process controllers to suppress them.

In the current subsection, the performance indicators ξ_g, ξ_l and η are plotted against the time-average gas core diameter $\overline{d}_{ert}$ to investigate if the cyclone performance can be controlled based on the phase distribution upstream of the pickup tube, measured by tomography, without targeting the flow pattern fluctuations. The obtained results are a good approximation of the axial cyclone response to real-time controllers that filter out the fast flow pattern phase distribution fluctuations when computing control actions to suppress (slow) process disturbances, as in chapter 5.

Figure 4.11 presents the gas capture ξ_g as function of the time-average gas core diameter, showing that ξ_g decreases with the increase in $\overline{d}_{ert}$. The capture of the vast majority of the gas flow by the pickup tube is obtained for time-average gas core diameters below $0.15D - 0.20D$ ($\overline{d}_{ert}$ is normalized by the inner diameter of the pipe), with exact value depending on the process conditions (gas mass flow rate, pump shaft speed and HPO valve opening). The fraction of the total gas flow captured by the pickup tube strongly decreases with the increase in the time-average gas core diameter outside the high ξ_g plateau obtained for small $\overline{d}_{ert}$, with a steeper decrease in ξ_g with the increase in $\overline{d}_{ert}$ observed for lower gas mass flow rates.

The time-average gas core diameters upstream of the pickup tube which result in high ξ_g are considerably smaller than the inner diameter of the pickup tube ($0.44D$), due to the large amplitude of the local flow pattern fluctuations (Figure 4.8). The gas core measurement $0.9D$ upstream of the pickup tube also contributes to the effect, with the plotted curves of Figure 4.11 suggesting that $\xi_g = 0$ is obtained for $\overline{d}_{ert} < 0.44$; since no flow can

enter in the pickup tube when the LPO valve is fully closed, a time-average gas core greater than the outer diameter of the pickup tube ($0.49D$) is necessarily formed at the tip of the outlet to satisfy the gas mass balance of the flow.

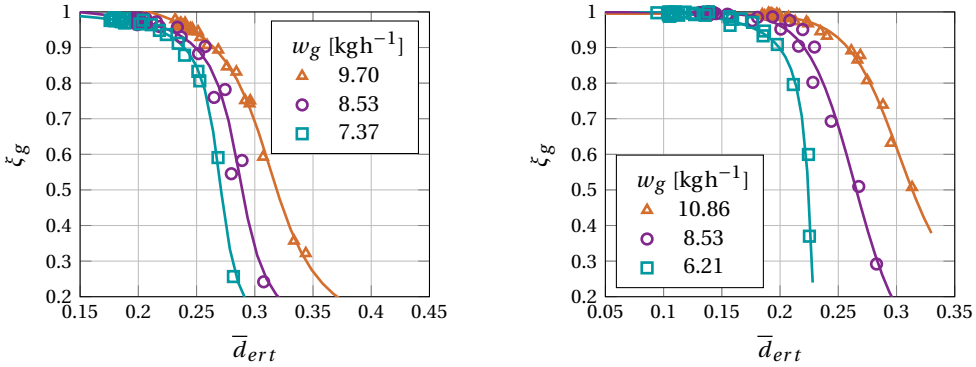

Figure 4.11: Fraction of the total gas mass flow rate captured by the pickup tube (ξ_g) as function of the time-average gas core diameter ($\overline{d}_{ert}$) and gas mass flow rate (w_g). Left image: pump shaft speed $\omega_p = 2430$ rpm and normalized position of the HPO valve diaphragm $x_{hpo} \approx 0.74$. Right image: $\omega_p = 2700$ rpm and $x_{hpo} \approx 0.80$.

The total liquid flow fraction captured by the outer tube, ξ_l, is presented as function of the average gas core diameter in Figure 4.12, showing that the capture of liquid by the outer tube increases linearly with the time-average gas core diameter. The impact of the gas mass flow rate on the curves is evident, with lower ξ_l obtained for the same time-average gas core diameter at higher gas mass flow rates, due to the increase in the amplitude of the flow pattern fluctuations with the increase in w_g (Figure 4.8). The capture of the vast majority of the liquid flow by the outer tube is obtained for sufficiently wide gas cores, indicating that large gas core diameter controller setpoints can be used to maintain a high liquid capture by the outer tube during process disturbances.

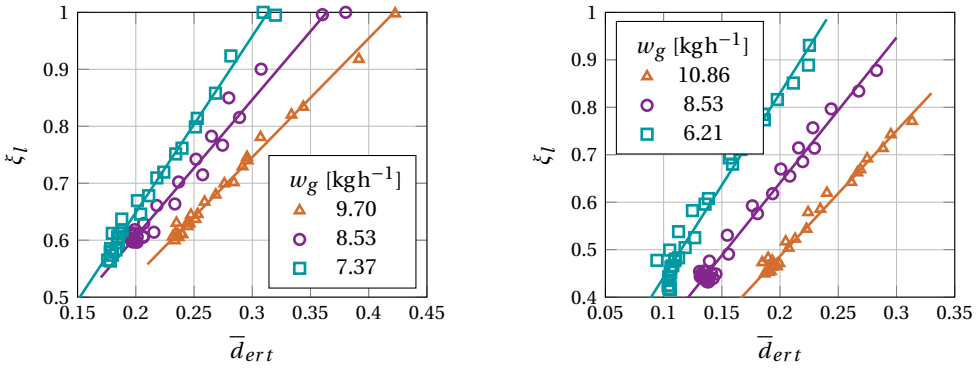

Figure 4.12: Fraction of the total liquid flow rate captured by the outer tube (ξ_l) as function of the time-average gas core diameter ($\overline{d}_{ert}$) and gas mass flow rate (w_g). Left image: pump shaft speed $\omega_p = 2430$ rpm and normalized position of the HPO valve diaphragm $x_{hpo} \approx 0.74$. Right image: $\omega_p = 2700$ rpm and $x_{hpo} \approx 0.80$.

The overall efficiency of separation is plotted against the time-average gas core diameter in Figure 4.13.

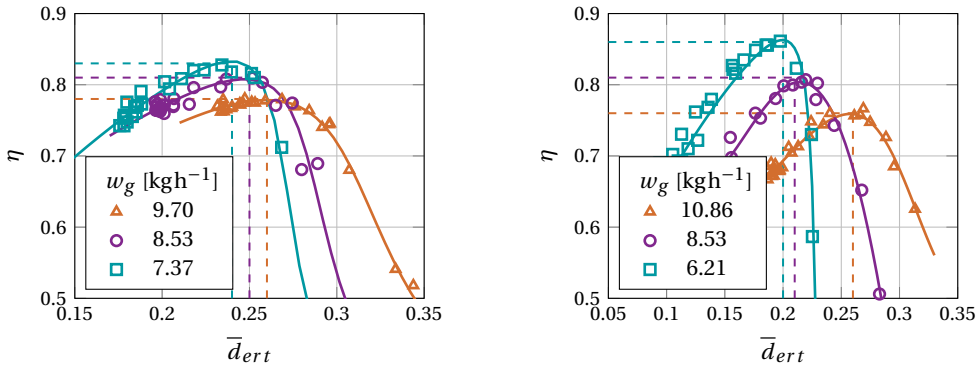

Figure 4.13: Overall efficiency of separation (η) as function of the time-average gas core diameter ($\overline{d}_{ert}$) and gas mass flow rate (w_g). Left image: pump shaft speed $\omega_p = 2430$ rpm and normalized position of the HPO valve diaphragm $x_{hpo} \approx 0.74$. Right image: $\omega_p = 2700$ rpm and $x_{hpo} \approx 0.80$.

Figure 4.13 shows that η initially increases with the increase in the time-average gas core diameter, as the increase in $\overline{d}_{ert}$ increases ξ_l without significantly decreasing ξ_g. However, when the gas core diameter becomes sufficiently large, the increase in $\overline{d}_{ert}$ results in a decrease in ξ_g stronger than the increase in ξ_l, resulting in the decay of η with the increase in the time-average gas core diameter. The peak in the overall efficiency of separation occurs for time-average gas core diameters significantly smaller than the pickup tube inner diameter. Moreover, the $\overline{d}_{ert}$ that maximizes the overall efficiency of separation depends on the liquid and gas flow rates in the axial cyclone, due to the impact of these quantities on the amplitude of the flow pattern fluctuations. The flow pattern fluctuations also impact the maximum overall efficiency of separation that can be obtained by the axial cyclone, with lower peaks in η obtained for higher gas mass flow rates, where the flow pattern phase distribution fluctuations are larger (Figure 4.8). The maximum overall efficiency of separation, and its corresponding time-average gas core diameter, are presented for each process condition investigated in Table 4.1, at the end of the current section.

Since the maximum overall efficiency of separation is not a one-variable function of the time-average gas core diameter, controlling the phase distribution upstream of the pickup tube without acting on the flow pattern fluctuations is insufficient to control the overall efficiency of the process. In other words, if a tomography-based controller is unable to act on the flow pattern fluctuations, process disturbances in the inlet of the axial cyclone will impact η despite the filtered (or time-average) gas core diameter upstream of the pickup tube being maintained around its setpoint. For instance, consider a tomography-based controller with d_{ert} setpoint 0.20, designed based on the conditions that maximize the cyclone performance for $\omega_p = 2700$ rpm, $x_{hpo} \approx 0.80$ and $w_g = 6.21$ kgh^{-1}. Figure 4.13-right shows that if a process disturbance increases the gas mass flow rate in the inlet of the axial cyclone from 6.21 kgh^{-1} to 10.86 kgh^{-1}, the overall efficiency of separation decreases from $\eta \approx 0.86$ to $\eta \approx 0.68$ if the gas core diameter is maintained around $\overline{d}_{ert} = 0.20$.

4.3.3. PRESSURE DROP RATIO AS PERFORMANCE INDICATOR

Subsection 4.3.2 showed that, in general, tomography-based controllers which do not control the flow pattern fluctuations are unable to maintain an optimal separation in the axial cyclone during process disturbances. In the current subsection, the relation between cyclone performance and time-average PDR is investigated to evaluate if the cyclone performance can be controlled via the PDR without acting on the flow pattern fluctuations, making (slow) PDR-based controllers a better alternative to control the separation than (slow) tomography-based controllers.

The fraction of the total gas flow captured by the pickup tube, ξ_g, is plotted against the Pressure Drop Ratio in Figure 4.14.

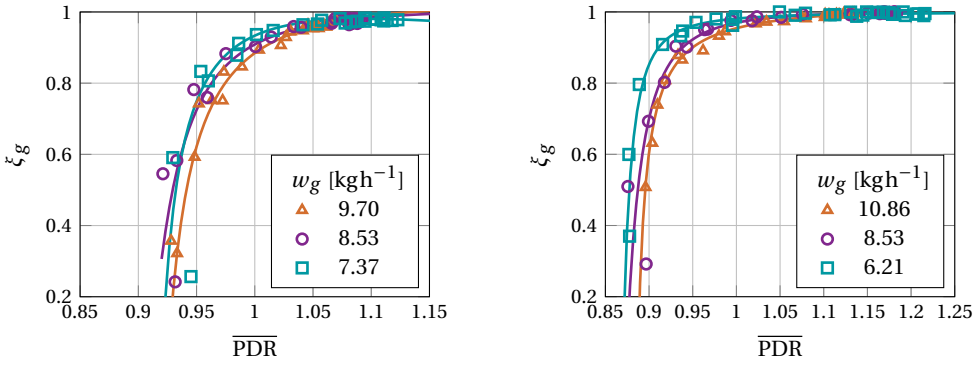

Figure 4.14: Fraction of the total gas mass flow rate captured by the pickup tube (ξ_g) as function of the time-average Pressure Drop Ratio ($\overline{\text{PDR}}$) and gas mass flow rate (w_g). Left image: pump shaft speed $\omega_p = 2430$ rpm and normalized position of the HPO valve diaphragm $x_{hpo} \approx 0.74$. Right image: $\omega_p = 2700$ rpm and $x_{hpo} \approx 0.80$.

Figure 4.14 shows that ξ_g sharply increases with the increase in the time-average Pressure Drop Ratio for $\overline{\text{PDR}}$ in the range $0.85 - 1.00$, reaching a high ξ_g plateau for time-average Pressure Drop Ratios above $1.00 - 1.05$ for the conditions investigated in the current chapter. The increase in ξ_g with the increase in $\overline{\text{PDR}}$ is explained by the flow bending towards the pickup tube for higher PDRs, due to a larger pressure difference between the inlet and pickup tube (PDR numerator) than between the inlet and outer tube (PDR denominator), that reduces the gas core diameter upstream of the pickup tube (Figure 4.6). Since $\xi_g \approx 1$ for high $\overline{\text{PDR}}$, axial cyclone separators that prioritize the capture of gas by the pickup tube can be controlled using high Pressure Drop Ratio setpoints.

The fraction of the total liquid flow captured by the outer tube, ξ_l, is plotted against the time-average Pressure Drop Ratio in Figure 4.15. The plots of Figure 4.15 show that the liquid capture by the outer tube decreases as the $\overline{\text{PDR}}$ increases, which is also observed for de-oiling tangential cyclones [50, 57]. The decrease in ξ_l with the increase in the Pressure Drop Ratio is a direct consequence of the flow bending towards the pickup tube with the increase in the PDR, reducing the fraction of the total liquid flow that is captured by the outer tube. Figure 4.15-left shows that the vast majority of the liquid is captured by the outer tube for sufficiently low $\overline{\text{PDR}}$, indicating that separation processes which prioritize

the capture of liquid by the outer tube can be controlled using low Pressure Drop Ratio setpoints, whether or not controlling the flow pattern fluctuations.

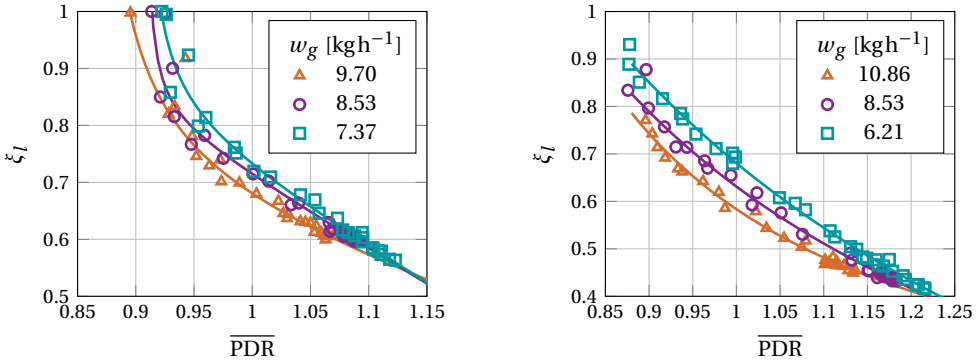

Figure 4.15: Fraction of the total liquid flow rate captured by the outer tube (ξ_l) as function of the time-average Pressure Drop Ratio ($\overline{\text{PDR}}$) and gas mass flow rate (w_g). Left image: pump shaft speed ω_p = 2430 rpm and normalized position of the HPO valve diaphragm $x_{hpo} \approx 0.74$. Right image: ω_p = 2700 rpm and $x_{hpo} \approx 0.80$.

The relation between the overall efficiency of separation η and the time-average Pressure Drop Ratio is presented in Figure 4.16, showing that the maximum η was obtained for $\overline{\text{PDR}}$ in the range 0.9-1.0 in the experiments of this chapter. The peak of η in relation to the PDR occurs due to the opposite behavior of ξ_g and ξ_l in relation to the time-average Pressure Drop Ratio, similarly to the relation between η and x_{lpo}, or between η and $\overline{d}_{ert}$. Figure 4.16 also shows a significant dependency of the η-PDR relation on the process conditions, with the peak in the overall efficiency of separation significantly reducing for higher gas mass flow rates, and shifting towards lower time-average Pressure Drop Ratios for higher pump shaft speeds and smaller HPO valve openings. The maximum η of each curve, and its corresponding time-average PDR, are summarized in Table 4.1.

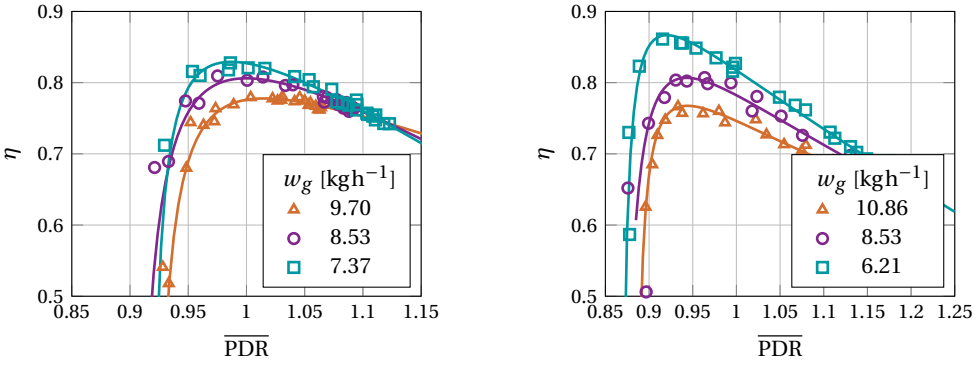

Figure 4.16: Overall efficiency of separation (η) as function of the time-average Pressure Drop Ratio ($\overline{\text{PDR}}$) and gas mass flow rate (w_g). Left image: pump shaft speed ω_p = 2430 rpm and normalized position of the HPO valve diaphragm $x_{hpo} \approx 0.74$. Right image: ω_p = 2700 rpm and $x_{hpo} \approx 0.80$.

Figure 4.16 shows that the overall efficiency of separation cannot be written as a one-variable function of the time-average Pressure Drop Ratio. For instance, the overall efficiency of separation decreases from $\eta > 0.85$ to $\eta < 0.70$ for $\overline{\text{PDR}}$ in the range 0.90-0.95 when shifting from the green curve of Figure 4.16-right ($\omega_p = 2700$ rpm, $w_g = 6.21$ kgh^{-1} and $x_{hpo} \approx 0.80$) to the orange curve of Figure 4.16-left ($\omega_p = 2430$ rpm, $w_g = 9.70$ kgh^{-1} and $x_{hpo} \approx 0.74$). Therefore, controlling the filtered PDR (i.e., without accounting for the flow pattern fluctuations) is also insufficient to control the separation in axial cyclones.

Table 4.1: Diaphragm position of the LPO valve (x_{lpo}), time-average gas core diameter ($\overline{d}_{ert}$) and time-average Pressure Drop Ratio ($\overline{\text{PDR}}$) that maximize the overall efficiency of separation η for different pump shaft speeds (ω_p) and gas mass flow rates (w_g).

ω_p	w_g	η_{max}	$x_{lpo}(\eta_{max})$	$\overline{d}_{ert}(\eta_{max})$	$\overline{\text{PDR}}(\eta_{max})$
2430 rpm	9.70 kgh^{-1}	0.78	0.57	0.26	1.02
	8.53 kgh^{-1}	0.81	0.68	0.25	1.00
	7.37 kgh^{-1}	0.83	0.76	0.24	0.99
2700 rpm	10.86 kgh^{-1}	0.76	0.74	0.26	0.94
	8.53 kgh^{-1}	0.81	0.80	0.21	0.94
	6.21 kgh^{-1}	0.86	0.86	0.20	0.92

4.4. CONCLUSION

The relation between axial cyclone performance, time-average gas core diameter upstream of the pickup tube and time-average Pressure Drop Ratio was investigated in the current chapter, providing an approximation of the axial cyclone performance with process controllers which suppress (slow) process disturbances in the phase distribution or PDR without acting on the flow pattern fluctuations.

The experiments performed in the current chapter showed that:

- Small gas core diameters (in tomography-based control) and large Pressure Drop Ratios (in pressure-based control) can be used to control the cyclone performance in processes that prioritize the capture of gas by the pickup tube. However, this comes with the disadvantage of high liquid flow rates in the pickup tube, and a relatively low overall efficiency of separation.

- Large gas core diameters (in tomography-based control) and small Pressure Drop Ratios (in pressure-based control) can be used to control the cyclone performance in processes where the liquid capture by the outer tube is prioritized. However, the approach has the drawback of a large capture of gas by the outer tube, and a relatively low overall efficiency of separation.

- The overall efficiency of separation of axial cyclones cannot be written as a one-variable function of the time-average gas core diameter upstream of the pickup tube or time-average Pressure Drop Ratio. As consequence, the suppression of process

disturbances in the phase distribution upstream of the pickup tube by tomography-based controllers, or in the Pressure Drop Ratio by pressure-based controllers, is insufficient to control the separation if the flow pattern fluctuations are filtered out from the controller calculations.

Regarding the tomography-based real-time control of axial cyclones, an almost perfect separation is expected if the gas core diameter can be maintained between the inner and outer pickup tube diameters. However, the approach would require the suppression of the fast flow pattern fluctuations in the local phase distribution, which is impossible with common flow actuators, such as control valves.

When uncontrolled, the flow pattern fluctuations shift the maximum efficiency of separation to time-average gas core diameters significantly smaller than the inner diameter of the pickup tube. Such time-average gas core diameters can be used as setpoint for slow process controllers that do not act on the flow pattern fluctuations, as in chapter 5. However, the lack of a universal gas core diameter setpoint that maximizes the overall efficiency of separation for such controllers limits the advantages of tomography-based control over pressure-based control.

The investigation of this chapter was performed with Bursting Columns, and the values reported along the text are restricted to the flow pattern and setup used in the experiments. The relation between overall efficiency of separation, time-average gas core diameter and time-average Pressure Drop Ratio may be different for flow patterns with smaller gas core fluctuations, such as Weakly Oscillating Columns (chapter 3), and must be investigated in future works.

CHAPTER 5

PHASE DISTRIBUTION DYNAMICS AND TOMOGRAPHY-BASED REAL-TIME CONTROL

5.1. INTRODUCTION

Multiphase flows are found in a wide range of industrial processes, e.g. in heat exchangers [1, 2], bubble column reactors [3], oil and gas industry [19, 20] and nuclear power plants [32, 141]. A fundamental aspect of multiphase flows is that the distribution of phases plays a major role in the performance and safety of the equipment and, therefore, the real-time control of multiphase flow processes is ideally performed based on real-time phase distribution measurements.

Several techniques were developed over the years to measure the distribution of phases in multiphase flows, for instance industrial tomography [28, 64–66] and Wire-Mesh Sensors (WMS) [77, 92–96]. However, until recently, the real-time control of multiphase flow processes was limited to flow variables such as pressure [14, 15, 57–59], due to (i) the slow image reconstruction of tomography compared to the phase distribution dynamics, and (ii) the nonexistence of real-time wire-mesh sensors.

A real-time Electrical Resistance Tomography (ERT) sensor and image processing algorithm were developed in this dissertation (chapter 2) to investigate the tomography-based real-time control of the distribution of phases in multiphase flows. The tomography-based real-time control investigation is performed in a gas-liquid axial cyclone, where actions in the Light Phase Outlet (LPO) valve of the cyclone are performed by an electrical resistance tomography-based controller based on gas core measurements upstream of the pickup tube, as shown in Figure 5.1.

The gas core dynamics in the axial cyclone has contributions of the upstream flow and of the pickup and outer tube pressures. The phase distribution right downstream of the swirl element is determined by the centripetal force effects on the upstream gas-liquid distribution. For instance, Bubbly flows upstream of the swirl element are transformed into a centered gas core surrounded by a liquid annulus downstream of the swirl element for sufficiently high centripetal forces, as illustrated in Figure 5.1. Once inside the cyclone, the phase distribution (gas core) created by the addition of swirl to the upstream flow travels towards the pickup and outer tubes, being modified by the pressure distribution in the outlets of the cyclone before departing from the equipment. The pickup and outer tube pressures are related to the LPO and HPO valve openings, that can be changed to manip-

This chapter is based on the publication Garcia *et al.* [140].

ulate the gas core upstream of the pickup tube and, in principle, control the capture of gas and liquid by the pickup and outer tubes.

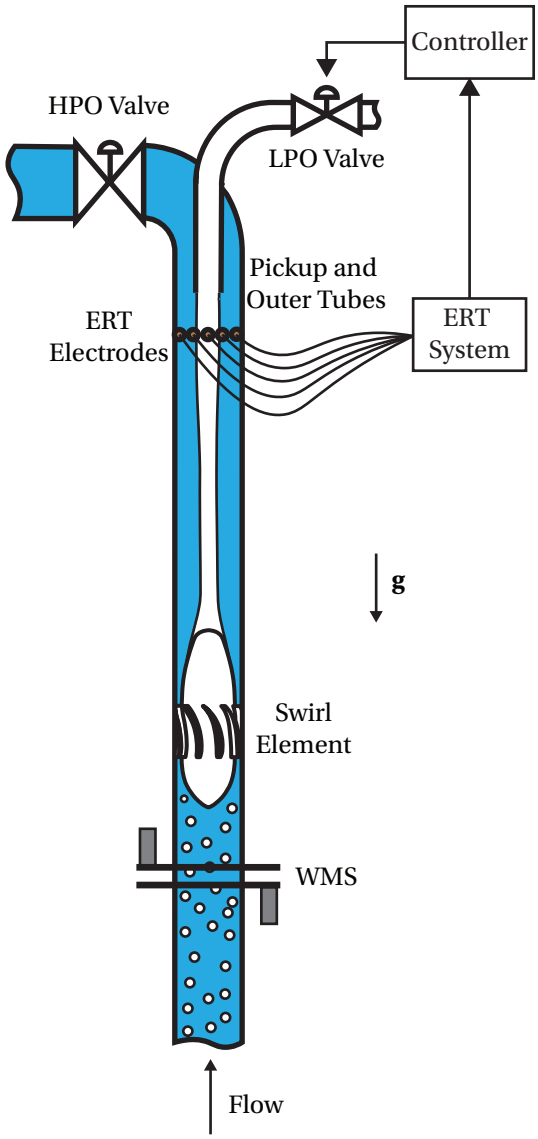

Figure 5.1: Gas-liquid axial cyclone with tomography-based real-time control and double-layer wire-mesh sensor upstream of the swirl element. The tomography-based feedback controller uses the gas core diameter measured by Electrical Resistance Tomography (ERT) to act on the Light Phase Outlet (LPO) valve.

While Bubbly flows upstream of the swirl element transform into well-behaved gas cores in the axial cyclone, due to the continuous gas flow to the cyclone in the form of discrete bubbles, upstream Slug flows (illustrated in Figure 5.2) are transformed by the

swirl into unsteady gas cores with strong gas-liquid interface fluctuations (chapter 3). The phase distribution dynamics of upstream Slug flows, and the resulting phase distribution dynamics downstream of the swirl element, are *intrinsic* to the nonlinear multiphase flow physics, and concurrent to external process disturbances or control actions. When external disturbances are applied in the system, such as changes in the gas flow rate upstream of the axial cyclone, the gas-liquid distributions upstream and downstream of the swirl element show both the intrinsic (flow pattern) dynamics and the system response to the external disturbance.

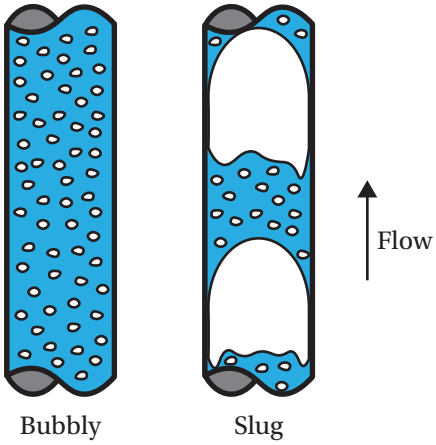

Figure 5.2: Phase distribution in Bubbly (left) and Slug (right) flows.

The distinction between the phase distribution response to external disturbances and the intrinsic (flow pattern) dynamics, proposed in this thesis, is relevant to the design of actuators and process controllers for multiphase flow processes. The intrinsic phase distribution dynamics is characterized by high-amplitude flow pattern fluctuations, with time-constants in the order of 0.1 s. External process disturbances are process-dependent, and can impact the phase distribution in time-scales considerably larger than the intrinsic dynamics. The intrinsic dynamics are too fast compared to the response of common flow actuators, such as pneumatic control valves (chapter 2). However, the intrinsic dynamics can be filtered out from the real-time controller calculations if there is a clear separation between the time-scales of the intrinsic dynamics and external disturbances, e.g., for external process disturbances with time-constants in the order of 10 s or larger, allowing to design slow process controllers (compared to the intrinsic dynamics) to suppress external disturbances in the phase distribution, as performed in the current chapter.

The objective of this chapter is to investigate the phase distribution dynamics in the axial cyclone and, based on the identified dynamics, the possibilities and limitations of tomography-based real-time control of the separator. The chapter is divided in two parts. In part I, the intrinsic phase distribution dynamics upstream and downstream of the swirl element are presented, and the upstream flow contribution to the (intrinsic) gas core dynamics in the axial cyclone is investigated in the absence external disturbances. In part II, the gas core dynamics upstream of the pickup tube is investigated from a system dynamics

perspective, and the model obtained used to design a electrical resistance tomography-based feedback controller to suppress external disturbances in the gas core diameter. The analysis of part II is performed via discrete-time models and discrete-time transfer functions, which are introduced to readers outside the System Dynamics and Control field in Appendix D. The conclusions of part I and part II are presented together in section 5.8.

PART I: INTRINSIC PHASE DISTRIBUTION DYNAMICS

In this part, the intrinsic phase distribution dynamics upstream and downstream of the swirl element is investigated for multiple statistically-steady gas and liquid flow rates, i.e., in the absence of external disturbances. The experiments performed are described in section 5.2, and the measured intrinsic phase distribution dynamics upstream and downstream of the swirl element are presented in section 5.3. The cross-correlation between the upstream and downstream gas fractions is investigated in section 5.4, to analyze (i) the upstream flow contribution to the (intrinsic) gas core dynamics inside the axial cyclone, and (ii) the potential use of upstream phase distribution measurements, by wire-mesh sensors or tomography, in the real-time control of the separator.

5.2. METHODS OF PART I

The experimental facility used in this thesis was described in details in chapter 2. A simplified drawing of the flow loop with its main dimensions is presented in Figure 5.3, where $D = 81.4$ mm is the inner diameter of the cyclone. As shown in Figure 5.3, the phase distribution $4.4D$ upstream of the swirl element is measured by a double-layer wire-mesh sensor, and the phase distribution $5.7D$ downstream of the swirl element is measured by a high-speed camera (Basler acA1920 150uc with 8mm lenses by Computar).

The wire-mesh sensor measures the gas-liquid distribution upstream of the swirl element at 5 kHz in two layers separated by 25.7 ± 0.1 mm from each other. The working principle of the wire-mesh sensor was described in section 2.4. The gas fraction in each wire-mesh sensor layer is obtained from the cross-sectional average of the gas distribution. The gas fractions measured in each layer of the wire-mesh sensor are cross-correlated in time to estimate the gas velocity of the upstream flow U_{wms}, obtained dividing the distance between the two wire-mesh layers by the time-delay that maximizes the cross-correlation between their gas fractions.

The camera records the gas core at 1250 frames per second with a spatial resolution of 3.4 pixels/mm. The length of the visualization window of the camera in the axial direction was chosen based on the thickness of one wire-mesh sensor layer. Since the camera records the flow at 1250 frames per second and the wire-mesh sensor measures the phase distribution upstream of the swirl element at 5 kHz, the wire-mesh signal is averaged every four frames to match the camera frequency (1.25 kHz) in the study of the cross-correlation between the bottom layer of the wire-mesh sensor and the camera; during tests, a similar cross-correlation was obtained if only one every four frames is considered in the WMS

data, mimicking an acquisition at 1.25 kHz.

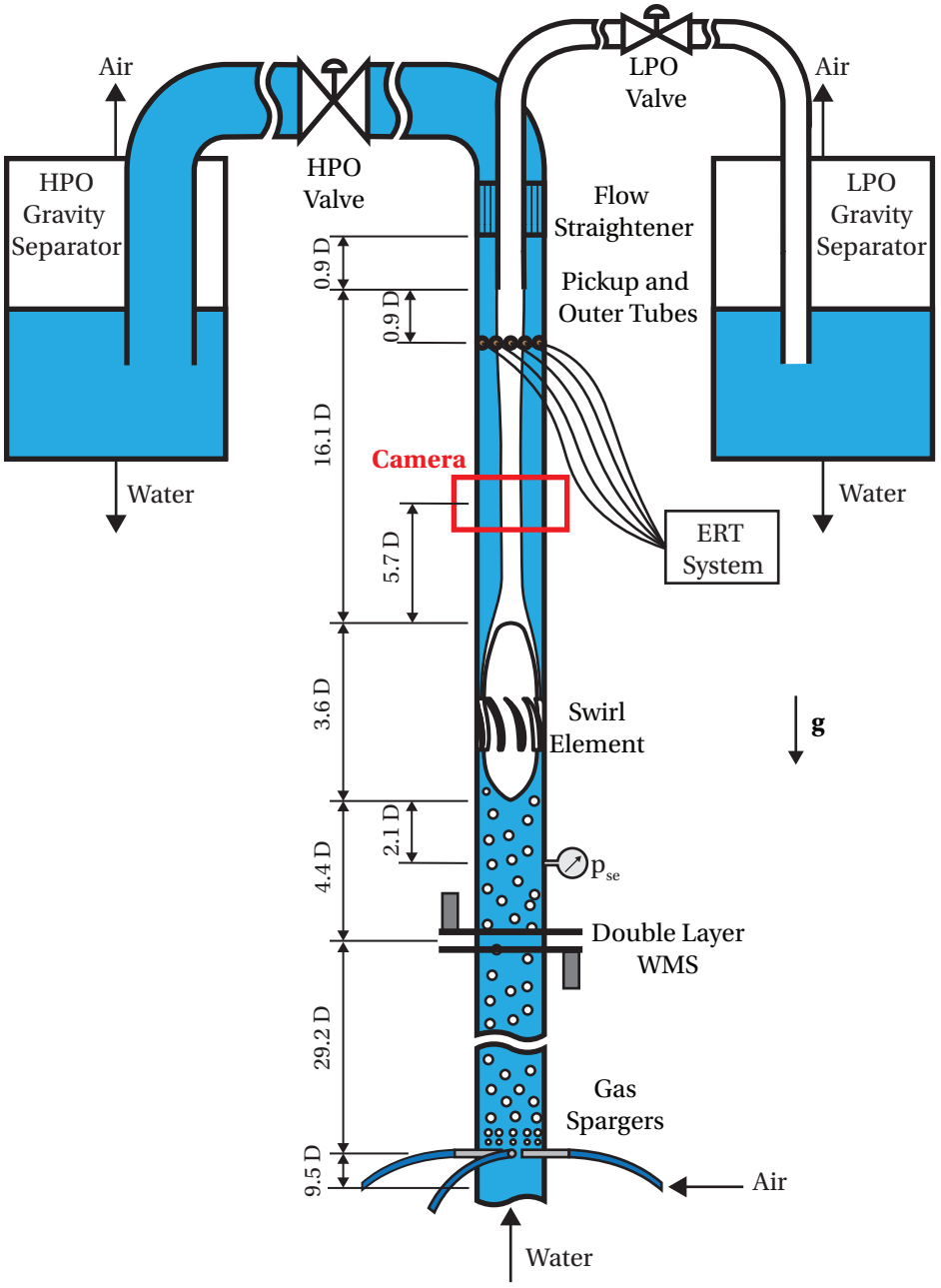

Figure 5.3: Schematics of the flow loop with the double-layer wire-mesh sensor 4.4D upstream of the swirl element, region recorded by the high-speed camera 5.7D downstream of the swirl element and ERT electrodes 0.9D upstream of the pickup tube. D = 81.4 mm is the inner diameter of the cyclone.

Thirty-five combinations of statistically-steady liquid and gas flow rates, summarized in Table 5.1 and related to Bubbly and Slug flows upstream of the axial cyclone, are used in the experiments of part I of this chapter. The experiments are performed with Swirl Element 3, described in section 2.3, the LPO valve fully open and the diaphragm position of the HPO valve[1] $x_{hpo} \approx 0.80$. The upstream and cyclone phase distributions of each experimental point are recorded for 20 s by the wire-mesh sensor and camera, respectively.

Table 5.1: Average liquid and gas flow rates covered in the experiments of part I of chapter 5.

Water Flow Rate [$m^3 h^{-1}$]	Air Flow Rate [$kg h^{-1}$]
4.80	1.55, 2.33, 3.10, 3.88, 5.43
6.00	2.33, 3.10, 3.88, 5.43, 6.98
7.20	3.10, 3.88, 5.43, 6.98, 8.53
8.40	3.88, 5.43, 6.98, 8.53, 10.09
9.00	1.55, 2.33, 3.10, 3.88, 4.65, 5.43, 6.98, 8.53, 10.09, 11.64
9.60	6.98, 8.53, 10.09, 11.64, 13.19

The cross-correlation between the gas fractions measured by bottom layer of the wire-mesh sensor and the camera is used to investigate the propagation of intrinsic dynamics from the upstream flow to the cyclone. The gas fraction time-series downstream of the swirl element, required for the cross-correlation, is obtained extracting the gas core diameter $d_i(t)$ from each frame recorded by the camera via the image processing routine described in Appendix A, and replacing it into:

$$\alpha_{cam}(t) = \left(\frac{d_i(t)}{D}\right)^2 \tag{5.1}$$

The wire-mesh sensor and the camera measure the cross-sectional phase distribution of the flow. Two-dimensional images of the phase distribution, as the one presented in Figure 5.4 and the ones in section 5.3, are obtained stacking the gas-liquid distribution measured by one of the center wires of the wire-mesh sensor or by the camera over time, where the column of pixels corresponds to the phase distribution measured in one line of the flow by the sensors, and the position in the horizontal axis of the images corresponds to the time of each measurement. The images obtained do not represent the instantaneous phase distribution in the radial and axial directions.

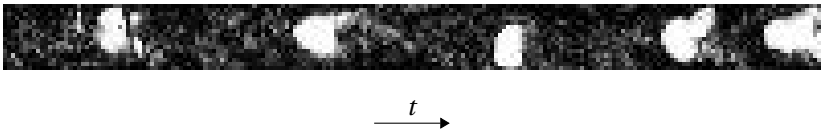

Figure 5.4: Reconstruction of the phase distribution measured by one of the center wire-mesh sensor wires by staking line measurements over time. The horizontal axis of the image is time, and not the axial position in the upstream flow or cyclone (as in an instantaneous picture of the flow).

[1] The LPO and HPO diaphragm positions are presented in this thesis normalized by their maximum range, where $x = 0$ is obtained for the valve fully open and $x = 1$ for the valve fully closed.

5.3. UPSTREAM AND CYCLONE PHASE DISTRIBUTIONS

As described in chapter 3, different upward vertical gas-liquid flow patterns are formed upstream and downstream of the swirl element depending on the time-average gas and liquid flow rates. The flow rates covered in the experiments of this chapter result in Bubbly and Slug flows upstream of the swirl element, and Weakly Oscillating and Bursting Columns in the axial cyclone.

Weakly Oscillating Columns are well behaved gas cores formed downstream of the swirl element for upstream bubbly flows at sufficiently large liquid flow rates (chapter 3). The phase distribution and gas fraction of a bubbly flow upstream of the swirl element, measured by the wire-mesh sensor, are presented as function of time in Figure 5.5. The corresponding Weakly Oscillating Column downstream of the swirl element, measured by the high-speed camera, is presented in Figure 5.6.

Bursting Columns are unsteady swirling gas-liquid flow patterns that occur in the axial cyclone for upstream slug flows at sufficiently large liquid flow rates (chapter 3). The phase distribution and gas fraction of a slug flow upstream of the swirl element, measured by the wire-mesh sensor, are presented as function of time in Figure 5.7. The phase distribution and gas fraction of the Bursting Column downstream of the swirl element, created by the upstream slug flow of Figure 5.7 and measured by the camera, are presented as function of time in Figure 5.8. Please note that the y-axis scale of Figures 5.7 and 5.8 is different from the y-axis scale of Figures 5.5 and 5.6.

The time-average and standard deviation of the gas fraction measured in the upstream and cyclone flows of Figures 5.5-5.8 is presented in Table 5.2.

Table 5.2: Time average ($\overline{\alpha}$) and standard deviation $\sigma(\alpha)$ of the gas fraction of Figures 5.5-5.8.

Pattern	$\overline{\alpha}$	$\sigma(\alpha)$
Bubbly (Figure 5.5)	0.061	0.029
Weakly Oscillating Column (Figure 5.6)	0.0036	0.0018
Slug (Figure 5.7)	0.21	0.14
Bursting Column (Figure 5.8)	0.052	0.044

Table 5.2 shows that columnar flows in the cyclone have considerably smaller average gas-fraction than their upstream flow counterparts. The effect is a consequence of the annular flow structure with thick liquid film of weakly oscillating and bursting columns, where the pressure gradient in the gas is determined by the interface shear stress, scaling with the gas density and axial gas velocity squared, and the pressure gradient in the liquid is determined by the liquid density and gravity. Since the density of the liquid is about three orders of magnitude larger than the density of the gas, axial gas velocities orders of magnitude above the axial liquid velocity are required to maintain a similar pressure drop in the two phases, keeping them apart. As the difference between the axial gas and liquid velocities (slip velocity) in bubbly and slug flows is much smaller than in annular flows, the conservation mass across the swirl element results in average gas fractions much smaller in the cyclone than in the upstream flow. The reader is referred to subsection 3.6.3 of chapter 3 for more details about the physics of vertical swirling gas-liquid columnar flows.

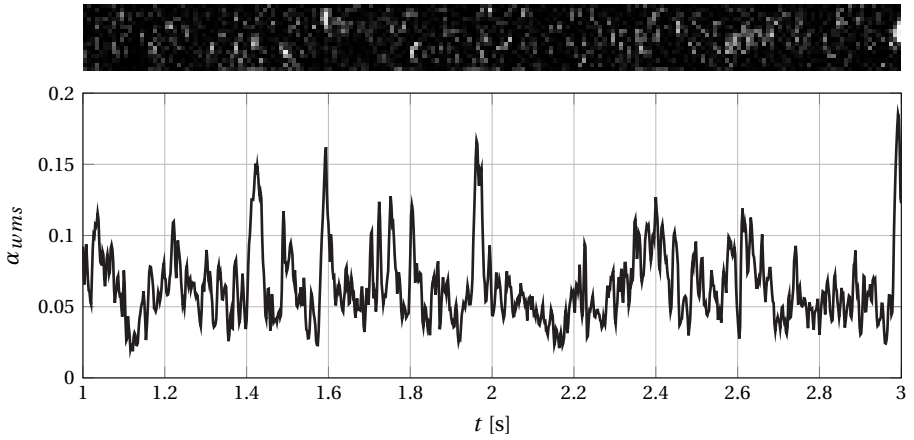

Figure 5.5: Reconstructed phase distribution (top) and gas fraction (bottom) of a Bubbly flow upstream of the axial cyclone, measured by the wire-mesh sensor. Images for a water flow rate of 9 $m^3 h^{-1}$ and an air mass flow rate of 1.55 $kg h^{-1}$. The two images are based on the same data and share the same time axis in the horizontal direction. Gas is white and liquid is black in top image. Gray pixels correspond to intermediary gas fractions (e.g., due to bubbles smaller than the sensing area of the wire-mesh sensor).

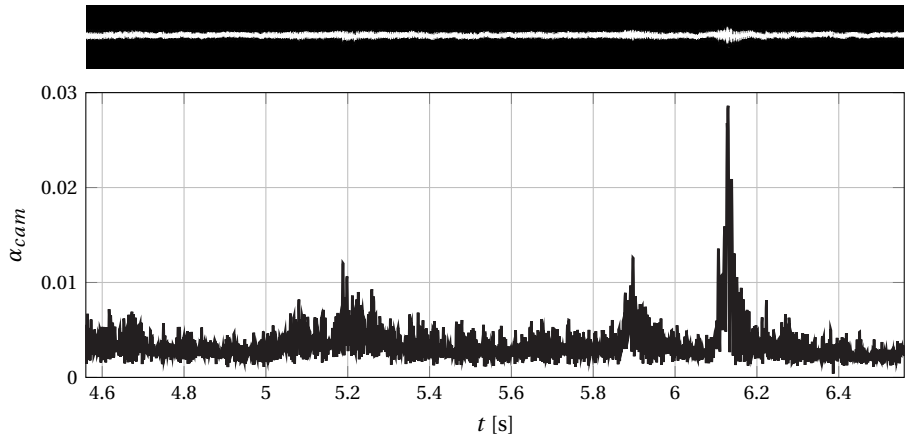

Figure 5.6: Reconstructed phase distribution (top) and gas fraction (bottom) of a Weakly Oscillating Column, measured in the axial cyclone by the high-speed camera. Images for a water flow rate of 9 $m^3 h^{-1}$ and an air mass flow rate of 1.55 $kg h^{-1}$. The two images are based on the same data and share the same time axis in the horizontal direction. Gas is white and liquid is black in the phase distribution of the top image.

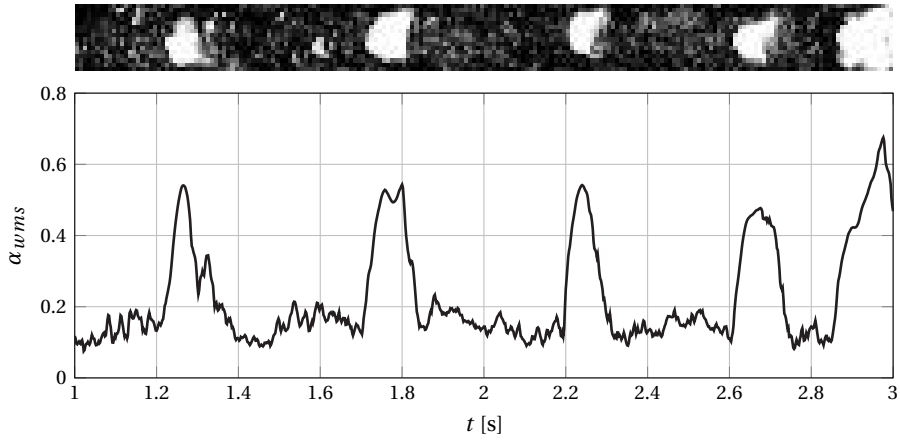

Figure 5.7: Reconstructed phase distribution (top) and gas fraction (bottom) of a Slug flow upstream of the axial cyclone, measured by the wire-mesh sensor. Images for a water flow rate of 4.8 $m^3\,h^{-1}$ and an air mass flow rate of 5.43 $kg\,h^{-1}$. The two images are based on the same data and share the same time axis in the horizontal direction. Gas is white and liquid is black in the phase distribution of the top image, with the gray pixels representing intermediary gas fractions (e.g., due to bubbles smaller than the sensing area of the wire-mesh sensor).

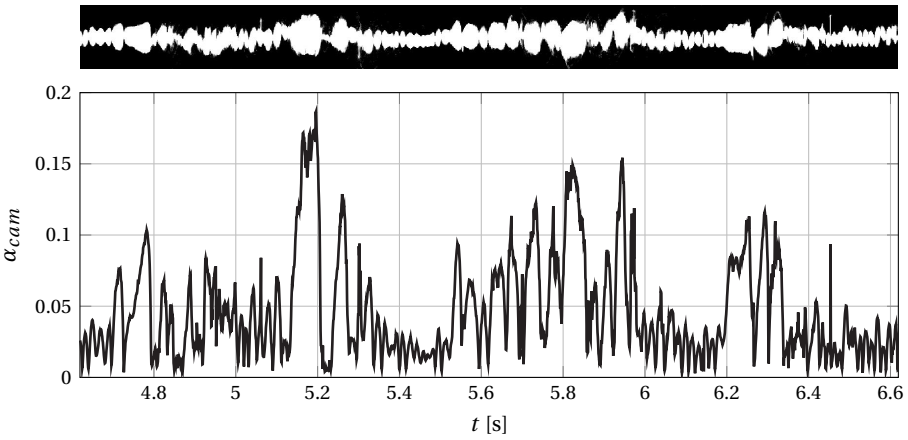

Figure 5.8: Reconstructed phase distribution (top) and gas fraction (bottom) of a Bursting Column, measured in the axial cyclone by the high-speed camera. Images for a water flow rate of 4.8 $m^3\,h^{-1}$ and an air mass flow rate of 5.43 $kg\,h^{-1}$. The two images are based on the same data and share the same time axis in the horizontal direction. Gas is white and liquid is black in the phase distribution of the top image.

The standard deviations presented in Table 5.2 show that bubbly flows have small gas fraction fluctuations compared to slug flows. This occurs due to the homogeneous flow of discrete bubbles in the wire-mesh sensor cross-section in the bubbly regime, in contrast to the quasi-periodic gas distribution into large gas pockets (Taylor bubbles) alternating with bubbly flow regions (liquid slugs) of slug flows. Moreover, the continuous flow of gas across the swirl element for upstream bubbly flows results in small gas core fluctuations in the weakly oscillating column formed inside the axial cyclone. On the other hand, the large gas pockets (Taylor bubbles) of upstream slug flows result in strong gas fraction fluctuations in the bursting regime downstream of the swirl element.

While the flow pattern fluctuations of Weakly Oscillating Columns have a relatively small impact on the distribution of phases and efficiency of the cyclone, the large amplitude of the intrinsic dynamics of bursting columns is particularly challenging to the tomography-based real-time control of the equipment, as discussed in section 5.7.

5.4. UPSTREAM FLOW PROPAGATION TO THE CYCLONE

The relation between the upstream and cyclone flows in the absence of external disturbances is investigated based on the cross-correlation between the upstream and cyclone gas fractions. Figure 5.9 shows the cross-correlation coefficient as function of the lag (delay) for one out of the thirty-five experimental conditions investigated, where a peak in the cross-correlation correlation coefficient above 0.8 is obtained for the delay $T_d = 0.384$ s. Similar cross-correlation curves were obtained for each experimental point investigated.

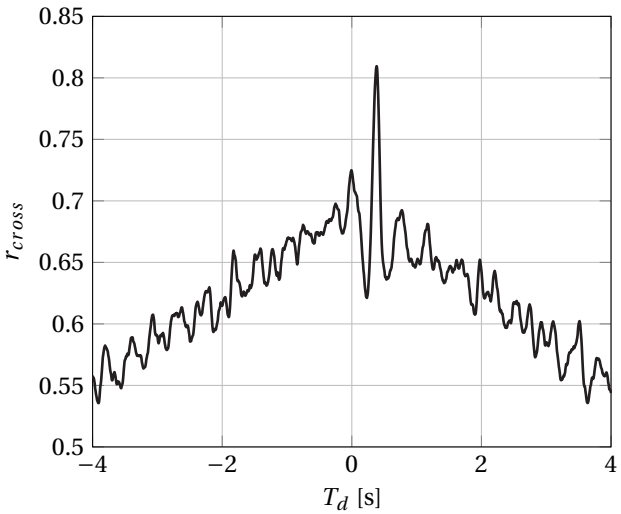

Figure 5.9: Cross-correlation coefficient (r_{cross}) between the camera and wire-mesh sensor gas fractions as function of the lag between the signals (T_d) for a liquid flow rate of 9.6 $m^3\,h^{-1}$ and a gas mass flow rate of 13.19 $kg\,h^{-1}$.

A clear peak with relatively high cross-correlation coefficient r_{cross} was obtained for every experimental point of the dataset, confirming that the intrinsic dynamics of the

upstream and cyclone flow patterns are interconnected. The time delay that maximizes the cross-correlation is determined by the average gas velocity between the cross-sections measured by the wire-mesh sensor and the camera, related to the gas and liquid flow rates used in the experiments. Since the wire-mesh sensor velocity U_{wms} is related to the time-average gas velocity of the upstream flow, a clear trend between the delay that maximizes the cross-correlation and U_{wms} is obtained when the quantities are plotted against each other, as shown in Figure 5.10.

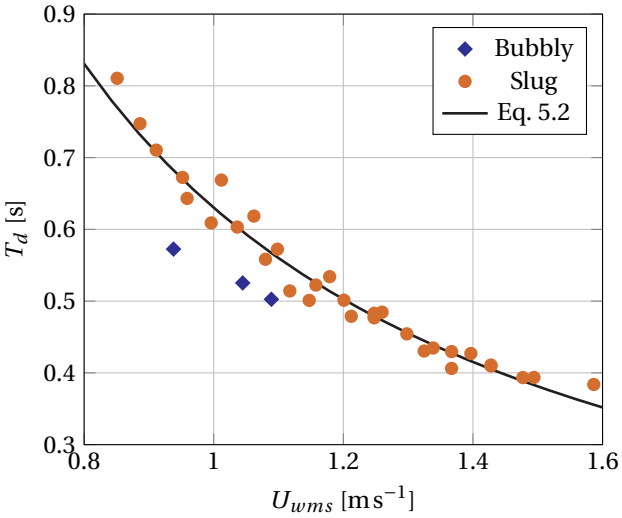

Figure 5.10: Delay that maximizes the cross-correlation between the camera gas fraction and the wire-mesh sensor gas fraction (T_d) as a function of the velocity measured by the double-layer wire-mesh sensor U_{wms}. Marks: experimental data. Black line: empirical fit described by Equation 5.2.

Figure 5.10 shows that the relation between the delay and the wire-mesh sensor velocity follows a monotonic curve for each flow pattern upstream of the separator. Moreover, the delay between the two signals decreases with the increase in the wire-mesh sensor velocity, which is expected: if the gas moves faster, the time required for the disturbances detected by the wire-mesh sensor to travel to the location recorded by the camera becomes smaller. A setup-dependent empirical correlation to predict the delay T_d (in seconds) that maximizes the cross-correlation between the pipe positions recorded by the wire-mesh sensor and camera for upstream slug flows, based on the wire-mesh sensor velocity U_{wms} (in meters per second) and shown in Figure 5.10, is:

$$T_d = 0.63 U_{wms}^{-1.24} \tag{5.2}$$

The delay predicted by Equation 5.2 can be used to shift the time-series of the camera recordings with respect to the time-series of the wire-mesh sensor, synchronizing the phase distribution measured by the two sensors in relation to the intrinsic dynamics. The result obtained for one experimental point is presented in Figure 5.11.

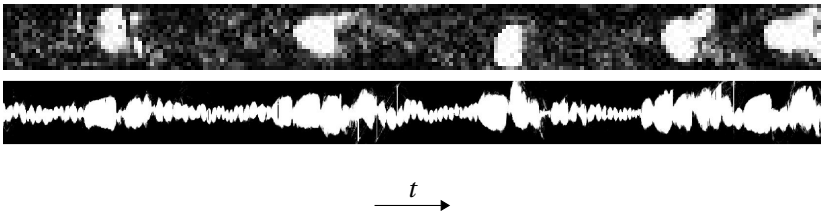

Figure 5.11: Phase distributions measured by the wire-mesh sensor (top) and camera (bottom) for a water flow rate of 4.8 $m^3 h^{-1}$ and an air mass flow rate of 5.43 $kg h^{-1}$, synchronized by the delay of Figure 5.10. The top image shows a Slug flow, where gas is distributed into large gas pockets (in white) separated by regions with small bubbles (gray pixels). The bottom image shows a Bursting Column, with alternating wide and thin gas core regions. The images together show that small bubbles upstream of the swirl element are transformed into thin gas core regions, while the large gas pockets are transformed into wide gas core regions.

Figure 5.11 shows that the small bubbles between the large gas pockets (Taylor bubbles) in the upstream slug flow are transformed by the swirl element into thin gas core regions in the axial cyclone, while the large gas pockets are transformed into wide gas core regions inside the separator; the alternating thin and wide gas core regions in the axial cyclone characterize the Bursting Column regime. The upstream gas distribution into discrete bubbles between the large gas pockets result in a roughly constant gas flow to the cyclone, as observed by the gas volume fraction curve of Figure 5.7, resulting in small gas core fluctuations downstream of the swirl element. On the other hand, the large gas pockets of the upstream flow cause a strong rise in the volume of gas reaching the swirl element (Figure 5.7), leading to an enlargement of the gas core to accommodate the additional gas volume. Apart from the clear conversion of small bubbles into thin cores and large bubbles into thick cores, Figure 5.11 shows a complex relation between the two locations: the original gas pockets of the upstream flow get deformed and stretched inside the separator, due to the impact of the nonlinear swirl flow physics on the phase distribution traveling in the axial cyclone.

The experimental results obtained along this section confirm that the intrinsic gas core dynamics in the axial cyclone are strongly connected to the upstream flow. Therefore, dynamic models can be developed to predict the intrinsic gas core dynamics downstream of the swirl element from upstream gas fraction measurements, e.g., based on the delay T_d of the current section.

In principle, since the axial cyclone phase distribution can be predicted based on the upstream flow, measurements of phase distribution upstream of the swirl element by real-time tomography or real-time wire-mesh sensors can be included in the real-time control of the phase distribution upstream of the pickup tube, where the phase separation obtained by the axial cyclone is determined. The upstream flow addition to the control loop can be made, for instance, via control actions directly computed based on the upstream phase distribution by a feedforward controller, or by the inclusion of the upstream gas fraction as measured disturbance in a model predictive controller.

Even if the upstream phase distribution is included in the control loop, valves are too slow compared to the time-scales of the intrinsic dynamics, and new actuators must be developed to act on the fast flow pattern fluctuations. A potentially interesting option to be investigated is the angle of the swirl element vanes, impacting the swirl intensity in

the axial cyclone. However, due to its non-linear and chaotic nature, it may be that the intrinsic dynamics can never be (fully) controlled, regardless of how fast the actuators are.

Since the double-layer wire-mesh sensor used in the experiments does not operate in real-time, and the LPO valve is too slow to control the intrinsic dynamics, the tomography-based feedforward control of the axial cyclone is not investigated in this work. Instead, the part II of the current chapter focus on the gas core dynamics upstream of the pickup tube due to inputs in the LPO valve, and on the suppression of external disturbances in the local gas core diameter by an electrical resistance tomography-based feedback controller.

PART II: GAS CORE DYNAMICS UPSTREAM OF THE PICKUP TUBE AND TOMOGRAPHY-BASED FEEDBACK CONTROL

In this part, a system dynamics model for the response of the gas core diameter upstream of the pickup tube to inputs in the LPO valve is proposed, and used to design a simple feedback controller to suppress external disturbances in the local phase distribution. The controller is designed around an operating point that maximized the overall efficiency of separation of the cyclone in chapter 4, and the gain in cyclone performance obtained with the suppression of external disturbances is evaluated in the current chapter.

The experimental methods of part II are described in section 5.5, and the system dynamics model of the gas core dynamics is proposed in section 5.6. The controller design, implementation and response are described in section 5.7. A conclusion of the whole chapter is provided in section 5.8.

5.5. METHODS OF PART II

The same experimental setup of part I is used in the experiments of part II. The most relevant equipment used in the experiments of this part are the LPO valve and ERT system.

GAS CORE DYNAMICS

The LPO valve is a pneumatic diaphragm valve with diaphragm position x_{lpo} manipulated via the control pressure imposed in the cavity of the valve by an Electro-Pneumatic Regulator (EPR). During the study of the gas core dynamics, the system inputs are made via the control pressure signal of the Electro-Pneumatic Regulator, u_{p_c}, resulting in a control pressure variation inside the LPO valve described by the EPR dynamics. Meanwhile, the control pressure variation in the cavity of the LPO valve impacts its diaphragm position, x_{lpo}, according to the LPO valve dynamics (section 2.5), and the resulting x_{lpo} variation impacts the gas core diameter in the cross-section $0.9D$ upstream of the pickup tube according to the multiphase flow dynamics. The gas core diameter is measured by the ERT system normalized by the inner diameter of the pipe, i.e., $d_{ert} = d_i/D$. The ERT system and Electro-Pneumatic Regulator operate in discrete-time, at a frequency of 10 Hz, both in the study of the gas core dynamics and in the real-time feedback control of the phase

distribution upstream of the pickup tube.

The gas core dynamics is investigated in the current chapter at two operating points with Bursting Columns upstream of the pickup tube. Although the gas core response to actions on the LPO valve is clearly visible to the naked eye in Weakly Oscillating Columns, the flow pattern is not covered in the experiments due to limitations in the resolution of ERT, which cannot detect gas cores smaller than 10% of the pipe inner diameter (section 2.8). The operating points are characterized by the combination between the speed of the experimental facility pump[2] ω_p, inlet gas mass flow rate w_g and HPO valve diaphragm position x_{hpo}, kept constant during the LPO valve inputs. Operating Point I is determined by $\omega_p = 2430$ rpm, $w_g = 8.53\ \mathrm{kg\,h^{-1}}$ and $x_{hpo} \approx 0.74$, and Operating Point II is determined by $\omega_p = 2700$ rpm, $w_g = 8.53\ \mathrm{kg\,h^{-1}}$ and $x_{hpo} \approx 0.80$.

Bursting Columns are characterized by strong gas core fluctuations (intrinsic dynamics), covering a wide range of frequencies, that act as high magnitude noise in the identification of the gas core response to inputs in the LPO valve control pressure. To be able to distinguish between the intrinsic gas core dynamics and the gas core response to the LPO valve, individual sine inputs of relatively large amplitude in the LPO valve control pressure are used in the system identification experiments, resulting in a clear peak in the gas core diameter spectrum for the frequency excited by each input.

The LPO valve has a damping response, with hysteresis, detailed in section 2.5. For a control pressure input u_{p_c} of constant amplitude, the damping response of the valve reduces the amplitude of the valve motion as the frequency of the input is increased, resulting in a poor signal-to-noise ratio of the gas core response to the valve at high frequencies due to the intrinsic dynamics. The Zero-Order Holding (see Appendix D) discrete-time transfer function with sample time 0.1 s,

$$\frac{u'_{p_c}(z)}{r'_{x_{lpo}}(z)} = 3.6 - 3.0z^{-1}, \tag{5.3}$$

is used to increase the amplitude of u_{p_c} at high frequencies, maintaining a large range of motion of the LPO valve diaphragm during the experiments. The approach results in a good signal-to-noise ratio of the gas core diameter response to the LPO valve in relation to the intrinsic dynamics for the whole range of frequencies investigated in the current chapter.

Equation 5.3 is based on a linear approximation of the inverse valve dynamics (without accounting for hysteresis), where $u'_{p_c} = u_{p_c} - \overline{u}_{p_c}$ is the control pressure input variation in bar, $r'_{x_{lpo}} = r_{x_{lpo}} - \overline{r}_{x_{lpo}}$ is the reference dimensionless LPO valve diaphragm position variation, and z is the Z-transform variable, a dimensionless complex number of discrete-time transfer functions that resembles the Laplace variable s of continuous-time transfer functions (Appendix D).

[2] A centrifugal pump is used in the experimental facility, and the liquid flow rate produced by the pump is impacted by changes in the LPO valve (section 2.6). Since the gas core in the axial cyclone strongly depends on the gas and liquid flow rates, part of the gas core dynamics upstream of the pickup tube occurs due to the liquid flow rate dynamics in the experimental facility. Therefore, the pump speed ω_p, a user input related to the pressure-liquid flow rate coupling of the pump and maintained constant during the experiments, is used to describe the operating point of the system.

The inputs used in the system identification experiments are summarized in Table 5.3. A minimum of five cycles per frequency of excitation was used during the experiments.

Table 5.3: Sine inputs used to study the gas core diameter response to control pressure inputs in the LPO valve. The inputs are given by $u_{p_c}(t) = \overline{u}_{p_c} + u'_{p_c}(t)$, where $\overline{u}_{p_c}$ is the sine wave offset (and time average) and $u'_{p_c}(t)$ is the input variation around the offset. The input variation $u'_{p_c}(t)$ is computed from variations in the reference diaphragm position of the LPO valve $r'_{x_{lpo}}(t)$ via Equation 5.3.

Number	Operating Point	Input	Frequencies
1	I	$\overline{u}_{p_c} = 4.39$ barg and $r'_{x_{lpo}} = 0.1\sin(2\pi f t)$	0.01 Hz to 2 Hz
2	I	$\overline{u}_{p_c} = 4.39$ barg and $r'_{x_{lpo}} = 0.2\sin(2\pi f t)$	0.01 Hz to 1 Hz
3	II	$\overline{u}_{p_c} = 4.48$ barg and $r'_{x_{lpo}} = 0.1\sin(2\pi f t)$	0.01 Hz to 2 Hz
4	II	$\overline{u}_{p_c} = 4.39$ barg and $r'_{x_{lpo}} = 0.2\sin(2\pi f t)$	0.01 Hz to 1 Hz

TOMOGRAPHY-BASED FEEDBACK CONTROL

A Proportional-Integral (PI) feedback controller is used to demonstrate the suppression of external disturbances by tomography-based controllers. The investigation is performed for the pump speed $\omega_p = 2700$ rpm and the HPO valve diaphragm position $x_{hpo} \approx 0.80$, where the gas mass flow rate of the experimental facility is alternated between $w_g = 8.53\ \mathrm{kgh^{-1}}$ (operating point) and $w_g = 10.86\ \mathrm{kgh^{-1}}$ every 40 s to disturb the gas core upstream of the pickup tube.

The impact of the tomography-based controller on the gas-liquid separation promoted by the axial cyclone is evaluated based on gas flow fraction captured by the pickup tube, $\xi_g \triangleq w_{g,lpo}/w_g$, the liquid flow fraction captured by the outer tube, $\xi_l \triangleq q_{l,hpo}/q_l$, and the overall efficiency of separation, $\eta \triangleq (\xi_g \cdot \xi_l)^{0.5}$, introduced as performance indicators of the axial cyclone in chapter 4. The LPO and HPO flow rates are estimated from the flow rates measured in the outlets of the LPO and HPO gravity separators (Figure 5.3), as described in Appendix B. The PI controller uses the setpoint $r_{d_{ert}} = 0.2$, chosen based on the conditions that maximized the overall efficiency of separation η of the axial cyclone in chapter 4.

5.6. GAS CORE DYNAMICS UPSTREAM OF THE PICKUP TUBE

The complete gas core dynamics upstream of pickup tube has a complex behavior, described by the nonlinear Navier-Stokes Partial Differential Equations (PDEs). These PDEs can be discretized into multiple interconnected Ordinary Differential Equations (ODEs) to describe the time-evolution of the gas core upstream of the pickup tube based on the physics of the process. However, since a single input (LPO valve control pressure) and a single output (gas core diameter measured by ERT) are used in the tomography-based feedback control investigation of this chapter, a simple and efficient alternative to the PDE discretization is the approximation of the gas core dynamics by an empirical transfer function, obtained via system identification. Since the phase distribution physics is originally described by PDEs, high-order transfer functions (with multiple poles and zeros) are re-

quired to capture the gas core dynamics in the simplified model.

Approximating the gas core dynamics upstream of the pickup tube as linear around the operating point, the normalized gas core diameter $d_{ert}(t)$ can be written as the superposition[3] between: (i) the average normalized gas core diameter of the operating point, $\overline{d}_{ert}$; (ii) the normalized gas core diameter variation caused by changes in the LPO valve, δ; (iii) the normalized gas core diameter variation due to external disturbances, ζ, e.g., from changes in the inlet gas and liquid flow rates of the axial cyclone; (iv) the random zero-average intrinsic gas core dynamics ϵ, caused by the swirling gas-liquid flow patterns:

$$d_{ert}[k] = \overline{d}_{ert} + \delta[k] + \zeta[k] + \epsilon[k] \tag{5.4}$$

In Equation 5.4, k is the sample number, related to (continuous) time via $t = kT_s$. The ERT system used in the experiments has a sample time $T_s = 0.1$ s, based on the measurement rate of 10 Hz of the ERT system.

Following the linear approximation of the gas core dynamics around the operating point, the gas core diameter variations created by LPO valve control pressure input variations are described by the transfer function

$$P(z) \triangleq \frac{\delta(z)}{u'_{p_c}(z)}, \tag{5.5}$$

where $u'_{p_c} \triangleq u_{p_c} - \overline{u}_{p_c}$ is the control pressure input variation in relation to the operating point, in bar. By definition, $\overline{u}_{p_c}$ is the control pressure required to obtain the time-average gas core diameter $\overline{d}_{ert}$ in the absence of external disturbances ($\zeta = 0$) for $\delta = 0$. Since δ is dimensionless, $P(z)$ has unit bar^{-1}.

The transfer function $P(z)$ is the Plant of the tomography-based controller described in section 5.7, and includes the dynamics of the Electro-Pneumatic Regulator and valve (actuator), flow (process) and ERT system (sensor). Although not pursued in the current chapter, ζ and ϵ are strongly related to the upstream flow and can be modeled based on the upstream flow gas fraction to design feedforward or predictive controllers (part I).

As described in section 5.5, the gas core dynamics is studied in the absence of external disturbances ($\zeta = 0$) via sine inputs of large amplitude in u'_{p_c}, resulting in a small contribution of ϵ in relation to δ to the gas core diameter spectrum for the frequency excited at each input. As consequence, the gas core response to the valve, δ, can be approximated as $\delta(\omega) \approx d'_{ert}(\omega)$ for the angular frequency ω of the sine input, where $d'_{ert} \triangleq d_{ert} - \overline{d}_{ert}$ is the normalized gas core diameter variation and $d'_{ert}(\omega)$ is the Fourier Transform of $d'_{ert}(t)$.

Figure 5.12 presents the experimental magnitude and phase of $P(z)$, computed based on the Fourier Transforms of $d'_{ert}(t)$ and $u'_{p_c}(t)$ measured in the axial cyclone for the inputs described in Table 5.3. The data presented shows a similar system response for Operating Point I (inputs 1 and 2) and Operating Point II (inputs 3 and 4) and, therefore, a single model for the axial cyclone dynamics is proposed for both operating points.

[3] The superposition is an approximation that simplifies the system dynamics modeling and controller design. In reality, the intrinsic dynamics are impacted by changes in the gas and liquid flow rates of the system, thus being affected by external disturbances. For instance, the length of Taylor bubbles and liquid slugs upstream of the swirl element, strongly related to the intrinsic dynamics in the axial cyclone, is determined by the gas and liquid flow rates of the system. Additionally, the superposition hypothesis may also break for external disturbances and LPO valve inputs at frequencies close to the intrinsic dynamics, due to the strong nonlinear flow behavior.

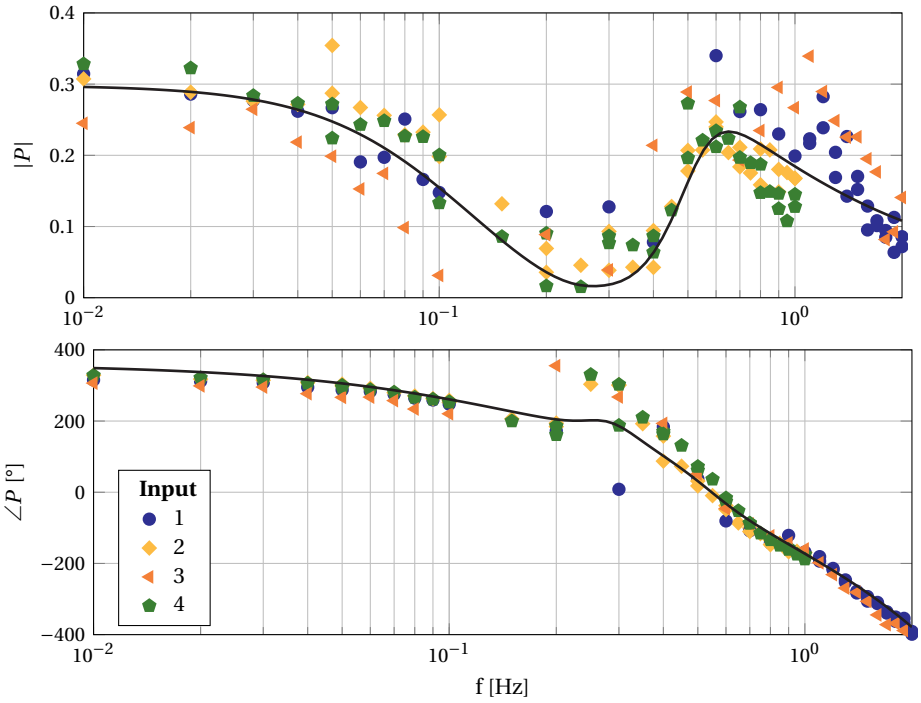

Figure 5.12: Magnitude ($|P|$) and phase ($\angle P$) of the discrete-time transfer function $P(z)$. Colored marks: measured data for the control pressure inputs described in Table 5.3. Continuous black line: Bode plot of $P(z)$ based on Equation 5.6.

Linear systems always have the same transfer function magnitude and phase, regardless of the form or amplitude of the input. The experimental data of Figure 5.12 shows that, in reality, the gas core has a nonlinear response to control pressure inputs, with different magnitudes of $P(z)$ being obtained for the same frequency of excitation in different inputs. The nonlinearity in the system response arises from the valve hysteresis (subsection 2.5.3 of chapter 2) and the nonlinear impact of the LPO valve diaphragm position on the gas core diameter (subsection 4.3.1 of chapter 4). Since modeling valve hysteresis is complex and beyond the scope of this research, the gas core dynamics around both Operating Points I and II is approximated by the (setup-dependent) fifth-order discrete-time (linear) transfer function with sample time $T_s = 0.1$ s:

$$P(z) = \frac{0.0860(z^2 - 1.9106z + 0.9355)(z^2 - 2.0541z + 1.0951)}{(z - 0.6218)(z - 0.8791)(z - 0.9371)(z^2 - 1.7114z + 0.8137)} z^{-4} \tag{5.6}$$

The magnitude and phase of $P(z)$ as function of the frequency, obtained for $z = e^{i2\pi f T_s}$ (Appendix D), are plotted as continuous black lines in Figure 5.12.

The transfer function $P(z)$ has 5 poles, 4 zeros and a delay of four samples. The poles and zeros of $P(z)$ are presented in Figure 5.13, and the delay of four samples (0.4 s) is represented by the term z^{-4} in Equation 5.6.

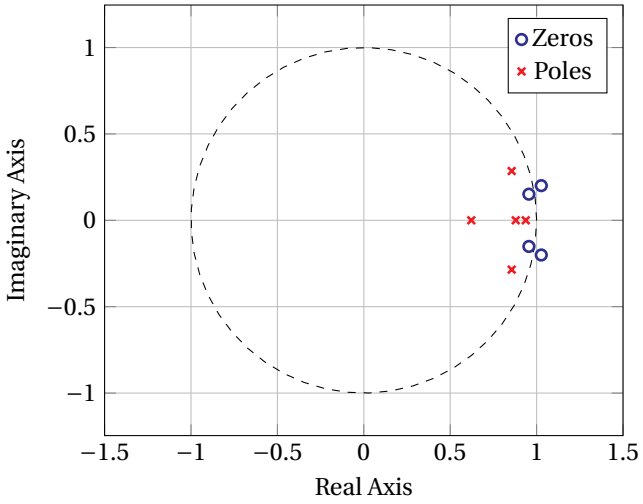

Figure 5.13: Poles and zeros of the discrete-time transfer function $P(z)$, described by Equation 5.6.

As shown in Figure 5.13, all five poles of $P(z)$ are inside the complex plane unit circle and, therefore, the system is stable. However, two out of the four zeros of the transfer function are outside the unit circle (nonminimum-phase zeros), which can cause the feedback loop to become unstable depending on the controller gains. Moreover, zeros outside the unit circle can reverse the initial motion of the system towards the steady state solution, as illustrated by the unit step response of $P(z)$ presented in Figure 5.14.

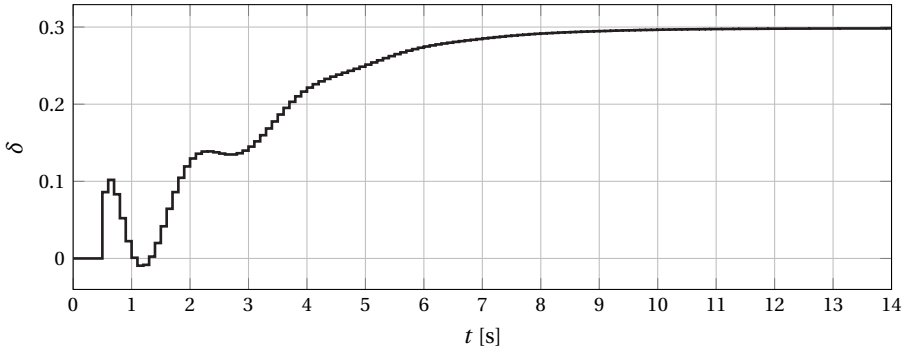

Figure 5.14: Unit step response of $P(z)$.

Figure 5.14 shows that the variation in the gas core diameter component δ quickly increases to $\delta \approx 0.1$ around 0.5 s after a unit step change is made in the LPO valve control pressure variation u'_{p_c}. However, instead of continuing to grow towards the steady state solution $\delta \approx 0.3$, the gas core diameter component related to the LPO valve decreases back of $\delta \approx 0$ due to the nonminimum-phase zeros of $P(z)$, only reaching 95% of the steady state value 6.8 s after the step input is made in the system (settling time).

5.7. TOMOGRAPHY-BASED FEEDBACK CONTROL

A feedback PI controller was implemented in the LabVIEW code of the experimental facility to demonstrate the suppression of external disturbances in the gas core diameter upstream of the pickup tube by tomography-based feedback controllers. The PI controller uses Electrical Resistance Tomography (ERT) measurements of the gas core diameter in the cross-section $0.9D$ upstream of the pickup tube to compute control actions in the LPO valve, as previously illustrated in Figure 5.1. The tomography-based feedback controller is implemented according to the block diagram of Figure 5.15.

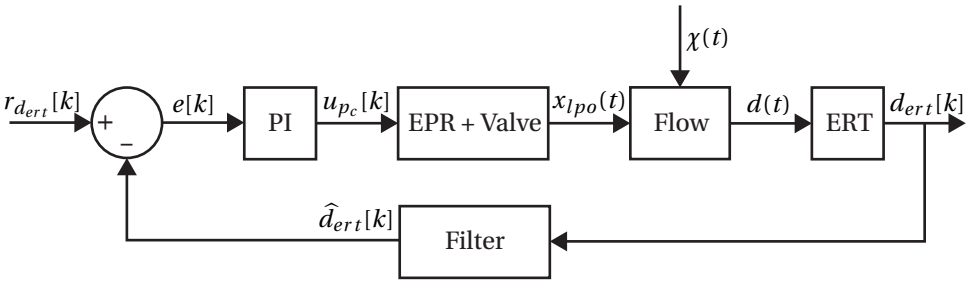

Figure 5.15: Closed-loop block diagram of the gas core diameter measured by ERT with a PI controller that acts on the LPO valve. The gas core diameter upstream of the pickup tube divided by the inner diameter of the pipe, $d(t)$ (continuous-time signal), is sampled by the ERT system at 10 Hz as $d_{ert}[k]$ (discrete-time signal). The ERT signal is filtered into $\widehat{d}_{ert}[k]$ and subtracted from the reference normalized gas core diameter $r_{d_{ert}}[k]$, resulting in the error signal $e[k]$ that is used by the PI controller to compute the input $u_{p_c}[k]$ sent to the Electro-Pneumatic Regulator (EPR) of the LPO valve. The controller output $u_{p_c}[k]$ changes the LPO valve diaphragm position $x_{lpo}(t)$, impacting the normalized gas core diameter $d(t)$. The gas mass flow rate, pump speed and HPO valve opening also play a role in the gas core diameter upstream of the pickup tube, being combined in the term $\chi(t)$.

In the block diagram of Figure 5.15, the gas core diameter divided by the inner diameter of the pipe, $d(t)$, is determined by flow dynamics based on (i) the LPO valve diaphragm position $x_{lpo}(t)$, and (ii) the gas mass flow rate, pump speed and HPO valve opening, summarized in the term $\chi(t)$. The pump speed and HPO valve opening are kept constant during the experiments, while the gas mass flow rate is manipulated to create external disturbances in the gas core diameter via $\chi(t)$.

The normalized gas core diameter is measured upstream of the pickup tube by the ERT system at 10 Hz as $d_{ert}[k]$, where k is the k-th sample of the ERT sensor signal. Inside the controller, the ERT signal is filtered into $\widehat{d}_{ert}[k]$ by a low-pass filter, and compared to the normalized gas core diameter reference $r_{d_{ert}}[k]$, to compute the control pressure input $u_{p_c}[k]$ sent to the Electro-Pneumatic Regulator (EPR) connected to the LPO valve. A Zero-Order Holding of $u_{p_c}[k]$ is maintained between samples by the feedback controller, which operates with sample time $T_s = 0.1$ s based on the frequency of 10 Hz of the ERT system.

The controller adjusts the control pressure input $u_{p_c}[k]$ whenever disturbances are detected in the gas core diameter ($d_{ert}[k] \neq r_{d_{ert}}[k]$), changing the diaphragm position of the LPO valve $x_{lpo}(t)$ according to the EPR and LPO valve dynamics (EPR+Valve block). The resulting change in $x_{lpo}(t)$ impacts the gas core diameter upstream of the pickup tube

according to the flow response to the LPO valve (Flow block).

The high amplitude and frequency of the intrinsic dynamics in the Bursting regime cannot be suppressed by the tomography-based feedback controller, particularly due to the slow LPO valve response. Since there is a clear separation between the time-constants of the intrinsic dynamics ($\mathcal{O}(0.1\text{ s})$) and external disturbances ($\mathcal{O}(10\text{ s})$) for the conditions investigated in the current chapter, the intrinsic dynamics are filtered out from the controller computations by a low-pass filter to stabilize the closed loop response of the system. The filter time constant $\tau_f = 1$ s (cutoff frequency 1 rad s^{-1}) was chosen to remove the majority of the intrinsic dynamics from the controller calculations, while still retaining a relatively fast detection of external disturbances in the gas core diameter by the controller. The low-pass filter is implemented in discrete-time as[4]:

$$\widehat{d}_{ert}[k] = \frac{10\widehat{d}_{ert}[k-1] + d_{ert}[k]}{11}, \tag{5.7}$$

corresponding to the discrete-time transfer function:

$$H(z) \triangleq \frac{\widehat{d}_{ert}(z)}{d_{ert}(z)} = \frac{z}{11z-10} \tag{5.8}$$

The removal of the intrinsic dynamics from the control loop computations impacts the choice of gas core diameter setpoint of the controller, and the maximum efficiency of separation that can be obtained by tomography-based controllers. For instance, it is expected that a perfect separation of the phases is obtained in the axial cyclone for a gas core diameter equal to the pickup tube diameter, making the pickup tube diameter a natural choice for the gas core diameter setpoint of the tomography-based controller ($r_{d_{ert}} \approx 0.45$). However, as shown in chapter 4, the maximum efficiency of separation that can be obtained in the cyclone without controlling the intrinsic dynamics occurs for time-average gas cores diameters significantly smaller than the pickup tube diameter, due to the impact of the strong flow pattern fluctuations of Bursting Columns on the capture of gas and liquid by the pickup and outer tubes, respectively.

The maximum overall efficiency of separation for a pump speed $\omega_p = 2700$ rpm, gas mass flow rate $w_g = 8.53$ kg h^{-1} and diaphragm position of the HPO valve $x_{hpo} \approx 0.80$, corresponding to Operating Point II of the axial cyclone, was obtained for time-average gas core diameters around 20% of the inner diameter of the pipe in chapter 4. Therefore, the reference $r_{d_{ert}} = 0.2$ is used in the tomography-based real-time control experiments of the current chapter.

[4] In continuous-time, a low-pass filter based on the gas core diameter is described by:

$$\tau_f \frac{d\widehat{d}_{ert}}{dt} + \widehat{d}_{ert} = d_{ert}$$

Based on the implicit Euler method, the equation can be approximated in discrete-time as:

$$\tau_f \frac{\widehat{d}_{ert}[k] - \widehat{d}_{ert}[k-1]}{T_s} + \widehat{d}_{ert}[k] = d_{ert}[k]$$

Equation 5.7 is obtained evaluating the equation above for $\tau_f = 1$ s and $T_s = 0.1$s.

Figure 5.16 presents the gas core diameter measured by ERT d_{ert} (in blue), and the filtered gas core diameter $\widehat{d}_{ert}$ (in orange), for Operating Point II with $x_{lpo} \approx 0.81$ in the absence of external disturbances or control actions.

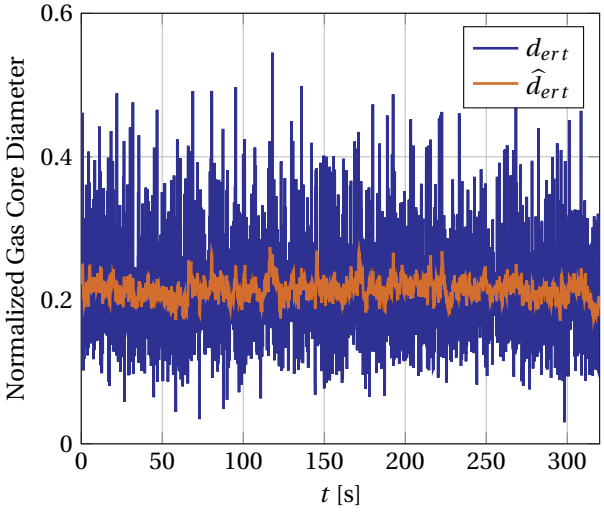

Figure 5.16: Normalized gas core diameter obtained for a pump speed $\omega_p = 2700$ rpm, gas mass flow rate $w_g = 8.53\ \mathrm{kg\,h^{-1}}$, diaphragm position of the LPO valve $x_{lpo} \approx 0.81$ and diaphragm position of the HPO valve $x_{hpo} \approx 0.80$. Blue: gas core diameter divided by the inner diameter of the pipe measured by the ERT system (d_{ert}). Orange: output of the low-pass filter with time constant 1 s ($\widehat{d}_{ert}$).

The high amplitude of the intrinsic dynamics is evident in the blue signal of Figure 5.16, that has time-average $\overline{d}_{ert} = 0.21$ and standard deviation $\sigma(d_{ert}) = 0.072$. A clear damping of the intrinsic dynamics by the low-pass filter is observed in the orange signal of Figure 5.16, that has the same time-average of $d_{ert}(t)$, $\overline{d}_{ert} = 0.21$, but a much lower standard deviation, $\sigma(\widehat{d}_{ert}) = 0.015$. The capture of gas by the pickup tube, liquid by the outer tube, and the overall efficiency of separation obtained for the gas core of Figure 5.16 are $\xi_g = 0.88$, $\xi_l = 0.74$ and $\eta = 0.81$, respectively.

5.7.1. CONTROLLER DESIGN

The Proportional-Integral (PI) feedback controller, used to suppress external disturbances in the gas core diameter measured by ERT, is implemented in discrete-time based on the trapezoidal rule approximation of continuous-time PI controllers:

$$u_{p_c}[k] = u_{p_c}[k-1] + K\left(e[k] - e[k-1] + \frac{T_s}{T_i}\frac{e[k]+e[k-1]}{2}\right), \tag{5.9}$$

In Equation 5.9, K is the proportional gain of the controller, T_i is the integration time and $e[k] = r_{d_{ert}}[k] - \widehat{d}_{ert}[k]$ is the error signal. The PI controller of Equation 5.9 has the discrete-time transfer function:

$$C(z) \triangleq \frac{u'_{p_c}(z)}{e(z)} = K\frac{(1+0.5T_s/T_i)\,z-(1-0.5T_s/T_i)}{z-1} \tag{5.10}$$

Following the linear model for the gas core dynamics proposed in section 5.6, the normalized gas core diameter measured by ERT is modeled as

$$d'_{ert}(z) = \delta(z) + \zeta(z) + \epsilon(z), \tag{5.11}$$

where $\delta = Pu'_{p_c}$ is the linear approximation of the gas core response to control pressure inputs in the LPO valve, described by Equation 5.6, and ζ is the normalized gas core diameter variation due to external disturbances.

Since the controller is designed with the constant reference $r_{d_{ert}} = \overline{d}_{ert}$, the error signal can be written as $e[k] = -\widehat{d}'_{ert}[k]$. Therefore, from Equation 5.10, the controller output can be written based on the filtered gas core diameter variation as $u'_{p_c} = -C\widehat{d}'_{ert}$, and, from Equation 5.8, the filtered gas core diameter variation can be written as $\widehat{d}'_{ert} = Hd'_{ert}$. Then, based on the block diagram of Figure 5.15, the linear approximation of the closed loop response of the gas core diameter upstream of the pickup tube is given by

$$d'_{ert}(z) = \frac{\zeta(z)+\epsilon(z)}{1+H(z)C(z)P(z)}, \tag{5.12}$$

where $H(z)$, $C(z)$ and $P(z)$ are the (discrete-time) transfer functions of the low-pass filter (Equation 5.8), controller (Equation 5.10) and Plant (Equation 5.6), respectively.

Equation 5.12 shows that both external disturbances and intrinsic dynamics impact the controlled gas core diameter. By design, the filter transfer function $H(z)$ has a low amplitude for high frequencies, damping the product HCP and resulting in gas core variations approximately equal to the intrinsic dynamics ($d'_{ert}(z) \approx \epsilon(z)$) in the absence of external disturbances ($\zeta = 0$).

The product HCP becomes significant at low frequencies, due to the high amplitude of the low-pass filter response, allowing to tune controller gains to suppress external process disturbances in ζ. From Equation 5.12, the closed-loop gas core diameter response to external disturbances, without accounting for the contribution of the intrinsic dynamics to d'_{ert} ($\epsilon = 0$), is described by:

$$\frac{d'_{ert}(z)}{\zeta(z)} = \frac{1}{1+H(z)C(z)P(z)}, \tag{5.13}$$

The controller constants $K = 1.5$ bar and $T_i = 2$ s were chosen based on Equation 5.13 targeting a step response to external disturbances with settling time below 10 s. The unit step response of Equation 5.13 for a gain of $K = 1.5$ bar and integral time of $T_i = 2$ s is presented in Figure 5.17.

Figure 5.17 shows that the gas core variation d'_{ert} decays to zero with settling time 8.2 s (based on the 5% threshold interval). A step change in ζ represents a sudden change in the gas core diameter upstream of the pickup tube, created by an external disturbance, that is detected by the tomography-based controller. Although faster decays in the step response can be obtained increasing K, the increase in the controller gain leads to larger overshoots and, as consequence, larger settling times in the closed loop response of the system.

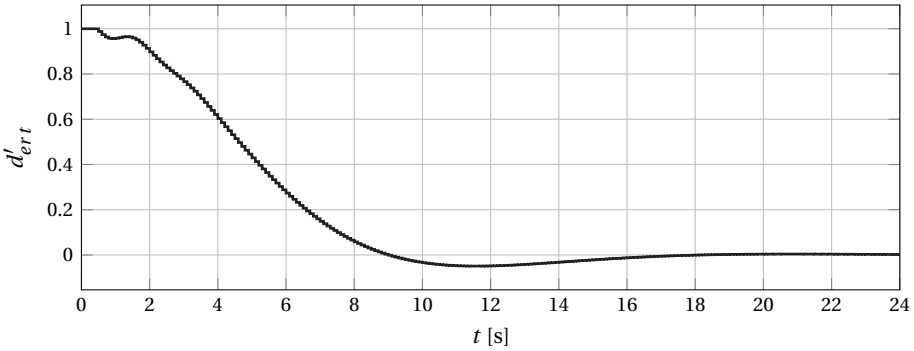

Figure 5.17: Closed loop response of the gas core diameter variation d'_{ert} to a unit step in ζ, obtained from Equation 5.13 for $K = 1.5$ bar and $T_i = 2$ s. The intrinsic dynamics ϵ is not included in the plot.

5.7.2. CONTROL IN THE ABSENCE OF EXTERNAL PROCESS DISTURBANCES

Since the nonlinearities in the system response (valve hysteresis and nonlinear impact of x_{lpo} on the gas core diameter) are not included in the design of the controller, the closed loop stability of the system is experimentally verified for statistically-steady process conditions prior to the suppression of external disturbances. As the control actions are based on the filtered ERT signal, which removes the majority of the intrinsic dynamics from the control loop, a minor impact of the tomography-based PI controller on the gas core diameter is expected in the absence of external process disturbances. Figure 5.18 shows the controlled gas core diameter upstream of the pickup tube for Operating Point II in the absence of external process disturbances.

A small reduction in the time-average gas core diameter was obtained for the controlled gas core diameter of Figure 5.18, where $\overline{d}_{ert} = 0.20$, in relation to the uncontrolled gas core diameter of Figure 5.16, where $\overline{d}_{ert} = 0.21$ was obtained for the constant LPO valve diaphragm position $x_{lpo} \approx 0.81$. The small reduction in the time-average gas core diameter occurred because the controller adjusted the LPO valve to bring the filtered gas core diameter closer to its setpoint, $r_{d_{ert}} = 0.2$. In relation to the intrinsic dynamics, the gas core diameter measured by ERT has the same standard deviation $\sigma(d_{ert}) = 0.072$ for both the uncontrolled and controlled scenarios, indicating a negligible impact of the controller on the intrinsic gas core dynamics.

The control of the gas core diameter in the absence of external disturbances results in the gas capture by the pickup tube $\xi_g = 0.92$, liquid capture by the outer tube $\xi_l = 0.70$, and overall efficiency of separation $\eta = 0.80$. When compared to the uncontrolled case of Figure 5.18, where $\xi_g = 0.88$, $\xi_l = 0.74$ and $\eta = 0.81$, an increase of 0.04 in the gas capture by the pickup tube, a decrease of 0.04 in the liquid capture by the outer tube, and roughly the same η, were obtained by the controller. The small impact of the controller on the efficiency of the process occurs due to the slight reduction in the time average gas core diameter, leading to a larger fraction of the total gas and liquid flows captured by the pickup tube, increasing ξ_g and decreasing ξ_l.

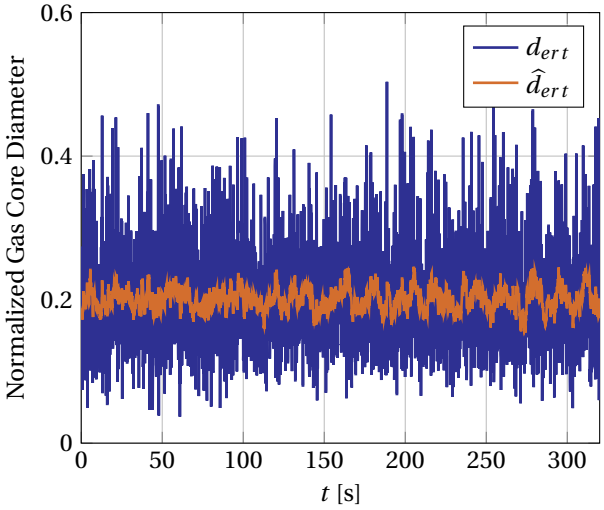

Figure 5.18: Controlled gas core diameter obtained for a pump speed $\omega_p = 2700$ rpm, gas mass flow rate $w_g = 8.53\ \mathrm{kg\,h^{-1}}$ and diaphragm position of the HPO valve $x_{hpo} \approx 0.80$. Blue: gas core diameter divided by the inner diameter of the pipe measured by the ERT system. Orange: output of the low-pass filter with time constant 1 s.

The results obtained in the current subsection show that the control loop is stable in the absence of external disturbances, despite the nonlinearities of the real system. Additionally, despite shifting the average gas core diameter to its reference, the tomography-based real-time controller has a minor impact on the efficiency of separation compared to the uncontrolled case in the absence of external disturbances, which was expected since the intrinsic dynamics are filtered out from the controller calculations.

5.7.3. CONTROL IN THE PRESENCE OF EXTERNAL PROCESS DISTURBANCES

A square wave that alternates the gas mass flow rate of the experimental facility between $w_g = 8.53\ \mathrm{kg\,h^{-1}}$ and $w_g = 10.86\ \mathrm{kg\,h^{-1}}$, every 40 s, is used to evaluate the suppression of external process disturbances in the phase distribution upstream of the pickup tube by the tomography-based feedback controller. Figure 5.19 shows the impact of the (external) gas mass flow rate disturbance on the gas core diameter for Operating Point II in the absence of control actions.

Figure 5.19 shows that both the gas core diameter d_{ert} and the filtered gas core diameter $\widehat{d}_{ert}$ follow the square wave changes in the gas mass flow rate of the experimental facility without the tomography-based controller, with the filtered gas core diameter alternating between $\widehat{d}_{ert} \approx 0.21$ for $w_g = 8.53\ \mathrm{kg\,h^{-1}}$ and $\widehat{d}_{ert} \approx 0.28$ for $w_g = 10.86\ \mathrm{kg\,h^{-1}}$. When compared to the undisturbed gas core diameter of Figure 5.16, the disturbance leads to an increase in the standard deviation of the gas core diameter from $\sigma(d_{ert}) = 0.072$ to $\sigma(d_{ert}) = 0.090$, and filtered gas core diameter from $\sigma(d_{ert}) = 0.015$ to $\sigma(d_{ert}) = 0.032$.

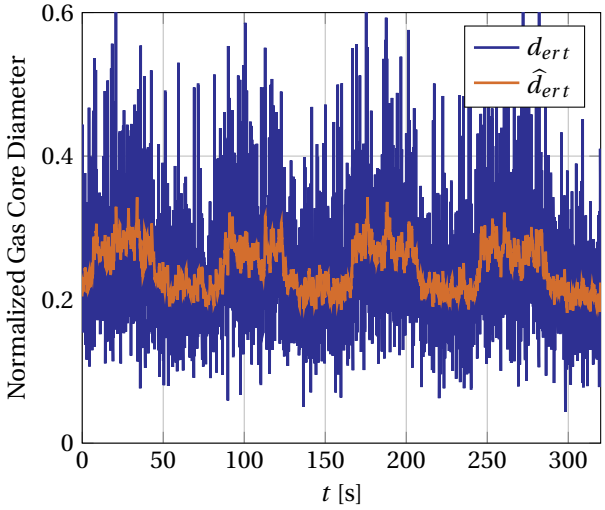

Figure 5.19: Uncontrolled gas core diameter obtained for a pump speed ω_p = 2700 rpm, gas mass flow rate alternating between w_g = 8.53 kgh^{-1} and w_g = 10.86 kgh^{-1} every 40 s, diaphragm position of the LPO valve $x_{lpo} \approx 0.82$ and diaphragm position of the HPO valve $x_{hpo} \approx 0.80$. Blue: gas core diameter divided by the inner diameter of the pipe measured by the ERT system. Orange: output of the low-pass filter with time constant 1 s.

The disturbance results in $\xi_g = 0.76$, $\xi_l = 0.75$ and, as consequence, an overall efficiency of separation $\eta = 0.75$. A relatively low capture of gas by the pickup tube is obtained in the axial cyclone for the disturbed flow compared to the uncontrolled and undisturbed scenario of Figure 5.16, where $\xi_g = 0.88$, $\xi_l = 0.74$ and $\eta = 0.81$. The reduction in ξ_g with the disturbance is a consequence of the widening of the gas core for w_g = 10.86 kgh^{-1}, resulting in the capture of a larger fraction of the total gas flow rate in the inlet of the axial cyclone by the outer tube. The capture of liquid by the outer tube was roughly the same for the undisturbed and disturbed scenarios, resulting in a decay of 0.06 in the overall efficiency of separation in relation to the condition without disturbances or control actions (Figure 5.16).

Figure 5.20 presents the gas core diameter upstream of the pickup tube regulated by the tomography-based PI controller in the presence of the square-wave external disturbance in the gas mass flow rate of the experimental facility.

Figure 5.20 shows that the filtered gas core diameter $\widehat{d}_{ert}$ is kept around the controller reference $r_{d_{ert}} = 0.2$ during the entire measurement, despite the gas mass flow rate disturbance. When compared to the uncontrolled and undisturbed scenario of Figure 5.16, a small increase in the standard deviation of the gas core diameter from $\sigma(d_{ert}) = 0.072$ to $\sigma(d_{ert}) = 0.080$ is obtained when suppressing the external disturbance with the controller, due to the larger amplitude of the intrinsic gas core dynamics for w_g = 10.86 kgh^{-1}.

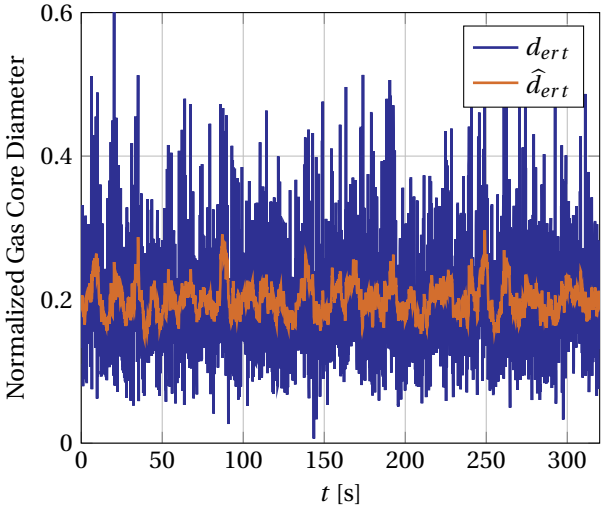

Figure 5.20: Controlled gas core diameter obtained for a pump speed ω_p = 2700 rpm, gas mass flow rate alternating between w_g = 8.53 kgh^{-1} and w_g = 10.86 kgh^{-1} every 40 s, and diaphragm position of the HPO valve $x_{hpo} \approx 0.80$. Blue: gas core diameter divided by the inner diameter of the pipe measured by the ERT system. Orange: output of the low-pass filter with time constant 1 s.

The real-time control of the gas core diameter upstream of the pickup tube during the external gas mass flow rate disturbance results in $\xi_g = 0.93$, $\xi_l = 0.63$ and $\eta = 0.77$. Compared to the uncontrolled case with the same external disturbance (Figure 5.19), where $\xi_g = 0.76$, $\xi_l = 0.75$ and $\eta = 0.75$, the controller suppression of external disturbances results in an increase of 0.17 in the capture of air by the pickup tube and a decrease of 0.12 in the capture of water by the outer tube, due to a reduction in the gas core diameter upstream of the pickup tube when $w_g = 10.86$ kgh^{-1}. The combined increase in gas capture by the pickup tube and decrease in liquid capture by the outer tube resulted in an increase of 0.02 in the overall efficiency of separation in relation to the uncontrolled scenario. Despite the small gain in η, a notorious increase in ξ_g was achieved by the controller, showing that it can be used in applications where the capture of gas by the pickup tube is more important than the capture of liquid by the outer tube.

The results described along section 5.7 are summarized in Table 5.4.

Table 5.4: Standard deviation of the gas core diameter and cyclone performance indicators obtained for the process conditions presented in section 5.7.

Condition	$\sigma(d_{ert})$	$\sigma(\widehat{d}_{ert})$	ξ_g	ξ_l	η
Undisturbed and Uncontrolled (Figure 5.16)	0.072	0.015	0.88	0.74	0.81
Undisturbed and Controlled (Figure 5.18)	0.072	0.015	0.92	0.70	0.80
Disturbed and Uncontrolled (Figure 5.19)	0.090	0.032	0.76	0.75	0.75
Disturbed and Controlled (Figure 5.20)	0.080	0.023	0.93	0.63	0.77

The current section showed that tomography-based feedback controllers can suppress external process disturbances in the distribution of phases of multiphase flows, as demon-

strated by the maintenance of the filtered gas core diameter upstream of the pickup tube around its setpoint for ~ 25% gas mass flow rate disturbances in the cyclone inlet. However, Table 5.4 shows that the suppression of external disturbances by the tomography-based controller has a limited impact on the overall efficiency of separation obtained by the axial cyclone.

As discussed in chapter 4, the large-amplitude intrinsic dynamics plays a big role in the overall efficiency of the axial cyclone. Therefore, faster actuators must be developed to attempt to control the intrinsic dynamics, maximizing the performance gains that can be obtained with tomography-based controllers. However, even faster actuators might be unable to (fully) control the intrinsic dynamics, due to its nonlinear and chaotic nature.

5.8. CONCLUSION

The objective of this chapter was to investigate (i) the phase distribution dynamics, and (ii) the possibilities and limitations of tomography-based real-time control of axial cyclone separators. The research performed showed that:

- The gas core dynamics in the axial cyclone can be split into two components: (i) the intrinsic dynamics, related to the swirling gas-liquid flow patterns and resulting in an unsteady (chaotic) phase distribution in the cyclone with time-constants in the order of 0.1 s; (ii) the phase distribution response to external disturbances, with time-scales in the same order of the process disturbance (in the order of 10 s in the current chapter). The intrinsic dynamics are too fast to be controlled with typical control valves, and must filtered out of the calculations performed by slow process controllers, designed to suppress external disturbances in the phase distribution with time-constants considerably larger than the intrinsic dynamics.
- The phase distribution inside the axial cyclone and upstream of the swirl element are connected via conservation of mass, with the majority of the intrinsic gas core dynamics propagating from the upstream flow (section 5.3). Therefore, in principle, phase distribution measurements of the upstream flow can be used to act on the system (e.g., via a feedforward controller connected to the LPO valve) before the upstream flow pattern fluctuations reach the pickup tube, impacting the separation.
- External disturbances in the gas core upstream of the pickup tube with time-scales in the order of 10 s can be suppressed by the electrical resistance tomography-based feedback controller presented in section 5.7, which was able to maintain the filtered gas core diameter upstream of the pickup tube within ~ 15% of its setpoint despite ~ 25% disturbances in the gas mass flow rate of the cyclone. The results obtained with the axial cyclone show that tomography-based real-time controllers are able to suppress slow external disturbances in the phase distribution of multiphase flows.
- A negligible gain in overall efficiency of separation was obtained by the tomography-based suppression of external disturbances in the distribution of phases upstream of the pickup tube for Bursting Columns; this occurred due to the large impact of the uncontrolled intrinsic dynamics (large-amplitude flow pattern fluctuations) on the capture of gas and liquid by the pickup and outer tubes.

- Since the intrinsic dynamics have a big impact on the axial cyclone performance, faster actuators must be developed in future works to try to act on the intrinsic dynamics, maximizing the gain in overall efficiency of separation which can be obtained with the tomography-based real-time control of the phase distribution in the equipment. However, even though faster actuators might be able improve the overall efficiency of separation, they might not be able to fully control the intrinsic dynamics due to the chaotic behavior of the nonlinear multiphase flow physics.

CHAPTER 6

CONCLUSION

The phase distribution plays a crucial role in multiphase flow processes and, therefore, the real-time control of the distribution of phases is desired. The phase distribution can be measured with industrial tomography, that became considerably faster in the recent years due to the increase in computational power, opening the door to real-time control applications. The main objective of this thesis was to investigate, for the first time, the possibilities and limitations of tomography-based real-time control of multiphase flows.

Multiphase flows have a complex phase distribution dynamics, that includes: (i) flow pattern fluctuations, *intrinsic* to the nonlinear physics of multiphase flows, and (ii) the flow response to external disturbances in the boundary conditions of the process, such as changes in the (ensemble-average) inlet flow rate of each phase. While the phase distribution dynamics due to the flow patterns is fast, with time-constants in the order of 0.1 s, external disturbances are process-dependent, impacting the phase distribution of multiphase flows in different time-scales. The distinction between intrinsic dynamics and external disturbances, proposed in this dissertation, is particularly useful for external disturbances considerably slower than the intrinsic dynamics.

Ideally, tomography-based real-time controllers should be able to maintain a phase distribution that maximizes the efficiency of the process in important locations of multiphase flow equipment, suppressing external disturbances and flow pattern fluctuations (intrinsic dynamics) in the distribution of phases. However, the real-time control of the intrinsic dynamics is challenging, due to its small time-constants and chaotic nature, in practice limiting the tomography-based real-time control of multiphase flows to the suppression of slow external process disturbances (e.g., with time-scales in the order of 10 s).

The field of multiphase flows is broad, with applications ranging from quasi-1D flows, such as gas-liquid flows in pipes, to three-dimensional flows, e.g., in bubble columns. Quasi-1D flows are simpler to measure and control than 3D flows, and a gas-liquid axial cyclone separator was used in this dissertation to investigate the key aspects of tomography-based real-time control of multiphase flows.

The analysis performed in the previous chapters addressed: (i) the design of a fast real-time tomography algorithm for axial cyclone separators (chapter 2); (ii) the swirling gas-liquid flow patterns that can be created in the axial cyclone, and their prediction via simple mechanistic models (chapter 3); (iii) the relation between phase distribution upstream of the pickup tube and axial cyclone separator performance (chapter 4); (iv) the phase distribution dynamics in the axial cyclone, and the design and implementation of an electrical resistance tomography-based feedback controller to suppress slow external disturbances in the distribution of phases upstream of the pickup tube (chapter 5). The current chapter reflects on the main takeaways obtained with the axial cyclone separator, and how they extend to the tomography-based control of other multiphase flows.

6.1. UPWARD SWIRLING GAS-LIQUID FLOW PATTERNS IN VERTICAL PIPES

The vertical upward swirling gas-liquid pipe-flow patterns can be divided into four classes (chapter 3):

- **Non-columnar flows**, obtained for low azimuthal liquid velocities. Non-columnar flows occur when the upstream flow patterns simply propagate across the swirl element, without a significant impact of the added swirl on the distribution of phases.
- **Centered flows**, formed downstream of the swirl element for intermediary azimuthal liquid velocities, where the centripetal force causes the accumulation of the gas regions of the upstream flow (e.g, bubbles) around the pipe centerline.
- **Columnar flows**, obtained in the axial cyclone when centered flows coalesce into stable gas cores, at high azimuthal liquid velocities. Columnar flows are the most relevant flow patterns for axial cyclones separators, where phase separation is obtained capturing the gas core with the pickup tube.
- **Swirling Annular flows**, obtained in swirling gas-liquid flows for high gas flow rates.

The flow patterns inside each class are determined by the flow pattern upstream of the swirl element. For instance, upstream Bubbly flows are transformed into Weakly Oscillating (gas) Columns downstream of the swirl element for sufficiently strong swirls, while upstream Slug flows are transformed into Bursting Columns, a swirling gas-liquid flow pattern characterized by strong phase distribution fluctuations. The strong dependency of the cyclone flow on the upstream flow was confirmed via cross-correlations in chapter 5.

The most important dimensionless numbers describing the flow pattern transitions in non-swirling gas-liquid flows in vertical pipes (and upstream of the swirl element) are the gas and liquid Froude numbers, Fr_g and Fr_l. The addition of swirl to the flow results in the two additional dimensionless numbers relevant to the swirling gas-liquid flow pattern transitions, the liquid swirl number, Ω_l, and the gas swirl number, Ω_g.

The gas swirl number is only relevant to Swirling Annular flows, and the remaining vertical upward swirling gas-liquid flow pattern transitions are mainly determined by the dimensionless numbers Fr_l, Fr_g and Ω_l. From this perspective, the liquid swirl number can be seen as a third axis added to classical non-swirling flow pattern maps for a wide range of conditions, where the non-swirling flow patterns are recovered for $\Omega_l = 0$.

The analysis of the physics behind Centered and Columnar flows revealed that the transition between Non-Columnar, Centered and Columnar flows is mainly determined by the product of the liquid Froude and Swirl numbers, $Fr_l\Omega_l$, related to (the square root of) the ratio between the centripetal and gravitational accelerations of the flow. Additionally, the observations made in the axial cyclone suggests that most flow pattern transitions inside each class are determined by the upstream flow pattern, that can be predicted via models for non-swirling upward gas-liquid flows in vertical pipes, e.g., the mechanistic flow pattern transition criteria of Taitel *et al.* [106] or Mishima and Ishii [107]. This led to the development of flow pattern maps for upward swirling gas-liquid flows using a mechanistic reasoning along the lines of the mechanistic reasoning used for non-swirling flows.

6.2. INTRINSIC DYNAMICS AND EFFICIENCY

The flow patterns are directly responsible for the intrinsic phase distribution dynamics of multiphase flows. The amplitude of the intrinsic dynamics, and the impact of the intrinsic dynamics on the process efficiency, are flow-pattern dependent.

Well-behaved multiphase flow patterns, such as Weakly Oscillating Columns in gas-liquid flows, have a negligible intrinsic dynamics that does not significantly impact the efficiency of the process. On the other hand, the intrinsic dynamics of intermittent multiphase flow patterns, such as Bursting Columns, have a substantial impact on the (overall) efficiency of separation of axial cyclones.

The relation between axial cyclone performance and time-average gas core diameter upstream of the pickup tube was investigated in chapter 4, providing an approximation of the separation obtained in the equipment with slow tomography-based real-time controllers, designed to suppress slow external process disturbances in the phase distribution upstream of the pickup tube without controlling the fast flow pattern fluctuations.

Based on the axial cyclone geometry, it was expected that an average gas core diameter equal to the inner diameter of the pickup tube would result in the capture of the majority of the gas by the pickup tube, and the majority of the liquid by the outer tube, maximizing the overall efficiency of separation independent of the process conditions. However, the maximum overall efficiency of separation of the cyclone was obtained for time-average gas core diameters significantly smaller than the pickup tube diameter, due to the impact of the large-amplitude intrinsic flow pattern fluctuations of Bursting Columns on the capture of gas by the pickup tube and liquid by the outer tube. Moreover, since the amplitude of the flow pattern fluctuations depends on the gas and liquid flow rates in the inlet of the axial cyclone, the time-average gas core diameter upstream of the pickup tube that maximizes performance depends on the inlet conditions of the equipment.

As the overall efficiency of separation cannot be maximized by a single time-average gas core diameter, the axial cyclone performance remains impacted by process disturbances, such as changes in the gas and liquid flow rates in the inlet of the axial cyclone, despite the tomography-based real-time control of the filtered gas core diameter upstream of the pickup tube (the filtered gas core diameter is the gas core diameter without flow pattern fluctuations, obtained, e.g., with a low-pass filter). The results obtained with the axial cyclone show that controlling only the lower frequencies of the distribution of phases of multiphase flows, related to slow external process disturbances, is insufficient to control the efficiency of the process. The full equivalence between controlling phase distribution and controlling efficiency in multiphase flow processes is expected if, and only if, the intrinsic dynamics are negligible or included in the tomography-based control loop. The possibility of controlling the intrinsic dynamics is discussed in section 6.5.

6.3. MULTIPHASE FLOW TIME-CONSTANTS AND CONTROLLER DESIGN

This section discusses how the fast multiphase flow time-constants impact the design of sensors and actuators for tomography-based real-time control.

6.3.1. REAL-TIME TOMOGRAPHY

Despite the significant increase in computational power in the recent years, phase distribution measurements with traditional electrical resistance tomography algorithms remain too slow compared to the intrinsic phase distribution dynamics of gas-liquid flows. Additionally, large measurement errors in the reconstructed distribution of phases in the axial cyclone were obtained with the fastest (non-iterative) ERT algorithms available.

The slow and inaccurate image reconstruction of traditional ERT algorithms severely limits the application of the technique in real-time process control, particularly in relation to the fast intrinsic dynamics of multiphase flows. To overcome this, an application-specific ERT algorithm was proposed in chapter 2.

The image reconstruction algorithm of chapter 2 is based on the physics of Columnar flows, where a roughly-circular gas core is present in the domain measured by ERT. The algorithm uses simple correlations to reconstruct the distribution of phases, resulting in precise phase distribution measurements three orders of magnitude faster than non-iterative ERT schemes, and making it suitable for real-time control applications. However, since the proposed algorithm relies on the formation of columnar flows in the system, it can only be used in axial cyclones with sufficiently high swirl intensities.

The small time-constants of the intrinsic phase distribution dynamics observed in the axial cyclone are also characteristic of other multiphase flows. Therefore, the development of fast application-specific image reconstruction algorithms is crucial to capture the intrinsic phase distribution fluctuations of multiphase flow processes with sufficient temporal and spatial resolution for real-time control. Moreover, although slower (but precise) tomographic sensors can be used if the intrinsic dynamics are irrelevant or not targeted by the controller, slow measurements remain undesired since the measurement rate of the ERT system determines the time step of the tomography-based controller, determining the frequency of external disturbances that can be measured and suppressed by the control loop.

6.3.2. ACTUATOR

Apart from slow (tomographic) sensors, slow actuators also limit the range of frequencies that can be controlled in the phase distribution of multiphase flows.

Despite being common actuators in fluid processes, control valves are not a good choice for tomography-based real-time control due to their slow response with hysteresis (chapter 2), and the risk of water hammers and pressure spikes in the system if the equipment is accelerated to match the time-constants of the intrinsic dynamics. Therefore, alternative actuators, such as variations in the swirl element vanes in axial cyclone separators, are desired when attempting to control the intrinsic dynamics of multiphase flows. Control valves can still be used to suppress slow phase distribution variations due to external disturbances if the intrinsic dynamics are filtered out from the control loop calculations. However, limited efficiency gains are obtained if the tomography-based real-time control of the process is limited to the suppression of slow external disturbances in the phase distribution, as discussed in section 6.2.

6.4. TOMOGRAPHY-BASED CONTROL LOOPS

Tomography-based controllers can be implemented based on the phase distribution measured at different locations of multiphase flow equipment. A natural choice is to control the distribution of phases where it determines the efficiency of the process, for instance, upstream of the pickup tube in axial cyclones (feedback control). However, the inclusion of the phase distribution measured in additional locations of the equipment to the control loop is also potentially interesting.

The gas core dynamics in the axial cyclone depends on the upstream flow, from conservation of mass, and on the pressure distribution in the pickup and outer tubes. A high cross-correlation exists between the phase distribution upstream and downstream of the swirl element, indicating that the majority of the intrinsic dynamics in the axial cyclone are convected from the upstream flow (chapter 5).

Since the phase distribution inside the axial cyclone is strongly correlated to the phase distribution upstream of the swirl element, phase distribution measurements in the inlet of the equipment can be included in the tomography-based real-time control of the process, together with the distribution of phases upstream of the pickup tube. For instance, a feedforward controller can be used to act on the phase distribution upstream of the pickup tube directly based on the upstream flow, via a model that relates the gas core dynamics upstream of the pickup tube to the phase distribution dynamics upstream of the swirl element. Another alternative is to include the upstream phase distribution as measured disturbance in model predictive controllers, where the upstream flow measurement is used to predict the gas core upstream of the pickup tube in future time steps, and the predicted phase distribution used to compute the control actions.

The prediction of the phase distribution in the axial cyclone departing from the upstream flow relies on convection, and a similar behavior is expected for other quasi-1D multiphase flows. The inclusion of upstream phase distribution measurements in the real-time control of multiphase flow processes is particularly interesting when attempting to control the intrinsic dynamics, where the controller can benefit from the travel time of the intrinsic dynamics inside the equipment to act on the process. If the intrinsic dynamics are not considered in the real-time control of the process, the (filtered) phase distribution variations caused by slow external disturbances can be successfully suppressed by tomography-based feedback controllers (chapter 5), making the inclusion of upstream flow measurements in the control loop unnecessarily complicated.

6.5. TOWARDS TOMOGRAPHY-CONTROLLED MULTIPHASE FLOWS

The suppression of external disturbances in the phase distribution is most likely sufficient to control the performance of industrial processes with well-behaved multiphase flow patterns, such as Weakly Oscillating Columns. However, due to limitations in the ERT resolution, the real-time control of such flow patterns was not investigated in this thesis. The tomography-based real-time control of such processes can be investigated in future works and, if the expectation is confirmed, multiphase flow equipment should be designed to operate with well-behaved flow regimes whenever possible.

If strong phase distribution fluctuations are present in the process, for instance, in axial cyclones that operate with Bursting Columns, the analysis performed suggests that the suppression of external disturbances in the phase distribution is insufficient to maintain an optimal efficiency of the process. Controllers able to suppress the flow pattern fluctuations (intrinsic dynamics) are essential to obtain efficiency gains with tomography-based controllers in such cases and, therefore, the way forward towards the tomography-based real-time control of intermittent multiphase flows relies on the development of sensors and actuators to act on the intrinsic dynamics.

Realization of tomography-based real-time control of the entire phase distribution of quasi-1D multiphase flows is not to be expected, even with fast control loops. However, the control of the larger scales of the flow with fast actuators can be possible. For instance, if the current limitations in the velocity of control valves are removed, the valve in the Light Phase Outlet of the axial cyclone can be fully opened, and the valve in the Heavy Phase Outlet fully closed, to capture a Taylor bubble with the pickup tube. The valve openings can then be reversed when a liquid slug is detected upstream of the pickup tube, resulting in a good separation of the largest flow structures, with the highest impact on the efficiency of separation. However, it is unlikely that the bubbles in the liquid slugs can be controlled using valves, due to their three-dimensional distribution in the flow.

The tomography-based real-time control of three-dimensional multiphase flows remains an open topic to be investigated in future works. It is expected that the real-time control of the complete phase distribution, if possible, would require (i) sophisticated (application-specific) tomography algorithms, due to the large amount of variables required to describe the complete three-dimensional phase distribution, and (ii) distributed actuators, to act on specific regions of the flow. The complexity of designing such systems, together with the chaotic nature of multiphase flows, can make the tomography-based real-time control of three-dimensional systems technically impossible.

Numerical simulations are a great tool to remove the limitations in the closed-loop (controlled) phase distribution response created by slow sensors and actuators. Whenever possible, it is suggested to simulate the phase distribution response to instantaneous control actions before developing sophisticated tomographic sensors and actuators.

APPENDIX A

PROCESSING OF THE CAMERA RECORDINGS

A high-speed camera (Basler acA1920 150uc with 8 mm lenses by Computar) is used to record the gas-liquid distribution in the axial cyclone in some chapters of this thesis. The gas core is recorded as 8-bit grayscale images, that are processed to extract the gas core diameter as function of time used in the plots and calculations of chapters 3 and 5. This appendix describes the routine implemented in MATLAB to process the camera images.

The steps used to process the camera images in MATLAB are:

1. Compute the scale between pixels and mm, based on the outer diameter of the pipe (90 mm) in the pictures.
2. Crop the images to the flow region in a window symmetric in relation to the pipe centerline and with the desired length in the axial direction.
3. Subtract the cropped image from a picture of the pipe filled with water with the *imsubtract* function of MATLAB, and enhance the contrast of the resulting image via the *imadjust* function.
4. Binarize the image with the *imbinarize* function of MATLAB with threshold computed based on the Otsu method [142], resulting in white pixels with value 1 in the gas-liquid interface and black pixels with value 0 in the remaining region of the flow.
5. Remove small white regions from the binary image, corresponding to small bubbles or noise, with a moving-average filter. The moving-average sets the pixel in the center of the moving 5x5 window (25 pixels) to black (liquid) if the average pixel value inside the 5x5 window is below 0.5.
6. Fill the region inside the gas core with white pixels via the *imfill* function of MATLAB.
7. Correct the points measured by the camera (pixels) to the true locations inside the pipe, accounting for the refraction of light in the cylindrical wall of the axial cyclone. The correction of the camera images based on Snell's law is described in section A.1.
8. Sum the width of the white pixels corrected by refraction (no longer uniform as in the original picture), and divide the result by the number of pixels in the axial direction to obtain the (average) gas core diameter of a frame.
9. Repeat the process for each frame recorded by the camera to obtain the gas core diameter as function of time.

The image processing steps are illustrated in Figure A.1.

This appendix is based on the publications [88] and [140].

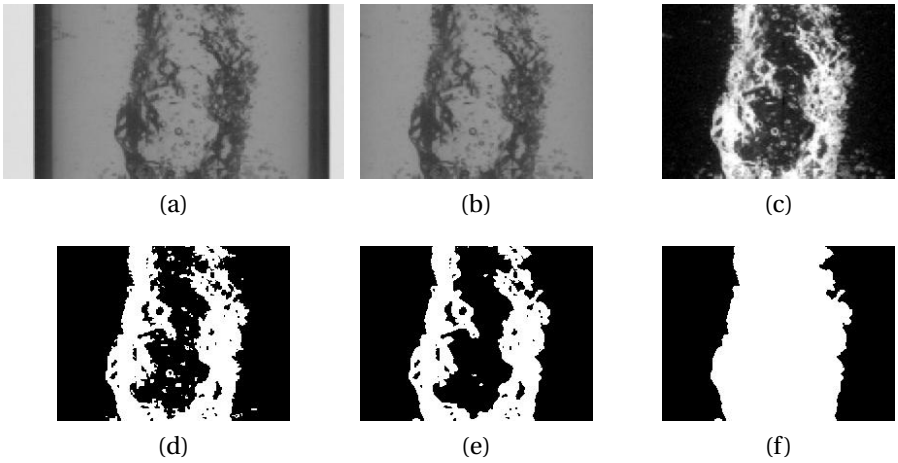

Figure A.1: Snapshots of the gas core during the image processing steps. a) Original picture. b) Image cropped to the flow region (step 2). c) Image subtracted from a picture of the pipe filled with water with enhanced contrast (step 3). d) Binary image (step 4). e) Filtered image (step 5). f) Image with the gas core in white and liquid annulus in black (step 6).

A.1. REFRACTION CORRECTION

The gas core in the camera images is distorted in relation to the real gas core inside the axial cyclone due refraction in the cylindrical pipe wall. A refraction correction algorithm based on [143] is used to correct the gas core recorded by the camera to the real gas core inside the pipe, departing from the path of the light rays crossing the pipe and reaching the camera during the measurements. A single light ray crossing the liquid and reaching the camera is illustrated in Figure A.2.

Due to refraction in the circular pipe wall, a Point P inside the liquid with position (y_P, z_P) is recorded at a position proportional to (y_E,0) in the camera images. To obtain the correct gas core dimensions in the axial cyclone departing from the camera recordings, the y-position of P is estimated based on (i) its apparent position y_E, (ii) the light ray geometry, and (iii) Snell's law.

From Snell's law, the change in the light ray angle at point B of Figure A.2 is

$$n_a \sin \vartheta_1 = n_p \sin \vartheta_2, \tag{A.1}$$

and the change in the light ray angle at point C is

$$n_p \sin \vartheta_3 = n_w \sin \vartheta_4 \tag{A.2}$$

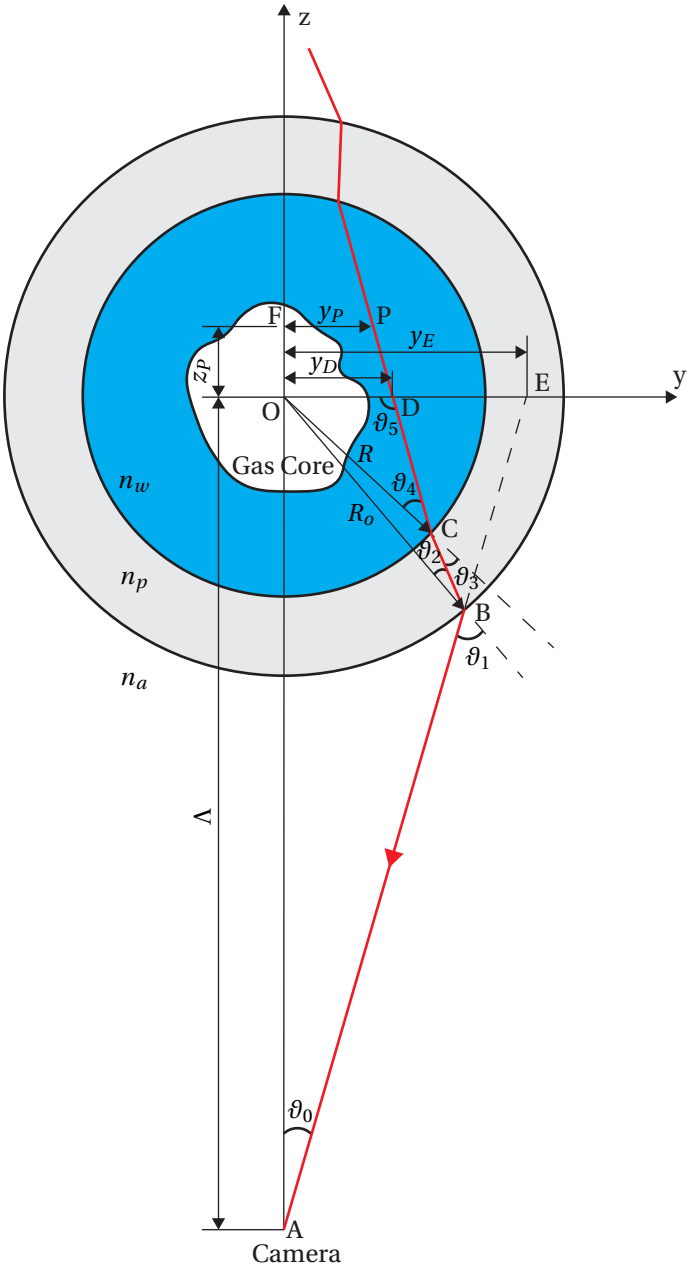

Figure A.2: Illustration of a light ray (in red) crossing the pipe and reaching the camera. The light ray path was chosen to provide a clear view of the variables involved in the refraction correction calculations, and do not necessarily represent a realistic path. Image not to scale.

The Law of Sines applied to the triangles OCD, OBC, and OAB of Figure A.2 results in

$$\frac{\sin\vartheta_5}{R} = \frac{\sin\vartheta_4}{y_D}, \tag{A.3}$$

$$\frac{\sin\vartheta_2}{R} = \frac{\sin\vartheta_3}{R_o}, \tag{A.4}$$

$$\frac{\sin\vartheta_1}{\Lambda} = \frac{\sin\vartheta_0}{R_o}, \tag{A.5}$$

respectively.

The apparent y-position of the point P in the camera images, y_E, is connected to the distance Λ between the camera and the pipe centerline via (triangle OAE):

$$\tan\vartheta_0 = \frac{y_E}{\Lambda} \tag{A.6}$$

Since $y_E \leq R_o$ and the camera is far from the pipe during the recordings ($R_o/\Lambda \ll 1$), ϑ_0 is close to zero and $\tan\vartheta_0 \approx \sin\vartheta_0$. Then, Equations A.5 and A.6 can be combined into:

$$\sin\vartheta_1 \approx \frac{y_E}{R_o} \tag{A.7}$$

Combining Equations A.1, A.2, A.3, A.4 and A.7:

$$y_D \approx \frac{n_a}{n_w}\frac{y_E}{\sin\vartheta_5} \tag{A.8}$$

The sum of the internal angles of the pentagon OABCD in Figure A.2 is 3π. Therefore:

$$\vartheta_0 - \vartheta_1 + \vartheta_2 - \vartheta_3 + \vartheta_4 + \vartheta_5 = \frac{\pi}{2} \tag{A.9}$$

Combining Equations A.8 and A.9 results in ($\vartheta_0 \approx 0$):

$$y_D \approx \frac{n_a}{n_w}\frac{y_E}{\cos(\vartheta_1 - \vartheta_2 + \vartheta_3 - \vartheta_4)} \tag{A.10}$$

Based on the geometry of the trapezoid ODPF, the y-position y_P of the Point P inside the liquid is related to y_D via:

$$y_P = y_D + \frac{z_P}{\tan\vartheta_5} \tag{A.11}$$

Combining Equations A.10 and A.11 results in:

$$y_P \approx \frac{n_a}{n_w}\frac{y_E}{\cos(\vartheta_1 - \vartheta_2 + \vartheta_3 - \vartheta_4)} - z_P\tan(\vartheta_1 - \vartheta_2 + \vartheta_3 - \vartheta_4) \tag{A.12}$$

In general, the correction of the apparent y-position y_E of the camera images to the true position y_P inside the axial cyclone via Equation A.12 requires z_P, which must be obtained with a second camera or camera view. However, since the gas core is roughly circular and centered in the pipe in the experiments of this dissertation, a single camera view is used and the gas core images are corrected assuming that $z_P \approx 0$. Then, the apparent y-position of a point in the liquid detected by the camera (y_E) is corrected to the real

y-position y_P of the point inside the pipe computing ϑ_1 from y_E via Equation A.7, ϑ_2 from ϑ_1 via Equation A.1, ϑ_3 from ϑ_2 via Equation A.4, ϑ_4 from ϑ_3 via Equation A.2, and $y_P \approx y_D$ from ϑ_1, ϑ_2, ϑ_3 and ϑ_4 via Equation A.10.

The position correction is applied to each pixel in the filled binary images (after image processing step 6), correcting their width and location in the y-axis before the gas core diameter is computed. The pixel sizes are corrected considering the refractive indexes $n_a = 1$ (air), $n_w = 1.333$ (water) and $n_p = 1.53$ (PVC). The comparison between Equations A.10 and A.12, evaluated for the two interface points in a line of pixels in y determining the local gas core diameter, reveals that the approximation $z_P \approx 0$ used to correct the images results in a measurement error in the gas core diameter below ±6% for gas cores with diameter $d_i \leq 0.8D$ and centroid z-position within $-0.2R \leq z_P \leq 0.2R$.

Figure A.3 presents a comparison between the gas core filled with white pixels obtained from the step 6 of the image processing algorithm (Figure A.3-left), and the gas core inside the pipe estimated by the refraction correction algorithm (Figure A.3-right). Black pixels were added to the sides of both images to make their width equal to the inner diameter of the pipe, since the corrected image is smaller than the original image in the horizontal direction due to the magnification of flow caused by the refraction of light in the pipe wall.

Figure A.3: Comparison between the gas core obtained in the camera images (left) and the expected gas core inside the cyclone (right), obtained correcting the pixel sizes based on the refraction of light in the pipe wall.

As shown in Figure A.3, the gas core in the camera images is considerably wider than in the axial cyclone. The ratio between the gas core diameter in the camera images and the true gas core diameter inside the pipe is around 1.3 (n_w / n_a) for centered gas cores with diameter $d_i \leq 0.8D$.

APPENDIX B

ESTIMATION OF THE HPO AND LPO GAS AND LIQUID FLOW RATES

In chapters 4 and 5, the axial cyclone efficiency is evaluated based on time average gas and liquid flow rates in the Light and Heavy Phase Outlets of the cyclone. This appendix describes the computation of the LPO and HPO flow rates based on the gas and liquid flow rates measured in the outlets of the LPO and HPO gravity separators. The same nomenclature of chapter 2 is used, i.e., AFM1 and WFM2 are the air and water flow meters installed in the gravity separator connected to the LPO, respectively, and AFM 2 and WFM 3 are the air and water flow meters installed in the gravity separator connected to the HPO, respectively, as shown in Figure 2.2.

In steady state, the liquid and gas balances of mass in the LPO gravity separator result in the equality between the gas and liquid flow rates in the LPO and the gas and liquid flow rates measured by AFM 1 and WFM 2 in the gravity separator outlets, respectively. Similarly, the HPO gas and liquid flow rates are the same as the AFM 2 and WFM 3 measurements in the HPO Gravity Separator. However, the gravity separators do not operate in steady-state due to changes in the liquid level and pressure during the experiments, caused, e.g., by changes in the flow split between the pickup and outer tubes due to control actions in the LPO valve. Because of the large volume of the gravity separators, small changes in the liquid level or pressure can significantly impact the extrapolation of the liquid and gas flow measured in the gravity separator outlets to the LPO and HPO. To compensate for the effect, changes in the mass of gas and liquid stored in the gravity separators must be accounted in the computation of the time average LPO and HPO flow rates.

The balance of mass of air in the LPO Gravity Separator is given by

$$\frac{d}{dt}\left(\rho_{g,lgs}\mathcal{V}_{g,lgs}\right) = w_{g,lpo} - w_{g,lgs}, \tag{B.1}$$

where $\mathcal{V}_{g,lgs}$ is the volume of gas (air) in the LPO Gravity Separator, $w_{g,lpo}$ is the gas mass flow rate entering the gravity separator from the LPO, and $w_{g,lgs}$ is the gas mass flow rate departing from the gravity separator to the building ventilation, measured by AFM 1.

Integrating Equation B.1 in the time interval between $t = 0$ and $t = T$, corresponding to the duration of one measurement, leads to

$$\overline{w}_{g,lpo} = \overline{w}_{g,lgs} + \frac{\left(\rho_{g,lgs}\mathcal{V}_{g,lgs}\right)_{t=T} - \left(\rho_{g,lgs}\mathcal{V}_{g,lgs}\right)_{t=0}}{T}, \tag{B.2}$$

where $\overline{w}_{g,lpo}$ is the time-average LPO gas mass flow rate and $\overline{w}_{g,lgs}$ is the time-average gas mass flow rate departing from the LPO Gravity Separator.

The volume of gas in the (cylindrical) LPO gravity separator can be written based on the liquid level $h_{l,lgs}$ (measured by the level meter L1), gravity separator height h_{gs} and gravity separator cross-sectional area A_{gs} as $\mathcal{V}_{g,lgs} = A_{gs}(h_{lgs} - h_{l,lgs})$, modifying Equation B.2 to:

$$\overline{w}_{g,lpo} = \overline{w}_{g,lgs} + A_{gs}\frac{\left[\rho_{g,lgs}(h_{gs} - h_{l,lgs})\right]_{t=T} - \left[\rho_{g,lgs}(h_{gs} - h_{l,lgs})\right]_{t=0}}{T} \tag{B.3}$$

Similarly, the liquid balance of mass in the LPO gravity separator leads to the average LPO liquid volume flow rate equation ($\mathcal{V}_{l,lgs} = A_{gs}h_{l,lgs}$),

$$\overline{q}_{l,lpo} = \overline{q}_{l,lgs} + A_{gs}\frac{h_{l,lgs}(t=T) - h_{l,lgs}(t=0)}{T}, \tag{B.4}$$

and the gas and liquid balances of mass in the HPO gravity separator lead to the average HPO gas mass flow rate and liquid volume flow rate

$$\overline{w}_{g,hpo} = \overline{w}_{g,hgs} + A_{gs}\frac{\left[\rho_{g,hgs}(h_{gs} - h_{l,hgs})\right]_{t=T} - \left[\rho_{g,hgs}(h_{gs} - h_{l,hgs})\right]_{t=0}}{T} \tag{B.5}$$

and

$$\overline{q}_{l,hpo} = \overline{q}_{l,hgs} + A_{gs}\frac{h_{l,hgs}(t=T) - h_{l,hgs}(t=0)}{T}, \tag{B.6}$$

respectively.

The accuracy of the LPO gas flow rate and HPO liquid flow rate are particularly important for the evaluation of the Axial Cyclone performance (chapter 4), being improved by the addition of the inlet gas and liquid flow rates to their computation. From conservation of mass in the whole loop, $\overline{w}_{g,lpo} = \overline{w}_g - \overline{w}_{g,hpo}$ and $\overline{q}_{l,hpo} = \overline{q}_l - \overline{q}_{l,lpo}$. Then, Equation B.3 is modified to compute the LPO gas mass flow rate via

$$\overline{w}_{g,lpo} = \frac{1}{2}\left(\overline{w}_g - \overline{w}_{g,hpo} + \overline{w}_{g,lgs} + A_{gs}\frac{\left[\rho_{g,lgs}(h_{gs} - h_{l,lgs})\right]_{t=T} - \left[\rho_{g,lgs}(h_{gs} - h_{l,lgs})\right]_{t=0}}{T}\right), \tag{B.7}$$

and Equation B.6 is modified to compute the HPO liquid flow rate via:

$$\overline{q}_{l,hpo} = \frac{1}{2}\left(\overline{q}_l - \overline{q}_{l,lpo} + \overline{q}_{l,hgs} + A_{gs}\frac{h_{l,hgs}(t=T) - h_{l,hgs}(t=0)}{T}\right) \tag{B.8}$$

Equations B.4, B.5, B.7 and B.8 are used to obtain the average LPO and HPO flow rates from experimental data based on (i) the gravity separator dimensions $A_{gs} = 0.184$ m^2 and $h_{gs} = 1.4$ m, (ii) water levels $h_{l,lgs}$ and $h_{l,hgs}$ measured by the ROSEMOUNT 3302 Guided Wave Radar Level and Interface Transmitters L1 and L2, and (iii) air density computed from the pressure measured by p_{lgs} and p_{hgs} assuming an air temperature of 20 °C.

The performance indicators ξ_g, ξ_l and η, introduced in chapter 4 and computed based on the LPO and HPO flow rates described in the current appendix, have an uncertainty of ± 0.02 based on (i) the resolution of the flow meters, and (ii) the comparison between the measured inlet, LPO and HPO flow rates and conservation of mass.

APPENDIX C

AVERAGE SOLUTION AND LINEAR STABILITY ANALYSIS OF COLUMNAR FLOWS

Some of the mechanistic models proposed in chapter 3 for the swirling gas-liquid flow pattern transitions rely on the prediction of the average gas core diameter and columnar flow stability, departing from the average gas and liquid flow rates and swirl intensity. The separated phases model used to predict the average gas core diameter is described in section C.1, and the linear stability analysis of columnar flows is investigated in section C.2.

The models of this section assume that the two phases are incompressible and separated into a cylindrical gas core centered in the pipe surrounded by a liquid annulus, as shown in Figure C.1.

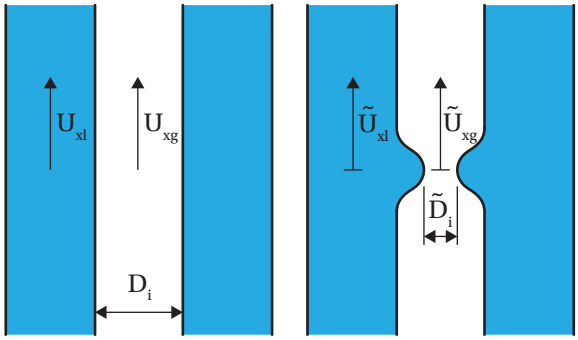

Figure C.1: Columnar gas-liquid flow in the absence (left) and presence (right) of a solitary wave.

C.1. A SEPARATED PHASES MODEL FOR SWIRLING GAS-LIQUID COLUMNAR FLOWS

The separated phases model for the average gas core diameter in columnar flows is obtained departing from the quasi-cylindrical Navier-Stokes equations [144, 145]:

$$\frac{\partial \rho u_r r}{\partial r} + \frac{\partial \rho u_x r}{\partial x} = 0 \tag{C.1}$$

$$\frac{\partial \rho u_r u_x r}{\partial r} + \frac{\partial \rho u_x^2 r}{\partial x} = -\frac{\partial p r}{\partial x} - \rho g r + \frac{\partial \tau_{rx} r}{\partial r} \tag{C.2}$$

$$\frac{\partial p}{\partial r} = \rho \frac{u_\theta^2}{r} \tag{C.3}$$

$$\frac{\partial \rho u_r u_\theta r^2}{\partial r} + \frac{\partial \rho u_x u_\theta r^2}{\partial x} = \frac{\partial \tau_{r\theta} r^2}{\partial r} \tag{C.4}$$

Integrating Equation C.3 in the radial direction based on the interface position $R_i(x)$ and interface pressure $p(x, R_i(x)) = p_i(x)$:

$$p(x,r) = p_i(x) + \int_{R_i(x)}^{r} \rho \frac{u_\theta^2(x,r)}{r} dr \tag{C.5}$$

Replacing the result in Equation C.2 leads to:

$$\frac{\partial \rho u_r u_x r}{\partial r} + \frac{\partial \rho u_x^2 r}{\partial x} = -\frac{dp_i r}{dx} - \frac{\partial}{\partial x}\left(r \int_{R_i}^{r} \rho \frac{u_\theta^2}{r} dr \right) - \rho g r + \frac{\partial \tau_{rx} r}{\partial r} \tag{C.6}$$

The (integral) balances of mass, linear momentum and angular momentum of a fluid annulus between $r = R_1$ and $r = R_2$ are obtained integrating Equations C.1, C.6 and C.4 in the radial direction, respectively:

$$\frac{d}{dx} \int_{R_1}^{R_2} \rho u_x r dr = 0 \tag{C.7}$$

$$\frac{d}{dx} \int_{R_1}^{R_2} \rho u_x^2 r dr = -\frac{R_2^2 - R_1^2}{2} \frac{dp_i}{dx} - \frac{d}{dx} \left[\int_{R_1}^{R_2} \left(\int_{R_i}^{r} \rho \frac{u_\theta^2}{r} dr \right) r dr \right] - \rho g \frac{R_2^2 - R_1^2}{2} + R_2 \tau_{rx}(R_2) - R_1 \tau_{rx}(R_1) \tag{C.8}$$

$$\frac{d}{dx} \int_{R_1}^{R_2} \rho u_x u_\theta r^2 dr = R_2^2 \tau_{r\theta}(R_2) - R_1^2 \tau_{r\theta}(R_1) \tag{C.9}$$

An analysis of order of magnitude of Equation C.8 reveals that the axial derivatives of the integrals of u_x and u_θ can be neglected in comparison to the gravity term for smooth gas core diameter gradients if $Fr^2 D/L_{st} \ll 1$ and $Fr^2 \Omega^2 D/L_{st} \ll 1$, respectively, where L_{st} is the length of the Swirl Tube. Since strong gradients in the gas core diameter were not observed in the experiments of chapter 3 and, if present, would most likely result in a flow pattern transition, the set of Equations C.7-C.9 can be written based on the assumption of uniform axial U_x and azimuthal U_θ velocities as[1]:

$$\frac{d}{dx} \left[U_x (R_2^2 - R_1^2) \right] = 0 \tag{C.10}$$

[1] For stability reasons, the azimuthal velocity must always tend to a solid body rotation in the center of the pipe (section 3.5). However, the inclusion of the solid body region in the model unnecessarily complicates the approach, since it does not have a significant impact on the swirl number calculation, and the gradient of centripetal acceleration integral of Equation C.8 is negligible compared to the gravity term.

$$\frac{dp_i}{dx} = -\rho g + 2\frac{R_2\tau_{rx}(R_2) - R_1\tau_{rx}(R_1)}{R_2^2 - R_1^2} \tag{C.11}$$

$$\rho U_x \frac{d}{dx}\left[U_\theta \frac{R_2^3 - R_1^3}{R_2^2 - R_1^2}\right] = 3\frac{R_2^2\tau_{r\theta}(R_2) - R_1^2\tau_{r\theta}(R_1)}{R_2^2 - R_1^2} \tag{C.12}$$

Equations C.10, C.11 and C.12 must be evaluated for each fluid in order to proceed with the analysis, which is performed considering that all the gas is between the centerline ($R_1 = 0$) and the interface ($R_2 = R_i$), and all the liquid is between the interface ($R_1 = R_i$) and the pipe wall ($R_2 = R$).

The evaluation of Equation C.10 for each phase results in the constant superficial gas and liquid velocity relations:

$$j_g = U_{xg}\frac{R_i^2}{R^2} \tag{C.13}$$

$$j_l = U_{xl}\frac{R^2 - R_i^2}{R^2} \tag{C.14}$$

When evaluated for each fluid, Equation C.11 describes the interface pressure gradient in the gas and liquid sides of the interface. Surface tension is negligible in comparison to the remaining flow forces, and the interface pressure can be approximated as the same in both fluids. Then, due to the lack of interest in solving $p_i(x)$, the individual gas and liquid axial momentum are combined into:

$$2\frac{R\tau_{rx}(R)}{R^2 - R_i^2} - 2\frac{R^2\tau_{rx}(R_i)}{R_i(R^2 - R_i^2)} = \left(\rho_l - \rho_g\right)g \tag{C.15}$$

Equation C.15 is equivalent to the separated phases model of non-swirling Annular flows. The similarity indicates that the interface shear-stress must counter the effects of gravity to keep the phases separated, which is only achieved with a large slip between the gas and the liquid in the axial direction ($U_{xg} \gg U_{xl}$). However, different from the non-swirling scenario, separated flows with thin gas cores ($R_i \ll R$) and low gas flow rates can exist in vertical swirling flows, due to the stabilizing effect of the centrifugal force. The stability of columnar gas-liquid swirl flows is investigated in section C.2.

Since the gas core diameter gradient is negligible, Equation C.12 can be written as

$$\frac{dU_{\theta g}}{dx} = \frac{3}{R_i}\frac{\tau_{r\theta}(R_i)}{\rho_g U_{xg}} \tag{C.16}$$

for the gas, and

$$\frac{dU_{\theta l}}{dx} = 3\frac{R^2\tau_{r\theta}(R) - R_i^2\tau_{r\theta}(R_i)}{\rho_l U_{xl}(R^3 - R_i^3)} \tag{C.17}$$

for the liquid.

Extending the single-phase shear-stress model of section 3.5 to separated two-phase flows, the wall and interface shear-stresses are written as ($U_{xg} \gg U_{xl}$ and $U_{tg} \gg U_{tl}$):

$$\tau_{rx}(R) \approx -f_w \rho_l \frac{|U_{tl}|U_{xl}}{2} = -f_w \sqrt{1+2.25\Omega_l^2}\,\rho_l \frac{|U_{xl}|U_{xl}}{2} \tag{C.18}$$

$$\tau_{r\theta}(R) \approx -f_w \rho_l \frac{|U_{tl}|U_{\theta l}}{2} = -f_w \sqrt{1+2.25\Omega_l^2}\,\rho_l \frac{|U_{xl}|U_{\theta l}}{2} \tag{C.19}$$

$$\tau_{rx}(R_i) = -f_i \rho_g \frac{|U_{tg}-U_{tl}|\left(U_{xg}-U_{xl}\right)}{2} \approx -f_i \sqrt{1+2.25\Omega_g^2}\,\rho_g \frac{|U_{xg}|U_{xg}}{2} \tag{C.20}$$

$$\tau_{r\theta}(R_i) = -f_i \rho_g \frac{|U_{tg}-U_{tl}|\left(U_{\theta g}-U_{\theta l}\right)}{2} \approx -f_i \sqrt{1+2.25\Omega_g^2}\,\rho_g \frac{|U_{xg}|\left(U_{\theta g}-U_{\theta l}\right)}{2} \tag{C.21}$$

Replacing the axial and azimuthal shear-stresses of Equations C.18-C.21 into Equations C.15, C.16 and C.17 results in the separated phases model equations ($U_{xl} > 0$ and $U_{xg} > 0$):

$$\frac{f_i}{R_i}\sqrt{1+2.25\Omega_g^2}\,\rho_g U_{xg}^2 - \frac{f_w}{R}\sqrt{1+2.25\Omega_l^2}\,\rho_l U_{xl}^2 = \frac{R^2-R_i^2}{R^2}\left(\rho_l-\rho_g\right)g \tag{C.22}$$

$$\frac{dU_{\theta g}}{dx} = -\frac{3}{2}\frac{f_i}{R_i}\sqrt{1+2.25\Omega_g^2}\left(U_{\theta g}-U_{\theta l}\right) \tag{C.23}$$

$$\frac{dU_{\theta l}}{dx} = \frac{3}{2}\left[-\frac{R^2}{R^3-R_i^3} f_w \sqrt{1+2.25\Omega_l^2}\,U_{\theta l} + \frac{R^2-R_i^2}{R^3-R_i^3}\frac{\rho_g j_g}{\rho_l j_l} f_i \sqrt{1+2.25\Omega_g^2}\left(U_{\theta g}-U_{\theta l}\right)\right] \tag{C.24}$$

Equation C.23 shows that the azimuthal velocity of the gas core tends to the azimuthal velocity of the liquid annulus in the flow direction, slowing down if $U_{\theta g} > U_{\theta l}$. For the liquid, Equation C.24 shows that $U_{\theta l}$ is always slowed down by the wall, while the interface shear-stress can increase $U_{\theta l}$ if $U_{\theta g} > U_{\theta l}$. However, since the acceleration of the liquid depends on the density ratio between the gas and the liquid, the effect is only noticeable for $U_{\theta g} \gg U_{\theta l}$.

The interface friction factor is flow pattern-dependent. It is described for Weakly Oscillating Columns in Equation 3.52 and for Swirling Annular flows in Equation 3.21.

C.2. COLUMNAR FLOW STABILITY

The transition to columnar flows depends on the formation of stable gas cores with the coalescence of Centered flows. The stability of the columnar flow patterns is modeled via the linear stability analysis of a solitary wave traveling in the gas column interface, as illustrated in Figure C.1-right. In this section, the tilde above the symbols represents the flow variables disturbed by the solitary wave.

The viscous effects are assumed negligible for small disturbances, and the disturbed flow conditions are obtained from the undisturbed conditions via the Bernoulli equation,

applied to a streamline on each side of the interface. For uniform axial gas and liquid velocities, and azimuthal velocities close to the interface $U_{\theta gi} = u_{\theta g}(r \to R_i^-)$ and $U_{\theta li} = u_{\theta l}(r \to R_i^+)$:

$$\rho_g \frac{\tilde{U}_{xg}^2 + \tilde{U}_{\theta gi}^2}{2} + \tilde{p}_{gi} = \rho_g \frac{U_{xg}^2 + U_{\theta gi}^2}{2} + p_{gi} \tag{C.25}$$

$$\rho_l \frac{\tilde{U}_{xl}^2 + \tilde{U}_{\theta li}^2}{2} + \tilde{p}_{li} = \rho_l \frac{U_{xl}^2 + U_{\theta li}^2}{2} + p_{li} \tag{C.26}$$

Besides mechanical energy, represented by the Bernoulli Equations C.25 and C.26, mass and angular momentum are conserved in inviscid swirling flows. The balance of mass assuming uniform axial velocity profiles leads to $\tilde{U}_{xg}\tilde{D}_i^2 = U_{xg}D_i^2$ for the gas and $\tilde{U}_{xl}(D^2 - \tilde{D}_i^2) = U_{xl}(D^2 - D_i^2)$ for the liquid. The conservation of angular momentum requires that the gas and liquid circulations close to the interface are conserved between the undisturbed and disturbed conditions, leading to $\tilde{U}_{\theta gi}\tilde{D}_i = U_{\theta gi}D_i$ and $\tilde{U}_{\theta li}\tilde{D}_i = U_{\theta li}D_i$, respectively. Replacing both the mass and angular momentum conservation results in Equations C.25 and C.26 leads to:

$$\tilde{p}_{gi} = p_{gi} + \rho_g \frac{U_{xg}^2}{2}\left(1 - \frac{D_i^4}{\tilde{D}_i^4}\right) + \rho_g \frac{U_{\theta gi}^2}{2}\left(1 - \frac{D_i^2}{\tilde{D}_i^2}\right) \tag{C.27}$$

$$\tilde{p}_{li} = p_{li} + \rho_l \frac{U_{xl}^2}{2}\left(1 - \frac{(D^2 - D_i^2)^2}{(D^2 - \tilde{D}_i^2)^2}\right) + \rho_l \frac{U_{\theta li}^2}{2}\left(1 - \frac{D_i^2}{\tilde{D}_i^2}\right) \tag{C.28}$$

A wave constricting the gas core ($\tilde{D}_i < D_i$) will grow, eventually causing the collapse of the gas core, if:

$$\tilde{p}_{li} > \tilde{p}_{gi} \tag{C.29}$$

Considering waves of small amplitude, linearizing $\tilde{D}_i$ around D_i, and neglecting surface tension effects (such that $p_{il} = p_{ig}$ in the undisturbed condition), a columnar flow is unstable from the perspective of linear stability analysis if:

$$\frac{2}{D_i}\rho_g U_{xg}^2 + \frac{2D_i}{(D^2 - D_i^2)}\rho_l U_{xl}^2 \geq \rho_l \frac{U_{\theta li}^2}{D_i} - \rho_g \frac{U_{\theta gi}^2}{D_i} \tag{C.30}$$

APPENDIX D

A BRIEF INTRODUCTION TO DISCRETE-TIME TRANSFER FUNCTIONS

Continuous-time transfer functions and Laplace transforms are widely known by engineers outside the field of System Dynamics and Control. However, the same does not hold for discrete-time transfer functions and Z-transforms. The objective of this appendix is to introduce the discrete-time transfer function and its properties to readers outside the field of System Dynamics and Control, providing a better understanding of the discrete-time models and controllers presented in chapter 5. The reader is referred to chapter 11 of Keviczkyn *et al.* [146] for more information about discrete-time systems.

Z-transforms and discrete-time transfer functions are somewhat similar to Laplace transforms and continuous-time transfer functions, and can be easily understood departing from them. The Laplace transform converts a continuous-time signal obtained in the time domain to a signal in the s-domain via:

$$\mathscr{L}\{f(t)\}(s) \triangleq \int_0^\infty f(t)e^{-st}dt \tag{D.1}$$

The derivative property of the Laplace transform,

$$\mathscr{L}\{\dot{f}(t)\}(s) = s\mathscr{L}\{f(t)\}(s) \tag{D.2}$$

for $f(0) = 0$ is fundamental for the obtainment of continuous-time transfer functions. For instance, linear time-invariant single-input single-output systems are described in the time domain by relations in the form:

$$a_0 y + a_1 \dot{y} + a_2 \ddot{y} + ... + a_m y^{(m)} = b_0 u + b_1 \dot{u} + b_2 \ddot{u} + ... + b_n u^{(n)}, \tag{D.3}$$

where $y(t)$ is the system output, $u(t)$ is the system input, a and b are constant coefficients, and m and n are non-negative integers representing the order of the input and output derivatives.

Continuous-time transfer functions are obtained applying the Laplace transform and its derivative property to the general linear time-domain model of Equation D.3, departing from zero initial conditions ($y(0) = 0$, $\dot{y}(0) = 0$,..., $y^{(m-1)}(0) = 0$):

$$\frac{y(s)}{u(s)} = \frac{\mathscr{L}\{y(t)\}(s)}{\mathscr{L}\{u(t)\}(s)} = \frac{b_0 + b_1 s + b_2 s + ... + b_n s^n}{a_0 + a_1 s + a_2 s + ... + a_m s^m} \tag{D.4}$$

The steady-state gain of the system is determined by transfer function value for $s = 0$, and its frequency response is obtained for $s = i\omega$, where ω is the angular frequency. The

stability of the transfer function is determined by the roots of its denominator (poles); linear systems are stable if, and only if, all its poles have negative real component.

The Z-transform is used to obtain the transfer function of discrete-time models. The Z-transform is defined as

$$\mathcal{Z}\{f[k]\}(z) \triangleq \sum_{k=0}^{\infty} z^{-k} f[k], \tag{D.5}$$

where $f[k]$ corresponds to the k-th value of a sequence. For a continuous function $f(t)$ sampled with frequency T_s^{-1}, the sequence $f[k]$ is related to $f(t)$ via $f[k] = f(t = kT_s)$.

The Z-transform has the time-shift property for $f[k < 0] = 0$:

$$\mathcal{Z}\{f[k-m]\} = z^{-m}\mathcal{Z}\{f[k]\} \tag{D.6}$$

While real systems operate in continuous time, their measurement and (real-time) control is often performed by digital sensors and computers. Digital controllers operate based on system output samples, $y[k]$, and maintain a certain pattern of $u(t)$ in the interval between the samples. A common pattern maintained by discrete-time controllers between samples is the Zero-Order Holding (ZOH) of the input, described by $u(t) = u[k]$ for $kT_s \leq t < (k+1)T_s$.

Linear discrete-time models relate the sampled outputs of the system $(y[k-m], ..., y[k-1], y[k])$ to the discrete inputs $(u[k-n], ..., u[k-1], u[k])$ via equations in the form

$$a_0 y[k] + a_1 y[k-1] + ... + a_m y[k-m] = b_0 u[k] + b_1 u[k-1] + ... + b_n u[k-n], \tag{D.7}$$

where $b_0 = 0$ for ZOH.

The a, b, m and n constants of Equation D.7 can be obtained fitting the input and output sequences departing from experimental data, or discretizing known continuous-time models. For instance, the time-derivative of the continuous-time model

$$\tau\dot{y} + y = u \tag{D.8}$$

can be approximated as $\dot{y}(t) \approx (y(t) - y(t - T_s))/T_s$, resulting in the discrete-time model $(t = kT_s)$:

$$\tau\frac{y[k] - y[k-1]}{T_s} + y[k] = u[k] \tag{D.9}$$

Discrete-time transfer functions are obtained applying the Z-transform and its time-shift property to Equation D.7:

$$\frac{y(z)}{u(z)} = \frac{\mathcal{Z}\{y[k]\}(z)}{\mathcal{Z}\{u[k]\}(z)} = \frac{b_0 z^m + b_1 z^{m-1} + ... + b_n z^{m-n}}{a_0 z^m + a_1 z^{m-1} + ... + a_m} \tag{D.10}$$

The similarity in the form of continuous-time transfer functions (Equation D.4) and discrete-time transfer functions (Equation D.10) is evident. However, there are notorious differences between the two when investigating the system behavior: (i) the steady-state gain of discrete-time systems is obtained for $z = 1$, and their frequency response is obtained for $z = e^{i\omega T_s}$; (ii) discrete-time systems are stable if, and only if, its poles (roots of the transfer function denominator) are inside the unit circle of the complex plane.

BIBLIOGRAPHY

[1] V. Grabenstein, A.-E. Polzin, and S. Kabelac, *Experimental investigation of the flow pattern, pressure drop and void fraction of two-phase flow in the corrugated gap of a plate heat exchanger,* International Journal of Multiphase Flow **91**, 155 (2017).

[2] R. L. Amalfi, F. Vakili-Farahani, and J. R. Thome, *Flow boiling and frictional pressure gradients in plate heat exchangers. part 1: Review and experimental database,* International Journal of Refrigeration **61**, 166 (2016).

[3] G. Besagni, F. Inzoli, and T. Ziegenhein, *Two-phase bubble columns: A comprehensive review,* ChemEngineering **2**, 13 (2018).

[4] A. J. Jaworski and G. Meng, *On-line measurement of separation dynamics in primary gas/oil/water separators: Challenges and technical solutions—a review,* Journal of Petroleum Science and Engineering **68**, 47 (2009).

[5] M. Simmons, J. Wilson, and B. Azzopardi, *Interpretation of the flow characteristics of a primary oil–water separator from the residence time distribution,* Chemical Engineering Research and Design **80**, 471 (2002).

[6] C. T. Crowe, J. D. Schwarzkopf, M. Sommerfeld, and Y. Tsuji, *Multiphase Flows with Droplets and Particles*, 2nd ed. (CRC Press, 2012).

[7] R. Clift, J. R. Grace, and M. E. Weber, *Bubbles, drops, and particles* (Academic Press, 1978).

[8] A. C. Hoffmann and L. E. Stein, *Gas Cyclones and Swirl Tubes. Principles, Design, and Operation* (Springer Berlin, Heidelberg, 2008).

[9] Y. Deng, L. Zhang, H. Hou, B. Yu, and D. Sun, *Modeling and simulation of the gas-liquid separation process in an axial flow cyclone based on the eulerian-lagrangian approach and surface film model,* Powder Technology **353**, 473 (2019).

[10] R. Flemmer and C. Banks, *On the drag coefficient of a sphere,* Powder Technology **48**, 217 (1986).

[11] L. J. A. M. van Campen, *Bulk dynamics of droplets in liquid-liquid axial cyclones,* Ph.D. thesis, Delft University of Technology, the Netherlands (2014).

[12] F.-R. Ahmadun, A. Pendashteh, L. C. Abdullah, D. R. A. Biak, S. S. Madaeni, and Z. Z. Abidin, *Review of technologies for oil and gas produced water treatment,* Journal of Hazardous Materials **170**, 530 (2009).

[13] E. T. Igunnu and G. Z. Chen, *Produced water treatment technologies,* International Journal of Low-Carbon Technologies **9**, 157 (2012).

[14] M. V. Bram, S. Jespersen, D. S. Hansen, and Z. Yang, *Control-oriented modeling and experimental validation of a deoiling hydrocyclone system,* Processes **8**, 1010 (2020).

[15] P. Durdevic, S. Pedersen, and Z. Yang, *Challenges in modelling and control of offshore de-oiling hydrocyclone systems,* Journal of Physics: Conference Series **783**, 012048 (2017).

[16] T. Das, S. J. Heggheim, M. Dudek, A. Verheyleweghen, and J. Jäschke, *Optimal operation of a subsea separation system including a coalescence based gravity separator model and a produced water treatment section,* Industrial & Engineering Chemistry Research **58**, 4168 (2019).

[17] P. D. Løhndorf, *Real-Time Monitoring and Robust Control of Offshore De-oiling Processes,* Ph.D. thesis, Aalborg University, Denmark (2017).

[18] S. Amini, D. Mowla, M. Golkar, and F. Esmaeilzadeh, *Mathematical modelling of a hydrocyclone for the down-hole oil–water separation (dows),* Chemical Engineering Research and Design **90**, 2186 (2012).

[19] S. Liu, Y. Yan, and Y. Gao, *Optimization of geometry parameters with separation efficiency and flow split ratio for downhole oil-water hydrocyclone,* Thermal Science and Engineering Progress **8**, 370 (2018).

[20] X. Zeng, L. Zhao, W. Zhao, M. Hou, F. Zhu, G. Fan, and C. Yan, *Experimental study on a novel axial separator for oil–water separation,* Industrial & Engineering Chemistry Research **59**, 21177 (2020).

[21] J. E. Hamza, H. H. Al-Kayiem, and T. A. Lemma, *Experimental investigation of the separation performance of oil/water mixture by compact conical axial hydrocyclone,* Thermal Science and Engineering Progress **17**, 100358 (2020).

[22] C. Matthews, R. Chachula, B. Peachey, and S. Solanki, *Application of downhole oil/water separation systems in the alliance field,* in *SPE Health, Safety and Environment in Oil and Gas Exploration and Production Conference* (New Orleans, Louisiana, 1996).

[23] O. O. Ogunsina and M. L. Wiggins, *A review of downhole separation technology,* in *SPE Production and Operations Symposium* (Oklahoma City, Oklahoma, 2005).

[24] P. Wei, D. Wang, P. Niu, C. Pang, and M. Liu, *A novel centrifugal gas liquid pipe separator for high velocity wet gas separation,* International Journal of Multiphase Flow **124**, 103190 (2020).

[25] E. Rosa, F. França, and G. Ribeiro, *The cyclone gas–liquid separator: operation and mechanistic modeling,* Journal of Petroleum Science and Engineering **32**, 87 (2001).

[26] S. Liu, L. le Yang, D. Zhang, and J. yu Xu, *Separation characteristics of the gas and liquid phases in a vane-type swirling flow field,* International Journal of Multiphase Flow **107**, 131 (2018).

[27] S. J. Ohrem, T. T. Kristoffersen, and C. Holden, *Adaptive feedback linearizing control of a gas liquid cylindrical cyclone,* in *2017 IEEE Conference on Control Technology and Applications (CCTA)* (Hawaii, USA, 2017).

[28] L. Yang, J. Zhang, Y. Ma, J. Xu, and J. Wang, *Experimental and numerical study of separation characteristics in gas-liquid cylindrical cyclone,* Chemical Engineering Science **214**, 115362 (2020).

[29] G. Wang, C. Yan, G. Fan, J. Wang, J. Xu, X. Zeng, and A. Liu, *Experimental study on a swirl-vane separator for gas–liquid separation,* Chemical Engineering Research and Design **151**, 108 (2019).

[30] S. S. Kolla, R. S. Mohan, and O. Shoham, *A study on the effect of fluid properties and watercut on liquid carry-over in gas-liquid cylindrical cyclone compact separators,* Journal of Fluids Engineering **141**, 091303 (2019).

[31] L. Liu and B. Bai, *Experimental study and similarity analysis of separation efficiency of swirl-vane separator,* Nuclear Engineering and Design **359**, 110442 (2020).

[32] H. Funahashi, K. Hayashi, S. Hosokawa, and A. Tomiyama, *Study on two-phase swirling flows in a gas–liquid separator with three pick-off rings,* Nuclear Engineering and Design **308**, 205 (2016).

[33] T. Matsubayashi, K. Katono, K. Hayashi, and A. Tomiyama, *Effects of swirler shape on swirling annular flow in a gas–liquid separator,* Nuclear Engineering and Design **249**, 63 (2012).

[34] S. Gao, Y. Liu, Y. Fan, and C. Lu, *Experimental assessment on an integral two-stage demister of coupling cyclonic separation and granular bed filtration,* Powder Technology **416**, 118178 (2023).

[35] S. Ouyang, Z. Xiong, J. Zhao, and R. Kang, *Separation efficiency theoretical model of swirl-vane separator based on bidirectional vortex,* Annals of Nuclear Energy **170**, 108984 (2022).

[36] Z. Xiong, M. Lu, M. Wang, H. Gu, and X. Cheng, *Study on flow pattern and separation performance of air–water swirl-vane separator,* Annals of Nuclear Energy **63**, 138 (2014).

[37] J. Yin, Y. Qian, Y. Ma, and D. Wang, *Experimental study on the bubble trajectory in an axial gas-liquid separator applied for tritium removal for molten salt reactors,* Nuclear Engineering and Design **320**, 133 (2017).

[38] J. Yin, Y. Qian, T. Zhang, and D. Wang, *Numerical investigation on the bubble separation in a gas-liquid separator applied in tmsr,* Annals of Nuclear Energy **114**, 122 (2018).

[39] J. Yin, Y. Qian, T. Zhang, and D. Wang, *Measurement on the flow structure of a gas-liquid separator applied in tmsr,* Annals of Nuclear Energy **126**, 20 (2019).

[40] J.-J. Li, Y.-L. Qian, J.-L. Yin, H. Li, W. Liu, and D.-Z. Wang, *Large eddy simulation of unsteady flow in gas–liquid separator applied in thorium molten salt reactor,* Nuclear Science and Techniques **29**, 62 (2018).

[41] S. Wang, L. Gomez, R. Mohan, O. Shoham, G. Kouba, and J. Marrelli, *The state-of-the-art of gas-liquid cylindrical cyclone control technology: From laboratory to field,* Journal of Energy Resources Technology **132**, 032701 (2010).

[42] S. Movafaghian, J. Jaua-Marturet, R. Mohan, O. Shoham, and G. Kouba, *The effects of geometry, fluid properties and pressure on the hydrodynamics of gas–liquid cylindrical cyclone separators,* International Journal of Multiphase Flow **26**, 999 (2000).

[43] G. Kouba, S. Wang, L. Gomez, R. Mohan, and O. Shoham, *Review of the state-of-the-art gas/liquid cylindrical cyclone (glcc) technology – field applications,* in *SPE International Oil and Gas Conference and Exhibition in China* (Beijing, China, 2006).

[44] Y. Tang, Z. Qiao, Y. Cao, F. Si, C. E. Romero, and C. Rubio-Maya, *Numerical analysis of separation performance of an axial-flow cyclone for supercritical co2-water separation in co2 plume geothermal systems,* Separation and Purification Technology **248**, 116999 (2020).

[45] M. Lazrag, D. L. Mejia-Mendez, C. Lemaitre, P. H. E. Stafford, R. Hreiz, R. Privat, A. Hannachi, and D. Barth, *Thermodynamic and hydrodynamic study of a gas-liquid flow in a cyclone separator downstream supercritical drying,* The Journal of Supercritical Fluids **118**, 27 (2016).

[46] M. P. Escudier, J. Bornstein, and T. Maxworthy, *The dynamics of confined vortices,* Proceedings of the Royal Society of London. Series A, Mathematical and Physical Sciences **382**, 335 (1982).

[47] O. Kitoh, *Experimental study of turbulent swirling flow in a straight pipe,* Journal of Fluid Mechanics **225**, 445 (1991).

[48] S. V. Alekseenko, P. A. Kuibin, V. L. Okulov, and S. I. Shtork, *Helical vortices in swirl flow,* Journal of Fluid Mechanics **382**, 195 (1999).

[49] S. ying Shi and J. yu Xu, *Flow field of continuous phase in a vane-type pipe oil–water separator,* Experimental Thermal and Fluid Science **60**, 208 (2015).

[50] T. Husveg, O. Rambeau, T. Drengstig, and T. Bilstad, *Performance of a deoiling hydrocyclone during variable flow rates,* Minerals Engineering **20**, 368 (2007).

[51] R. Hreiz, C. Gentric, N. Midoux, R. Lainé, and D. Fünfschilling, *Hydrodynamics and velocity measurements in gas–liquid swirling flows in cylindrical cyclones,* Chemical Engineering Research and Design **92**, 2231 (2014).

[52] J. D. Arthur, B. G. Langhus, and C. Patel, *Technical summary of oil & gas produced water treatment technologies*, Tech. Rep. (All Consulting, LLC, Tulsa, OK, 2005).

[53] H. fei Liu, J. yu Xu, J. Zhang, H. qiang Sun, J. Zhang, and Y. xiang Wu, *Oil/water separation in a liquid-liquid cylindrical cyclone,* Journal of Hydrodynamics **24**, 116 (2012).

[54] C. Oropeza-Vazquez, E. Afanador, L. Gomez, S. Wang, R. Mohan, O. Shoham, and G. Kouba, *Oil-water separation in a novel liquid-liquid cylindrical cyclone (llcc) compact separator – experiments and modeling,* Journal of Fluids Engineering **126**, 553 (2004).

[55] L. Yang, L. Zou, Y. Ma, J. Wang, and J. Xu, *Breakup, coalescence, and migration regularity of bubbles under gas–liquid swirling flow in gas–liquid cylindrical cyclone,* Industrial & Engineering Chemistry Research **59**, 2068 (2020).

[56] H. K. Eidt, C. C. Rodrigues, R. Dunaiski, C. Y. Ofuchi, D. Bertoldi, M. J. da Silva, F. Neves Jr, P. H. Santos, and R. E. Morales, *Numerical and experimental analysis of vertically ascending swirling liquid film flow,* Journal of Petroleum Science and Engineering **206**, 109030 (2021).

[57] A. Belaidi and M. Thew, *The effect of oil and gas content on the controllability and separation in a de-oiling hydrocyclone,* Chemical Engineering Research and Design **81**, 305 (2003).

[58] P. Durdevic, S. Pedersen, M. Bram, D. Hansen, A. Hassan, and Z. Yang, *Control oriented modeling of a de-oiling hydrocyclone,* IFAC-PapersOnLine **48**, 291 (2015).

[59] M. V. Bram, A. A. Hassan, D. S. Hansen, P. Durdevic, S. Pedersen, and Z. Yang, *Experimental modeling of a deoiling hydrocyclone system,* in *2015 20th International Conference on Methods and Models in Automation and Robotics (MMAR)* (Miedzyzdroje, Poland, 2015).

[60] S. Wang, R. S. Mohan, O. Shoham, J. D. Marrelli, and G. E. Kouba, *Control system simulators for gas-liquid cylindrical cyclone separators,* Journal of Energy Resources Technology **122**, 177 (2000).

[61] S. Wang, R. S. Mohan, O. Shoham, J. D. Marrelli, and G. E. Kouba, *Performance improvement of gas liquid cylindrical cyclone separators using integrated level and pressure control systems,* Journal of Energy Resources Technology **122**, 185 (2000).

[62] L. Hansen, P. Durdevic, K. L. Jepsen, and Z. Yang, *Plant-wide optimal control of an offshore de-oiling process using mpc technique,* IFAC-PapersOnLine **51**, 144 (2018).

[63] S. Wang, *Dynamic simulation, experimental investigation and control system design of gas-liquid cylindrical cyclone separators*, Ph.D. thesis, The University of Tulsa, United States (2000).

[64] W. Warsito and L.-S. Fan, *Measurement of real-time flow structures in gas–liquid and gas–liquid–solid flow systems using electrical capacitance tomography (ect),* Chemical Engineering Science **56**, 6455 (2001).

[65] X. Yan, X. Li, J. Li, L. Wang, H. Zhang, and Y. Cao, *Investigating the gas holdup in a gas-liquid cyclonic flotation column through the electrical resistance tomography,* International Journal of Coal Preparation and Utilization **42**, 3601 (2022).

[66] Z. Almutairi, F. M. Al-Alweet, Y. A. Alghamdi, O. A. Almisned, and O. Y. Alothman, *Investigating the characteristics of two-phase flow using electrical capacitance tomography (ect) for three pipe orientations,* Processes **8**, 51 (2020).

[67] R. Banasiak, R. Wajman, T. Jaworski, P. Fiderek, H. Fidos, J. Nowakowski, and D. Sankowski, *Study on two-phase flow regime visualization and identification using 3d electrical capacitance tomography and fuzzy-logic classification,* International Journal of Multiphase Flow **58**, 1 (2014).

[68] Z. Xu, F. Wu, X. Yang, and Y. Li, *Measurement of gas-oil two-phase flow patterns by using cnn algorithm based on dual ect sensors with venturi tube,* Sensors **20**, 1200 (2020).

[69] Y. Arellano, A. Hunt, O. Haas, and L. Ma, *On the life and habits of gas-core slugs: characterisation of an intermittent horizontal two-phase flow,* Journal of Natural Gas Science and Engineering **82**, 103475 (2020).

[70] F. Tao, H. Jin, G. He, X. Guo, L. Ma, and R. Zhang, *Two-phase flow characteristics of gas-liquids in microchannels using electrical resistance tomography,* Heat and Mass Transfer **58**, 99 (2022).

[71] V. Mosorov, G. Rybak, and D. Sankowski, *Plug regime flow velocity measurement problem based on correlability notion and twin plane electrical capacitance tomography: Use case,* Sensors **21**, 2189 (2021).

[72] S. Razzak, S. Barghi, and J.-X. Zhu, *Electrical resistance tomography for flow characterization of a gas–liquid–solid three-phase circulating fluidized bed,* Chemical Engineering Science **62**, 7253 (2007).

[73] C. Tan, Y. Murai, W. Liu, Y. Tasaka, F. Dong, and Y. Takeda, *Ultrasonic doppler technique for application to multiphase flows: A review,* International Journal of Multiphase Flow **144**, 103811 (2021).

[74] L. Fang, Q. Zeng, F. Wang, Y. Faraj, Y. Zhao, Y. Lang, and Z. Wei, *Identification of two-phase flow regime using ultrasonic phased array,* Flow Measurement and Instrumentation **72**, 101726 (2020).

[75] N. Li, M. Cao, K. Xu, J. Jia, and H. Du, *Ultrasonic transmission tomography sensor design for bubble identification in gas-liquid bubble column reactors,* Sensors **18**, 4256 (2018).

[76] M. Banowski, M. Beyer, L. Szalinski, D. Lucas, and U. Hampel, *Comparative study of ultrafast x-ray tomography and wire-mesh sensors for vertical gas–liquid pipe flows,* Flow Measurement and Instrumentation **53**, 95 (2017).

[77] Z. Zhang, M. Bieberle, F. Barthel, L. Szalinski, and U. Hampel, *Investigation of upward cocurrent gas–liquid pipe flow using ultrafast x-ray tomography and wire-mesh sensor,* Flow Measurement and Instrumentation **32**, 111 (2013).

[78] A. Aliseda and T. J. Heindel, *X-ray flow visualization in multiphase flows,* Annual Review of Fluid Mechanics **53**, 543 (2021).

[79] J. H. Collins, A. J. Sederman, L. F. Gladden, M. Afeworki, J. D. Kushnerick, and H. Thomann, *Characterising gas behaviour during gas–liquid co-current up-flow in packed beds using magnetic resonance imaging,* Chemical Engineering Science **157**, 2 (2017).

[80] N. Daidzic, E. Schmidt, M. Hasan, and S. Altobelli, *Gas–liquid phase distribution and void fraction measurements using mri,* Nuclear Engineering and Design **235**, 1163 (2005).

[81] L. F. Gladden and A. J. Sederman, *Recent advances in flow mri,* Journal of Magnetic Resonance **229**, 2 (2013).

[82] T. Rymarczyk and J. Sikora, *Applying industrial tomography to control and optimization flow systems,* Open Physics **16**, 332 (2018).

[83] U. Hampel, L. Babout, R. Banasiak, E. Schleicher, M. Soleimani, T. Wondrak, M. Vauhkonen, T. Lähivaara, C. Tan, B. Hoyle, and A. Penn, *A review on fast tomographic imaging techniques and their potential application in industrial process control,* Sensors **22**, 2309 (2022).

[84] R. Wajman, *Computer methods for non-invasive measurement and control of two-phase flows: a review study,* Journal of Information Technology and Control **48**, 464 (2019).

[85] Z. Ren, A. Kowalski, and T. Rodgers, *Measuring inline velocity profile of shampoo by electrical resistance tomography (ert),* Flow Measurement and Instrumentation **58**, 31 (2017).

[86] I. Ismail, J. Gamio, S. Bukhari, and W. Yang, *Tomography for multi-phase flow measurement in the oil industry,* Flow Measurement and Instrumentation **16**, 145 (2005).

[87] M. Mallach, M. Gevers, P. Gebhardt, and T. Musch, *Fast and precise soft-field electromagnetic tomography systems for multiphase flow imaging,* Energies **11**, 1199 (2018).

[88] M. A. Sattar, M. M. Garcia, R. Banasiak, L. M. Portela, and L. Babout, *Electrical resistance tomography for control applications: Quantitative study of the gas-liquid distribution inside a cyclone,* Sensors **20**, 6069 (2020).

[89] M. A. Sattar, *Tomography-Based Approaches for Process Visualization and Control: Exemplary Case of Inline Fluid Separation*, Ph.D. thesis, Lodz University Of Technology, Poland (2021).

[90] M. A. Sattar, M. M. Garcia, L. M. Portela, and L. Babout, *A fast electrical resistivity-based algorithm to measure and visualize two-phase swirling flows,* Sensors **22**, 1834 (2022).

[91] S. K. Star, *Pressure distribution in a liquid-liquid cyclone separator*, Master's thesis, Delft University of Technology, the Netherlands (2016).

[92] R. E. Vieira, N. R. Kesana, C. F. Torres, B. S. McLaury, S. A. Shirazi, E. Schleicher, and U. Hampel, *Experimental investigation of horizontal gas-liquid stratified and annular flow using wire-mesh sensor,* Journal of Fluids Engineering **136**, 121301 (2014).

[93] M. J. da Silva, E. N. dos Santos, U. Hampel, I. H. Rodriguez, and O. M. H. Rodriguez, *Phase fraction distribution measurement of oil-water flow using a capacitance wire-mesh sensor,* Measurement Science and Technology **22**, 104020 (2011).

[94] I. Rodriguez, H. Velasco Peña, A. Bonilla Riaño, R. Henkes, and O. Rodriguez, *Experiments with a wire-mesh sensor for stratified and dispersed oil-brine pipe flow,* International Journal of Multiphase Flow **70**, 113 (2015).

[95] E. N. dos Santos, T. P. Vendruscolo, R. E. M. Morales, E. Schleicher, U. Hampel, and M. J. da Silva, *Dual-modality wire-mesh sensor for the visualization of three-phase flows,* Measurement Science and Technology **26**, 105302 (2015).

[96] H. Velasco Peña and O. Rodriguez, *Applications of wire-mesh sensors in multiphase flows,* Flow Measurement and Instrumentation **45**, 255 (2015).

[97] H.-M. Prasser, A. Böttger, and J. Zschau, *A new electrode-mesh tomograph for gas–liquid flows,* Flow Measurement and Instrumentation **9**, 111 (1998).

[98] M. Hamdan and Z. Gao, *A novel pid controller for pneumatic proportional valves with hysteresis,* in *Conference Record of the 2000 IEEE Industry Applications Conference. Thirty-Fifth IAS Annual Meeting and World Conference on Industrial Applications of Electrical Energy (Cat. No.00CH37129)* (Rome, Italy, 2000).

[99] *Control Valve Handbook*, 5th ed. (Emerson Automation Solutions, 2019).

[100] S. Hall, *Rules of Thumb for Chemical Engineers*, 5th ed. (Butterworth-Heinemann, 2012).

[101] G. P. Das, *Hydraulic Engineering : Fundamental Concepts* (Momentum Press, 2015).

[102] H. Cheng, J. Hills, and B. Azzorpardi, *A study of the bubble-to-slug transition in vertical gas-liquid flow in columns of different diameter,* International Journal of Multiphase Flow **24**, 431 (1998).

[103] R. Kaji, B. Azzopardi, and D. Lucas, *Investigation of flow development of co-current gas–liquid vertical slug flow,* International Journal of Multiphase Flow **35**, 335 (2009).

[104] B. Wu, M. Firouzi, T. Mitchell, T. E. Rufford, C. Leonardi, and B. Towler, *A critical review of flow maps for gas-liquid flows in vertical pipes and annuli,* Chemical Engineering Journal **326**, 350 (2017).

[105] G. F. Hewitt and D. N. Roberts, *Studies of two-phase flow patterns by simultaneous x-ray and flast photography*, Tech. Rep. AERE-M-2159 (Atomic Energy Research Establishment, Harwell, England (United Kingdom), 1969).

[106] Y. Taitel, D. Barnea, and A. E. Dukler, *Modelling flow pattern transitions for steady upward gas-liquid flow in vertical tubes,* AIChE Journal **26**, 345 (1980).

[107] K. Mishima and M. Ishii, *Flow regime transition criteria for upward two-phase flow in vertical tubes,* International Journal of Heat and Mass Transfer **27**, 723 (1984).

[108] D. Barnea, *A unified model for predicting flow-pattern transitions for the whole range of pipe inclinations,* International Journal of Multiphase Flow **13**, 1 (1987).

[109] C. T. Crowe, *Multiphase flow handbook* (CRC Press, 2005).

[110] H. Shakutsui, K. Watanabe, H. Onari, T. Saga, and H. Kadowaki, *Flow patterns in swirl gas-liquid two-phase flow in a vertical pipe,* in *Proceedings of the 4th JSME-KSME Thermal Engineering Conference, Kobe, Japan* (2000).

[111] H. Shakutsui, K. Hayashi, and T. Suzuki, *Flow patterns of gas-liquid two-phase swirling flow in a vertical pipe,* Japanese journal of multiphase flow **24**, 305 (2010).

[112] L. Liu and B. Bai, *Flow regime identification of swirling gas-liquid flow with image processing technique and neural networks,* Chemical Engineering Science **199**, 588 (2019).

[113] L. Liu, K. Wang, and B. Bai, *Experimental study on flow patterns and transition criteria for vertical swirling gas-liquid flow,* International Journal of Multiphase Flow **122**, 103113 (2020).

[114] Y. Yang, H. Hu, H. Wang, C. Zhang, B. Yang, and H. Zhao, *Study on characteristics of phase-isolation caused by different classic axial flow swirlers in upward vertical gas-liquid two-phase flow,* Experimental Thermal and Fluid Science **150**, 111031 (2024).

[115] W. Liu, X. Lv, and B. Bai, *The effect of swirl on transition from churn flow to annular flow in an intermediate diameter pipe,* Experimental Thermal and Fluid Science **109**, 109861 (2019).

[116] L. Liu and B. Bai, *A mechanistic model for the prediction of swirling annular flow pattern transition,* Chemical Engineering Science **199**, 405 (2019).

[117] W. Liu, X. Lv, and B. Bai, *Axial development of air–water annular flow with swirl in a vertical pipe,* International Journal of Multiphase Flow **124**, 103165 (2020).

[118] W. Liu, X. Lv, H. Zhou, and X. Dou, *The effect of decay on churn flow transition in a vertical gas–liquid swirling flow,* Chemical Engineering Science **259**, 117843 (2022).

[119] L. Liu, J. Zhang, S. Liu, K. Wang, and H. Gu, *Decay law and swirl length of swirling gas-liquid flow in a vertical pipe,* International Journal of Multiphase Flow **137**, 103570 (2021).

[120] M. Escudier, *Vortex breakdown: Observations and explanations,* Progress in Aerospace Sciences **25**, 189 (1988).

[121] W. Steenbergen and J. Voskamp, *The rate of decay of swirl in turbulent pipe flow,* Flow Measurement and Instrumentation **9**, 67 (1998).

[122] G. B. Wallis, *One-dimensional two-phase flow* (McGraw-Hill, 1969).

[123] A. Sarrafi, M. Jamialahmadi, H. Müller-Steinhagen, and J. M. Smith, *Gas holdup in homogeneous and heterogeneous gas—liquid bubble column reactors,* The Canadian Journal of Chemical Engineering **77**, 11 (1999).

[124] A. D. Burns, T. Frank, I. Hamill, and J.-M. Shi, *The favre averaged drag model for turbulent dispersion in eulerian multi-phase flows,* in *5th International Conference on Multiphase Flow, ICMF'04* (Yokohama, Japan, 2004).

[125] N. Lubchenko, B. Magolan, R. Sugrue, and E. Baglietto, *A more fundamental wall lubrication force from turbulent dispersion regularization for multiphase cfd applications,* International Journal of Multiphase Flow **98**, 36 (2018).

[126] G. D. Scott, *Packing of spheres: packing of equal spheres,* Nature **188**, 908 (1960).

[127] R. Rzehak and E. Krepper, *Cfd modeling of bubble-induced turbulence,* International Journal of Multiphase Flow **55**, 138 (2013).

[128] G. Riboux, F. Risso, and D. Legendre, *Experimental characterization of the agitation generated by bubbles rising at high reynolds number,* Journal of Fluid Mechanics **643**, 509 (2010).

[129] F. Chang and V. Dhir, *Turbulent flow field in tangentially injected swirl flows in tubes,* International Journal of Heat and Fluid Flow **15**, 346 (1994).

[130] J. van 't Westende, H. Kemp, R. Belt, L. Portela, R. Mudde, and R. Oliemans, *On the role of droplets in cocurrent annular and churn-annular pipe flow,* International Journal of Multiphase Flow **33**, 595 (2007).

[131] R. Belt, J. Van't Westende, and L. Portela, *Prediction of the interfacial shear-stress in vertical annular flow,* International Journal of Multiphase Flow **35**, 689 (2009).

[132] R. Koto, R. Kurimoto, A. Imaizumi, K. Hayashi, and A. Tomiyama, *Effects of swirl intensity on interfacial and wall friction factors of annular flows in a vertical pipe,* Nuclear Engineering and Design **399**, 112001 (2022).

[133] H. Funahashi, K. Vierow Kirkland, K. Hayashi, S. Hosokawa, and A. Tomiyama, *Interfacial and wall friction factors of swirling annular flow in a vertical pipe,* Nuclear Engineering and Design **330**, 97 (2018).

[134] W. Liu and B. Bai, *Transition from bubble flow to slug flow along the streamwise direction in a gas–liquid swirling flow,* Chemical Engineering Science **202**, 392 (2019).

[135] J. O. Hinze, *Fundamentals of the hydrodynamic mechanism of splitting in dispersion processes,* AIChE Journal **1**, 289 (1955).

[136] T. Das and J. Jäschke, *Modeling and control of an inline deoiling hydrocyclone,* IFAC PapersOnLine **51**, 138 (2018).

[137] M. V. K G, C. Holden, and S. Skogestad, *A first-principles approach for control-oriented modeling of de-oiling hydrocyclones,* Industrial & Engineering Chemistry Research **59**, 18937 (2020).

[138] N. Meldrum, *Hydrocyclones: A solution to produced water treatment,* in *Offshore Technology Conference* (Houston, Texas, 1987).

[139] I. Cox, *Characterization of the Interplay between Separation Efficiency, Gas Core Size and Pressure Drop in a Gas-Liquid Inline Swirl Separator*, Bachelor's thesis, Delft University of Technology, the Netherlands (2021).

[140] M. M. Garcia, M. A. Sattar, H. Atmani, D. Legendre, L. Babout, E. Schleicher, U. Hampel, and L. M. Portela, *Towards tomography-based real-time control of multiphase flows: A proof of concept in inline fluid separation,* Sensors **22**, 4443 (2022).

[141] J. Yin, J. Li, Y. Ma, H. Li, W. Liu, and D. Wang, *Study on the air core formation of a gas-liquid separator,* Journal of Fluids Engineering **137**, 091301 (2015).

[142] N. Otsu, *A threshold selection method from gray-level histograms,* IEEE transactions on systems, man, and cybernetics **9**, 62 (1979).

[143] M. L. Lowe and P. H. Kutt, *Refraction through cylindrical tubes,* Experiments in Fluids **13**, 315 (1992).

[144] M. Hall, *The structure of concentrated vortex cores,* Progress in Aerospace Sciences **7**, 53 (1966).

[145] A. Mager, *Dissipation and breakdown of a wing-tip vortex,* Journal of Fluid Mechanics **55**, 609 (1972).

[146] L. Keviczkyn, R. Bars, J. Hetthéssy, and C. Bányász, *Control Engineering* (Springer Singapore, 2019).

OUTREACH

Journal Papers:

6. **M. M. Garcia** and L. M. Portela, *Mechanistic Models for Vertical Upward Swirling Gas-Liquid Pipe Flow*, in preparation to be submitted to the International Journal of Multiphase Flow.

5. **M. M. Garcia** and L. M. Portela, *An Experimental Study on Swirl Intensity and Decay in Vertical Upward Swirling Gas-Liquid Pipe-Flow Patterns*, in preparation to be submitted to the International Journal of Multiphase Flow.

4. **M. M. Garcia**, M. A. Sattar, H. Atmani, D. Legendre, L. Babout, E. Schleicher, U.Hampel, and L. M. Portela, *Towards Tomography-Based Real-Time Control of Multiphase Flows: A Proof of Concept in Inline Fluid Separation*, Sensors **22**, 4443 (2022).

3. M. A. Sattar, **M. M. Garcia**, L. M. Portela, and L. Babout, *A Fast Electrical Resistivity-Based Algorithm to Measure and Visualize Two-Phase Swirling Flows*, Sensors **22**, 1834 (2022).

2. M. A. Sattar, **M. M. Garcia**, R. Banasiak, L. M. Portela, and L. Babout, *Electrical Resistance Tomography for Control Applications: Quantitative Study of the Gas-Liquid Distribution inside A Cyclone*, Sensors **20**, 6069 (2020).

1. B. Sahovic, H. Atmani, M. A. Sattar, **M. M. Garcia**, E. Schleicher, D. Legendre, E. Climent, R. Zamansky, A. Pedrono, L. Babout, R. Banasiak, L. M. Portela, and U. Hampel, *Controlled Inline Fluid Separation Based on Smart Process Tomography Sensors*, Chemie Ingenieur Technik **92** (2020).

Conference Papers:

2. **M. M. Garcia** and L. M. Portela *System Dynamics and Tomography-Based Control of a Gas-Liquid Inline Swirl Separator*, Proceedings of the ASME 2022 Fluids Engineering Division Summer Meeting (Toronto, Ontario, Canada, 2022).

1. **M.M. Garcia**, B. Sahovic, M. A. Sattar, H. Atmani, E. Schleicher, U. Hampel, L. Babout, D. Legendre, and L. M. Portela, *Control of a Gas-Liquid Inline Swirl Separator Based on Tomographic Measurements*, IFAC-PapersOnLine **53**, 11483 (2020).

Videos:

2. **M. M. Garcia** and L. M. Portela, *Swirl Effects On Gas-Liquid Upward Vertical Pipe Flow*, Journal of Fluids Engineering **145** (2022). First place winner of the Flow Visualization Competition of the ASME 2022 Fluids Engineering Division Summer Meeting (FEDSM 2022).
`youtu.be/Qa60JqxuAJE`

1. **M. M. Garcia** and L. M. Portela, *TOMOCON Inline Fluid Separation Demonstration (2022).*
`youtu.be/3ymh7SpQTWQ`

ACKNOWLEDGEMENTS

A PhD is a long project and many people have contributed to this journey over the last years.

I would like to start with the people most involved in this project besides me. **Luis**, thank you for all our interesting scientific discussions, often long and outside office hours, inside and outside the scope of this thesis. Our talks substantially contributed to my understanding of fluid dynamics, particularly in the multiphase flow field. I also truly admire your academic ethics. **Chris**, thanks for helping me to plan my dissertation and to keep up with its progress. Without your fast and valuable feedback I would not have been able to complete my thesis within the PhD-in-4 deadline.

This PhD project involved the construction of a large experimental facility, which was only possible with the help of **Evert**, that, together with **Kevin** (from DEMO in the Reactor), helped me to design it and was deeply involved in its construction, and **Christiaan**, who supported us with the electrical connections of the flow loop and set up the first LabVIEW code to run it. **Christiaan**, a special thanks for the Rammstein concert in 2022, it was great!

Education is a big part of the PhD cycle in TU Delft. **David** and **Bijoy**, it was great working in the LO2 courses with you. To my students, **Dion** and **Bart**, your Master thesis projects were essential to my current understanding of the swirling gas-liquid flows physics, and the foundation stone to the mechanistic models proposed in chapter 3. **Isaak**, despite the short time, your interesting Bachelor thesis had a strong contribution to chapter 4. I also truly liked the Schrobbelèr that you gifted me.

Taking a few steps back to before I moved to the Netherlands, I would like to thank my bachelor's and master's thesis supervisor, **Marcelo**, for recommending me this PhD position, and **Jennifer** for helping me arrange my first house in Delft with DUWO. **Matheus**, without your incentive I would not have started a scientific initiation project during our mechanical engineering studies at UNICAMP, sparkling my passion for research and ultimately leading me to the decision of pursuing a PhD.

I shared my time in the Transport Phenomena (TP) group of TU Delft with many colleagues during my PhD trajectory. **Davi**, thanks for the great trips and beers that we shared in our first months in the Netherlands. **Rense**, thanks for the dinners and movie night that you organized. It was a pleasure to meet you, by chance, in Izmir for **Ece** and **Mert**'s wedding last year. **Xiaolin**, thanks for the nice moments and delicious hotpots. One of my favorite memories in TP is from when we tried herring for the first time and had to chug a lot of beer to overcome its taste. **Elin**, thanks for all the deep conversations, dinners, cycling trips, museums, plants and snowmen that we shared so far. It is quite funny how we ended up unintentionally flipping our subjects, with you going to the continuum regime and me moving to the rarefied. It was a pleasure to be your paranymph and I look forward to having you and your family in my defense. **Manas**, **Kosta** and **Inês**, thanks for all the events that you invited me over the years. You (and your houses) played a big role in my social life during the PhD. Thanks to you I had company for New Year's Eve during covid and ice-skated for the first time. **Sid**, thanks for introducing me to Brazilian music, some-

thing that I have not payed enough attention before. Let us not forget the great metal talks that we also had. I really like your computational art and I hope that you are having a nice life. **Manu**, it was a pleasure sharing my weekends in TP with you. It is a bit early, but Happy New Year! **Artem**, thanks for sharing the office with me during your final PhD year and inviting me to your wedding. We had great chats (with many complains about the PhD life) and I hope that you are doing well in ASML. **Lorenz**, thanks for lending me the fairy costume in your first Halloween party in Delft. It was a pleasure doing the first Graduate School courses with you. Keep up with the blueberry breakfasts! **Debasish**, thanks for the chats about Dresden, the trip to Leiden, and to teach me that there is life beyond a PhD. **Brice**, our slow motion flow recordings in a random day ended up becoming the cover of this thesis. **Jorrit**, it was a pleasure to help you remove the trees of your family's garden for an ice cream a few years ago. Jokes apart, thanks for all the dinners that we shared, for taking me to watch my first soccer game in a stadium (quite an achievement considering that I lived in Brazil for almost 25 years), and for the dutch translation of my Summary (Samenvatting). Our long walk in the cold rain in early January 2025, followed by tasty warm pancakes in your favorite spot, powered me to conclude this thesis. Thanks for all the support that you gave me so far, specially in this last year, and let's keep feeding this great friendship in the next ones! **Saikat**, thanks for introducing me to espresso martini and for withstanding my "pub philosophy". We should also not forget the good moments that we spent together, as the TP barbecue and the dinner at **Elin**'s. It was nice to meet you in Netherlands earlier this year, **Athanasia** and I are still enjoying the Jardin Bleu tea that you gifted us. **Yanyan**, it was a pleasure to share the boat in the TP barbecue with you. **Christel**, **Jan-Willem**, **Vojtech** and **Yu-Fan**, you brought a lot of energy, physical activities, caipirinha consumption and joy to TP. Thanks for all the dinosaur-themed gifts that you gave me when I turned 29. **Juliana**, it was nice having you around during your short exchange. I was happy to hear that you recently defended your PhD. **Dohni** and **Ruipeng**, we shared a short but joyful time in F2.150. **Maria**, thanks for all the chats that we had in the corridors and for making my office a bit little less disorganized. **Sandra**, thanks for helping me whenever I needed and for always making sure that I get my hospitality extensions on time. **Sasa**, **Valeria**, **Annekatrien**, **Maulik**, **Iman**, **Romana**, **Lars**, **Alireza**, **Nathalie**, **Aron**, **Luca** and **Daiqi**, thanks for all the nice moments that we shared in TP. For the ones that started in TP after I was no longer going to the office, good luck with your PhD projects! I do not want to sound too pessimistic, but you will probably need it.

The strong collaboration with academic and industrial partners of TOMOCON brought me additional colleagues outside Delft. **Laurent** and **Radek**, thanks for hosting me in the TU Lodz in 2019, and for all the help with the Electrical Resistance Tomography sensor afterwards. I could learn a lot about Tomography in the month that I spent in your lab. **Muhammad**, it was nice working with you during my visit to Lodz and during your consecutive visits to Delft. I am happy that we could get two nice publications, and part of chapter 2, from our cooperation. **Guru**, thanks for the nice dinner in Lodz. You have a lovely family. **Uwe** and **Eckhard**, thanks for hosting me for two months in HZDR back in 2020, and for all the help me with the wire-mesh sensor afterwards. **Felipe**, it was great sharing my time in Dresden with you. **Rafael,** our hike in Nationalpark Sächsische Schweiz was fantastic. **Rainer**, thanks for hosting me for two months in Linde in 2021. **Omar** and **Burak**, I had a lot of fun sharing the lab and lunches with you while I was in Munich.

Athanasia, thanks for being a great partner in the last 4 years. Thanks to you I exercised more (the 10 km run in Leiden was hard but fun), traveled around the world (so many weddings!), tried questionable foods (e.g., goat organs and snails), risked my life climbing Mytikas without proper safety gear (there must be some mountain goat DNA running in your family), got new friends and improved my diet (although now it has too much zucchini).

Cederik and **Dirk**, thanks for all the support that you gave me in TNO in the first weeks of 2025. Without your help, **Jorrit**'s and **Athanasia**'s, I would not have been able to complete this thesis. **Marcelo** and **Leonardo**, meeting you in Amsterdam in the end of January gave me an extra push to finish it.

Aos meus amigos de infância **Pedro Ernesto**, **Thales**, **Luiz Guilherme**, **Cleyton**, **Raoni** e **Orlando**: apesar do longo tempo escrevendo, lancei meu livro antes do The Winds of Winter, para a vossa infelicidade. Brincadeiras a parte, obrigado por todo o suporte inconvencional de vocês e me desculpe por não estar tão presente quanto eu gostaria nos últimos anos.

Finalmente, eu gostaria de agradecer à minha família por todo o apoio contínuo. Em particular aos meus pais **Valdomiro** e **Carmen**, sem o esforço de vocês eu não teria tido a boa educação que me trouxe até aqui. O meu mais sincero muito obrigado.

Matheus Martinez Garcia
Delft, 05 September 2025

About the Author

Matheus Martinez Garcia was born on 3 September 1994 in Jundiaí, Brazil. He finished his high school in Colégio São Vicente de Paulo in 2011. In 2013, he joined the School of Mechanical Engineering of the State University of Campinas (UNICAMP), where he obtained his engineering degree in 2017 and Master's degree in 2018. His Master's project was focused on numerical simulations (CFD) of gas-liquid slug flows.

In 2019, Matheus moved to the Netherlands to pursue his PhD in the Transport Phenomena group of the Faculty of Applied Sciences of Delft University of Technology, where he worked on a multidisciplinary project combining multiphase flow physics, industrial tomography, system dynamics and real-time control. During his PhD project, Matheus had short secondments in Lodz University of Technology (1 month), Helmholtz-Zentrum Dresden-Rossendorf (2 months) and Linde (2 months).

Since 2023, he has been working as Flow and Thermal Scientist in the Semicon Equipment Metrology department of the Dutch Organization for Applied Scientific Research, TNO.